Experimentele studie en numerieke simulatie
van materiaalmigratie in de VISIONI-plasmasimulator

Experimental Study and Numerical Simulation
of Material Migration in the VISIONI Plasma Simulator

Olivier Van Hoey

Promotor: prof. dr. ir. G. Van Oost
Proefschrift ingediend tot het behalen van de graad van
Doctor in de Ingenieurswetenschappen: Toegepaste Natuurkunde

Vakgroep Toegepaste Fysica
Voorzitter: prof. dr. ir. C. Leys
Faculteit Ingenieurswetenschappen en Architectuur
Academiejaar 2014 - 2015

UNIVERSITEIT
GENT

ISBN 978-90-8578-728-0
NUR 924, 928
Wettelijk depot: D/2014/10.500/74

Partners

Ghent University
Faculty of Engineering and Architecture
Department of Applied Physics
Sint-Pietersnieuwstraat 41 B4
9000 Ghent
Belgium

This work was carried out at

SCK-CEN
Nuclear Materials Science
Structural Materials
Boeretang 200
2400 Mol
Belgium

in collaboration with

Forschungszentrum Jülich
Institute of Energy and Climate Research
Leo-Brandt-Straße
52428 Jülich
Germany

and financed by an aspirant grant from

FWO Vlaanderen
Egmontstraat 5
1000 Brussels
Belgium

Examining board

Prof. Dr. Ir. Rik Van de Walle, Chairman
Ghent University

Prof. Dr. Ir. Guido Van Oost, Supervisor
Ghent University

Dr. Inge Uytdenhouwen, Mentor
Belgian Nuclear Research Centre SCK-CEN, Mol

Dr. Andreas Kirschner
Forschungszentrum Jülich

Dr. Dmitry Matveev
Forschungszentrum Jülich

Prof. Dr. Ir. Martine Baelmans
Catholic University of Leuven

Prof. Dr. Ir. Michaël Van Schoor
Royal Military Academy, Brussels

Prof. Dr. Ir. Kim Verbeken
Ghent University

Prof. Dr. Ir. Veronique Van Speybroeck
Ghent University

Prof. Dr. Ir. Jean-Marie Noterdaeme
Ghent University

Prof. Dr. Geert Verdoolaege
Ghent University

Publications

A1 papers

A. Kirschner, H. G. Esser, D. Matveev, **O. Van Hoey**, D. Borodin, A. Galonska, K. Ohya, V. Philipps, A. Pospieszczyk, U. Samm, O. Schmitz, P. Wienhold, the TEXTOR team
Modelling of carbon deposition from CD_4 injection in the far scrape-off layer of TEXTOR
Physica Scripta, Volume T145, December 2011, Article number 014005

O. Van Hoey, A. Kirschner, C. Björkas, D. Borodin, D. Matveev, I. Uytdenhouwen, G. Van Oost
Improved carbon migration modelling with the ERO code
Journal of Nuclear Materials, Volume 438, Supplement, July 2013, Pages S891-S894

D. Matveev, A. Kirschner, H.G. Esser, M. Freisinger, A. Kreter, **O. Van Hoey**, D. Borodin, A. Litnovsky, P. Wienhold, J.W. Coenen, H. Stoschus, V. Philipps, S. Brezinsek, G. Van Oost, the TEXTOR team
Carbon deposition at the bottom of gaps in TEXTOR experiments
Journal of Nuclear Materials, Volume 438, Supplement, July 2013, Pages S775-S779

A. Kirschner, P. Wienhold, D. Borodin, C. Björkas, **O. Van Hoey**, D. Matveev, S. Brezinsek, A. Kreter, M. Laengner, K. Ohya, V. Philipps, A. Pospieszczyk, U. Samm, B. Schweer, TEXTOR team
Studies of impurity migration in TEXTOR by local tracer injection
Journal of Nuclear Materials, Volume 438, Supplement, July 2013, Pages S723-S726

K. Krieger, S. Brezinsek, M. Reinelt, S.W. Lisgo, J.W. Coenen, S. Jachmich, S. Marsen, A. Meigs, G. van Rooij, M. Stamp, **O. van Hoey**, D. Ivanova, T. Loarer, V. Philipps, JET EFDA contributors
Beryllium migration and evolution of first wall surface composition in the JET ILW configuration

Journal of Nuclear Materials, Volume 438, Supplement, July 2013, Pages S262-S266

D. Borodin, M.F. Stamp, A. Kirschner, C. Björkas, S. Brezinsek, J. Miettunen, D. Matveev, C. Silva, **O. Van Hoey**, M. Groth, S. Marsen, V. Philipps, the JET-EFDA contributors
Spectroscopic measurements of Be erosion at JET ILW and interpretation with ERO modelling
Journal of Nuclear Materials, Volume 438, Supplement, July 2013, Pages S267-S271

O. Van Hoey, J. Schuurmans, I. Uytdenhouwen, G. Van Oost
Analytical and experimental determination of the multipole cusp magnetic field in the VISIONI plasmatron
Fusion Engineering and Design, Volume 88, Issues 6-8, October 2013, Pages 661-665

C2 conference abstracts

O. Van Hoey, A. Kirschner, I. Uytdenhouwen, G. Van Oost and R. Chaouadi
Tracing of hydrogen isotopes with the ERO code
13th PFMC Workshop / 1st FEMaS Conference, Rosenheim, May 9th - 13th, 2011

O. Van Hoey, I. Uytdenhouwen, J. Schuurmans and G. Van Oost
Plasma simulation for the VISIONI plasmatron by means of a Monte Carlo particle tracing code
26th NNV-symposium on Plasma Physics and Radiation Technology, 5 and 6 March 2013, Lunteren, The Netherlands

O. Van Hoey, I. Uytdenhouwen, J. Schuurmans and G. Van Oost
Plasma simulation for the VISIONI plasmatron by means of a Monte Carlo particle tracing code
14th International Conference on Plasma-Facing Materials and Components for Fusion Applications, May 13th -17th 2013, Forschungszentrum Juelich, Germany

O. Van Hoey, I. Uytdenhouwen, J. Schuurmans and G. Van Oost
VISIONI plasma simulation with a Monte Carlo particle tracing code
40th EPS Conference on Plasma Physics, July 1st-5th 2013, Espoo, Finland

Acknowledgement

This work could never have been realized without the support of a lot of people. First of all I am very grateful to the Fonds Wetenschappelijk Onderzoek Vlaanderen (FWO) for providing me with an Aspirant grant during these four years. This financial support was of great help for the start of my carrier as a researcher. The administration always went very smoothly and the large working budget allowed me to attend any conference or course of interest for my PhD.

I also wish to thank my Alma Mater Ghent University. I look back with great pleasure to the enriching time I had as a student in Physics and Astronomy. It was also an honour for me to perform my PhD as a student of Ghent University. Many thanks go of course to my supervisor Prof. Dr. Ir. Guido Van Oost. He woke my interest in fusion research during my studies. His advise was of great value for defining my PhD topic. I could always rely on him in case of questions or problems concerning my project. I also wish to thank Anton Nikiforov for helping me with the optical emission spectroscopy measurements at the VISIONI plasma simulator with the overview spectrometer of the Department of Applied Physics.

The major part of my work was performed at the Belgian Nuclear Research Centre (SCK-CEN). It has been really great to work at SCK-CEN during the four years of my PhD and I am sure that I will spend many more interesting years here now that I obtained a contract as a researcher in the radiation dosimetry group. I want to thank in particular my mentor Dr. Inge Uytdenhouwen who kept me on the right track and gave me a lot of interesting ideas concerning the experimental side of my work. Special thanks also go to Johan Schuurmans. Without his help the experimental part of my work would not have been possible. He designed and developed the new sample holder and the movable Langmuir probe for the VISIONI plasma simulator. He also performed a lot of experiments for my PhD and was always there to solve technical issues. Further, I thank Yves Parthoens for his help with the optical profilometry measurements, Willem Leysen for his help with the optical emission spectroscopy and Wouter Van Renterghem for explaining me how to perform the SEM and EDX measurements and helping me with the interpretation of the measurements. I also wish to thank my colleagues and office mates Herman Van Eyck, Wouter Broeckx,

Kris Dylst, Yevhen Zayachuk, Hua Sheng and Klaas Poelmans. It was a pleasure for me to work with all these very nice people.

During my PhD I regularly visited Forschungszentrum Jülich (FZJ). My visits to FZJ were always very helpful for the progress of my PhD. There are a lot of fusion experts working there, both on the experimental and the simulation side. I wish to thank especially Andreas Kirschner, Dmitry Matveev, Dmitry Borodin and Carolina Björkas who were of great help for the ERO code developments and simulations. Despite their often busy schedules they were always willing to make time for discussing my results. I also wish to thank Sebastijan Brezinsek for helping me with interpretation of the experimental optical emission spectroscopy results from TEXTOR, Arkadi Kreter for helping me with the interpretation of the experimental carbon deposition results from TEXTOR and for providing me with the graphite samples for the experiments in VISIONI and Gerald Pintsuk and Gaby Knauf for performing the laser profilometry measurements of the samples exposed in VISIONI. I wish to thank also the other colleagues I met at FZJ. They were all very nice people to work with.

Last but certainly not least, I wish to thank also my family and friends. Their continuous support and interest for what I am doing definitely helped me to persevere during difficult times. I wish to thank in particular my girlfriend Lisanne. We are together now for almost nine fantastic years and I really cannot imagine how I could live without her. She is always there to comfort me when I have a difficult or stressful time and she always supports me. Special thanks also go to my parents. They have always been extremely supportive of the choices I made and I am very grateful to them for giving me all the chances required to get in life where I am now. Without them none of this would have been possible.

Mol, September 2014
Olivier Van Hoey

Contents

Physical constants

pi	π	=	3.14159
base natural logarithm	e	=	2.71828
electron charge	q_e	=	1.60218×10^{-19} C
electron mass	m_e	=	9.10938×10^{-31} kg
Avogadro constant	N_A	=	6.02214×10^{23} mol^{-1}
atomic mass unit	m_u	=	1.66054×10^{-27} kg
vacuum light speed	c	=	2.99792×10^{8} m/s
vacuum permittivity	ϵ_0	=	8.85419×10^{-12} F/m
vacuum permeability	μ_0	=	$4\pi \times 10^{-7}$ H/m
Planck constant	h	=	6.62607×10^{-34} Js
Boltzmann constant	k	=	1.38065×10^{-23} J/K
Richardson constant	A_R	=	1.20173×10^{6} $\mathrm{A/m^2K^2}$
Bohr radius	r_B	=	5.29177×10^{-11} m
Stefan constant	σ	=	5.67037×10^{-8} $\mathrm{Js^{-1}m^{-2}K^{-4}}$

Acronyms

ABR	Allen-Boyd-Reynolds theory for ion collection
BCA	Binary Collision Approximation
BRL	Bernstein-Rabinowitz-Laframboise theory for ion collection
CFC	carbon-fiber composite
CPU	Central Processing Unit
DBTT	ductile-to-brittle transition temperature
EC-JRC	European Commission - Joint Research Centre
EDX	Energy-Dispersive X-ray spectroscopy
EEDF	electron energy distribution function
ELM	edge localized mode
EM	electromagnetic
EPDF	electron probability distribution function
ETHEL	European Tritium Handling Experimental Laboratory
FZJ	Forschungszentrum Jülich
GUI	Graphical User Interface
HPC	High Performance Computing
IR	infrared
ITER	International Thermonuclear Experimental Reactor
LCFS	Last Closed Flux Surface
MC	Monte Carlo
MD	Molecular Dynamics
OML	orbital motion limit theory for ion collection
PDF	probability distribution function
PIC	particle-in-cell code
PIC-MCC	particle-in-cell Monte-Carlo collision code
PSI	plasma-surface interaction
PWI	plasma-wall interaction
PFC	plasma-facing component

RBS	Rutherford Backscatter Spectrometry
SCK-CEN	Belgian Nuclear Research Center
SEM	Scanning Electron Microscopy
SIMS	secondary ion mass spectroscopy
SOL	scrape-off layer
TEXTOR	Tokamak Experiment for Technology Oriented Research
TRIM	Transport of Ions in Matter
UHV	Ultra High Vacuum
VISIONI	Versatile Instrument for the Study of ION Interaction
VMCPT	VISIONI Monte-Carlo Charged Particle Tracker
VUV	Vacuum Ultra Violet
XRD	X-Ray Diffraction

Symbols

γ	recombination probability	
ϵ	electric permittivity	$[\mathrm{Fm}^{-1}]$
$\vec{\Phi}$	particle flux	$[\mathrm{m}^{-2}\mathrm{s}^{-1}]$
λ	wavelength	[m]
λ_c	collision mean free path	[m]
μ	mobility	$[\mathrm{m}^2\mathrm{V}^{-1}\mathrm{s}^{-1}]$
μ_m	magnetic moment	$[\mathrm{Am}^2]$
ν_c	collision frequency	$[\mathrm{s}^{-1}]$
ν_m	momentum transfer frequency	$[\mathrm{s}^{-1}]$
ρ	electric charge density	$[\mathrm{Cm}^{-3}]$
σ_c	collision cross section	$[\mathrm{m}^2]$
τ_c	collision time	[s]
τ_{cycl}	cyclotron time	[s]
τ_W	wall loss time	[s]
ω_{cycl}	cyclotron frequency	$[\mathrm{rads}^{-1}]$
ω_p	plasma frequency	$[\mathrm{rads}^{-1}]$
A	area	$[\mathrm{m}^2]$
A_f	filament area	$[\mathrm{m}^2]$
$\vec{B}$	magnetic induction	[T]
B_r	remanent magnetic field	[T]
b	impact parameter	[m]
$\vec{D}$	electric displacement field	$[\mathrm{Cm}^{-2}]$
$\vec{E}$	electric field	$[\mathrm{Vm}^{-1}]$
E	energy	[J]
E_W	work function	[J]
E_F	Fermi energy	[J]
f_{eh}	hot electron fraction	
f_H	atomic hydrogen fraction	
$\vec{H}$	magnetic field	$[\mathrm{Am}^{-1}]$
I	electric current	[A]
I_a	anode current	[A]

I_f	filament heating current	[A]
I_{sat}	saturation current	[A]
I_t	target current	[A]
J	electric current density	[Am^{-2}]
J_s	equivalent surface current density	[Am^{-1}]
$\vec{L}$	angular momentum	[$\mathrm{kgm}^2\mathrm{s}^{-1}$]
L_D	Debye length	[m]
$\vec{M}$	magnetization	[Am^{-1}]
m	mass	[kg]
n	density	[m^{-3}]
n_n	neutral density	[m^{-3}]
$\vec{P}$	polarization	[Cm^{-2}]
$\vec{p}$	momentum	[kgms^{-1}]
p	pressure	[Pa]
q	electric charge	[C]
R	reaction rate coefficient	[$\mathrm{m}^3\mathrm{s}^{-1}$]
R_{dis}	dissociation rate coefficient	[$\mathrm{m}^3\mathrm{s}^{-1}$]
R_{pe}	primary electron emission rate	[s^{-1}]
R_{cycl}	cyclotron or Larmor radius	[m]
$\vec{r}$	position	[m]
T	temperature	[K]
T_{ec}	cold electron temperature	[eV]
T_{eh}	hot electron temperature	[eV]
T_f	filament temperature	[K]
t	time	[s]
U	potential energy	[J]
V	electric potential	[V]
V_{ac}	cathode-anode potential difference	[V]
V_{as}	sample-anode potential difference	[V]
V_{tc}	cathode-target potential difference	[V]
V_{sat}	saturation voltage	[V]
$\vec{v}$	velocity	[ms^{-1}]
Z	electric charge number	

Integral identities

$$\int dx \frac{x}{(x^2+a^2)\sqrt{x^2+a^2+b^2}} = \frac{1}{2b} \ln\left(\frac{\sqrt{x^2+a^2+b^2}-b}{\sqrt{x^2+a^2+b^2}+b}\right) \tag{1}$$

$$\int dx \frac{\frac{1}{x^2+a^2}+\frac{1}{x^2+b^2}}{\sqrt{x^2+a^2+b^2}} = -\frac{1}{ab} \arctan\left(\frac{ab}{x\sqrt{x^2+a^2+b^2}}\right) \tag{2}$$

$$\int \frac{dx}{(x^2+a^2)^{3/2}} = \frac{x}{a^2\sqrt{x^2+a^2}} \tag{3}$$

$$\int \frac{dx}{x^2\sqrt{a-b/x-c/x^2}} = \frac{1}{\sqrt{c}} \arccos\left(\frac{\frac{2c}{bx}+1}{\sqrt{\frac{4ac}{b^2}+1}}\right) \tag{4}$$

$$\int_{-\infty}^{+\infty} dx \exp\left(-ax^2\right) = \sqrt{\frac{\pi}{a}} \tag{5}$$

$$\int dx x \exp\left(-ax^2\right) = -\frac{1}{2a} \exp\left(-ax^2\right) \tag{6}$$

$$\int_{-\infty}^{+\infty} dx x^2 \exp\left(-ax^2\right) = \frac{1}{2}\sqrt{\frac{\pi}{a^3}} \tag{7}$$

English summary

The impending energy crisis is probably one of the most challenging problems mankind will have to face in the near future. The coming decades the demand for energy will unavoidably increase due to demographic and economical growth. These days the majority of our energy is coming from fossil fuels. However, the fossil fuel reserves are shrinking rapidly. Furthermore, burning of fossil fuels is accompanied by the massive exhaust of CO_2. The huge increase of the CO_2 level in the atmosphere since the Industrial Revolution might be leading to an irreversible change of the earth's climate and energy balance. Therefore, fossil fuels have to be replaced as soon as possible by an alternative sustainable energy source.

Thermonuclear fusion is a very promising candidate to solve the impending energy crisis. Rearrangement of the nuclear bonds during fusion of light nuclei leads to the release of enormous amounts of energy. The fusion of deuterium and tritium is the most convenient reaction for controlled energy production on earth. Fusing 250 kg of deuterium and tritium releases as much energy as burning 2 700 000 tons of coal. However, it has turned out to be extremely challenging to use fusion as a controllable energy source. In essence this is caused by the Coulomb repulsion between the positive nuclei that has to be overcome before they can fuse together. A lot of progress has been made on the road towards a commercial fusion power plant during the last decades. Presently the most advanced concept is that of thermonuclear fusion in a so called tokamak. In a tokamak the energy to overcome the Coulomb barrier is supplied by heating the deuterium-tritium fuel until a plasma is obtained with a core temperature of about 100 million K. The charged ions and electrons of this hot plasma are confined by means of a strong helically twisted magnetic field created by multiple magnetic field coils surrounding the toroidally shaped vacuum vessel. At this moment the International Thermonuclear Experimental Reactor (ITER) is being built in Cadarache near Aix-en-Provence in southern France. With this highly international project scientists and engineers want to prove the feasibility of a commercial thermonuclear fusion power plant.

One of the toughest issues remaining in thermonuclear fusion research is the interaction between the very hot deuterium-tritium plasma and the inner reactor materials. Huge fluxes of neutrons, ions, atoms, molecules

and radicals from the hot deuterium-tritium plasma continuously hit the plasma-facing materials. This interaction leads to a variety of detrimental effects. Examples are crack formation, thermal fatigue, creep, melting, sublimation, evaporation, blistering, neutron induced defects, neutron activation, physical sputtering, chemical erosion, layer deposition, material mixing and tritium retention. An effective scientific programme for ITER can only be guaranteed if these effects remain under control. Therefore, it is of primordial importance to make reliable predictions for ITER such that one can mitigate the detrimental effects of plasma-material interaction already during the design phase. These predictions require a synergy of dedicated experiments in present small scale fusion experiments and advanced computer simulations. The simulations are indispensable for extrapolation from the present small scale fusion experiments to ITER and future thermonuclear fusion power plants.

This work focuses on one aspect of plasma-material interaction in thermonuclear fusion devices, namely material migration. Continuous bombardment of the inner reactor materials by ions, atoms, molecules and radicals leads to substantial physical sputtering and chemical erosion of these materials. Part of the eroded particles is removed by pumping, but the majority of the species is transported through the plasma and eventually gets deposited at various locations inside the device where they can possibly be re-eroded. Areas of the plasma-facing materials exposed to large fluxes of energetic particles undergo net erosion, while more remote areas undergo net deposition. The interplay between erosion, transport, deposition and re-erosion is called material migration. It is an important issue for three main reasons. Firstly, the existence of net erosion zones limits the lifetime of the plasma-facing materials. Secondly, material migration can lead to the mixing of different materials and the degradation of their properties. Thirdly, material migration is a safety issue because the deposited layers can contain a significant amount of co-deposited radioactive tritium. Further, these layers can form an important source of dust entering the reactor due to flaking. In case of accidental loss of vacuum this dust could induce explosions.

Several aspects of material migration are not yet fully understood. There is quite some scatter in the experimental and simulated physical sputtering and chemical erosion yields. Furthermore, several studies have indicated that deposited particles might be eroded much more easily than bulk material. The physical sputtering yields, the chemical erosion yields and the enhanced re-erosion of deposited particles have a serious impact on the eventual erosion-deposition balance in a thermonuclear fusion reactor and thus also on the predicted lifetime of the plasma-facing components. Therefore, it is of primordial importance to get a more fundamental understanding of these phenomena. The goal of this work was to contribute in this field.

This work consists out of two main parts. The first part of this work concerned modelling of previous $^{13}CH_4$ injection experiments in the TEX-

TOR tokamak at Forschungszentrum Jülich with the ERO Monte Carlo impurity tracking code. The aim of this study was to investigate the enhanced re-erosion of redeposited ^{13}C. First, the plasma-surface interaction database in ERO was updated. The additional erosion due to hydrogenic species from injected $^{13}CH_4$ was taken into account by tracking of these species with ERO. Further, recent more realistic physical sputtering yields and hydrocarbon reflection probabilities were implemented in ERO. Then the transport and chemistry data used for tracking of the hydrogenic species was verified by modelling the hydrogen Balmer line emission caused by the injected species with ERO and comparing the simulation results with the experimental results. Finally, it was demonstrated that even with this updated plasma-surface interaction database the very low ^{13}C deposition efficiencies observed experimentally during the $^{13}CH_4$ injection experiments could only be reproduced with ERO by assuming a strongly enhanced re-erosion of deposited ^{13}C with an enhancement factor of about 50. This study clearly confirmed that enhanced re-erosion of redeposited species is an important issue that strongly influences the erosion/deposition balance in a thermonuclear fusion reactor and definitely requires further investigation.

The second part of this work had as main goal the start-up of material migration studies in the VISIONI plasma simulator to investigate the enhanced re-erosion of deposited species further. VISIONI is a filament driven DC discharge confined by means of a strong multidipole magnetic field. It is located at the Belgian Nuclear Research Centre SCK-CEN and mimics the conditions expected at the first wall of ITER. The advantage of this device for material migration studies is that it is much more flexible than a tokamak. The plasma conditions and the surface temperature of the exposed samples can be perfectly controlled. Furthermore, the exposed samples can be extracted easily for analysis after a single experiment.

Due to the limited amount of diagnostics in VISIONI and the need of the plasma properties as an input for the ERO code an important share of the second part of this work consisted of the detailed characterization of VISIONI. First, the strong magnetic field in VISIONI created by permanent samarium-cobalt magnets was calculated analytically by integrating Biot-Savart's law. The calculated field was benchmarked and verified by means of Hall probe measurements. The agreement between the calculations and the measurements was very good. It was found that the magnetic field is highest at the poles of the samarium-cobalt magnets with a magnitude of about 0.2 T and decreases very rapidly over about two orders of magnitude towards the centre of the plasma chamber. The derived analytical expressions are very convenient for direct use in computer simulation codes.

Then a simple iterative finite difference code was developed to calculate the electrostatic field in VISIONI in the absence of the plasma by solving Laplace's equation. This code was first tested by calculating the analytically solvable case without biasing of the tungsten filaments. For this case perfect agreement was found between the finite difference calculations and

the analytical solution. Then biasing of the filaments was implemented as well. Additionally the possibility of solving Poisson's equation for a given charge distribution was implemented in this finite difference code.

Also the deuterium plasma in VISIONI was characterized. For this the VISIONI Monte Carlo Charged Particle Tracker or shortly VMCPT code was developed from scratch to simulate the plasma. This code takes into account the thermionic emission of electrons by the tungsten filaments, the motion of the charged particles in the magnetostatic field and collisions of the charged particles with other charged particles, neutrals and the walls of the plasma chamber. The most important approximation in the VMCPT code is the fact that the bulk electric field is neglected. In principle the finite difference Poisson solver could be used in the VMCPT code to solve the electric field in the plasma self-consistently. However, this would require an unrealistically large amount of CPU time. Solving the electric field in VISIONI self-consistently could become possible in the future by using a much more efficient electric field solver, massive parallelization and a state of the art High Performance Computing system. This would eliminate the most important approximation in the VMCPT code and thus greatly improve the quality of the simulations.

To check the simulation results experimentally a Langmuir probe movable along the central axis of the plasma chamber was designed and developed for VISIONI. Also software was developed to automatically derive the plasma properties from the Langmuir probe I-V characteristic. In general the agreement between the simulations and the measurements was rather good. The observed deviations are probably caused by the uncertainties in the deuterium collision cross sections and by the absence of a self-consistent electric field calculation in VMCPT. Other possible explanations for the deviations are the inherent uncertainties on the plasma properties derived from the Langmuir probe I-V characteristic and the disturbance of the Langmuir probe measurements by the magnetic field and the presence of the probe itself.

The combination of VMCPT simulations and Langmuir probe measurements resulted in a much better understanding of the deuterium plasma in VISIONI. Basically the plasma properties are determined by three free parameters. The first free parameter is the heating current I_f running through the tungsten filaments. It determines the filament temperature T_f and thus also the primary electron emission rate R_{pe}. Empirical and theoretical relations between I_f, T_f and R_{pe} were derived. However, the applicability of these relations is limited due to aging effects of the tungsten filaments and the additional discharge current running through the tungsten filaments during plasma operation. Therefore, it was decided to use I_f simply as a tuning parameter to keep the target current I_t at the desired value. The second free parameter is the potential difference V_{ac} between the tungsten filaments and the side and bottom of the plasma chamber. As the potential drop is concentrated in a very thin sheath layer around the tungsten

filaments, V_{ac} determines the initial energy of the primary electrons. The third free parameter is the neutral gas pressure p which is regulated by the pressure control valve and determines the collisionality. The dependence of the plasma properties on these three free parameters was investigated in detail with the VMCPT code and Langmuir probe measurements.

An important conclusion from the plasma characterization was that the electron energy distribution function or shortly EEDF of a deuterium plasma in VISIONI is bi-Maxwellian. This has important consequences for the reaction rate coefficients in the plasma. About $98-99\%$ of the electrons belong to the cold bulk electron population with a temperature of about $1-2$ eV, while a small fraction of about $1-2\%$ of the electrons belong to a hot electron population in the tail of the EEDF with a temperature of about $20-25$ eV. The cold electron population consists mainly of secondary electrons created by ionization and electron ejection by electron impact on the plasma chamber walls with a smaller contribution from the primary electrons that lost most of their energy by collisions with the neutral gas molecules. The hot electron population consists mainly of primary electron that experienced only a few collisions with a smaller contribution from the secondary electrons. The bi-Maxwellian EEDF is a result of the limited collisionality between the charged particles in the low density plasma of VISIONI. Especially the energetic primary electrons have not enough time to equilibrate.

Another important conclusion was that D_2^+ ions, D_3^+ ions, electrons and D_2 molecules are the dominant species for the deuterium plasma in VISIONI. D^- ions could not be observed, while D^+ ions were found to contribute less than 1% to the total ion content. D_2^+ ions and D_3^+ ions dominate at respectively low and high pressures with a transition at about 0.15 Pa. This is due to the very efficient conversion reaction in which D_2^+ ions can be transformed into D_3^+ ions by collisions with D_2 molecules. The dissociation degree of the neutral gas was found to be below 0.1%.

Finally, it was also found that the deuterium plasma in VISIONI exhibits strong inhomogeneities. The ion density, the ion flux to the target plate and the hot electron population are strongly increased at the edges of the plasma chamber around the tungsten filaments. Furthermore, an asymmetry was observed for mirroring with respect to the vertical symmetry plane of the tungsten filaments. These inhomogeneities are caused by the typical trajectories of the primary electrons emitted by the tungsten filaments induced by the strong multidipole magnetic field.

After this detailed characterization of VISIONI a new version of ERO was developed to simulate material migration experiments in VISIONI. This ERO-VISIONI code takes into account the particular geometry of VISIONI, the permanent magnetic field as calculated analytically and verified by means of Hall probe measurements, the spatial dependence of the plasma parameters as simulated with VMCPT and measured with the Langmuir probe and some additional processes important for VISIONI such as colli-

sions with neutrals and recombination of ions.

Eventually also three experimental material migration campaigns were performed in VISIONI. During the first campaign copper samples were exposed to a deuterium plasma. This campaign allowed to study pure physical sputtering under impact of molecular deuterium ions. The aim was also to investigate whether VISIONI is an appropriate tool to study erosion yields. The next campaign involved exposure of graphite samples to a deuterium plasma. This allowed to study also chemical erosion under impact of molecular deuterium ions. The erosion yields were calculated by means of mass loss measurements and profilometry. These measured yields were compared with theoretical predictions. For these predictions it was assumed that the molecular deuterium ions dissociate immediately upon impact at the surface of the samples and thus that impact of a molecular D_n^+ ion with total impact energy E_i is equivalent with n atomic D^+ ions with an impact energy E_i/n. The measured physical sputtering yields for copper were significantly below these predictions. However, simulations with the SDTrimSP binary collision code showed that this deviation could be explained by the observed presence of carbon and oxygen impurities on the surface or by retention of implanted deuterium in the surface layer. The measured erosion yields for graphite, comprising both physical and chemical sputtering, were systematically a factor of about 3 higher than the predictions. This was in agreement with observations in other studies indicating that the erosion yields for molecular hydrogen ions are a factor 2-3 higher than for atomic hydrogen ions. This effect might be caused by molecular ions not immediately dissociating upon impact. The more massive molecular ions can then create more damage than atomic ions in the surface layer of the graphite samples which enhances the chemical erosion.

During the last campaign graphite samples were again exposed to a deuterium plasma but now with simultaneous injection of $^{13}CH_4$ to study the migration and possible enhanced re-erosion of ^{13}C. Even with $^{13}CH_4$ injection there was net erosion of the graphite samples. However, RBS measurements of the graphite samples after exposure in VISIONI showed that a significant amount of ^{13}C above the natural abundance was present at the graphite surface. The areal density of the additional ^{13}C was in good agreement with ERO simulations. This agreement was obtained without the assumption of enhanced re-erosion. This supports the recently proposed idea that enhanced re-erosion is a saturation effect caused by too many species trying to stick simultaneously to the surface while being bombarded by a large flux of ions. The sticking species are then eroded by the impinging ions before they manage to properly stick to the surface. It is thus an in-situ effect. In VISIONI this effect is much smaller as the fluxes of sticking species and impinging ions are about two orders of magnitude lower than for instance in TEXTOR. This could explain the absence of enhanced re-erosion in VISIONI.

Nederlandse samenvatting

De dreigende energiecrisis is waarschijnlijk één van de meest uitdagende problemen waar de mensheid mee zal moeten kampen in de nabije toekomst. De komende decennia zal de vraag naar energie onvermijdelijk alleen maar toenemen door de demografische groei en de economische ontwikkeling. Tegenwoordig komt het merendeel van onze energie van fossiele brandstoffen. De reserves aan fossiele brandstoffen slinken echter zienderogen. Bovendien gaat het verbranden van fossiele brandstoffen ook steeds gepaard met de uitstoot van CO_2. Door de enorme toename van de CO_2 concentratie in de atmosfeer sinds de Industriële Revolutie stevenen we mogelijks af op een irreversibele verandering van het klimaat en de energiebalans van de aarde. Daarom moeten fossiele brandstoffen zo gauw mogelijk vervangen worden door een alternatieve duurzame energiebron.

Thermonucleaire fusie is een ideale kandidaat om de dreigende energiecrisis op te lossen. Herschikking van de nucleaire bindingen tijdens de fusie van lichte kernen zorgt voor het vrijkomen van enorme hoeveelheden energie. De fusie van deuterium en tritium is de meest geschikte fusiereactie voor energieproductie op aarde. Het fuseren van 250 kg deuterium en tritium doet evenveel energie vrijkomen als het verbranden van 2 700 000 ton kolen. Het is echter enorm uitdagend gebleken om fusie te ontwikkelen als een controleerbare energiebron op aarde. In essentie komt dit door de Coulomb afstoting tussen de positieve kernen die overwonnen moet worden vooraleer ze kunnen fuseren. Er is de voorbije decennia wel een enorme vooruitgang geboekt op de weg naar een commerciële fusiecentrale. Momenteel is thermonucleaire fusie in een zogenaamde tokamak het verst gevorderde concept. In een tokamak wordt de energie de nodig is om de Coulomb barrière te overwinnen aan de kernen gegeven door de deuterium-tritium brandstof te verhitten tot een plasma wordt bekomen met een temperatuur van ongeveer 100 miljoen K. De geladen ionen en elektronen van dit hete plasma worden opgesloten door middel van een sterk helisch magneetveld. Dit magneetveld wordt gecreëerd door verscheidene spoelen rondom een toroidale vacuümkamer. Momenteel is men bezig met de bouw van de International Thermonuclear Experimental Reactor (ITER) in Cadarache vlakbij Aix-en-Provence in het Zuiden van Frankrijk. Met dit hoogst internationale project willen wetenschappers en ingenieurs de haalbaarheid van een commerciële

fusiecentrale aantonen.

Eén van de hardnekkigste problemen waar men momenteel nog mee te kampen heeft in het onderzoek naar thermonucleaire fusie is de interactie tussen het zeer hete deuterium-tritium plasma en de binnenste reactormaterialen. Enorme fluxen van neutronen, ionen, atomen, moleculen en radicalen van het hete deuterium-tritium plasma treffen continu de binnenste reactormaterialen. Deze interactie leidt tot een breed scala aan nadelige effecten voor de materialen. Voorbeelden zijn scheurvorming, thermische vermoeiing, kruip, smelten, sublimatie, evaporatie, blaarvorming, neutrongeïnduceerde defecten en activatie, fysische sputtering, chemische erosie, depositie, materiaalmenging en tritiumretentie. Een effectief wetenschappelijk programma voor ITER kan slechts gegarandeerd worden als al deze effecten onder controle blijven. Daarom is het van primordiaal belang om betrouwbare voorspellingen te maken voor ITER zodanig dat men de nadelige effecten van plasma-materiaalinteractie reeds kan trachten te minimaliseren tijdens het ontwerp. Zulke voorspellingen vereisen een synergie van specifieke experimenten in de huidige kleinschalige opstellingen en geavanceerde computersimulaties. De simulaties zijn onontbeerlijk voor de extrapolatie van de huidige kleinschalige opstellingen naar ITER en toekomstige fusiecentrales.

Dit werk focust op één bepaald aspect van plasma-materiaalinteractie, namelijk materiaalmigratie. Continu bombardement van de binnenste reactormaterialen met ionen, atomen, moleculen en radicalen veroorzaakt substantiële fysische sputtering en chemische erosie van deze materialen. Een deel van de geërodeerde deeltjes wordt weggepompt, maar het merendeel van de deeltjes wordt getransporteerd doorheen het plasma en uiteindelijk gedeponeerd op een andere locatie in de reactor waar ze opnieuw kunnen geërodeerd worden. Gebieden die onderhevig zijn aan hoge fluxen van energetische deeltjes ondergaan netto erosie, terwijl meer afgeschermde gebieden netto depositie ondergaan. Het samenspel van erosie, transport, depositie en opnieuw erosie wordt materiaalmigratie genoemd. Het is een belangrijke kwestie omwille van drie redenen. Ten eerste limiteert het bestaan van zones met netto erosie de levensduur van de binnenste reactormaterialen. Ten tweede kan materiaalmigratie leiden tot het mengen van verschillende materialen en op die manier tot de degradatie van hun eigenschappen. Ten derde kan materiaalmigratie ook veiligheidsproblemen opleveren omdat gedeponeerde lagen significante hoeveelheden radioactief tritium kunnen opslaan. Bovendien vormen gedeponeerde lagen ook een belangrijke bron van stof in de reactor door afschilfering. Tijdens ongewild verlies van het vacuüm kan stof mogelijks tot ontploffingen leiden.

Verscheidene aspecten van materiaalmigratie zijn nog niet volledig begrepen. Er is significante spreiding in de experimentele en gesimuleerde waarschijnlijkheden voor fysische sputtering en chemische erosie. Bovendien hebben verscheidene studies aangetoond dat gedeponeerde deeltjes blijkbaar veel gemakkelijker worden geërodeerd dan het oorspronkelijk materiaal. De

waarschijnlijkheden voor fysische sputtering en chemische erosie en de verhoogde erosie van gedeponeerde deeltjes hebben een grote impact op de uiteindelijke erosie-depositie balans in een fusiereactor en dus ook op de voorspelde levensduur van de binnenste reactormaterialen. Daarom is het van primordiaal belang om deze fenomenen beter te begrijpen. Het doel van dit werk was om een bijdrage te leveren in deze context.

Dit werk bestaat uit twee delen. Het eerste deel betreft het modeleren van vroegere experimenten met injectie van $^{13}CH_4$ in de TEXTOR tokamak in Forschungszentrum Jülich met de Monte Carlo code ERO. Deze code simuleert het transport van onzuiverheden en wordt veel gebruikt over de hele wereld voor het simuleren van materiaalmigratie in experimenten gerelateerd aan thermonucleaire fusie. Het doel van deze studie was om de verhoogde erosie van gedeponeerde ^{13}C verder te bestuderen. Eerst werd er een verbeterd plasma-oppervlakinteractie model geïmplementeerd in ERO. De extra erosie ten gevolge van waterstof van de geïnjecteerde $^{13}CH_4$ molecules werd in rekening gebracht door deze waterstof te traceren. Verder werden er recente en meer realistische fysische sputteringwaarschijnlijkheden en reflectiewaarschijnlijkheden voor koolwaterstofmolecules geïmplementeerd in ERO. Vervolgens werden de data voor het transport en de chemie van de getraceerde waterstof in ERO geverifieerd door het simuleren van de waterstof Balmer lijn emissie veroorzaakt door de geïnjecteerde deeltjes met ERO en de gesimuleerde resultaten te vergelijken met de experimentele resultaten. Tenslotte werd aangetoond dat zelfs met het verbeterde plasma-oppervlakinteractie model de zeer lage experimenteel waargenomen ^{13}C deposities enkel konden gereproduceerd worden met ERO door te veronderstellen dat de gedeponeerde ^{13}C veel gemakkelijker wordt geërodeerd. Deze studie confirmeerde duidelijk dat verhoogde erosie van gedeponeerde deeltjes een belangrijke kwestie is die de erosie/depositie balans in een fusiereactor sterk beïnvloed en dus zeker meer onderzoek vergt.

Het tweede deel van dit werk had als hoofddoel het opstarten van materiaalmigratiestudies in de VISIONI plasma simulator. VISIONI is een DC ontlading aangedreven door wolfraamfilamenten met opsluiting door middel van een sterk multidipool magneetveld. Dit toestel staat op het Studiecentrum voor Kernenergie in Mol en bootst de condities na die verwacht worden aan de binnenste reactormaterialen van ITER. Het voordeel van dit toestel voor materiaalmigratiestudies is dat het veel flexibeler is dan een tokamak. De plasmacondities en de oppervlaktetemperatuur van de blootgestelde proefstukken kunnen perfect gecontroleerd worden. Bovendien kunnen de proefstukken eenvoudig uit de plasmakamer worden genomen voor analyse na ieder experiment.

Door de beperkte diagnostische middelen in VISIONI en vanwege het feit dat de eigenschappen van het plasma nodig zijn als input voor de ERO code bedroeg een belangrijk deel van dit werk de gedetailleerde karakterisatie van VISIONI. Eerst werd het sterke magneetveld van de permanente samarium-kobalt magneten in VISIONI analytisch berekend door integratie

van de wet van Biot-Savart. Hall sonde metingen werden uitgevoerd om de absolute magnitude van het berekende magnetische veld te bepalen en om het berekende spatiale verloop te verefiëren. De berekeningen en metingen kwamen heel goed met elkaar overeen. Het magnetische veld is het sterkst rond de polen van de samarium-kobalt magneten met een sterkte van ongeveer 0.2 T en neemt sterk af met ongeveer twee grootteordes naar het centrum van de plasmakamer toe. De analytische formules zijn zeer geschikt voor direct gebruik in simulatiecodes.

Vervolgens werd er een eenvoudige iteratieve finite difference code ontwikkeld om het elektrostatische veld in VISIONI te berekenen in afwezigheid van het plasma door de Laplace vergelijking op te lossen. Deze code werd eerst getest door het berekenen van het analytisch oplosbare probleem zonder spanningsverschil tussen de filamenten en de anode. Voor dit geval werd een perfecte overeenkomst gevonden tussen de finite difference berekeningen en de analytische oplossing. Vervolgens werd ook het spanningsverschil tussen de filamenten en de anode geïmplementeerd. Bovendien werd het ook mogelijk gemaakt om de Poisson vergelijking voor een gegeven ladingsdistributie op te lossen met de finite difference code.

Uiteindelijk werd ook het deuteriumplasma in VISIONI gekarakteriseerd. Hiervoor werd de VISIONI Monte Carlo Charged Particle Tracker of kortweg VMCPT code ontwikkeld. Deze code simuleert de thermionische emissie van elektronen door de wolfraamfilamenten, de beweging van de geladen deeltjes in het magnetostatisch veld en botsingen van de geladen deeltjes met andere geladen deeltjes, neutrale deeltjes en de wanden van de plasmakamer. De belangrijkste approximatie in de VMCPT code is het feit dat het elektrische veld in het plasma verwaarloosd wordt. In principe zou de finite difference code voor het oplossen van de Poisson vergelijking gebruikt kunnen worden om het elektrisch veld in de VMCPT code zelfconsistent te berekenen. Dit zou echter een onrealistisch grote hoeveelheid CPU tijd vereisen. Het zelf-consistent berekenen van het elektrische veld in VISIONI zou in de toekomst mogelijk kunnen worden door gebruik te maken van een meer efficiënte methode voor het oplossen van de Poisson vergelijking, grootschalige parallellisatie en een state of the art High Performance Computing systeem. Dit zou de belangrijkste benadering in de VMCPT code elimineren en dus de kwaliteit van de simulaties enorm verbeteren.

Om de simulaties experimenteel te controleren werd een beweegbare Langmuir sonde ontwikkeld voor VISIONI. Er werd ook software ontwikkeld voor het automatisch analyseren van de IV karakteristiek opgemeten met de sonde. Over het algemeen was de overeenkomst tussen simulaties en metingen redelijk goed. De verschillen werden waarschijnlijk veroorzaakt door onzekerheden in de werkzame doorsnedes voor botsingen van elektronen met deuterium en door de afwezigheid van een zelf-consistent elektrisch veld in VMCPT. Andere mogelijke verklaringen voor de verschillen zijn de inherente onzekerheden op de plasmaparameters afgeleid uit de IV karakteristiek opgemeten met de Langmuir sonde en de verstoring van de Langmuir

sonde metingen door het magnetische veld en de aanwezigheid van de sonde zelf.

De combinatie van VMCPT simulaties en Langmuir sonde metingen resulteerde in een veel beter begrip van het deuteriumplasma in VISIONI. De eigenschappen van het plasma worden bepaald door drie vrije parameters. De eerste vrije parameter is de elektrische stroom I_f voor het verhitten van de wolfraamfilamenten. Deze stroom bepaalt de temperature T_f van de filamenten en dus ook het emissietempo R_{pe} van de primaire elektronen. Er werden empirische en theoretische relaties afgeleid tussen I_f, T_f en R_{pe}. De toepasbaarheid van deze relaties is echter beperkt door verouderingseffecten van de wolfraamfilamenten en de extra ontladingsstroom door de filamenten in aanwezigheid van het plasma. Daarom werd beslist I_f slechts te gebruiken als parameter om de stroom op de target plaat af te stemmen op de gewenste waarde. De tweede vrije parameter is het potentiaalverschil V_{ac} opgelegd tussen de wolfraamfilamenten en de zijkant en bodem van de plasmakamer. Aangezien de potentiaalval geconcentreerd is in een zeer dunne laag rond de wolfraamfilamenten, bepaald V_{ac} de initiële energie van de primaire elektronen. De derde vrije parameter is de gasdruk p die geregeld wordt door de drukregelklep. Die bepaalt de collisionaliteit. De relatie tussen deze drie vrije parameters en de eigenschappen van het plasma werd in detail bestudeerd met de VMCPT code en Langmuir sonde metingen.

Een belangrijke conclusie van de karakterisatie van het plasma was dat de elektronen energie distributie functie of kortweg EEDF van het deuteriumplasma in VISIONI bimaxwelliaans is. Dit heeft belangrijke gevolgen voor de reactiewaarschijnlijkheden in het plasma. Ongeveer $98-99\%$ van de elektronen behoort tot de koude elektronenpopulatie met een temperatuur van ongeveer $1-2$ eV, terwijl een kleine fractie van ongeveer $1-2\%$ van de elektronen tot een warme elektronpopulatie in de staart van de EEDF behoort met een temperatuur van ongeveer $20-25$ eV. De koude elektronenpopulatie bestaat voornamelijk uit secundaire elektronen gecreëerd door ionisatie en elektronenejectie door elektronenimpact op de wanden van de plasmakamer. Een kleinere contributie wordt gevormd door primaire elektronen die het merendeel van hun energie verloren hebben door botsingen met het neutrale gas. De warme elektronenpopulatie bestaat voornamelijk uit primaire elektronen die slechts enkele botsingen ondergingen met een kleinere contributie van energetische secundaire elektronen. Het bimaxwelliaanse karakter van de EEDF wordt veroorzaakt door de beperkte collisionaliteit van het plasma in VISIONI met zijn beperkte dichtheid. Voornamelijk de energetische primaire elektronen hebben te weinig tijd om tot evenwicht te komen.

Een andere belangrijke conclusie was dat D_2^+ ionen, D_3^+ ionen, elektronen en D_2 molecules de dominante deeltjes zijn in deuterium plasma in VISIONI. D^- ionen konden niet worden waargenomen, terwijl D^+ ionen slechts minder dan 1% bijdragen tot de totale ionenpopulatie. D_2^+ ionen en D_3^+

ionen domineren respectievelijk bij lage en hoge drukken met een transitie rond 0.15 Pa. Die transitie wordt veroorzaakt door de erg efficiënte conversiereactie waarbij D_2^+ ionen kunnen worden omgezet in D_3^+ ionen door botsing met D_2 molecules. De dissociatiegraad van het neutrale gas bleek lager dan 0.1%.

Tenslotte werd ook vastgesteld dat het deuteriumplasma in VISIONI sterke inhomogeniteiten vertoont. De ionendichtheid, de ionenflux naar de target plaat en de warme elektronenpopulatie nemen sterk toe in de rand van de plasmakamer nabij de wolfraamfilamenten. Bovendien werd er ook een asymmetrie vastgesteld voor spiegeling ten opzichte van het verticale symmetrievlak van de wolfraamfilamenten. Die inhomogeniteiten worden veroorzaakt door de typische banen van de primaire elektronen onder invloed van het sterke multidipool magneetveld.

Na deze gedetailleerde karakterisatie van VISIONI werd er een nieuwe versie van ERO ontwikkeld voor het simuleren van materiaalmigratie in VISIONI. De ERO-VISIONI code bevat de specifieke geometrie voor VISIONI, het permanente magneetveld zoals analytisch berekend en geverefiëerd door middel van Hall sonde metingen, de spatiale afhankelijkheid van de plasmaparameters zoals gesimuleerd met VMCPT en gemeten met de Langmuir sonde en enkele extra processesn die belangerijk zijn in VISIONI zoals botsingen met de neutrale gasmolecules en recombinatie van ionen.

Uiteindelijk werden er ook drie experimentele materiaalmigratiecampagnes uitgevoerd in VISIONI. Tijdens de eerste campagne werden koperproefstukken blootgesteld aan een deuteriumplasma. Die campagne werd uitgevoerd om pure fysische sputtering onder invloed van impact met moleculaire deuteriumionen te bestuderen. Vervolgens werd een campagne uitgevoerd waarin grafietproefstukken werden blootgesteld aan een deuteriumplasma. Tijdens die campagne kon ook chemische erosie onder invloed van impact met moleculaire deuteriumionen bestudeerd worden. De sputteringwaarschijnlijkheden werden berekend aan de hand van massaverlies en profilometrie. De experimentele yields werden vergeleken met theoretische voorspellingen. Voor deze voorspellingen werd aangenomen dat de moleculaire deuteriumionen onmiddellijk dissociëren bij impact op het oppervlak van de proefstukken en dus dat de impact van een moleculair D_n^+ ion met totale impactenergie E_i equivalent is met de impact van n atomaire D^+ ionen met een impactenergie E_i/n. De experimentele waarschijnlijkheden voor fysische sputtering van koper waren significant lager dan de voorspellingen. Simulaties met de binaire botsingscode SDTrimSP toonden echter aan dat het verschil verklaard kan worden door de koolstof en zuurstof waargenomen op het oppervlak van de koperproefstukken of door retentie van geïmplanteerd deuterium in de oppervlaktelaag. De experimentele waarschijnlijkheden voor erosie van grafiet, een combinatie van fysische en chemische sputtering, waren systematisch ongeveer een factor 3 hoger dan de voorspellingen. Dit was in overeenstemming met de observaties van andere studies die erop wezen dat de waarschijnlijkheden voor erosie van

grafiet voor moleculaire waterstofionen een factor 2-3 hoger zijn dan voor atomaire waterstofionen. Dit effect wordt mogelijks veroorzaakt door moleculaire ionen die niet onmiddellijk dissociëren bij impact. De massievere moleculaire ionen kunnen dan meer schade aanrichten in de oppervlaktelaag van de grafietproefstukken dan atomaire ionen wat kan leiden tot de waargenomen verhoogde chemische erosie.

Tijdens de laatste campagne werden weerom grafietproefstukken blootgesteld aan een deuteriumplasma, maar nu met gelijktijdige injectie van $^{13}CH_4$ om migratie en mogelijkse verhoogde reërosie van ^{13}C te bestuderen. Zelfs met $^{13}CH_4$ injectie was er netto erosie aan het oppervlak van de grafietproefstukken. RBS metingen aan het oppervlak van de grafietproefstukken gaven na blootstelling in VISIONI toch een significant hogere hoeveelheid ^{13}C dan de natuurlijke abundantie. Die verhoogde ^{13}C concentratie was in goede overeenkomst met ERO simulaties. De overeenkomst werd bekomen zonder verhoogde reërosie te veronderstellen. Dit ondersteunt het recent voorgestelde idee dat de verhoogde reërosie een saturatie-effect is veroorzaakt door te veel deeltjes die tegelijkertijd een binding met het oppervlak trachten te vormen terwijl ze gebombardeerd worden door een hoge ionenflux. De deeltjes worden dan geërodeerd door de invallende ionen vooraleer ze erin slagen een echte binding met het oppervlak te vormen. In VISIONI is dit saturatie-effect veel kleiner aangezien de flux van bindingvormende deeltjes en de flux van invallende ionen ongeveer twee grootteordes kleiner zijn dan bijvoorbeeld in TEXTOR. Dit verklaart mogelijks de afwezigheid van verhoogde reërosie in VISIONI.

My contribution to this work

The main part of the work presented in this thesis was performed of course by myself. However, some parts were performed by colleagues. Therefore, I would like to clarify here my personal contribution to this work.

The implementation of the updated plasma-surface interaction database in ERO was done mainly by myself. Only the implementation of the new physical sputtering yield formulas was done for the largest part by my colleagues Carolina Björkas and Andreas Kirschner at Forschungszentrum Jülich. The nozzle and roof limiter experiments in TEXTOR discussed in this work were performed by the TEXTOR team at Forschungszentrum Jülich already before I started my PhD. However, the simulations for these experiments with ERO after implementation of the updated plasma-surface interaction model were carried out by myself.

For the characterization and the material migration experiments in VISIONI all data analysis, calculations, code developments and simulations were performed by myself. I also did post-mortem surface analysis of the exposed samples by means of SEM, EDX and optical profilometry. However, the laser profilometry measurements were performed at Forschungszentrum Jülich by Gaby Knauf and the RBS measurements and analysis were performed at the IFIN-HH facility in Romania by Cristian Lungu and Corneliu Porosnicu. For the experimental side of the work in VISIONI I got a lot of help from Johan Schuurmans. The experiments and measurements in VISIONI were proposed by me but mainly carried out by Johan. He also designed with my input the movable Langmuir probe and the sample holder with the cold finger.

Chapter 1

Motivation and outline

Thermonuclear fusion is a very promising candidate to solve the impending energy crisis. At this moment the International Thermonuclear Experimental Reactor (ITER) is being built in Cadarache near Aix-en-Provence in southern France. With this highly international project scientists and engineers want to demonstrate the feasibility of a thermonuclear fusion power plant. However, there are still several obstacles on the road towards the first commercial thermonuclear fusion power plant.

One of the toughest issues remaining in thermonuclear fusion research is the interaction between the very hot deuterium-tritium plasma and the inner reactor materials. Huge fluxes of neutrons, ions, atoms, molecules and radicals from the plasma continuously hit the plasma-facing materials. This interaction leads to a variety of detrimental effects. Examples are crack formation, thermal fatigue, creep, melting, sublimation, evaporation, blistering, neutron induced defects, neutron activation, physical sputtering, chemical erosion, layer deposition, material mixing and tritium retention. An effective scientific programme for ITER can only be guaranteed if these effects can be kept under control. Therefore, it is of primordial importance to make reliable predictions for ITER such that one can mitigate the detrimental effects of plasma-material interaction already during the design phase. These predictions require a synergy of dedicated experiments in the present small scale fusion experiments and advanced computer simulations. The simulations are indispensable for extrapolation from the present small scale fusion experiments to ITER and future thermonuclear fusion power plants.

This work focusses on one aspect of plasma-material interaction in thermonuclear fusion devices, namely material migration. Continuous bombardment of the inner reactor materials by ions, atoms, molecules and radicals leads to substantial physical sputtering and chemical erosion of these materials. Part of the eroded particles is removed by pumping, but the majority of the species is transported through the plasma and eventually gets de-

posited at various locations inside the device where they can possibly be re-eroded. Areas of the plasma-facing materials exposed to large fluxes of energetic particles undergo net erosion, while more remote areas undergo net deposition. The interplay between erosion, transport, deposition and re-erosion is called material migration. It is an important issue for three main reasons. Firstly, the existence of net erosion zones limits the lifetime of the plasma-facing materials. Secondly, material migration can lead to the mixing of different materials and the degradation of their properties. Thirdly, material migration is a safety issue because the deposited layers can contain a significant amount of co-deposited radioactive tritium. Further, these layers can form an important source of dust entering the reactor due to flaking. In certain accident scenarios with loss of vacuum this dust could induce explosions.

Several aspects of material migration are not yet fully understood. There is quite some scatter in the experimental and simulated physical sputtering and chemical erosion yields. Furthermore, several studies have indicated that deposited particles might be eroded much more easily than bulk material. The physical sputtering yields, the chemical erosion yields and the enhanced re-erosion of deposited particles have a serious impact on the eventual erosion-deposition balance in a thermonuclear fusion reactor and thus also on the predicted lifetime of the plasma-facing components. Therefore, it is of primordial importance to get a more fundamental understanding of these phenomena. The goal of this work was to contribute in this field.

This work consists out of two main parts. In the first part the plasma-surface interaction database in the ERO impurity transport code was updated. The ERO code is commonly used to simulate material migration in thermonuclear fusion devices all over the world. The code is maintained at Forschungszentrum Jülich. The updated plasma-surface interaction database was benchmarked by simulating methane injection experiments performed in the TEXTOR tokamak at Forschungszentrum Jülich. Eventually it was demonstrated that even with this updated plasma-surface interaction database the experimental results from a $^{13}CH_4$ injection experiment in TEXTOR could only be explained by a strongly enhanced re-erosion of deposited ^{13}C with an enhancement factor of about 50.

The second part of this work had as main goal the start-up of material migration studies in the VISIONI plasma simulator to further study the enhanced re-erosion of redeposited species. VISIONI is a filament driven DC discharge confined by means of a strong multidipole magnetic field. It is located at the Belgian Nuclear Research Centre SCK-CEN and mimics the conditions expected at the first wall of ITER. The advantage of this device for material migration studies is that it is much more flexible than a tokamak. The plasma conditions and the surface temperature of the exposed samples can be perfectly controlled. Furthermore, the exposed samples can be extracted easily for analysis after a single experiment.

Due to the limited amount of diagnostics in VISIONI and the need of

the plasma properties as an input for the ERO code an important share of this work consisted of the detailed characterization of VISIONI. Firstly, the strong magnetic field in VISIONI created by the permanent samarium-cobalt magnets was calculated analytically and verified by means of Hall probe measurements. Next, a simple iterative finite difference code was developed to calculate the electrostatic field in VISIONI in the absence of the plasma. Finally, also the plasma was characterized. The VISIONI Monte Carlo Charged Particle Tracker or shortly VMCPT code was developed from scratch to simulate the plasma. To check the simulation results experimentally a Langmuir probe movable along the central axis of the plasma chamber was designed and developed for VISIONI. Software was developed to automatically derive the plasma parameters from the Langmuir probe IV curves. In the end a much better understanding of the characteristics of the VISIONI plasma simulator was obtained and the results could be implemented in the ERO code.

Finally, three experimental campaigns were performed in VISIONI. During the first campaign copper samples were exposed to a deuterium plasma. This campaign allowed to study pure physical sputtering under impact of molecular deuterium ions. The next campaign involved exposure of graphite samples to a deuterium plasma. This allowed to study also chemical erosion under impact of molecular deuterium ions. In the last campaign graphite samples were exposed again to a deuterium plasma. During these exposures $^{13}CH_4$ was injected into the plasma to study the transport, deposition and especially the possibly enhanced re-erosion of deposited ^{13}C.

The outline of this work is as follows. Chapter 2 elaborates the theoretical background of this work in more detail. Chapter 3 describes the experimental set-up of the TEXTOR tokamak and the VISIONI plasma simulator. Chapter 4 discusses the code development performed during this work: the improved plasma-surface interaction model in ERO, the development of ERO-VISIONI for simulating material migration experiment in VISIONI, the VMCPT code and the Langmuir probe IV characteristic analyser software. The next three chapters deal respectively with the demonstration of enhanced re-erosion of deposited carbon in TEXTOR, the characterization of the VISIONI plasma simulator and the experimental material migration campaigns in VISIONI.

Chapter 2

Theoretical background

This chapter elaborates the theoretical background of this work. Thermonuclear fusion is studied because it is a very promising candidate to solve the impending energy crisis. The first section shortly discusses the impending energy crisis. The next section explains the basics of thermonuclear fusion and shows why it is a good candidate for solving the impending energy crisis. The last two sections introduce the concepts of plasma physics and plasma-surface interaction needed for this work.

2.1 The world energy issue

Global warming, CO_2 emission reduction, the ecological footprint, greenhouse gases, renewable energy sources, nuclear non-proliferation, ... Anyone who claims never to have heard about these things must be living on a different planet. Newspapers, the internet, magazines and television shows bulge with these trendy terms. Googling for "global warming" results in no fewer than 18 million hits! Al Gore's effort for spreading his "Inconvenient Truth" delivered him the Noble Peace Prize. Nowadays the public support for environmental protection and wise energy management is getting wider and wider. Unfortunately it is not just a hype. There really is a problem.

It is not easy to gain objective information about this complex issue. Most publications are highly coloured by the interests of the author. The best thing to do, is looking up the numbers and based on these draw your own conclusions. But even numbers appear to be very dependent on the source in this case. A lot of political and economical interests are intertwined with the energy problem. Though it is very important that people form an opinion about the issue. The future of mother earth is something that involves everyone. A very good book in this context is [1]. In this work MacKay tries to cover the issue as objective as possible with a lot of facts and figures. In this introductory chapter I will try to convince you that

Table 2.1: Per capita total primary power consumption for some selected countries [2]

Country	**Per capita consumption (2004)**
Qatar	28 000 W
United Arab Emirates	31 000 W
Iceland	16 800 W
Norway	14 200 W
Canada	14 000 W
Kuwait	15 700 W
USA	11 400 W
Australia	8 800 W
Belgium	9 000 W
The Netherlands	8 400 W
Russia	7 000 W
Japan	6 000 W
Germany	6 000 W
Europe (West and East)	4 900 W
South Africa	3 900 W
Brazil	1 660 W
Cuba	1 400 W
China	1 500 W
Zimbabwe	570 W
India	490 W
Vietnam	380 W
Mozambique	240 W
Congo (Kinshasa)	51 W
Chad	12 W
World	2 340 W

there is indeed a problem. The used numbers and graphs are based on [2]. Of course this is not the place to elaborate the whole issue. The only point I want to make, is that something has to be done. We have to stop the talking and start the acting.

How much energy do we use now and how much energy will we use in the future? Table 2.1 shows the per capita primary power consumption in 2004 for some selected countries. Most striking is the large spread. A Qatari consumes 28 000 W, while a Chadian has to be satisfied with 12 W. An average earthling consumes 2 340 W, which is still low compared to the European energy need of 4 900 W. Based on this information it is not difficult to predict that during the coming decades the average energy need per person will increase drastically due to the economical growth in the less developed countries. Especially densely populated giants in full development such as China and India will give and enormous boost to the

Table 2.2: Contribution of different energy sources to the primary energy production in the world [2]

Energy source	**Contribution to primary energy production (2001)**
Oil	38%
Coal	24%
Gas	24%
Fission	6.3%
Hydro-electricity	6.4%
Solar, wind, wood, waste	1.3%

Table 2.3: Years of use of different fuels at the current consumption rate [2]

Fuel	**Proved recoverable reserves (2003)**	**Years of use at the current rate of consumption**
Coal	$0.9 \cdot 10^{12}$ tons	210
Crude oil	$1.2 \cdot 10^{12}$ barrels	30-40
Natural gas	$170 \cdot 10^{12}$ m^3	60-70
Uranium	$2.0 \cdot 10^{6}$ tons	2400-3000

world energy demand. An amplifying factor is the increase of the world population. The most realistic model of a study made by the World Energy Council and the International Institute for Applied System Analysis at the end of last century predicts a doubling of the world energy demand from 15 TWyr to 30 TWyr by 2050.

Where is our energy coming from? Table 2.2 shows the contribution of different energy sources to the world primary energy production. Table 2.3 shows how long it will take us to consume all known reserves of fossil fuels and uranium ore at the current rate of consumption. More than 92 % of our energy originates from these raw materials. Fossil fuels on their own are responsible for 86 %. It is clear that these materials are not inexhaustible at all. At the current pace we will run out of fossil fuels very soon. This would not only lead to political instabilities and price increases. The exhaustion of the valuable fossil materials would be a disaster for the chemical and pharmaceutical industry as well.

And what about global warming? This is a very controversial topic. Fact is that the earth is a very complex ecosystem in which everything is related to everything. Even specialists disagree on the issue. I will thus not venture to make a statement about the different theories. I will only focus on the observations considering the evolution of the CO_2 content in the earth's atmosphere. The contribution in ppm during the last 1000 years is given in figure 2.1. What we see here cannot be misunderstood. The CO_2 concentration has been levelled at a value of about 280 ppm for a long time.

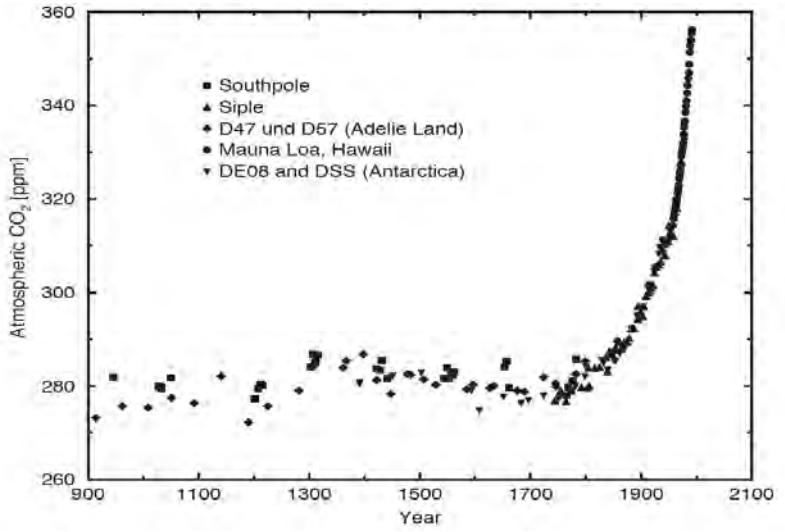

Figure 2.1: Evolution of the CO_2 concentration in the atmosphere during the last 1000 years [2]

There is even evidence that the concentration has remained at this level for the last 160 000 years. But around the Industrial Revolution the concentration suddenly started increasing steeper and steeper. Today we are already at a level of more than 360 ppm. When you see this graph, there is no doubt that the CO_2 emission by our intensive use of fossil fuels is the cause of this clear change. The next step in the reasoning is much more difficult. What is the effect of this change? A lot of scientists claim that it causes a steady increase of the average earth temperature. "Nice!", you could say, "No thick coats any more!". Unfortunately it is not that simple. Even a small temperature increase could imply a complex sequence of events very difficult to predict. Ocean currents, winds and the sea level are all very dependent on the earth's temperature. And at this very moment there are indeed clear proofs that temperature is increasing. The most famous example is the melting of the glaciers. Although one cannot yet prove with 100% certainty a causal link between the CO_2 level and the temperature increase, the fact remains that we are performing a very dangerous experiment with ourselves as guinea pigs. If this change in CO_2 level indeed appears to have adverse effects to our ecosystem in a few decades, then we cannot just stop these effects. First of all, we cannot simply end the emission immediately. Secondly, the CO_2 cycle is very slow. It would take at least 100 years for the earth to restore the situation. And last but not least, nobody knows if this playing with our ecosystem is a reversible process. There is a chance

that hysteresis will prevent us from restoring the ecosystem's original state.

I think my message is clear. Let me summarize. Today fossil fuels form the bulk of our energy production. There are two big problems with these kind of fuels. Firstly, they are exhaustible. Even at the current pace of consumption we will run out of fossil fuels very soon. Furthermore, it will be impossible not to exceed this pace greatly because the energy demand per person and the world population are both increasing. For political stability, energy prizes and the chemical and pharmaceutical industry it would be much better not to use up all the fossil fuels. Secondly, the CO_2 emission, inevitably coupled to fossil fuels, causes a clear change in the composition of the earth's atmosphere. This could be very dangerous. So there are no excuses. We have to change our current way of energy production and consumption drastically. Everybody has to increase the efficiency of their energy use. Scientists and engineers have to develop alternative ways of energy production. World leaders have to stimulate, support and guide the transition.

2.2 Thermonuclear fusion in tokamaks

Thermonuclear fusion is a very promising candidate to solve the impending energy crisis discussed in the previous section. This section gives a concise introduction to the broad field of thermonuclear fusion research. The first subsection gives a short historical sketch of the research. The next subsection explains why fusing light nuclei together releases huge amounts of energy. In subsection 2.2.3 it is discussed that it is basically the repulsion between the positive nuclei that makes it so challenging to use this fusion energy for commercial energy production. The fourth subsection introduces the tokamak as one of the currently most advanced concepts for a future thermonuclear fusion power plant. Subsection 2.2.5 gives a short overview of the international ITER project which aims to demonstrate that the tokamak is indeed a viable candidate for future commercial energy production. The final subsection gives a summary of the main advantages and disadvantages of the tokamak as power plant of the future. More detailed information on thermonuclear fusion and tokamaks can be found for instance in [3].

2.2.1 A brief history of fusion research

Fusion research already has a long history. The discovery of the fusion process fits in the mid 19th century's solar energy riddle. People were wondering where the sun's energy is coming from. The first idea was a simple combustion similar to the burning of a fire. However, as geologists stated that the earth's shaping processes must have been active during at least a few hundred thousand of years, simple combustion would require inconceivable amounts of matter. In the same century Hermann von Helmholtz and

Lord Kelvin proved that also a steady gravitational collapse of the sun could not account for all the produced energy. A first clue on the actual origin of the solar energy was the energy-mass equivalence postulated by Einstein in 1905. It indicates that even a small amount of mass can be converted into an enormous amount of energy. In 1920 Francis William Aston observed that the mass of a helium atom was somewhat smaller than the summed mass of 4 hydrogen atoms. Based on Aston's measurement, astronomer Sir Arthur Eddington suggested that the sun produces its energy by converting hydrogen atoms into helium atoms. In 1939 Hans Bethe wrote the article "Energy production in stars", elaborating the fusion processes occurring in the stars more profoundly. This paper delivered Bethe the Nobel Prize for Physics in 1968 and once and for all solved the solar energy riddle.

After the theoretical successes of the first half of the 20th century, a lot of experimental progress on fusion was made during the second half of last century. After World War II and the "successful" Manhattan project there was an increased interest in fusion and nuclear physics in general. Scientists started thinking about possible ways in which the fusion process could be used for commercial energy production. During the next two decades research groups in the UK, the USA, the USSR, Japan, France and Germany developed different kinds of fusion reactors such as stellarators, magnetic pinch devices and inertial fusion devices. Important names occurring in this period are Sir George Thomson (Imperial College), Peter Thonemann (Oxford), Lyman Spitzer (Princeton), James Tuck (Los Alamos) and Edward Teller (Lawrence Livermore Laboratory). In the beginning fusion research was classified as "Top Secret" due to the Cold War. It is only after the famous "Atoms for Peace" conference in 1958 in Geneva that the first steps towards international cooperation were made.

On the third IAEA "International Conference on Plasma Physics and Controlled Nuclear Fusion Research" in 1968 in Novosibirsk fusion research was completely re-oriented due to the announcement of the very successful experiments on the Russian tokamaks. Figure 2.2 shows a photograph of the Russian T1 at the Kurchatov Institute in Moscow. This was the world's first tokamak. The name "tokamak" is an acronym for the Russian words "toroidalnaya kamera" or "toroidal chamber" and "magnitnaya katushka" or "magnetic coil". The concept was developed by Igor Tamm and Andrei Sakharov in the 1950's. Lev Artsimovich led the experimental program in Moscow at the Kurchatov Institute, while the theoretical studies were directed by Mikhail Leontovich. The generated temperatures were about 10 times higher than in any other fusion device at that moment. Also the energy confinement times were much higher. Therefore, most fusion research groups started concentrating on tokamak research. Even today the majority of the research groups still focuses on tokamaks. They can be found all over the world. Every single tokamak is unique. Different research groups deal with different aspects of the tokamak research. Presently the Joint European Torus (JET) at Culham in the UK, shown in figure 2.3, is

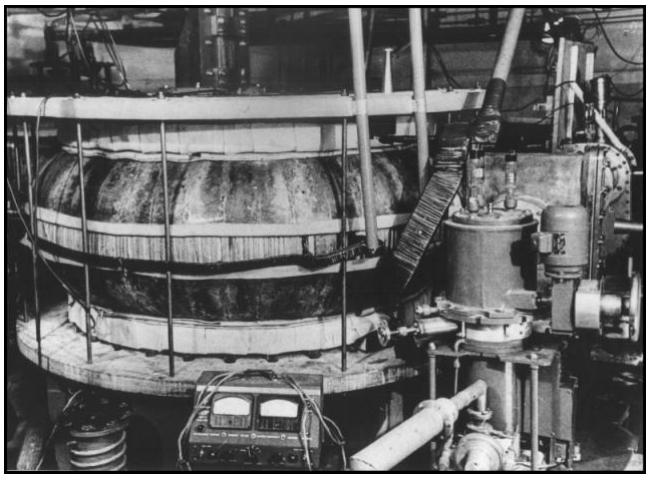

Figure 2.2: The Russian T1 at the Kurchatov Institute in Moscow was the first tokamak [4]

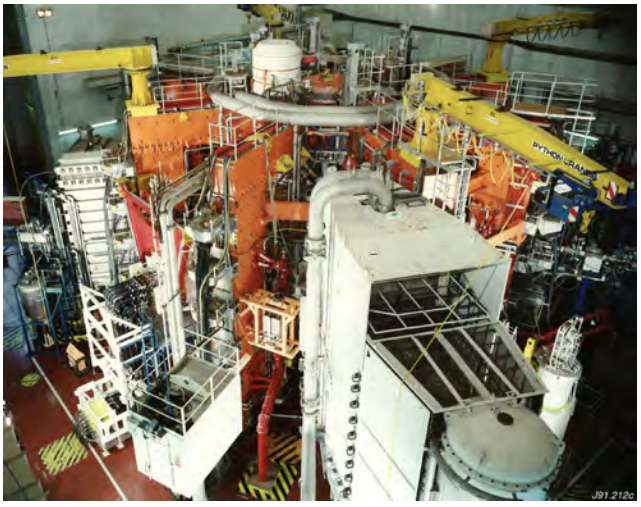

Figure 2.3: JET at Culham (UK), the current world's biggest tokamak [4]

the biggest tokamak in the world. Other tokamaks are TEXTOR (Jülich, Germany), JT-60U (Naka, Japan), Tore Supra (Cadarache, France), DIII-D (San Diego, USA), COMPASS (Prague, Czech Republic), ASDEX Upgrade (Garching, Germany), KSTAR (Daejon, South Korea), HT-7 (Hefei, China) and TCV (Lausanne, Switzerland).

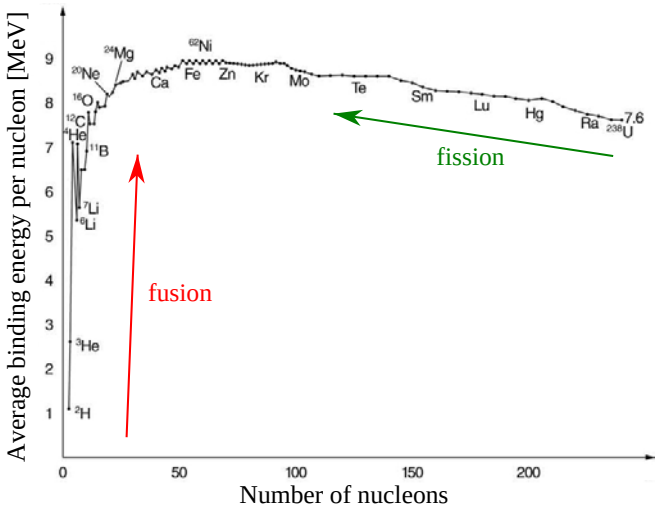

Figure 2.4: Average binding energy per nucleon as function of the number of nucleons in the nucleus [5]

2.2.2 Energy release by nuclear fusion reactions

How can one produce energy by fusing nuclei together? The production of fusion energy is in a way similar to the burning of fossil fuels. During combustion of traditional raw materials such as oil, gas and coal the chemical bonds of the hydrocarbons are broken in order to form stronger bound molecules with oxygen from the surrounding air such as H_2O and CO_2. This rearrangement of chemical bounds leads to a small decrease Δm of the total mass and the corresponding release of an amount of energy $E = \Delta m c^2$ according to Einstein's famous energy-mass equivalence. Chemical bonds are realized by the electromagnetic interaction. Typical binding energies are in the electronvolt range. Hence, one can expect an energy release of the same order of magnitude.

During fusion it are the nuclear bonds of the fusing nuclei that are rearranged to get stronger bound nuclei leading again to an exothermic reaction. The nuclear interaction is much stronger than the electromagnetic interaction. Typical nuclear binding energies are in the mega-electronvolt range which is about six orders of magnitude higher than chemical binding energies. Therefore, one can also expect that the energy released during fusion reactions is about six order of magnitude higher than the energy released during chemical reactions.

The average binding energy per nucleon as function of the number of nucleons in the nucleus is depicted in figure 2.4. The shape of this curve can

Table 2.4: Fuel consumption for different energy production methods [2]

Method	**Annual fuel consumption for a 1 GW power plant**
Coal	2 700 000 tons
Oil	1 900 000 tons
Fission	28 tons of $U0_2$
Fusion	250 kg deuterium-tritium

be understood by taking into account Coulomb repulsion between protons, nuclear attraction between all nucleons and some less intuitive quantum mechanical effects as described in detail in [6]. The curve exhibits a maximum for ^{56}Fe which is hereby the strongest bound nucleus. This shows that there are two possibilities to produce energy by rearranging the nuclear bonds. In a common nuclear power plant one goes from the right towards the ^{56}Fe peak by splitting heavy nuclei such as ^{235}U in two lighter and stronger bound nuclei resulting in an energy release of about 1 MeV per nucleon. In a fusion reaction the ^{56}Fe peak is approached from the left by colliding light nuclei such as hydrogen, deuterium and tritium to form heavier more strongly bound nuclei resulting in an energy release of about 10 MeV per nucleon. Hence, expressed as energy released per unit of fuel mass fusion is even more efficient than fission as could be expected from the steeper slope of the binding energy curve in the low mass region. This high efficiency of fusion is also illustrated in table 2.4 listing the annual fuel consumption of a 1 GW power plant for different burning processes which shows that 250 kg of deuterium-tritium fuel can replace as many as 2.7 million tons of coal.

2.2.3 The Coulomb barrier

If fusion is so efficient, why don't we then have a fusion power plant yet? It has turned out to be extremely challenging to use fusion as a controllable energy source. In essence this is due to the so called Coulomb barrier. As the range of the attractive nuclear force is only a few femtometers, the positively charged nuclei are initially repelling each other due to the long range Coulomb force. As shown schematically in figure 2.5 this leads to a barrier with height E_{bar} that has to be overcome before the attractive nuclear force comes into play. Classically the nuclei have to collide with a centre of mass energy E_{cm} higher than E_{bar} in order not to be reflected, but according to quantum mechanics also nuclei colliding with E_{cm} lower than E_{bar} have a finite chance of tunnelling through the Coulomb barrier. However, the tunnelling probability decreases exponentially with decreasing E_{cm}. The Coulomb barrier leads to very low fusion cross sections. Cross sections are a measure for the probability of a reaction as will be explained in 2.3.4.5. A comparison of the cross sections for the most common fusion

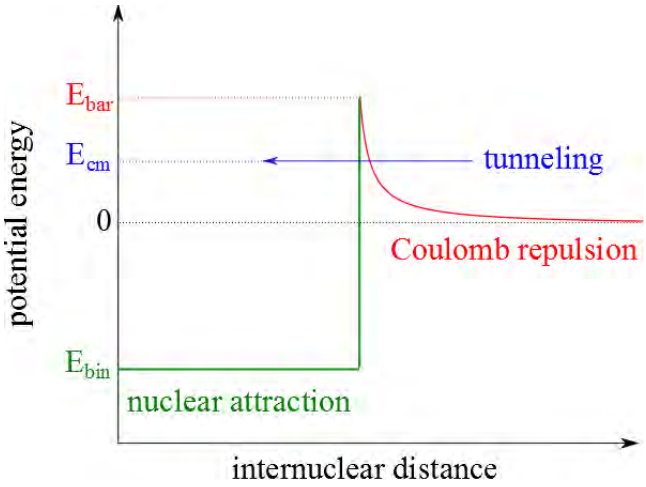

Figure 2.5: The Coulomb barrier experienced by two light nuclei

reactions is shown in figure 2.6. The cross section dependence on the centre of mass energy of the colliding nuclei exhibits a maximum. This can be explained by the fact that for too low centre of mass energies the nuclei are reflected by the Coulomb barrier, while for too high energies the nuclear interaction potential is too low in comparison with the kinetic energy. One can see that the fusion reaction

$$\mathrm{D} + \mathrm{T} \rightarrow^4 \mathrm{He}(3.52\ \mathrm{MeV}) + \mathrm{n}(14.08\ \mathrm{MeV}) \tag{2.1}$$

between deuterium and tritium can be realized most easily. Its cross section is the highest for low centre of mass energies and exhibits a maximum for 100 keV. During the deuterium-tritium reaction 17.59 MeV of fusion energy is liberated. This energy is released as kinetic energy distributed over the reaction products. As the initial energy can usually be neglected with respect to the large fusion energy, momentum conservation implies that the helium nucleus and the neutron receive respectively 1/5 and 4/5 of the fusion energy.

With the above considerations in mind one could now think of a very easy way to create a fusion power plant. Just create a huge deuterium ice cube and hit it with a dense tritium ion beam with an ion energy of 100 keV. In this way one will indeed induce deuterium-tritium fusion reactions. However, one will always have to invest more power into the acceleration of the ion beam than one could ever get back from the fusion reactions. This is because most of the ion energy is simply lost as heat and light by interaction with the electrons and elastic collisions with the nuclei of the densely packed deuterium atoms. The cross section for the deuterium-tritium fusion

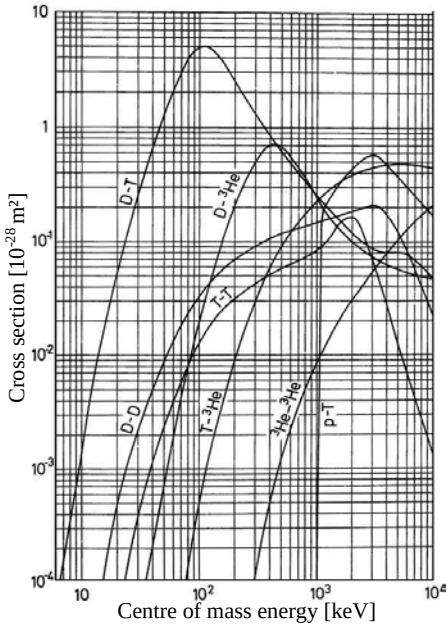

Figure 2.6: Fusion cross sections as function of centre of mass energy [7]

reaction is way too small for this concept to work. Therefore, scientists and engineers had to come up with much more sophisticated concepts.

2.2.4 Magnetically confined fusion in tokamaks

In the previous subsection we have learned that in order to produce net energy by fusing deuterium and tritium nuclei one has to fulfil two conditions. Firstly, one initially has to provide the nuclei with enough energy to overcome the Coulomb barrier such that fusion reactions can take place. Secondly, one has to make sure that the provided energy is not lost too rapidly in order to guarantee that the power produced by the rare fusion reactions exceeds the power invested to provide the nuclei with sufficient initial energy. Presently two concepts exist to fulfil these two conditions. The first concept is that of inertial fusion. In this case a small deuterium-tritium pellet is compressed by means of very intense lasers to conditions with extremely high density and temperature. This concept falls outside the scope of this work. More information can be found for instance in [8]. The second concept is that over magnetic confinement which will be discussed in detail in this subsection.

In case of magnetically confined or thermonuclear fusion a deuterium-tritium gas mixture is heated up to a very high temperature by means of

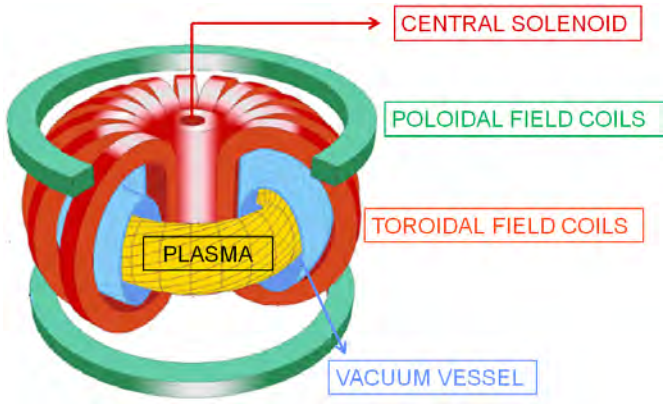

Figure 2.7: Schematic representation of the tokamak concept [9]

Ohmic heating, injection of energetic deuterium atoms and electromagnetic wave heating. The optimum temperature is of the order of 150 million K or 10 keV as can be seen from a detailed power balance analysis [10], [3]. At this temperature the deuterium-tritium gas becomes a fully ionized plasma. In order to confine the energy as much as possible the negatively charged electrons and positively charged deuterium and tritium ions are confined by means of a strong magnetic field.

The theory of charged particle motion in electromagnetic fields is discussed in detail in 2.3.3. The most simple magnetic confinement configuration one can think of is that of several current carrying coils centred around a cylindrical vacuum vessel creating a quasi-homogeneous magnetic field directed along the axis of the cylinder. If the magnetic field is taken strong enough the charged particles will gyrate around the magnetic field lines with a gyration radius much smaller than the radius of the cylinder. This ensures confinement in the radial direction. However, the charged particles can easily escape in the axial direction. A logic solution for these end losses is joining the two ends in a torus. However, such a configuration is characterized by a radial expansion of the plasma. The magnetic field in such a torus decreases with increasing radius. This radial magnetic field gradient generates vertical $\vec{\nabla}B$ drifts which are in opposite directions for positively and negatively charged particles. The charge separation in turn results in a vertical electric field which leads to an outwards $\vec{E} \times \vec{B}$ drift for all charged particles. This lack of confinement can be avoided by the introduction of an additional poloidal magnetic field component such that one gets helically twisted magnetic field lines on nested toroidally shaped magnetic flux surfaces. There are two possibilities to generate such a field. The first approach is the tokamak concept sketched schematically in figure

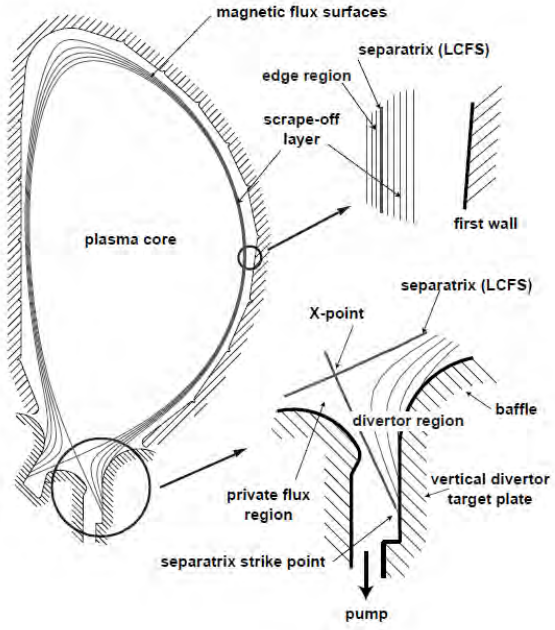

Figure 2.8: Schematic representation of the divertor geometry in a tokamak [11]

2.7. By ramping up an electric current through a winding in the centre of the torus a toroidal current is induced in the plasma which can be seen as the secondary winding of a transformer. Without additional current drive by means of neutral beam injection or electromagnetic waves a tokamak is thus intrinsically a pulsed device. The toroidal plasma current induces the desired poloidal magnetic field component. For better control of the shape and position of the plasma column in a tokamak one usually adds also some poloidal magnetic field coils circulating the tokamak in the toroidal direction. The second approach to get helically twisted magnetic field lines is the stellarator concept. In this case the magnetic field coils are designed in very special shapes in order to generate the desired helically twisted magnetic field directly. No current has to be induced in the plasma. Therefore, a stellarator is not pulsed and is not subject to plasma current driven instabilities. This work focusses on the tokamak concept. More information on the stellarator and other magnetic confinement configurations can be found for instance in [12].

Despite the magnetic confinement, interaction between the hot fusion plasma and the surface of the plasma-facing materials is unavoidable. A

magnetic field can never fully confine a plasma due to diffusion perpendicular to the magnetic field, turbulence and disruptions. Furthermore, the plasma-surface interaction is even necessary for two reasons. Firstly, the helium ashes produced during the fusion reactions have to be extracted in order not to dilute the deuterium-tritium fuel too much. Secondly, the fusion energy has to be extracted from the plasma in order to produce electricity. Energetic particles bombarding the inner reactor materials lead to heating of the cooling water which is then used to produce electricity by means of a conventional steam cycle.

As discussed in detail in 2.4 the plasma-surface interaction leads to a variety of detrimental effects on the plasma-facing components. Usually the magnetic field configuration and the plasma-facing components are tailored such that the plasma-surface interaction is focussed on several dedicated components. The oldest concept is that of the limiter. A limiter is a protruding element of the plasma-facing components. Beyond a certain radius the magnetic field lines intersect with the limiter causing the particles to hit the limiter surface much more than the remaining plasma-facing materials which are shielded in this way from the core plasma. The magnetic flux surface just in front of the limiter surface is called the last closed flux surface or separatrix. It separates the core plasma from the so called scrape-off layer. The problem with the limiter concept is that particles eroded from the limiter surface enter the core plasma directly. Therefore, the more sophisticated divertor concept has been introduced. The divertor geometry is shown schematically in figure 2.8. The main difference with the limiter is that in the divertor the plasma-surface interaction occurs remotely from the core plasma. An electric current running parallel with the plasma current through a toroidal conductor underneath the vessel modifies the magnetic field such that one creates a so called X point where the poloidal magnetic field vanishes. As in the limiter case the last closed flux surface or separatrix is the magnetic flux surface separating the core plasma with closed magnetic flux surfaces from the scrape off layer with magnetic flux surfaces intersecting with the plasma-facing components. The inner and outer divertor components where the plasma-surface interaction is concentrated are called the vertical target plates. The regions above the vertical target plates are called the baffles. The region below the X point is called the private flux region. The divertor component below the private flux region is called the dome. Plasma-surface interaction in the divertor leads to the production of neutrals. This allows pumping out of impurities and helium ashes from the divertor region. The plasma-facing components different from the limiter or divertor components are called the first wall. Here the plasma-surface interaction is less intense.

2.2.5 The ITER project

The power balance of a tokamak dictates that a future power plant will have to be much larger than the present experimental devices. Eventually a full scale experimental reactor will have to be built in order to prove the feasibility of commercial energy production by means of thermonuclear fusion. As building such a huge machine is financially very demanding it was first proposed at the "Geneva Superpower Summit" in 1985 to start up an international collaboration. This was the birth of the ITER project. ITER stands for "International Thermonuclear Experimental Reactor" and also means "the way" in Latin. It is supported by 7 parties representing over half of the world's population: Russia, the USA, the EU, Japan, China, South Korea and India. The project is one of the largest and most ambitious international science projects ever conducted due to the numerous organizational, legal, logistics, financial and last but not least engineering issues. The ITER site was determined in June 2005 to be located at Cadarache, near Aix-en-Provence in Southern France. The ITER Organization was officially established in October 2007. The site preparation works including obligatory archaeological diggings and fauna and flora protection measures began in January 2007. The actual construction of the scientific buildings and facilities began in July 2010. The status of the constructions can be followed via the ITER website [13]. In the mean time a lot of components are being produced all over the world and shipped to the ITER site. Some components are extremely large and heavy. In order to allow also delivery of these components heavy road works have been carried out along the 104 km itinerary between the harbour of For-sur-Mer and the ITER site. The first plasma is planned for 2020. According to the design ITER will deliver 500 MW fusion power from 50 MW input power. So, it will be the first tokamak producing net energy. ITER will be a very complex device. As shown in figure 2.9 the main components are

- **Magnets:** The magnet system of ITER comprises 18 superconducting toroidal field coils, 6 poloidal field coils, a set of correction coils and a central solenoid. The extremely high magnetic fields up to 13 T required for confining the fusion plasma make the use of superconducting magnets necessary. The superconductors will be cooled by supercritical helium. The main function of the toroidal field magnets is to confine the plasma particles. The 18 coils are composed out of strands with a total length of 150 000 km and a weight of 6540 tons. The poloidal field coils, placed outside the toroidal field coils, pinch the plasma away from the wall and contribute to the shaping and stability of the plasma. Both the poloidal and toroidal field coils lie between the vacuum vessel and the cryostat. At this position they are cooled and shielded from the high-energy neutrons at the same time. The central solenoid functions as large transformer by inducing the main toroidal plasma current up to 17 MA and forms at the same

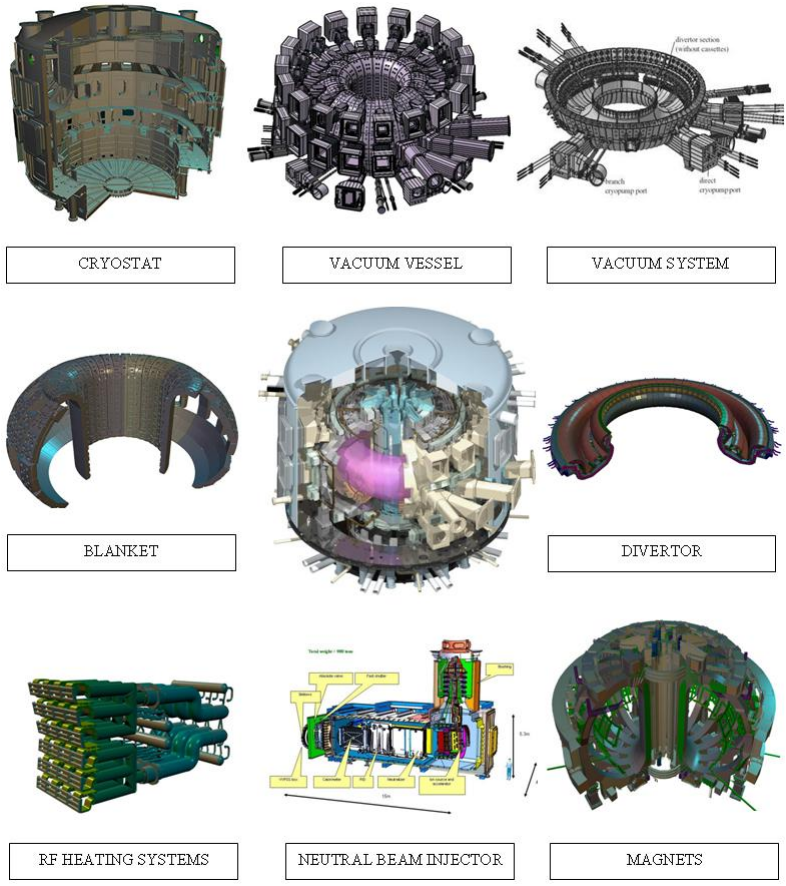

Figure 2.9: Schematic view of ITER and its main components [13]

time also the backbone of the magnet system.

- **Vacuum vessel:** The ITER vacuum vessel is a hermetically sealed, toroidally shaped, stainless steel container inside the cryostat providing an enclosed vacuum environment for the fusion reactions. With its height of 11 m and internal diameter of 6 m the vessel will be twice as large and sixteen times as heavy as any previous tokamak. The double steel walls will allow cooling water to circulate between them. The inner surfaces of the vessel will be covered by blanket modules for shielding from the hot fusion plasma and the high-energy neutrons. Together with its 44 ports for remote handling, diagnostic systems, heating systems and vacuum systems the vacuum vessel will weigh

about 8000 tons. This is slightly more than the Eiffel Tower.

- **Blanket:** The blanket is one of the most critical and technically challenging components in the ITER tokamak. It provides shielding of the outer components from the high heat load and the fast neutrons inside. The neutrons lose their kinetic energy in the blanket by converting it into heat. This heat is then collected by the coolants and will be used in DEMO and the later commercial reactors for electrical energy production as in an ordinary power plant. For purposes of maintenance of the vacuum vessel, the blanket wall will be modular. Each of the 440 individual segments will measure 1m x 1.5m and weigh up to 4.6 tons. A segment will consist in turn out of two parts. The first part is a detachable plasma facing first wall consisting out of beryllium for removal of the plasma heat load. The second part is a semi-permanent shield out of high-strength copper and stainless steel dedicated to the neutron shielding. Later in the ITER project, sophisticated modules will be inserted for testing the concept of tritium breeding out of lithium.

- **Divertor:** The divertor is also a plasma facing component and thus critical. It is located at the bottom inside the vacuum vessel and its function is to extract heat, helium ash and impurities from the plasma. With magnetic coils the field lines are shaped such that the divertor region is removed from the plasma core with its closed flux surfaces. The plasma layer between the last closed flux surface and the plasma facing material is called the scrape-off layer. In this layer the plasma particles are directed towards the divertor target plates where they can be extracted. The divertor supporting structure in ITER will be made primarily from stainless steel. The plasma facing parts will be made from tungsten and beryllium.

- **Neutral Beam Injector:** A tokamak power plant requires temperatures around 150 000 000 K. With only the Ohmic heating resulting from the induced plasma current such temperatures will never be reached. Therefore, additional heating methods will be used in ITER. One of these is neutral beam injection. One starts with negative deuterium ions. These are accelerated up to 1 MeV and neutralized. Neutral particles can enter the plasma without any problem. Once in the plasma, they transfer their energy by means of collisions with the plasma particles.

- **RF heating system:** The ITER fusion plasma will also be heated by radio waves at certain frequencies. In Ion Cyclotron Resonance Heating the ions are heated, while in Electron Cyclotron Resonance Heating the energy is transferred to the electrons. This requires a wave generator, a transmission line and an antenna coupling the waves into

the plasma. It is very difficult to tune the system such that the waves heat the plasma efficiently.

- **Cryostat:** The ITER cryostat is a very large, stainless steel structure surrounding the vacuum vessel and the superconducting magnets. It provides a super-cool, vacuum environment. The gap between the two concentric walls is filled with helium gas slightly above one atmosphere, acting as thermal barrier. The cryostat is 31 m high and 36.5 m wide. There are many openings in it for the cooling system, auxiliary heating, magnet feeders, diagnostics and removal of blanket and divertor parts.

With all the technologically very advanced systems listed above the story is not yet finished. ITER will also have different diagnostic systems, a sophisticated vacuum system, a remote handling system and hot cells for the treatment of contaminated materials, a power supply system providing up to 620 MW energy in peak periods, a tritium recovery system, a fuelling system and a cryoplant with cooling circuit. More details can be found on the ITER website [13].

And what after ITER? Hopefully the ITER project will show that thermonuclear fusion is a feasible option for commercial energy production. The next step is then a demonstration power plant. Scientists and engineers are now already thinking about the conceptual design of this DEMO reactor. According to the current fusion road map DEMO should put its first fusion power into the grid as early as 2040. But that is for the far future. Now it is important that research groups all over the world perform dedicated experiments with their small scale fusion relevant devices. Results from these studies will be indispensable for the design, construction and operation of ITER and DEMO because there are still several important problems to be tackled.

2.2.6 Advantages and disadvantages of tokamaks

In this section some general aspects of thermonuclear fusion in tokamaks have been discussed. There appears to be many advantages in comparison to other energy sources. Unfortunately, there are some drawbacks as well. The most important pros and cons are summarized below.

Advantages

- Deuterium is not radioactive and does not impose any health or environmental risks. It can be extracted from seawater in which it occurs with a concentration of about 154 ppm. The technology for extracting deuterium by destillation and electrolysis is well developed since large amounts of D_2O are used in heavy water nuclear power plants. Therefore, deuterium can be considered as virtually inexhaustible.

- No toxic or greenhouse gases are emitted during fusion of deuterium and tritium.
- Fusion can only occur under very strict conditions. An uncontrolled chain reaction is excluded. Any deviation from normal operation will automatically stop the fusion reactions.
- The raw materials needed for fusion cannot be used for the production of nuclear weapons. The radioactive tritium isotope is produced and consumed inside the reactor. Furthermore, at any time only a limited amount of tritium will be present in the reactor.
- The needed amount of fuel is very small.
- Fusion allows quite compact large scale power plants of 1 GW and more.

Disadvantages

- Tritium is a radioactive isotope decaying by electron emission with an average energy of about 5.7 keV. As such an electron cannot cross the dead layer of our skin. Only inhalation or ingestion of tritium poses health risks. Especially tritiated water and organically bound tritium are very dangerous as discussed in [14]. Therefore, the amount of tritium present in the reactor should at all times remain below a safety limit guaranteeing no adverse effects to the population or the environment in case of accidental release.
- Due to its short lifetime of about 12.3 years tritium occurs only as a trace element in nature. Therefore, tritium will be produced inside the reactor by neutron bombardment of lithium. The rather limited lithium reserves could pose a problem in the not so far future, especially when the lithium battery market keeps booming. By making the extraction process of lithium from seawater more efficient this problem could be solved.
- Fusion research is very time and money consuming. After decades of research still no net energy has been produced. Hopefully the ITER project will show us that fusion research is really worth all that patience and money.
- Nuclear waste is unavoidable due to tritium retention and neutron activation. Careful material selection and design can, however, limit the amount and lifetime of the nuclear waste such that the reactor materials could be reused already after about 100 years.
- The laws of nature prohibit small scale fusion power plants. Net production of energy unavoidably implies a minimum reactor size. This

could be a problem in desolated areas, where small scale power plants are more desirable.

It is clear that also thermonuclear fusion will never be without disadvantages. I think the perfect energy source does not exist. Renewables, fission and fusion, according to me, all three have their task. The efficiency of renewables is quite low, but will for sure be improved significantly during the next decades. Renewables will probably never be able to provide energy worldwide and uninterrupted. They are, however, very useful for less populated and desolated areas and as support for a more stable and large scale energy source. Large scale energy production is today provided by fission and fossil fuel burning. As explained in 2.1 fossil fuel burning is just no option. So, of the present energy sources only fission remains. Fission power plants, however, are still subject to a non-negligible risk of severe accidents and unavoidably produce a large amount of long lived radioactive waste. Unfortunately, it is presently not straightforward to replace the existing fission power plants by a good alternative. Hence, it is very important to support also the research on fission. In this way fission power plants can be made safer and more efficient and the long lived radioactive waste can be reduced as much as possible. In the mean time, scientists and engineers have to think about an alternative for fission. This is where fusion comes into play. Considering all good things it could offer us, it would be a shame losing courage because a fusion power plant is so hard to realize. Hopefully ITER will shows us that we are on the right track.

2.3 Plasma physics

The deuterium-tritium fuel in a thermonuclear fusion reactor is in the plasma state. Therefore, plasma physics is an important aspect of thermonuclear fusion research. A plasma is a quasi-neutral medium containing charged particles that exhibit a collective behaviour. It can be created by heating up a gas to very high temperatures or by running a high electric current through a gas. In this way one partially or fully ionizes the gas. As such the transition to a plasma is not characterized by a clear phase transition. Anyhow, plasma is often called the fourth state of matter because it has such peculiar properties.

Around 1920 Irving Langmuir laid the foundations of plasma physics and introduced the name "plasma". In the 1920's and 1930's plasmas were studied systematically for the first time in order to understand the effect of the ionosphere on long distance radio wave propagation and for the optimization of electron tubes for use in pre-semiconductor electronics. Over the years the extraordinary properties of plasmas has led to their use for a wide variety of applications such as thermonuclear fusion, plasma thrusters for space propulsion, plasma display panels, fluorescent lighting, surface modification and air purification.

Plasma physics is a very complex and broad topic. This section discusses only a slight part of plasma physics relevant for this work. This section forms the theoretical background for the VMCPT plasma simulation code discussed in 4.2, the Langmuir probe analysis software discussed in 4.3 and the characterization of the VISIONI plasma simulator described in chapter 6. Therefore, the focus is on the physics relevant for the low temperature, weakly ionized plasma in VISIONI. The first subsection gives a short general introduction on the peculiarities of a plasma such as collective behaviour, Debye shielding and quasi-neutrality. This subsection also discusses the concept of plasma temperature. Subsection 2.3.2 discusses the different available techniques for modelling a plasma analytically and numerically as a support for the choice of the most appropriate model for studying the plasma in VISIONI. Subsection 2.3.3 gives some insight in the motion of charged particles in a magnetized plasma by looking at the motion from the single particle point of view. This will turn out to be helpful for understanding of the inhomogeneities observed during the characterization of the plasma in VISIONI. The kinematics and dynamics of collisions between plasma particles are treated in subsection 2.3.4. This theory forms the basis of the collision module in the VMCPT code. Subsection 2.3.5 gives a general description of the macroscopic charged particle transport comprising drift due to electric fields and diffusion related to thermal motion and the influence magnetic fields and collisions have on these macroscopic charged particle transport phenomena. In subsection 2.3.6 it is explained how a sheath layer is formed at locations where the plasma is in contact with materials because sheath formation is an important feature of all laboratory plasmas and also as a support for the Langmuir probe theory presented in subsection 2.3.7 which forms the background for the Langmuir probe analysis software developed for VISIONI.

2.3.1 The plasma state

Plasmas have a number of properties which are not in line with our daily experience. First of all, the concept of temperature has to be revised. In ordinary life matter is usually in local thermal equilibrium at molecular level and can be characterized by a local temperature. This local temperature is a measure of the thermal motion of a set of particles in mutual equilibrium at a certain location. Local thermal equilibrium requires that the collision time of the particles is much shorter than the time over which the state of the system changes under influence of external forces. This is definitely not always the case in a plasma. Often the collisionality is too low or the electric field is too high. Especially between electrons and ions there is rarely a local equilibrium because momentum transfer between particles with large mass difference is very inefficient as will be shown in 2.3.4. Therefore, it is common that electrons and ions only reach separate states of local equilibrium characterized by an electron temperature T_e and an ion temperature

T_i which can be very different. It should be mentioned that the temperature in plasma physics is by convention not stated in Kelvin but in electron volt by implicitly multiplying with k/q_e.

As for ordinary matter the energies and velocities of the plasma particles in thermal equilibrium are distributed according to the Maxwell-Boltzmann or Maxwell distribution. This distribution can be derived using statistical mechanics [15] or by looking for steady state solutions of the fundamental Boltzmann equation with collision term [16]. According to a Maxwellian distribution the probability that a particle has x, y and z velocity components between v_x and $v_x + dv_x$, between v_y and $v_y + dv_y$ and between v_z and $v_z + dv_z$ respectively is given by

$$f_{MB}(v_x, v_y, v_z)dv_x dv_y dv_z \tag{2.2}$$

with f_{MB} the Maxwell-Boltzmann distribution defined as

$$f_{MB}(v_x, v_y, v_z) = \left(\frac{m}{2\pi kT}\right)^{3/2} \exp\left(-\frac{m(v_x^2 + v_y^2 + v_z^2)}{2kT}\right) \tag{2.3}$$

So each velocity component v_i is distributed according to

$$f_{MB}(v_i)dv_i = \sqrt{\frac{m}{2\pi kT}} \exp\left(-\frac{mv_i^2}{2kT}\right) dv_i \tag{2.4}$$

which can be recognized as a Gaussian distribution with mean 0 and standard deviation $\sigma = \sqrt{kT/m}$. For an isotropic velocity distribution a distribution for the magnitude of the velocity can be found from (2.3) by transforming to spherical coordinates. The probability that a particle has a speed between v and $v + dv$ is then given by

$$f_{MB}(v)dv = 4\pi \left(\frac{m}{2\pi kT}\right)^{3/2} \exp\left(-\frac{mv^2}{2kT}\right) v^2 dv \tag{2.5}$$

This distribution function can be converted to an energy distribution function by the substitution $v = \sqrt{2E/m}$. The probability that a particle has an energy between E and $E + dE$ is then given by

$$f_{MB}(E)dE = 2\sqrt{\frac{E}{\pi}} \left(\frac{1}{kT}\right)^{3/2} \exp\left(-\frac{E}{kT}\right) dE \tag{2.6}$$

Sometimes one also defines the energy probability distribution function or EPDF as the energy distribution function divided by $\sqrt{E}$ because this factor only takes into account the density of states in energy space. Using the above distribution functions one can calculate that the most probable speed is given by

$$v_p = \sqrt{\frac{2kT}{m}} \tag{2.7}$$

the average speed by

$$< v >= \sqrt{\frac{8kT}{\pi m}} \tag{2.8}$$

and the average energy by

$$< E >= \frac{3}{2}kT \tag{2.9}$$

Another important property of a plasma is that it exhibits collective behaviour of charged plasma particles. Neutral gas particles interact by means of the short-ranged van der Waals interaction which decays with inter-particle distance to the power -6. Therefore, they interact only when they are very near to each other during a collision. Charged particles, on the other hand, interact through the long-ranged Coulomb interaction which decays only with inter-particle distance to the power -2. Therefore, there is even interaction between very remote particles. This causes the collective behaviour that leads to all kind of phenomena that are typical for plasmas such as plasma waves.

Although a plasma contains a huge amount of charged particles it is a quasi-neutral medium. This means that the plasma deviates from neutrality only on very small length scales due to the shielding effect of the charged particles. Imagine for instance starting with an infinitely large, homogeneous plasma where the charges of negative electrons and singly charged positive ions perfectly compensate each other throughout the whole volume. Now suppose that due to thermal fluctuations a small net charge $+Q$ is introduced at the origin of the coordinate system. This positive charge attracts electrons and repels ions. Further it is assumed that the changes in the plasma are slow enough such that both the electrons and ions stay in thermal equilibrium. The modification of the electron and ion density around the charge $+Q$ can then be described by the Boltzmann relation as

$$n_e(\vec{r}) = n_0 \exp\left(\frac{+q_e V(\vec{r})}{kT_e}\right) \approx n_0 \left(1 + \frac{q_e V(\vec{r})}{kT_e}\right) \tag{2.10}$$

$$n_i(\vec{r}) = n_0 \exp\left(-\frac{q_e V(\vec{r})}{kT_i}\right) \approx n_0 \left(1 - \frac{q_e V(\vec{r})}{kT_i}\right) \tag{2.11}$$

where it was taken into account that the density n_0 before the additional charge was introduced is equal for electrons and ions due to the assumed neutrality and that the fluctuations of the electric potential $V(\vec{r})$ introduced by the small additional charge is small such that one can say that $q_e V(\vec{r}) << kT_e, kT_i$. This modification of the charged particle densities leads to shielding of the positive charge from the plasma. This can be shown more quantitatively by solving Poisson's equation for the electric potential. Taking into account the spherical symmetry of the problem and inserting

the Boltzmann relations for the charged particle densities Poisson's equation becomes

$$\frac{\partial^2 V}{\partial r^2} + \frac{2}{r}\frac{\partial V}{\partial r} = -\frac{1}{\epsilon_0}\left[Q\delta(r) - \frac{q_e^2 n_0}{kT_e}\Phi - \frac{q_e^2 n_0}{kT_i}\Phi\right] \tag{2.12}$$

which can be solved to give

$$V(r) = \frac{Q}{4\pi\epsilon_0 r}\exp\left(-\frac{r}{L_D}\right) \tag{2.13}$$

with the Debye length L_D defined as

$$\frac{1}{L_D^2} = \frac{1}{L_{De}^2} + \frac{1}{L_{Di}^2} = \frac{q_e^2 n_0}{\epsilon_0 kT_e} + \frac{q_e^2 n_0}{\epsilon_0 kT_i} \tag{2.14}$$

This is the ordinary Coulomb potential for a point charge but decaying exponentially with the Debye length as decay length. So the charge $+Q$ is shielded from the plasma over a few Debye lengths. The shielding is done in parallel by electrons and ions. This can be seen from the fact that the total Debye length L_D is shorter than both the electron Debye length L_{De} and the ion Debye length L_{Di}. The ions are much more massive than the electrons. Furthermore, in a lot of laboratory plasmas the power is mainly coupled to the electrons and the energy transfer between electron and ions is very low such that the ion temperature is much lower than the electron temperature [17]. Therefore, the ions in such plasmas are very slow. It is then no longer valid to assume they reach a Boltzmann equilibrium as was done in this calculation. The ions then do not contribute to the shielding and the ion contribution to the Debye length should be dropped. The Debye length is then defined as

$$L_D = \sqrt{\frac{\epsilon_0 kT_e}{q_e^2 n_e}} \tag{2.15}$$

It decreases with increasing electron density. This reflects the fact that shielding is more effective if there are a lot of electrons. The Debye length increases with increasing electron temperature. This reflects that electrons with higher energy are less influenced by the presence of an additional charge. This shielding behaviour causes the natural tendency of a plasma to remain neutral on length scales larger than the Debye length. Any disturbance of the electric potential such as a biased electrode is shielded from the plasma over a few Debye lengths. Only on the Debye length scale deviations from neutrality are possible.

2.3.2 Plasma modelling

A plasma is a very complex medium. Only very few plasma physics problems can be solved analytically. In most cases the relevant physics can only be

taken into account in a more sophisticated numerical model. This subsection summarizes the most commonly used computer simulation techniques in plasma physics. This discussion will be used later on in 4.2.1 to choose the most appropriate technique for simulating the plasma in VISIONI. More extensive overviews with state of the art examples can be found for instance in [18] and [19].

At the microscopic level a plasma is fully described at a certain time by the positions and velocities of all plasma particles (atoms, molecules, radicals, excited species, ions and electrons). In principle any initial state can be evolved in time by numerically integrating Newton's equation of motion for each particle, provided that the externally applied forces and the interaction mechanisms between the particles are known.

This easy to grasp single particle point of view is the underlying idea of Particle-In-Cell Monte Carlo Collision simulation (PIC-MCC). The main steps are shown in figure 2.10. The simulation is started by initializing the plasma particles with positions and velocities according to appropriate distributions. Then a loop is iterated until steady state is reached. The loop has four parts. Firstly, the electric charge and current densities are calculated from the charged particle positions and velocities. Subsequently, the charge and current densities are used to solve Maxwell's equations for the electric and magnetic fields on a grid resolving the Debye length. Then the positions and velocities of the plasma particles are updated by integrating Newton's equation of motion. For the charged particles the electric and magnetic fields are interpolated from the grid to the charged particle positions. For plasmas contained in a finite chamber plasma-surface interaction effects can be taken into account for particles impinging on the surface of the plasma chamber walls. This is done with a Monte Carlo scheme based on sputtering yields, secondary electron emission probabilities, reflection probabilities and recombination probabilities coming from theory, simulations or experiments. At the end of the time step the particles are also allowed to collide with each other. These collisions are treated with a Monte Carlo scheme as well. It is based on theoretical or experimental collision cross sections. The velocities of the colliding particles are updated and some reactions require the release (e.g. ionization) or removal (e.g. recombination) of new particles.

For almost any problem it is impossible to track all physical particles due to limitations in CPU time. Therefore, PIC-MCC typically makes use of super-particles representing a lot of physical particles. However, meaningful simulations imply an upper limit to the number of physical particles that can be represented by one super-particle. One has to make sure that the statistics of the simulation are high enough. Each cell of the grid for solving Maxwell's equations should contain a significant amount of super-particles. Special care should also be taken that the high energy tails of the energy distribution functions are resolved. The CPU time can also be reduced by limiting the number of tracked species. Often it is not necessary to track

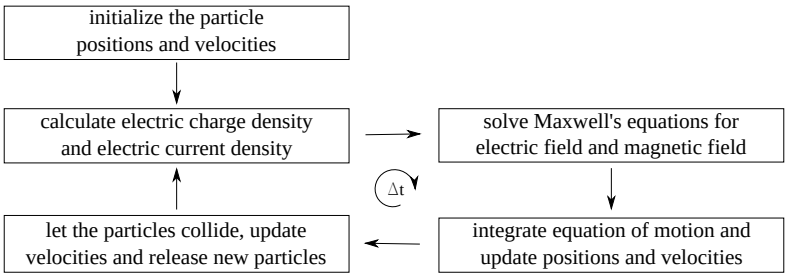

Figure 2.10: Basic steps of a Particle-In-Cell Monte Carlo Collision simulation

all species. In weakly ionized plasmas for instance it is realistic to assume that the neutral particles form a constant uniform background.

Besides the introduction of super-particles and the use of a grid for solving Maxwell's equations, no real approximations are used in PIC-MCC. The quality of the simulation is limited of course by the quality of the plasma-surface interaction and collision cross section data. PIC-MCC is a very powerful simulation technique resulting in spatially and temporally resolved data on particle densities, energy distributions, flows and self-consistent electromagnetic fields. Unfortunately, for a lot of systems PIC-MCC is computationally too demanding even for the most powerful supercomputers. This is especially true for large systems and for systems for which spatial 3D effects need to be taken into account. Often the bottleneck in PIC-MCC is solving Maxwell's equations on a Debye length resolving grid. One possibility is to use predefined electromagnetic fields based on measurements, theory or simulations. Such Monte Carlo simulations (MC) are computationally much less demanding. They still take into account the non-equilibrium behaviour of the plasma but they are not self-consistent with respect to the electromagnetic field. More details about PIC-MCC and MC can be found for instance in [20], [21] and [22].

Most simulation techniques do not use the single particle point of view introduced above. They look at the plasma from a statistical point of view. The plasma is in this case characterized by a set of particle phase space distribution functions $f_i(\vec{r}, \vec{v}, t)$ for the different plasma species i. The functions $f_i(\vec{r}, \vec{v}, t)$ represent the particle phase space densities at location $(\vec{r}, \vec{v})$ and time t and allow to calculate directly macroscopic quantities such as the particle densities $n_i(\vec{r}, t)$ and particle fluxes $\Phi_i(\vec{r}, t)$ by multiplying respectively with 1 and $\vec{v}$ and integrating over the whole velocity space. In the statistical point of view Newton's equation of motion is replaced by the Boltzmann equation

$$\frac{\partial f_i}{\partial t} + \vec{v} \cdot \frac{\partial f_i}{\partial \vec{r}} + \frac{\vec{F}}{m} \cdot \frac{\partial f_i}{\partial \vec{v}} = \left(\frac{\partial f_i}{\partial t} \right)_{coll} \tag{2.16}$$

It describes the time evolution of the phase space distribution function due to propagation, acceleration and collisions of the particles. By recalling Newton's equation of motion one can see that the left hand side of the Boltzmann equation is actually the total or convective derivative of the phase space distribution function. So the Boltzmann equation states that in a reference frame travelling together with the particles the phase space distribution function can only change due to scattering, particle creation and particle loss by collisions. Each species i has its own Boltzmann equation. Together they form a set of complicated integrodifferential equations which are coupled through the collision term and through Maxwell's equations for the self-consistent electromagnetic field. In practice one has to make almost always simplifying assumptions in order to solve this complicated set of equations.

The simplest model to solve the set of Boltzmann equations is a so called global model. In this case it is assumed that the plasma is spatially uniform. Furthermore, non-equilibrium or kinetic effects are not taken into account. This means that the particle energies are supposed to be distributed according to the Maxwellian equilibrium distribution discussed in 2.3.1. The set of Boltzmann equations can then be integrated over the whole phase space resulting in an easy to solve set of coupled rate equations for the time evolution of the total number of particles N_i for each species i of the form

$$\begin{aligned} \frac{dN_i}{dt} = & \sum_j N_j S_{i,j} + \sum_{j,k} N_j N_k S_{i,jk} + \sum_{j,k,l} N_j N_k N_l S_{i,jkl} + S_i \\ & - N_i L_i - \sum_j N_i N_j L_{i,j} - \sum_{j,k} N_i N_j N_k L_{i,jk} \end{aligned} \tag{2.17}$$

The first four terms on the right hand side represent sources due to respectively radiative decay and wall collisions, due to two-body collisions, due to three-body collisions and due to injection of particles. The next three terms represent losses due to respectively radiative decay and wall collisions, due to two-body collisions and due to three-body collisions. The rate coefficients are averaged values over the predefined Maxwellian energy distribution functions.

A global model allows very fast calculation of the evolution of the average densities of the different species. It is easy to take into account a lot of species and chemical reactions. Spatial effects and electromagnetic fields can, however, not explicitly be taken into account in a global model. It is also necessary to assume certain predefined energy distributions for the species in order to calculate the appropriate averaged rate coefficients. This

limiting assumption can be avoided by combining the global model with a self-consistent calculation of the electron energy distribution function based on the electron Boltzmann equation. The electron energy distribution is very often not Maxwellian and strongly influences critical reaction rates. The electron Boltzmann equation can be converted to a set of coupled first order differential equations by finite differencing the electron energy axis into a number of cells [23], [24]. One can also expand the phase space distribution function in spherical harmonics. An approximate solution of the electron Boltzmann equation can then be found by keeping only the first two terms in the expansion in case of small anisotropy [25], [26] or if necessary truncate the expansion at a higher order term [27].

The set of coupled Boltzmann equations can also be solved in a less approximate way with a fluid model. The basic idea is to replace the Boltzmann equation by its equivalent infinite series of velocity moments. The nth moment is calculated by multiplying the Boltzmann equation with the nth power of the velocity and integrating it over the whole velocity space. The first two moments are the continuity equation and the momentum equation that can be written as

$$\frac{\partial n}{\partial t} + \vec{\nabla} \cdot (n\vec{u}) = \left(\frac{\partial n}{\partial t}\right)_{coll} \tag{2.18}$$

$$mn\left[\frac{\partial \vec{u}}{\partial t} + (\vec{u} \cdot \vec{\nabla})\vec{u}\right] = n\vec{F} - \vec{\nabla} \cdot P + mn\left(\frac{\partial \vec{u}}{\partial t}\right)_{coll} \tag{2.19}$$

with n the particle density and $\vec{u} = \Phi/n$ the average flow velocity. P is the stress tensor. Its diagonal terms take into account the pressure gradient force, while its off-diagonal terms represent viscosity effects. The last terms on the right hand side of the first and second equation represent respectively the change in particle density and momentum density due to collisions. The continuity and momentum equations are equivalent to the continuity and Navier-Stokes equations in fluid mechanics. The next velocity moment of the Boltzmann equation is the energy equation. Truncating the infinite series of velocity moment equations requires a closure condition because each equation contains an unknown determined by the next equation. Closure usually involves some assumptions for the velocity distribution. The kind of closure depends on the type of application. Most fluid models contain the continuity, momentum and energy equations for electrons and ions. One of the most famous fluid models is that derived by Braginskii [28]. The plasma fluid equations are normally coupled with Maxwell's equations to calculate the electromagnetic field self-consistently. This is important for taking into account the sheath and presheath formed where the plasma is in contact with the surrounding materials. The boundary conditions allow taking into account the specific geometry of the problem. Solving this complicated set of equations eventually results in spatially resolved

Table 2.5: Comparison of different plasma simulation techniques

	PIC-MCC	MC	fluid	hybrid	global
EM field	self-consistent	predefined	self-consistent	self-consistent	not explicit
kinetic effects	fully kinetic	fully kinetic	indirect	partly kinetic	indirect
spatial effects	yes	yes	yes	yes	no
CPU time	very long	long	long	long	very short

information on the densities and flows of the different species and on the self-consistent electromagnetic field. The advantage of fluid simulations is that they are much faster than PIC-MCC simulations. However, kinetic effects can only be taken into account indirectly by transport and rate coefficients calculated with a Boltzmann solver. Sometimes it is possible to combine the best of both worlds. In so called hybrid models one can for instance treat ions and neutrals as a fluid, while using PIC-MCC for the electrons for which kinetic effects are more important.

This short overview of plasma simulation techniques is of course not exhaustive. There exists no simulation technique which can solve all problems. Each technique has its advantages and disadvantages. The most suitable simulation technique depends on the peculiarities of the problem and on the kind of information one wants to get out of the simulation. Table 2.5 summarizes the most important advantages and disadvantages of the simulations techniques discussed above.

2.3.3 Charged particle motion

Although a plasma is characterized by collective behaviour of charged particles, one can get already a lot of insight in the behaviour of a plasma by looking at charged particle motion from a single particle point of view. The motion of an electrically charged particle with mass m and charge q in an electromagnetic field is governed by the Newton-Lorentz equation of motion

$$m\frac{d\vec{v}(t)}{dt} = q\left[\vec{v}(t)\times\vec{B}(\vec{r}(t),t)+\vec{E}(\vec{r}(t),t)\right] \quad (2.20)$$

$$\frac{d\vec{r}(t)}{dt} = \vec{v}(t) \quad (2.21)$$

In the general case of a time and space dependent electromagnetic field the trajectories can become very complicated and impossible to calculate analytically. However, in this subsection it will be shown that for fields slowly varying both in time and in space it is possible to calculate an approximate solution analytically. Slowly varying will be specified more quantitatively below. This theory will be used in 6.3.4.1 for explaining the observed inhomogeneities in the magnetized edge of the plasma in VISIONI. A more detailed treatment of this topic can be found for instance in [29] and [30].

Let us start with the very simple case of a magnetic field that is constant both in time and space. The direction of the magnetic field is defined as the z direction. Equation (2.20) then becomes.

$$m\frac{d\vec{v}(t)}{dt} = q\vec{v}(t) \times \vec{B} \tag{2.22}$$

By elaborating the vector product the components of the equation read

$$\begin{aligned}
\frac{dv_x(t)}{dt} &= \frac{qB}{m}v_y && (2.23)\\
\frac{dv_y(t)}{dt} &= -\frac{qB}{m}v_x && (2.24)\\
\frac{dv_z(t)}{dt} &= 0 && (2.25)
\end{aligned}$$

By taking the time derivative of the equations for the x and y component of the velocity one can easily find that the time evolution of the velocity is given by

$$\begin{aligned}
v_x(t) &= v_{cycl}\sin\left(\frac{qB}{m}t + \Phi\right) && (2.26)\\
v_y(t) &= v_{cycl}\cos\left(\frac{qB}{m}t + \Phi\right) && (2.27)\\
v_z(t) &= v_{||} && (2.28)
\end{aligned}$$

These equations clearly show that the magnitudes of the velocity parallel and perpendicular to the magnetic field are constant in time and given by the integration constants $v_{||}$ and v_{cycl} respectively. Φ is the third integration constant depending on the initial velocities in the x and y direction. Integrating a second time gives the trajectory

$$\begin{aligned}
x(t) &= x_0 - \frac{mv_{cycl}}{qB}\cos\left(\frac{qB}{m}t + \Phi\right) && (2.29)\\
y(t) &= y_0 + \frac{mv_{cycl}}{qB}\sin\left(\frac{qB}{m}t + \Phi\right) && (2.30)\\
z(t) &= z_0 + v_{||}t && (2.31)
\end{aligned}$$

with x_0, y_0 and z_0 the three integration constants depending on the initial position. These equations show that the particle moves in a helix. Parallel with the magnetic field it moves with a constant velocity, while simultaneously describing circles in the plane perpendicular to the magnetic field with angular frequency given by the cyclotron frequency

$$\omega_{cycl} = \frac{qB}{m} \tag{2.32}$$

and radius given by the cyclotron or Larmor radius

$$R_{cycl} = \frac{mv_{cycl}}{qB} \tag{2.33}$$

If one looks at the xy plane from the hemisphere with $z > 0$ one sees positively and negatively charged particles describing circles in respectively clockwise and anticlockwise direction. This helical motion is illustrated schematically for a positively charged particle in the diagrams (a) and (b) in figure 2.11. For particles in thermal equilibrium with a Maxwellian velocity distribution with temperature T as explained in 2.3.1 one usually defines the average cyclotron radius $< R_{cycl} >$. This requires calculation of the average velocity in the xy plane $< v_{cycl} >$ by performing the integration

$$\left(\frac{m}{2\pi kT}\right)^{3/2} \int_{-\infty}^{+\infty} dv_z \exp\left(-\frac{mv_z^2}{2kT}\right) \int_0^{2\pi} d\theta \int_0^{+\infty} dv_r v_r^2 \exp\left(-\frac{mv_r^2}{2kT}\right)$$

Using the integral identities 5 and 7 this gives

$$< v_{cycl} >= \sqrt{\frac{\pi kT}{2m}} \tag{2.34}$$

and thus

$$< R_{cycl} >= \sqrt{\frac{\pi kTm}{2}} \frac{1}{qB} \tag{2.35}$$

Let us now make the situation a bit more complex by introducing additionally an electric field which is also constant both in time and space. Equation (2.20) then becomes

$$m\frac{d\vec{v}(t)}{dt} = q\left[\vec{v}(t) \times \vec{B} + \vec{E}\right] \tag{2.36}$$

By substituting $\vec{v}(t)$ by $\vec{v}'(t) + \vec{v}_{gc}$ with $\vec{v}_{gc}$ a constant drift velocity given by

$$\vec{v}_{gc} = \frac{\vec{E} \times \vec{B}}{B^2} \tag{2.37}$$

and again elaborating the vector product gives then for the components

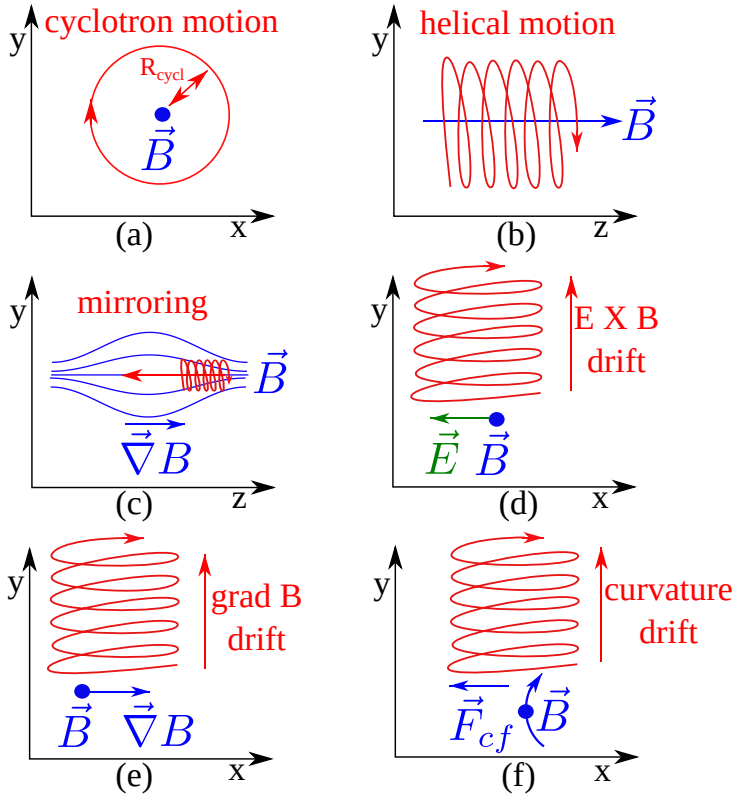

Figure 2.11: Different types of charged particle motion in an electromagnetic field illustrated for a positively charged particle

$$\frac{dv'_x(t)}{dt} = \frac{qB}{m}v'_y \tag{2.38}$$

$$\frac{dv'_y(t)}{dt} = -\frac{qB}{m}v'_x \tag{2.39}$$

$$\frac{dv'_z(t)}{dt} = \frac{qE_{||}}{m} \tag{2.40}$$

The equations for the motion in the plane perpendicular to the magnetic field are then the same as in the previous case without the electric field. This means that the motion perpendicular to the magnetic field is now a superposition of the cyclotron motion as before with an additional constant drift of the guiding centre of the cyclotron motion with velocity $\vec{v}_{gc}$ perpendicular to both $\vec{E}$ and $\vec{B}$. As illustrated in diagram (d) in figure 2.11

this can be understood by noticing that the cyclotron motion will not consist of perfect circles due to the electric field perpendicular to the magnetic field. One half of the cyclotron motion the particle is accelerated by the electric field, one half it is decelerated. It is this asymmetry that leads to the perpendicular drift. As for particles with opposite electric charge both the direction of the cyclotron motion and the electric force is inverted, the direction of the $\vec{E} \times \vec{B}$ drift remains unchanged. The motion parallel to the magnetic field is as before not influenced by the magnetic field. The parallel velocity is increasing uniformly with acceleration $qE_{||}/m$.

Let us now make the situation even more complex by allowing electric and magnetic fields to change in space but slowly in comparison with R_{cycl}. This condition is valid for the magnetized plasma in the edge of VISIONI. We will show that also in this case the motion can in good approximation be considered as a superposition of the fast cyclotron motion and a slow drift of the guiding centre of the cyclotron motion. With this idea in mind the following notations are introduced

$$\vec{r}(t) = \vec{r}_{gc}(t) + \vec{r}_{cycl}(t) \tag{2.41}$$
$$\vec{v}(t) = \vec{v}_{gc}(t) + \vec{v}_{cycl}(t) \tag{2.42}$$

Here $\vec{r}_{gc}(t)$ and $\vec{v}_{gc}(t)$ describe the slow drift of the guiding centre, while $\vec{r}_{cycl}(t)$ and $\vec{v}_{cycl}(t)$ describe the fast cyclotron motion around the guiding centre. Considering the slow change of the electric and magnetic fields in comparison with R_{cycl}, the fields can be approximated by truncating their Taylor expansions around the guiding centre position after the first order term according to

$$\vec{B}(\vec{r}(t)) = \vec{B}(\vec{r}_{gc}(t)) + (\vec{r}_{cycl}(t) \cdot \vec{\nabla})\vec{B}(\vec{r}_{gc}(t)) \tag{2.43}$$
$$\vec{E}(\vec{r}(t)) = \vec{E}(\vec{r}_{gc}(t)) + (\vec{r}_{cycl}(t) \cdot \vec{\nabla})\vec{E}(\vec{r}_{gc}(t)) \tag{2.44}$$

Substitution of (2.41-2.44) into the equation of motion (2.20), taking into account that by definition $\vec{v}_{cycl}(t)$ should obey

$$m\frac{d\vec{v}_{cycl}(t)}{dt} = q\vec{v}_{cycl}(t) \times \vec{B}(\vec{r}_{cycl}(t)) \tag{2.45}$$

and averaging the equation of motion over one cyclotron period such that all terms linear in the cyclotron motion disappear gives

$$m\frac{d\vec{v}_{gc}}{dt} = q\left[\vec{v}_{gc} \times \vec{B} + < \vec{v}_{cycl} \times (\vec{r}_{cycl} \cdot \vec{\nabla})\vec{B} >_{cycl} + \vec{E}\right] \tag{2.46}$$

where the time and space dependencies were no longer written down explicitly. The averaging in the second term on the right hand side can be done

by using for r_{cycl} and v_{cycl} the equations (2.26-2.31) with $x_0 = y_0 = z_0 = 0$ and by noticing that according to Maxwell's equations $\vec{\nabla} \cdot \vec{B} = 0$ and that $B_z \approx B$. One then gets

$$< \vec{v}_{cycl} \times (\vec{r}_{cycl} \cdot \vec{\nabla})\vec{B} >_{cycl} = -\frac{m v_{cycl}^2}{2qB} \vec{\nabla} B \tag{2.47}$$

Next we want to separate the motion parallel and perpendicular to the magnetic field. Splitting into components of $\vec{v}_{gc}$ gives

$$\vec{v}_{gc} = \vec{v}_{gc,\perp} + v_{gc,||} \frac{\vec{B}}{B} \tag{2.48}$$

In lowest order one has

$$\frac{d}{dt}\left(\frac{\vec{B}}{B}\right) = v_{gc,||} \frac{\vec{B} \cdot \vec{\nabla}}{B} \left(\frac{\vec{B}}{B}\right) \tag{2.49}$$

The time derivative of $\vec{v}_{gc}$ is then given by

$$\frac{d\vec{v}_{gc}}{dt} = \frac{d\vec{v}_{gc,\perp}}{dt} + \frac{dv_{gc,||}}{dt}\frac{\vec{B}}{B} + v_{gc,||}^2 \frac{\vec{B} \cdot \vec{\nabla}}{B}\left(\frac{\vec{B}}{B}\right) \tag{2.50}$$

With these decompositions equation (2.46) can now be split into a parallel and perpendicular component according to

$$m\frac{dv_{gc,||}}{dt} = \quad qE_{||} - \frac{m v_{cycl}^2}{2B}\left[\vec{\nabla} B\right]_{||} \tag{2.51}$$

$$m\frac{d\vec{v}_{gc,\perp}}{dt} = \quad q\vec{E}_{\perp} - \frac{m v_{cycl}^2}{2B}\left[\vec{\nabla} B\right]_{\perp} - \frac{m v_{gc,||}^2}{B}\vec{B} \cdot \vec{\nabla}\left(\frac{\vec{B}}{B}\right) + q\vec{v}_{gc,\perp} \times \vec{B} \tag{2.52}$$

Let us start with the perpendicular motion described by (2.52). The perpendicular drift velocity $\vec{v}_{gc,\perp}$ is assumed to have a very slow time dependence. Therefore, the left hand side of the perpendicular equation of motion becomes zero and $\vec{v}_{gc,\perp}$ can simply be eliminated. By taking the cross product with $\vec{B}$ one gets

$$\vec{v}_{gc,\perp} = \frac{\vec{E} \times \vec{B}}{B^2} + \frac{m v_{cycl}^2}{2qB^3}\vec{B} \times \vec{\nabla} B + \frac{m v_{gc,||}^2}{qB^3}\vec{B} \times \vec{B} \cdot \vec{\nabla}\left(\frac{\vec{B}}{B}\right) \tag{2.53}$$

The first contribution to the drift velocity is the $\vec{E} \times \vec{B}$-drift

$$\vec{v}_{\vec{E}\times\vec{B}} = \frac{\vec{E}\times\vec{B}}{B^2} \tag{2.54}$$

due to the perpendicular electric field. This drift was discussed already above. The second term is the $\vec{\nabla}B$-drift

$$\vec{v}_{\vec{\nabla}B} = \frac{mv_{cycl}^2}{2qB^3}\vec{B}\times\vec{\nabla}B \tag{2.55}$$

due to the perpendicular magnetic field gradient. As shown in diagram (e) in figure 2.11 this gradient leads to an asymmetry in the cyclotron orbits which causes the perpendicular drift. This drift is in opposite directions for particles with opposite electric charge. The third term is the centrifugal drift

$$\vec{v}_{cf} = \frac{mv_{gc,||}^2}{qB^3}\vec{B}\times\vec{B}\cdot\vec{\nabla}\left(\frac{\vec{B}}{B}\right) \tag{2.56}$$

due to the curvature of the magnetic field lines. This can be seen as follows. Imagine a curved magnetic field line. Take a cylindrical coordinate system with the radial coordinate equal to the local radius of curvature R_{curv} of the field line. The coordinate along the magnetic field line is then the azimuthal coordinate. Therefore, one has

$$\frac{\vec{B}\cdot\vec{\nabla}}{B}\left(\frac{\vec{B}}{B}\right) = \vec{e}_\theta\cdot\vec{\nabla}\vec{e}_\theta = -\frac{\vec{e}_r}{R_{curv}} \tag{2.57}$$

which allows to rewrite the third term in the perpendicular equation of motion as

$$\vec{F}_{cf} = \frac{mv_{gc,||}^2}{R_{curv}}\vec{e}_r \tag{2.58}$$

This is the typical expression for the centrifugal force. It is a pseudo-force taking into account the fact that in case the magnetic field line is curved the perpendicular equation of motion is seen from a reference frame that moves along a curved path and thus undergoes an acceleration perpendicular to the magnetic field. As illustrated in diagram (f) in figure 2.11 the centrifugal force leads to a drift which is in opposite directions for particles with opposite electric charge. Finally, it will be shown that for a vacuum or force-free magnetic field for which Maxwell's equations dictate that $\vec{\nabla}\times\vec{B} = 0$ the centrifugal drift is in the same direction as the $\vec{\nabla}B$-drift. Using vector calculus one can show that

$$\vec{B}\cdot\vec{\nabla}\left(\frac{\vec{B}}{B}\right) = \frac{\vec{B}\cdot\vec{\nabla}}{B}\vec{B} - \frac{\vec{B}}{B^2}\vec{B}\cdot\vec{\nabla}B \tag{2.59}$$

and thus that

$$\vec{B} \times \vec{B} \cdot \vec{\nabla} \left(\frac{\vec{B}}{B} \right) = \vec{B} \times \frac{\vec{B} \cdot \vec{\nabla}}{B} \vec{B} \tag{2.60}$$

For the special case $\vec{\nabla} \times \vec{B} = 0$ one has

$$\vec{B} \times (\vec{\nabla} \times \vec{B}) = \frac{1}{2} \vec{\nabla} (\vec{B} \cdot \vec{B}) - \vec{B} \cdot \vec{\nabla} \vec{B} = 0 \tag{2.61}$$

from which we find that

$$\frac{\vec{B} \cdot \vec{\nabla}}{B} \vec{B} = \frac{1}{2B} \vec{\nabla} (\vec{B} \cdot \vec{B}) = \vec{\nabla} B \tag{2.62}$$

Combining (2.60) and (2.62) one eventually finds that the centrifugal drift is indeed in the same direction as the $\vec{\nabla} B$-drift according to

$$\vec{v}_{cf} = \frac{m v_{gc,||}^2}{q B^3} \vec{B} \times \vec{\nabla} B \tag{2.63}$$

Now we will discuss the parallel motion described by (2.51). The first term describes the force due to the parallel electric field. As was discussed already in the beginning of this subsection it simply leads to a constant acceleration of the particle along the magnetic field lines. The second term describes a force related to the parallel gradient of the magnetic field. This force is called the magnetic mirroring force. To explain why it is called like that we start by multiplying the parallel equation of motion with $v_{gc,||}$ giving

$$\frac{d}{dt} \left(\frac{1}{2} m v_{gc,||}^2 + qV \right) = - \frac{m v_{cycl}^2}{2B} \frac{dB}{dt} \tag{2.64}$$

It was taken into account in this step that an electrostatic field $\vec{E}$ can be derived from an electrostatic potential V as $\vec{E} = -\vec{\nabla} V$. Dotting the total equation of motion (2.20) with $\vec{v}$ shows as usual that the total energy

$$E = \frac{1}{2} m \vec{v}^2 + qV \tag{2.65}$$

is a constant of motion. By splitting $\vec{v}$ into its components and averaging over one cyclotron period this can be rewritten as

$$E = \frac{1}{2} m v_{gc,\perp}^2 + \frac{1}{2} m v_{gc,||}^2 + \frac{1}{2} m v_{cycl}^2 + qV \tag{2.66}$$

As was discussed during treatment of the perpendicular motion $v_{gc,\perp}$ is a very slowly varying drift such that the sum of the last three term of the energy should also be equal to a constant that we will call E'.

$$E' = \frac{1}{2}mv_{gc,||}^2 + \frac{1}{2}mv_{cycl}^2 + qV \tag{2.67}$$

Using this in (2.64) shows that the magnetic moment μ_m defined as

$$\mu_m = \frac{mv_{cycl}^2}{2B} \tag{2.68}$$

is also a constant of motion. Let us look at the case without electric field to explain the magnetic mirroring. The constancy of E' and μ_m implies that a particle moving from a region with magnetic field B_i towards a region with a higher magnetic field B_f will have increasing v_{cycl} and decreasing $v_{gc,||}$. The initial velocities will be denoted as $v_{gc,||,i}$ and $v_{cycl,i}$. One can now easily calculate that if

$$\frac{B_f}{B_i} > 1 + \frac{v_{gc,||,i}^2}{v_{cycl,i}^2} \tag{2.69}$$

$v_{gc,||}$ will become zero and the particle will be reflected back. This is called magnetic mirroring and is shown schematically in diagram (c) in figure 2.11. Whether mirroring occurs depends on the ratio of the magnetic field strengths in the two regions and on the ratio of the initial parallel guiding centre velocity and the cyclotron velocity. For a mirror with a certain ratio of magnetic field strengths particles can escape through the mirror if their parallel velocity is high enough in comparison with the cyclotron velocity. This portion of velocity space is called the loss cone and does not depend on mass or charge of the particles. Particles which are originally not in this loss cone can still be scattered into it by collisions.

To summarize the motion of an electrically charged particle in a time independent electromagnetic field that is slowly varying in comparison with the cyclotron radius is composed of

- fast cyclotron motion in the plane perpendicular to the magnetic field
- acceleration along the magnetic field lines due to the parallel electric field
- mirroring along the magnetic field lines due to the parallel magnetic field gradient
- drifts perpendicular to the magnetic field due to the perpendicular electric field, the perpendicular magnetic field gradient and the curvature of the magnetic field lines

2.3.4 Particle collisions

Collisions between particles are very important in a plasma. They strongly influence both the energy and the particle balance. Different reactions can take place such as elastic momentum transfer, charge exchange, proton transfer, electronic excitation, vibrational excitation, rotational excitation, ionization and dissociation. This subsection forms the theoretical background for the collision module in the VMCPT code developed to simulate the plasma in VISIONI as described in 4.2.6. More details on collisions can be found for instance in [31], [32] and [33]. Firstly, 2.3.4.1 introduces the laboratory and the centre of mass reference frames as they are used in the subsequent theory to simplify the calculations. Then in 2.3.4.2 it is shown that, as the particle collisions can be treated as a two-body central force problem, they can be translated into an equivalent one-body problem. A classical equation is then derived for this one-body problem to calculate the trajectories of the colliding particles from the interaction potential. In 2.3.4.3 it is shown that the post-collision velocities can be calculated from the pre-collision velocities, based on energy and momentum conservation only. However, this requires the knowledge of the scattering angles. Therefore, it is demonstrated in 2.3.4.4 that the centre of mass scattering angles can be calculated from the classical trajectory equation derived in 2.3.4.2 for the special cases of Coulomb scattering and hard sphere scattering. Further, it is discussed in 2.3.4.5 that the collision probability and the probability for scattering in a certain direction are usually treated by introducing the concepts of cross section and differential cross section. Finally, in 2.3.4.6 it is shown that the average effect of Coulomb collisions in a plasma can be treated in good approximation as a diffusive process.

2.3.4.1 Laboratory and centre of mass reference frame

Consider the collision of two particles in an arbitrary reference frame. The positions and velocities in this frame are denoted by $\vec{r}_1$, $\vec{r}_2$, $\vec{v}_1$ and $\vec{v}_2$. The particle masses are denoted by m_1 and m_2. Sometimes it is more convenient to perform calculations in another special reference frame and then after the calculation transform the results back to the original reference frame. Two such frames that are used throughout this subsection are the laboratory frame and the centre of mass frame.

In the laboratory frame one of the two particles is at rest before the collision takes place. This particle is called the target. The other particle is called the projectile. The positions and velocities in this frame are denoted by $\vec{r}_p$, $\vec{r}_t$, $\vec{v}_p$ and $\vec{v}_t$. The particle masses are denoted by m_p and m_t. It does not matter which of the two particles is taken to be the target.

In the centre of mass frame the origin is pinned on the centre of mass of the two particles. Introducing the total mass $m_{tot} = m_1 + m_2$, the position $\vec{r}_{cm}$ and velocity $\vec{v}_{cm}$ of the centre of mass in the original frame are given

by

$$\vec{r}_{cm} = \frac{m_1\vec{r}_1 + m_2\vec{r}_2}{m_{tot}} \tag{2.70}$$

$$\vec{v}_{cm} = \frac{m_1\vec{v}_1 + m_2\vec{v}_2}{m_{tot}} \tag{2.71}$$

The centre of mass velocity $\vec{v}_{cm}$ is constant in the absence of external forces as will be shown in 2.3.4.2. Introducing the relative position $\vec{r}$, the relative velocity $\vec{v}$ and the reduced mass m_r defined by

$$\vec{r} = \vec{r}_1 - \vec{r}_2 \tag{2.72}$$

$$\vec{v} = \vec{v}_1 - \vec{v}_2 \tag{2.73}$$

$$m_r = \frac{m_1 m_2}{m_{tot}} \tag{2.74}$$

the relations (2.70-2.71) can be inverted to give

$$\vec{r}_1 = \vec{r}_{cm} + \frac{m_r}{m_1}\vec{r} \tag{2.75}$$

$$\vec{v}_1 = \vec{v}_{cm} + \frac{m_r}{m_1}\vec{v} \tag{2.76}$$

$$\vec{r}_2 = \vec{r}_{cm} - \frac{m_r}{m_2}\vec{r} \tag{2.77}$$

$$\vec{v}_2 = \vec{v}_{cm} - \frac{m_r}{m_2}\vec{v} \tag{2.78}$$

From the definition of the centre of mass frame it is then clear that the positions $\vec{r}_{1,cm}$ and $\vec{r}_{2,cm}$ and the velocities $\vec{v}_{1,cm}$ and $\vec{v}_{2,cm}$ in this frame are given by

$$\vec{r}_{1,cm} = \frac{m_r}{m_1}\vec{r} \tag{2.79}$$

$$\vec{v}_{1,cm} = \frac{m_r}{m_1}\vec{v} \tag{2.80}$$

$$\vec{r}_{2,cm} = -\frac{m_r}{m_2}\vec{r} \tag{2.81}$$

$$\vec{v}_{2,cm} = -\frac{m_r}{m_2}\vec{v} \tag{2.82}$$

These relations show that the particle velocities in the centre of mass system are oriented in opposite directions along $\vec{v}$. The positions and velocities in the original frame can easily be written in terms of the centre of mass positions and velocities as

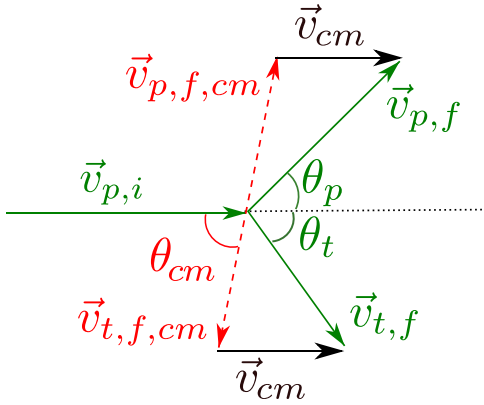

Figure 2.12: Relation between the laboratory and centre of mass scattering angles

$$\vec{r}_1 = \vec{r}_{cm} + \vec{r}_{1,cm} \tag{2.83}$$
$$\vec{v}_1 = \vec{v}_{cm} + \vec{v}_{1,cm} \tag{2.84}$$
$$\vec{r}_2 = \vec{r}_{cm} + \vec{r}_{2,cm} \tag{2.85}$$
$$\vec{v}_2 = \vec{v}_{cm} + \vec{v}_{2,cm} \tag{2.86}$$

These results imply that also scattering angles are different in different reference frames. The relations between the polar centre of mass scattering angle θ_{cm} and the polar laboratory scattering angles θ_p and θ_t for the projectile and the target can be derived from figure 2.12. The subscripts i and f respectively denote the initial and final velocities before and after the collision. Using (2.71) and the definition of the laboratory frame one can see that the constant centre of mass velocity $\vec{v}_{cm}$ is given in the laboratory frame by

$$\vec{v}_{cm} = \frac{m_r}{m_t}\vec{v}_{p,i} \tag{2.87}$$

The relative pre-collision velocity is in the laboratory frame of course

$$\vec{v}_i = \vec{v}_{p,i} \tag{2.88}$$

The relative post-collision velocity $\vec{v}_f$ is rotated with respect to $\vec{v}_i$ over the angle θ_{cm} and in case of an inelastic collision also rescaled according to

$$v_f = \sqrt{v_i^2 - \frac{2\Delta E_{inel}}{m_r}}$$

as will be shown in 2.3.4.3. From the equations (2.80) and (2.82) we have

$$\vec{v}_{p,f,cm} = \frac{m_r}{m_p}\vec{v}_f \tag{2.89}$$

$$\vec{v}_{t,f,cm} = -\frac{m_r}{m_t}\vec{v}_f \tag{2.90}$$

and from equations (2.84) and (2.86) together with the relations (2.87-2.90) we find

$$\vec{v}_{p,f} = \vec{v}_{cm} + \vec{v}_{p,f,cm} = \frac{m_r}{m_t}\vec{v}_{p,i} + \frac{m_r}{m_p}\vec{v}_f \tag{2.91}$$

$$\vec{v}_{t,f} = \vec{v}_{cm} + \vec{v}_{t,f,cm} = \frac{m_r}{m_t}\vec{v}_{p,i} - \frac{m_r}{m_t}\vec{v}_f \tag{2.92}$$

By dividing the vertical by the horizontal projections of these two equations the following relations between θ_p, θ_t and θ_{cm} are found

$$\tan\theta_p = \frac{\sin\theta_{cm}}{\cos\theta_{cm} + \frac{m_p v_i}{m_t v_f}} \tag{2.93}$$

$$\tan\theta_t = \frac{\sin\theta_{cm}}{\frac{v_i}{v_f} - \cos\theta_{cm}} \tag{2.94}$$

For the special case of an elastic collision (2.94) reduces to

$$\theta_t = \frac{\pi - \theta_{cm}}{2} \tag{2.95}$$

If additionally the masses of projectile and target are equal then (2.93) reduces to

$$\theta_p = \frac{\theta_{cm}}{2} = \frac{\pi}{2} - \theta_t \tag{2.96}$$

2.3.4.2 Equivalent one-body problem

A collision between two particles is an event in which two particles interact with each other by means of a mutual force. It is assumed here that this force is derivable from a central potential and that the external forces can be neglected with respect to this force during the collision. This assumption is widely valid. The motion of the two particles is then governed by Newton's equations

$$m_1\frac{d^2\vec{r}_1}{dt^2} = -\vec{\nabla}U_{21}(|\vec{r}_1 - \vec{r}_2|) \tag{2.97}$$

$$m_2\frac{d^2\vec{r}_2}{dt^2} = -\vec{\nabla}U_{12}(|\vec{r}_1 - \vec{r}_2|) \tag{2.98}$$

U_{ij} is the potential due to particle i felt by particle j. The exact implementation of this potential depends on the type of interaction. Newton's third law further dictates that

$$\vec{\nabla} U_{21}(|\vec{r}_1 - \vec{r}_2|) = -\vec{\nabla} U_{12}(|\vec{r}_1 - \vec{r}_2|) \tag{2.99}$$

The equations (2.97-2.98) can easily be written in terms of the centre of mass position $\vec{r}_{cm}$ and the relative position $\vec{r}$ by making the appropriate linear combinations

$$m_{tot} \frac{d^2 \vec{r_{cm}}}{dt^2} = 0 \tag{2.100}$$

$$m_r \frac{d^2 \vec{r}}{dt^2} = -\vec{\nabla} U(r) \tag{2.101}$$

This new set of equations decouples the motion in two independent parts. The first equation shows that the centre of mass moves with a constant velocity due to the absence of external forces. The second equation shows that the evolution of the relative position $\vec{r}$ is equivalent to the trajectory a fictitious particle with mass m_r under influence of the force $\vec{F} = -\vec{\nabla} U(r) = -\vec{\nabla} U_{21}(r)$. Only this equivalent one-body problem has to be solved. The particle positions and velocities can then easily be calculated from (2.75-2.78).

The equivalent one-body problem (2.101) is only a two-dimensional problem. This can be seen by vector multiplication by $\vec{r}$

$$\vec{r} \times m_r \frac{d^2 \vec{r}}{dt^2} = \frac{d}{dt} \left(m_r \vec{r} \times \vec{v} \right) = 0 \tag{2.102}$$

This shows that the motion of the fictitious particle is confined to a plane and that the angular momentum

$$\vec{L} = m_r \vec{r} \times \vec{v} \tag{2.103}$$

is a constant of motion. Scalar multiplication by $\vec{v}$

$$\vec{v} \cdot m_r \frac{d^2 \vec{r}}{dt^2} = \frac{d}{dt} \left(\frac{m_r}{2} \left(\frac{d\vec{r}}{dt} \right)^2 \right) = -\vec{v} \cdot \vec{\nabla} U(r) = \frac{d}{dt} \left(-U(r) \right) \tag{2.104}$$

shows that the energy

$$E = \frac{m_r}{2} \left(\frac{d\vec{r}}{dt} \right)^2 + U(r) \tag{2.105}$$

is a second constant of motion. Using the two constants of motion L and E expressed in polar coordinates (r, θ) in the plane of motion

$$L = m_r r^2 \frac{d\theta}{dt} \tag{2.106}$$

$$E = \frac{m_r}{2}\left[\left(\frac{dr}{dt}\right)^2 + r^2\left(\frac{d\theta}{dt}\right)^2\right] + U(r) \tag{2.107}$$

$$= \frac{m_r}{2}\left[\left(\frac{dr}{dt}\right)^2 + \frac{L^2}{m_r^2 r^2}\right] + U(r)$$

the trajectory of the fictitious particle can by calculate as

$$\theta = \int \frac{L dr}{r^2\sqrt{2m_r\left[E - U(r)\right] - L^2/r^2}} \tag{2.108}$$

The reference angle $\theta = 0$ for $t = 0$ has been chosen such that the integration constant disappears. When the interaction potential is known, this equation can be used to calculate the scattering angles and differential cross sections as shown in 2.3.4.4 and 2.3.4.5.

2.3.4.3 Energy and momentum conservation

It is now assumed that a collision has taken place and that the scattering angles in the centre of mass frame are known. The actual calculation of the scattering angles will be discussed in 2.3.4.4. Typically one wants to calculate the post-collision velocities $\vec{v}_{1,f}$ and $\vec{v}_{2,f}$ from the known pre-collision velocities $\vec{v}_{1,i}$ and $\vec{v}_{2,i}$. These velocities are defined long after and long before the collision such that the interaction force can be neglected. Hence, the relation between them can be derived simply from momentum and energy conservation without detailed knowledge of the interaction mechanism. One only has to know the inelastic energy loss due to the interaction.

To derive a relation between the pre-collision and post-collision velocities one can start by expressing the velocities in terms of the centre of mass velocity and the relative velocity using the equations (2.76) and (2.78)

$$\vec{v}_{1,i} = \vec{v}_{cm,i} + \frac{m_{r,i}}{m_{1,i}}\vec{v}_i \tag{2.109}$$

$$\vec{v}_{2,i} = \vec{v}_{cm,i} - \frac{m_{r,i}}{m_{2,i}}\vec{v}_i \tag{2.110}$$

$$\vec{v}_{1,f} = \vec{v}_{cm,f} + \frac{m_{r,f}}{m_{1,f}}\vec{v}_f \tag{2.111}$$

$$\vec{v}_{2,f} = \vec{v}_{cm,f} - \frac{m_{r,f}}{m_{2,f}}\vec{v}_f \tag{2.112}$$

A distinction is made between the masses before and after the collision in order to allow also reactions in which mass is transferred between the

colliding particles. Momentum conservation expressed in terms of the centre of mass velocity $\vec{v}_{cm}$ reduces to

$$m_{tot}\vec{v}_{cm,i} = m_{tot}\vec{v}_{cm,f} = m_{tot}\vec{v}_{cm} \tag{2.113}$$

This shows that $\vec{v}_{cm}$ remains unchanged by a collision as was already discussed in 2.3.4.2 and allows us to write the post-collision velocities in terms of the pre-collision velocities

$$\vec{v}_{1,f} = \vec{v}_{1,i} + \frac{m_{r,f}}{m_{1,f}}\vec{v}_f - \frac{m_{r,i}}{m_{1,i}}\vec{v}_i \tag{2.114}$$

$$\vec{v}_{2,f} = \vec{v}_{2,i} - \frac{m_{r,f}}{m_{2,f}}\vec{v}_f + \frac{m_{r,i}}{m_{2,i}}\vec{v}_i \tag{2.115}$$

From this it is clear that the post-collision velocities of the two particles can be calculated from the pre-collision velocities once the relative post-collision velocity $\vec{v}_f$ is known. To calculate $\vec{v}_f$ from the pre-collision velocities energy conservation is expressed in terms of the centre of mass velocity $\vec{v}_{cm}$ and the relative velocity $\vec{v}$

$$\frac{1}{2}m_{tot}v_{cm}^2 + \frac{1}{2}m_{r,i}v_i^2 = \frac{1}{2}m_{tot}v_{cm}^2 + \frac{1}{2}m_{r,f}v_f^2 + \Delta E_{inel} \tag{2.116}$$

ΔE_{inel} represents the possible inelastic energy loss. For an elastic collision $\Delta E_{inel} = 0$. For an excitation ΔE_{inel} is simply the excitation energy. For an ionization there is an additional contribution due to the kinetic energy transferred to the secondary electron. In case of an exothermic reaction ΔE_{inel} is taken to be negative. This shows that during an elastic collision the relative velocity $\vec{v}$ is only rotated. In case of an inelastic collision $\vec{v}$ is also rescaled according to

$$v_f = \sqrt{\frac{m_{r,i}}{m_{r,f}}v_i^2 - \frac{2\Delta E_{inel}}{m_{r,f}}} \tag{2.117}$$

This rescaling law shows that the pre-collision centre of mass energy $E_{i,cm} = \frac{1}{2}m_{r,i}v_i$ needs to be bigger than ΔE_{inel} for an inelastic collision to be allowed. So $\vec{v}_f$ can be calculated from $\vec{v}_i$ by first rescaling it to a parallel vector

$$\vec{v}_{i,r} = \frac{v_f}{v_i}\vec{v}_i \tag{2.118}$$

according to (2.117) and then rotating this rescaled vector. To perform the rotation the original xyz-system is first transformed to a coordinate system with the z-axis along $\vec{v}_i$ and $\vec{v}_{i,r}$. In figure 2.13 it is shown that this can

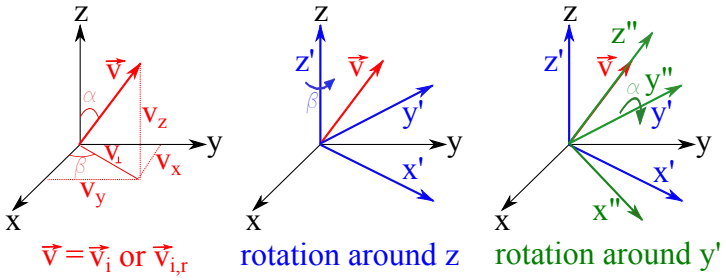

Figure 2.13: Rotation of the reference frame to align the z-axis with $\vec{v}_i$

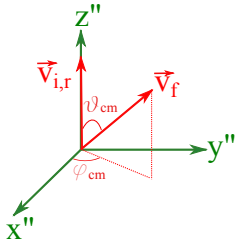

Figure 2.14: Rotation of the relative velocity during a collision

be done by first rotating the xyz-system over an angle β around the z-axis to get the $x'y'z'$-system. Then the $x'y'z'$-system is rotated over an angle α around the y'-axis to get the desired coordinate system $x"y"z"$. The angles α and β can be calculated from the components of $\vec{v}_i$ or $\vec{v}_{i,r}$ in the original xyz-system. The components of $\vec{v}_{i,r}$ are used because later in the calculation of the post-collision velocities some factors will then cancel out.

$$\cos\beta = \frac{v_{i,r,x}}{v_{i,r,\perp}} \tag{2.119}$$

$$\sin\beta = \frac{v_{i,r,y}}{v_{i,r,\perp}} \tag{2.120}$$

$$\cos\alpha = \frac{v_{i,r,z}}{v_{i,r}} \tag{2.121}$$

$$\sin\alpha = \frac{v_{i,r,\perp}}{v_{i,r,}} \tag{2.122}$$

with $v_{i,r,\perp}$ the component of the rescaled relative velocity in the xy plane. In this rotated $x"y"z"$ system the relative post-collision velocity is simply given by

$$\vec{v}_f" = \begin{pmatrix} v_{i,r}\sin\theta_{cm}\cos\phi_{cm} \\ v_{i,r}\sin\theta_{cm}\sin\phi_{cm} \\ v_{i,r}\cos\theta_{cm} \end{pmatrix} \tag{2.123}$$

θ_{cm} and ϕ_{cm} are respectively the polar and azimuthal angles over which the relative velocity vector rotates during the collision. This is shown in figure 2.14. These angles correspond with the scattering angles in the centre of mass frame because in this frame the particle velocities and the relative velocity have the same direction as was shown in 2.3.4.1. θ_{cm} and ϕ_{cm} are the only unknown parameters in this problem. In 2.3.4.4 it is shown that these angles can be calculated if the interaction potential is known. Once θ_{cm} and ϕ_{cm} are known, the post-collision velocities can be calculated. Applying the transformations deduced in appendix A, the relative post-collision velocity can be transformed back into the xyz frame.

$$\begin{aligned} \vec{v}_f &= \hat{R}_{\beta,z}\hat{R}_{\alpha,y}\vec{v}_f" \\ &= \begin{pmatrix} \cos\beta\cos\alpha & -\sin\beta & \cos\beta\sin\alpha \\ \sin\beta\cos\alpha & \cos\beta & \sin\beta\sin\alpha \\ -\sin\alpha & 0 & \cos\alpha \end{pmatrix} \vec{v}_f" \end{aligned} \tag{2.124}$$

Combining everything gives then eventually

$$\vec{v}_{1,f} = \vec{v}_{1,i} + \frac{m_{r,f}}{m_{1,f}}\Delta\vec{v} - \frac{m_{r,i}}{m_{1,i}}\vec{v}_i \tag{2.125}$$

$$\vec{v}_{2,f} = \vec{v}_{2,i} - \frac{m_{r,f}}{m_{2,f}}\Delta\vec{v} + \frac{m_{r,i}}{m_{2,i}}\vec{v}_i \tag{2.126}$$

where

$$\Delta\vec{v} = \begin{pmatrix} \frac{\sin\theta_{cm}}{v_{i,r,\perp}}\left(v_{i,r,x}v_{i,r,z}\cos\phi_{cm} - v_{i,r}v_{i,r,y}\sin\phi_{cm}\right) + v_{i,r,x}\cos\theta_{cm} \\ \frac{\sin\theta_{cm}}{v_{i,r,\perp}}\left(v_{i,r,y}v_{i,r,z}\cos\phi_{cm} + v_{i,r}v_{i,r,x}\sin\phi_{cm}\right) + v_{i,r,y}\cos\theta_{cm} \\ -v_{i,r,\perp}\sin\theta_{cm}\cos\phi_{cm} + v_{i,r,z}\cos\theta_{cm} \end{pmatrix}$$

With these equations one can now calculate the post-collision velocities $\vec{v}_{1,f}$ and $\vec{v}_{2,f}$ from the pre-collision velocities $\vec{v}_{1,i}$ and $\vec{v}_{2,i}$, the scattering angles θ_{cm} and ϕ_{cm} in the centre of mass frame and the inelastic energy loss ΔE_{inel}.

It is also interesting to have a look at the energy transferred during an elastic collision. This can be calculated easily in the laboratory frame. In this frame energy and momentum conservation can be expressed as

$$\frac{1}{2}m_p v_{p,i}^2 = \frac{1}{2}m_p v_{p,f}^2 + \frac{1}{2}m_t v_{t,f}^2 \tag{2.127}$$

$$m_p v_{p,i} = m_p v_{p,f}\cos\theta_p + m_t v_{t,f}\cos\theta_t \tag{2.128}$$

$$0 = m_p v_{p,f}\sin\theta_p - m_t v_{t,f}\sin\theta_t \tag{2.129}$$

Eliminating θ_p and $v_{p,f}$ from these equations it is found that the amount of energy transferred from the projectile to the target which was initially at rest is given by

$$E_{t,f} = \frac{4m_p m_t}{(m_p + m_t)^2} \cos^2 \theta_t E_{p,i} \tag{2.130}$$

Using (2.95) this can also be written as function of the centre of mass scattering angle θ_{cm}

$$E_{t,f} = \frac{2m_p m_t}{(m_p + m_t)^2} (1 - \cos \theta_{cm}) E_{p,i} \tag{2.131}$$

By taking the derivatives with respect to m_p and m_t and requiring both to be zero one finds that the energy transfer is maximal for $m_p = m_t$. By taking the limit for one of the two masses much bigger than the other mass one can see that for large mass differences the energy transfer is very inefficient.

2.3.4.4 Scattering angles

Calculating the scattering angles for a collision in general requires rigorous quantum mechanical treatment. For elastic Coulomb collisions and elastic hard sphere collisions it is, however, possible to calculate the scattering angles with classical mechanics.

Assume a central force elastic scattering collision. We recall the equivalent one-body problem derived in 2.3.4.2. It is depicted schematically in figure 2.15. The fictitious particle is initially infinitely far away from the scattering centre at the origin. The polar coordinates are then $r = \infty$ and $\theta = \theta_i$. The fictitious particle moves along a straight line with velocity $\vec{v}_i$. The perpendicular distance between this line and the scattering centre is called the impact parameter b. After a while the trajectory will of course start to deviate from this straight line due to the influence of the force exerted by the scattering centre. The fictitious particle will reach a point of minimal separation r_{min} from the scattering centre for polar angle θ_{min} and then travel again away from the scattering centre. After a while the fictitious particle can again be considered as infinitely far away from the scattering centre. It then has polar coordinates $r = \infty$ and $\theta = \theta_f$ and moves along a straight line with velocity $\vec{v}_f$. It can be seen that the point of minimal separation also lies on the symmetry line of the trajectory. The angle between $\vec{v}_i$ and $\vec{v}_f$, the relative velocities before and after the collision, is the polar scattering angle θ_{cm} in the centre of mass frame. The azimuthal scattering angle ϕ_{cm} is equal to the azimuthal angle before the collision because the trajectory is confined to a plane as was shown in 2.3.4.2. It is easy to see that the polar scattering angle θ_{cm} is given by

$$\theta_{cm} = \pi - |\theta_f - \theta_i| = \pi - 2|\theta_{min} - \theta_i| = \pi - 2|\theta_f - \theta_{min}| \tag{2.132}$$

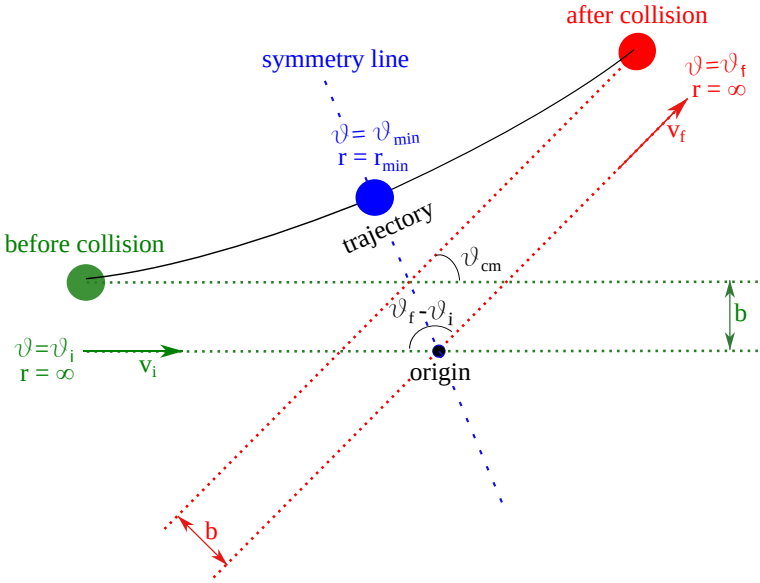

Figure 2.15: The equivalent one-body problem for a collision between two particles

Hence, θ_{cm} can easily be calculated if the angles θ_i, θ_{min} and θ_f are known. We will now calculate these angles for two important elastic scattering cases.

Coulomb scattering

The first case is Coulomb scattering. This is the scattering of two charged particles under influence of the electric Coulomb force. To determine θ_i, θ_{min} and θ_f we recall the classical trajectory equation derived in 2.3.4.2

$$\theta = \int \frac{Ldr}{r^2\sqrt{2m_r\left[E - U(r)\right] - L^2/r^2}} \tag{2.133}$$

The potential is in this case given by the Coulomb potential

$$U(r) = \alpha/r \tag{2.134}$$

with

$$\alpha = \frac{Z_1 Z_2 e^2}{4\pi\epsilon_0} \tag{2.135}$$

Using the integral identity (4) the trajectory equation can be solved to give

$$r = \frac{\frac{L^2}{m_r \alpha}}{\cos\theta\sqrt{\frac{2L^2E}{m_r\alpha^2}+1}-1} \tag{2.136}$$

This is the focal equation of a conic section. Because $\alpha > 0$ and $E > 0$ the equation represents a hyperbola. The angles θ_i and θ_f are the angles for which r becomes infinite

$$\theta_{i,f} = \pm \arccos\left(\frac{1}{\sqrt{1+\frac{2L^2E}{m_r\alpha^2}}}\right) \tag{2.137}$$

The angle θ_{min} is the angle for which r becomes minimal

$$\theta_{min} = 0 \tag{2.138}$$

The polar centre of mass scattering angle θ_{cm} can now be calculated as function of energy E and angular momentum L. It is, however, more useful to calculate the scattering angle as function of the impact parameter b and the magnitude of the relative velocity v. This can be done by expressing E and L as function of b and v

$$E = \frac{1}{2}m_r v^2 \tag{2.139}$$

$$L = m_r v b \tag{2.140}$$

with (2.132) it is then eventually found that

$$\theta_{cm} = \pi - 2\arccos\left(\frac{1}{\sqrt{1+\frac{m_r^2v^4b^2}{\alpha^2}}}\right) \tag{2.141}$$

or inverting it to find b as function of θ_{cm}

$$b = \frac{\alpha}{m_r v^2 \tan\frac{\theta_{cm}}{2}} \tag{2.142}$$

Hard sphere collision

Another important type of elastic collision is the hard sphere collision. This is the idealized case of two impenetrable spherical particles with radii R_1 and R_2. The polar centre of mass scattering angle θ_{cm} can in this case be calculated easily from geometrical arguments. Let us look back to figure 2.15. For a hard sphere collision the fictitious particle follows the green dashed line until the polar coordinates become equal to $r = r_{min} = R_1 + R_2$ and $\theta = \theta_{min}$. This is only possible if $b < R_1 + R_2$. Otherwise there can be no collision. The fictitious particle then bounces off and abruptly changes

its velocity direction, starts following the red dashed line. It is then easy to see that

$$\theta_{cm} = \pi - 2|\theta_{min} - \theta_i| = \pi - 2 \arcsin \frac{b}{R_1 + R_2} \tag{2.143}$$

or if we invert this relation

$$b = (R_1 + R_2) \cos \frac{\theta_{cm}}{2} \tag{2.144}$$

2.3.4.5 Cross section and differential cross section

Cross section

Let us now discuss the collision probability. The equations derived here will be used in the Monte Carlo collision scheme of the VMCPT plasma simulation code for VISIONI as discussed in 4.2.6. Assume a parallel mono-energetic beam with a flux Φ_p of projectiles with a velocity v_p propagating through a medium with a density n_t of targets at rest. The infinitesimal flux change $d\Phi_p$ due to projectiles removed from the beam by collisions with targets during travelling an infinitesimal distance dx is negative and proportional to the product $\Phi_p n_t dx$ of flux and target surface density. Let us call the proportionality constant σ_c. The infinitesimal flux change is then given by

$$d\Phi_p = -\Phi_p n_t \sigma_c dx \tag{2.145}$$

Consistency of dimensions requires σ_c to have area as dimensions. It can be regarded as the effective capturing area of a target and is, therefore, called the collision cross section. Cross sections can be defined for each type of reaction and are additive. One can for instance define an ionization cross section, an electronic excitation cross section, an elastic scattering cross section or a total cross section which is the sum of the cross sections for all possible reactions. These cross sections can be calculated from quantum mechanics and typically depend on the collision energy. Integrating (2.145) over the trajectory from 0 to x gives

$$\Phi_p(x) = \Phi_p(0) e^{-n_t \sigma_c x} \tag{2.146}$$

if it is assumed that σ_c and n_t remain constant over this trajectory. These assumptions are valid for the VMCPT code. The target density is uniformly distributed over space. Also the particle velocity and thus also σ_c remain constant during one time step as the electric field is neglected in VMCPT and the length of the time step is chosen such that the probability for more than one collision for one particle during one time step is negligible. From this equation the mean free path λ can be calculated. This is the

average distance a projectile travels through the medium before undergoing a collision.

$$\lambda = \frac{1}{\Phi_p(0)} \int_0^{+\infty} x d\Phi_p(x) = \frac{1}{n_t \sigma_c} \tag{2.147}$$

One can of course also express the flux attenuation as function of time

$$\Phi_p(t) = \Phi_p(0) e^{-n_t \sigma_c v_p t} \tag{2.148}$$

The mean collision time τ_c can be calculated similarly as the mean free path or even more simple as

$$\tau = \frac{\lambda}{v_p} = \frac{1}{n_t \sigma_c v_p} \tag{2.149}$$

The average collision frequency ν_c is given by the inverse of τ_c

$$\nu_c = \frac{1}{\tau_c} = n_t \sigma_c v_p \tag{2.150}$$

The reaction rate coefficient R is defined as

$$R = \sigma_c v_p \tag{2.151}$$

Reaction rate coefficients are often averaged over a Maxwellian energy distribution function. For a Maxwellian plasma the collision frequency can then easily be calculated by multiplying the density of the target particles with the Maxwellian reaction rate coefficient.

Differential cross section

Sometimes one is not only interested in whether a collision occurs or not, but also in which direction the projectile is scattered. In case of scattering by a central force it was shown in 2.3.4.2 that the trajectory is confined to a plane. Therefore, the azimuthal centre of mass scattering angle ϕ_{cm} is equal to the azimuthal impact angle ϕ_{impact}. In 2.3.4.4 the polar centre of mass scattering angle θ_{cm} turned out to be a function of the impact parameter b. The situation is sketched schematically in figure 2.16. Typically, however, the azimuthal impact angle and the impact parameter are not known. The projectile is assumed to be travelling through a medium with targets distributed uniformly with a density n_t. The impact parameters b and $\phi_{impact} = \phi_{cm}$ are then distributed according to the PDFs in appendix E.4 for a uniform distribution over a circle

$$P_{\phi_{cm}}(\phi_{cm}) d\phi_{cm} = \frac{1}{2\pi} d\phi_{cm} \tag{2.152}$$

$$P_b(b) db = \frac{2}{b_{max}^2} b db \tag{2.153}$$

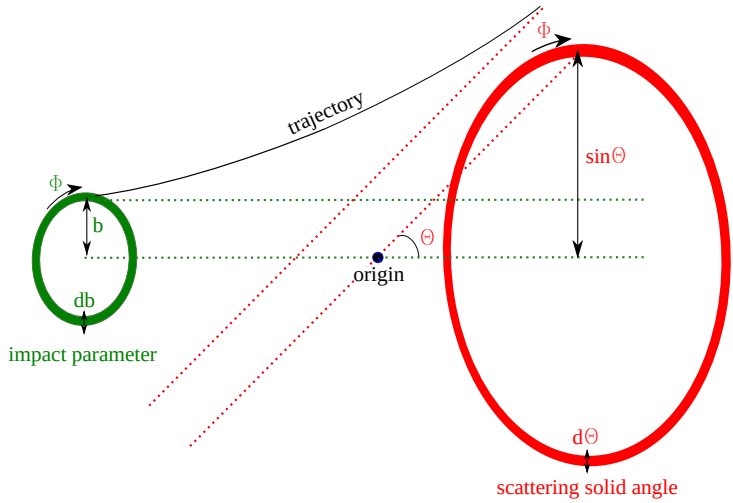

Figure 2.16: Relation between impact parameter b and centre of mass scattering angle θ_{cm}

b_{max} is the maximum impact parameter for which a collision can still occur. If b is a single valued function $b(\theta_{cm})$ of the polar centre of mass scattering angle θ_{cm}, then it is easy to find the probability distribution for θ_{cm} by stating that all projectiles entering through the annulus with impact parameter between $b(\theta_{cm})$ and $b(\theta_{cm}) + db$ should leave through the solid angle with polar scattering angle between θ_{cm} and $\theta_{cm} + d\theta_{cm}$ as shown in figure 2.16.

$$P_b(b)db = \frac{2}{b_{max}^2} b db = P_{\theta_{cm}}(\theta_{cm}) d\theta_{cm} \tag{2.154}$$

This leads to

$$P_{\theta_{cm}}(\theta_{cm}) d\theta_{cm} = \frac{2}{b_{max}^2} b \left| \frac{db}{d\theta_{cm}} \right| d\theta_{cm} \tag{2.155}$$

This allows us now to introduce the so called differential cross section $\sigma_c(\theta_{cm}, \phi_{cm})$ as

$$\frac{\sigma_c(\theta_{cm}, \phi_{cm})}{\pi b_{max}^2} \sin\theta_{cm} d\theta_{cm} d\phi_{cm} = P_{\theta_{cm}}(\theta_{cm}) P_{\phi_{cm}}(\phi_{cm}) d\theta_{cm} d\phi_{cm} \tag{2.156}$$

In case of a central force the differential cross section does not depend on ϕ_{cm} and, therefore, we write $\sigma_c(\theta_{cm})$. Together with (2.152) and (2.155) this gives

$$\sigma_c(\theta_{cm}) = \frac{b}{\sin\theta_{cm}} \left| \frac{db}{d\theta_{cm}} \right| \tag{2.157}$$

The total cross section σ_c can be calculated from the differential cross section as

$$\sigma_c = \int_0^{2\pi} \int_0^{\pi} \sigma_c(\theta_{cm}, \phi_{cm}) \sin\theta_{cm} d\theta_{cm} d\phi_{cm} \tag{2.158}$$

Using (2.142) it can then be calculated that for Coulomb scattering the differential cross section is given by

$$\sigma_c(\theta_{cm}) = \left(\frac{e^2 Z_1 Z_2}{8\pi\epsilon_0} \right)^2 \frac{1}{m^2 v^4 \sin^4(\theta_{cm}/2)} \tag{2.159}$$

Similarly with (2.144) the differential cross section for hard sphere scattering is

$$\sigma_c(\theta_{cm}) = \frac{(r_1 + r_2)^2}{4} \tag{2.160}$$

This last equation shows that hard sphere scattering is uniform in the centre of mass frame. There is namely no angular dependence in the differential cross section. This is, however, only the case in the centre of mass frame. In another frame one has other scattering angles as explained in 2.3.4.1 and, therefore, also another differential cross section. Integrating the differential cross section over all polar angles gives

$$\sigma_c = \pi(r_1 + r_2)^2 \tag{2.161}$$

which could be derived already beforehand due to the definition of hard sphere scattering. Only particles directly hitting each other can undergo a hard sphere collision.

2.3.4.6 Diffusive Coulomb scattering in a plasma

Coulomb scattering in a plasma is dominated by small angle scattering. The numerous collisions with high impact parameters and small scattering angles are much more important than the few collisions with small impact parameters and high scattering angles. This fact can be exploited to introduce a very efficient method for taking into account the average effect of Coulomb collisions between electrons in the VMCPT code as will be discussed in 4.2.6. During a time interval Δt small enough such that the total rotation angle $\theta(\Delta t)$ of the velocity is much smaller than $\frac{\pi}{2}$ but large enough such that a lot of Coulomb collisions happened the time evolution of the rotation angle $\theta(t)$ can be described as a random walk. Therefore, $\theta(\Delta t)$ is distributed according to a Gaussian with mean and variance given by

$$< \theta(\Delta t) > = 0 \tag{2.162}$$
$$< \theta(\Delta t)^2 > = N(\Delta t) < \theta_C^2 > \tag{2.163}$$

Here $N(\Delta t)$ is the number of collisions the charged particle undergoes during the time step Δt and $< \theta_C^2 >$ is the variance of the scattering angle due to one Coulomb collision. $N(\Delta t)$ can be calculated from the average collision time given in (2.149)

$$N(\Delta t) = \sigma_c n v \Delta t \tag{2.164}$$

Here σ_c is the Coulomb cross section, n the density of the considered charged targets and v the average relative velocity of projectile and target. In a plasma the Coulomb force does not penetrate infinitely far as it does in vacuum. As discussed in the introduction of this section the electric field due to a charged particle is attenuated due to the screening effect of the other charged particles in the plasma over the so called Debye length λ_D. This leads to a finite Coulomb cross section

$$\sigma_c = \pi \lambda_D^2 \tag{2.165}$$

Next we will calculate $< \theta_C^2 >$. This can be done by averaging θ over all impact parameters up to λ_D. From (2.142) we have

$$\tan \frac{\theta}{2} = \frac{b_0}{b} \tag{2.166}$$

with

$$b_0 = \left(\frac{q_e^2 Z_1 Z_2}{4\pi\epsilon_0 m_r v^2} \right) \tag{2.167}$$

the impact parameter for which the scattering angle is $\frac{\pi}{2}$. For the assumed small angle scattering the following approximation can be made

$$\theta \approx \sin\theta = \frac{2\tan\frac{\theta}{2}}{1 + \tan^2\frac{\theta}{2}} \tag{2.168}$$

The averaging then becomes

$$\begin{aligned} < \theta_C^2 > &= \frac{\int_0^{\lambda_d} \left(\frac{2\frac{b_0}{b}}{1+\left(\frac{b_0}{b}\right)^2} \right)^2 2\pi b db}{\pi \lambda_d^2} \\ &= \frac{4\pi b_0^2 \left[\ln\left(1 + \left(\frac{\lambda_D}{b_0}\right)^2\right) + \frac{1}{1+\left(\frac{\lambda_D}{b_0}\right)^2} - 1 \right]}{\pi \lambda_d^2} \end{aligned} \tag{2.169}$$

For a typical plasma $b_0 << \lambda_D$ and the term between squared brackets reduces to $2 \ln \frac{\lambda_D}{b_0}$. $\ln \Lambda = \ln \frac{\lambda_D}{b_0}$ is called the Coulomb logarithm and typically has a value of about 10 with little variation between different plasmas. Eventually the variance of the scattering angle after one time step Δt is then given by

$$< \theta(\Delta t)^2 >= \frac{n q_e^4 Z_1^2 Z_2^2 \ln \Lambda \Delta t}{2\pi \epsilon_0^2 m_r^2 v^3} \tag{2.170}$$

2.3.5 Drift and diffusion

Macroscopic particle transport in a plasma is governed by diffusion due to thermal motion and drift induced by electric fields. The transport is strongly influenced by collisions and magnetic fields. This subsection deals with diffusion and drift in weakly ionized plasmas both with and without magnetic field. At the end of this subsection transport in fully ionized plasmas is discussed very briefly because it is less important for this work.

First we will discuss transport in a weakly ionized plasma without magnetic field. Diffusion of particles is a stochastic process that can be treated as a random walk of the particles in which during each time step Δt the particle moves one step with size Δx in a random direction. As presented in [34] it can be calculated using probability theory for finite Δx and Δt or by deriving the diffusion equation for infinitesimal Δx and Δt that the root-mean-square distance $\sqrt{< x^2 >}$ travelled by the particle after a time t is given by

$$\sqrt{< x^2 >} = \sqrt{2Dt} \tag{2.171}$$

and that the particle flux due to diffusion is given by

$$\vec{\Phi}_{diff} = -D\vec{\nabla} n \tag{2.172}$$

with D the diffusion coefficient defined as

$$D = \frac{\Delta x^2}{2\Delta t} \tag{2.173}$$

and n the particle density. For weakly ionized plasmas the electrons and ions collide predominantly with the neutrals. Imagine that the collisions with the neutrals are characterized by a constant cross section σ_c, that the neutral density is given by n_n and that the particles have a Maxwellian velocity distribution with temperature T such that their velocity can be approximated by $v_p = \sqrt{2kT/m}$. The diffusion can then be seen as a random walk with as time step the collision time $\tau_c = 1/n_n \sigma_c v_p$ and as step size the collision mean free path $\lambda_c = 1/n_n \sigma_c$. According to (2.173) the diffusion coefficient can then be estimated as

$$D = \frac{\lambda_c^2}{2\tau_c} = \frac{\tau_c kT}{m} \tag{2.174}$$

This shows that the diffusion is driven by temperature and hampered by collisions and inertia. Ions are much more massive than electrons and in weakly ionized plasma usually also have much lower temperature. Therefore, ions typically have much lower diffusion coefficients than electrons in weakly ionized plasmas without magnetic field.

In addition to the random motion due to diffusion there is also a directed drift of charged particles under influence of the electric field. Without collisions the particles would continuously accelerate. With collisions the particles are on average accelerated only for a period equal to the collision time τ_c after which they are redirected. This leads to the following estimation for the particle flux due to drift

$$\vec{\Phi}_{drift} = \pm n\mu\vec{E} \tag{2.175}$$

with μ the mobility given by

$$\mu = \frac{q_e\tau_c}{m} \tag{2.176}$$

and the plus or minus sign for ions and electrons respectively. This shows that drift is driven by the electric field and just like diffusion hampered by collisions and inertia in absence of a magnetic field. Hence, electrons are also drifting much faster than ions.

The diffusion and drift are implicitly taken into account in the plasma fluid equations. As shown in [34] for a weakly ionized, isothermal plasma with low mean free path due to collisions with the neutral gas the momentum balance equation (2.19) leads directly to

$$\vec{\Phi} = \pm n\mu\vec{E} - D\vec{\nabla}n \tag{2.177}$$

with the same definitions for μ and D as above.

Up to now the diffusion and drift of electrons and ions was treated independently from each other. In reality electrons and ions diffuse collectively such that no charge builds up. Initially electrons are much more mobile. However, this leads very rapidly to an electric field that adjusts the electron and ion fluxes such that charge neutrality is assured. If equal numbers of electrons and ions are produced then the so called ambipolar electric field $\vec{E}_a$ can be calculated by equating (2.177) for electrons and ions while taking into account the neutrality condition $n_e = n_i = n$

$$\vec{E}_a = \frac{D_i - D_e}{\mu_i + \mu_e}\frac{\vec{\nabla}n}{n} \tag{2.178}$$

Inserting this expression into (2.177) gives the ambipolar flux

$$\vec{\Phi}_a = -D_a \vec{\nabla} n \tag{2.179}$$

with D_a the ambipolar diffusion coefficient defined as

$$D_a = \frac{\mu_i D_e + \mu_e D_i}{\mu_i + \mu_e} \tag{2.180}$$

For the common case $\mu_i << \mu_e$ and using the definitions of mobility and diffusion coefficient one finds that

$$D_a \approx D_i(1 + \frac{T_e}{T_i}) \tag{2.181}$$

So in weakly ionized plasmas for which $T_e >> T_i$ the electrons are slowed down by the ions, but their common diffusivity is increased with respect to the free ion diffusivity.

In the presence of a strong magnetic field it becomes more complicated. For the transport parallel to the magnetic field nothing changes. The diffusion and drift perpendicular to the magnetic field can be derived again from the momentum balance equation as shown in [34]. One finds that the mobility $\mu_\perp$ and diffusion coefficient $D_\perp$ perpendicular to the magnetic field are related to the mobility μ and diffusion coefficient D without magnetic field according to

$$\mu_\perp = \frac{\mu}{1 + (\omega_{cycl}\tau_c)^2} \tag{2.182}$$

$$D_\perp = \frac{D}{1 + (\omega_{cycl}\tau_c)^2} \tag{2.183}$$

with $\omega_{cycl} = qB/m$ the cyclotron frequency. For very high magnetic field $\omega_{cycl}\tau_c >> 1$ and the diffusion coefficient is given by

$$D_\perp = \frac{kT}{m\tau_c\omega_{cycl}^2} \tag{2.184}$$

This expression could also have been derived by considering a random walk with as step size the cyclotron radius instead of the collision mean free path and as time step again the collision time. This is easily understood by considering that a collision randomizes the phase of the cyclotron motion. It shows again that the diffusion is driven by temperature. In contrast to the case without magnetic field the diffusion is now enhanced by collisions and inertia. This can be explained by the fact that collisions allow particles to jump between different magnetic field lines and that more massive particles have larger cyclotron radii. For strong magnetic fields it can be that electrons are less mobile perpendicular to the magnetic field lines than ions. The ambipolar electric field then has to slow down the ions instead of the electrons.

For fully ionized plasmas the situation is completely different. Coulomb collisions between charged particles are now dominant. Collisions between like particles give no net diffusion. For each particle moving outward, there is another particle moving inward. Net diffusion occurs only due to collisions between electron and ions. The diffusion is automatically ambipolar. Classical theory gives also in this case a $D_\perp \propto 1/B^2$ dependence. As shown in [30] the perpendicular diffusion is given by

$$D_\perp = \frac{n\eta_\perp(kT_e + kT_i)}{B^2} \tag{2.185}$$

with $\eta_\perp$ the resistivity perpendicular to the magnetic field due to Coulomb collisions which is given for a hydrogen plasma by

$$\eta_\perp = 1.04 \cdot 10^{-4} \frac{Zln\Lambda}{T[eV]^{3/2}} \text{ ohm m} \tag{2.186}$$

However, experimentally it has been observed that in fully ionized, nearly collisionless plasmas the confinement usually has a much weaker dependence on the magnetic field. Also the absolute magnitude of $D_\perp$ appears to be higher than the classical prediction. This has lead to the definition of an upper limit, namely the Bohm diffusion coefficient

$$D_B = \frac{kT_e}{16q_eB} \tag{2.187}$$

The theoretical background of this anomalous diffusion is not yet fully understood.

2.3.6 Sheath formation at plasma boundaries

Laboratory plasmas are always produced in a finite plasma chamber. This leads unavoidably to contact between the plasma and the confining walls. At these contact zones very thin non-neutral sheath layers are formed. Qualitatively it is easy to understand how these sheaths originate. Electrons are much more mobile than ions due to the lower mass and typically also higher temperature. Hence, they escape more rapidly from the plasma chamber and leave the walls at a negative potential with respect to the plasma. Usually the plasma is slightly more positive than the most positively biased electrode. A very thin electropositive sheath of a few Debye lengths is then formed at the walls due to repulsion of electrons by the negative potential. This thin layer ensures neutrality of the bulk plasma and shields it from the strong electric field at the walls as explained in 2.3.1. Sheaths are very important because they strongly influence plasma-surface interaction. They are also crucial in understanding Langmuir probe measurements. In this subsection the basics of sheath physics are summarized. More detailed discussions can be found in [11], [35] and [36].

Calculating sheath potential profiles is in general very complicated and often requires numerical calculations or PIC-MCC simulations. Fortunately the basics can be grasped from an approximate calculation for a plasma with one type of singly ionized ions. The first assumption used in this calculation is that the sheath is collisionless and planar. This is often a realistic approximation because the thickness of a low voltage sheath is of the order of the Debye length, which is typically much smaller than the collision mean free path and the plasma chamber dimensions. Further, it is assumed that the ions are cold in comparison with the electrons. The last assumption is that the plasma at the sheath edge is neutral and free of electric fields. One can then start the calculation with the following four fundamental equations

$$n_i(x)v_i(x) = n_s v_{is} \tag{2.188}$$

$$\frac{1}{2}m_i v_i(x)^2 + q_e V(x) = \frac{1}{2}m_i v_{is}^2 \tag{2.189}$$

$$n_e(x) = n_s \exp\left(\frac{q_e V(x)}{kT_e}\right) \tag{2.190}$$

$$\frac{d^2V}{dx^2}(x) = \frac{q_e(n_e(x) - n_i(x))}{\epsilon_0} \tag{2.191}$$

representing respectively ion flux continuity, ion energy conservation, the Boltzmann density distribution for the electrons which are not disturbed too much by the presence of the sheath and the Poisson equation. The subscript s is used to represent quantities at the sheath edge at $x = 0$. The wall is located at $x = d_s$ with d_s the sheath thickness. The potential at the sheath edge was taken as the reference potential $V_s = 0$ and according to the assumed neutrality at the sheath edge one has $n_{es} = n_{is} = n_s$. Combining (2.188) and (2.189) one finds for the ion density

$$n_i(x) = \frac{n_s}{\sqrt{1 - \frac{q_e V(x)}{\frac{1}{2}m_i v_{i,s}^2}}} \tag{2.192}$$

Inserting electron and ion densities (2.190) and (2.192) in the Poisson equation (2.191) gives

$$\frac{d^2V}{dx^2}(x) = \frac{q_e n_s}{\epsilon_0}\left(\exp\frac{q_e V(x)}{kT_e} - \frac{1}{\sqrt{1 - \frac{q_e V(x)}{\frac{1}{2}m_i v_{is}^2}}}\right) \tag{2.193}$$

This equation determines the potential profile and the electron and ion density profiles.

The velocity v_{is} with which the ions enter the sheath cannot take any value. Equations (2.190) and (2.192) show that both electron and ion den-

sities decrease towards the wall due to the decreasing potential. To guarantee an electropositive sheath, the ion density at the sheath edge should decrease more slowly than the electron density. By comparing the derivatives of (2.190) and (2.192) at the sheath edge one can see that this leads to a lower limit

$$v_{is} \geq v_{Bohm} \tag{2.194}$$

with v_{Bohm} the ion acoustic wave velocity or Bohm velocity given by

$$v_{Bohm} = \sqrt{\frac{kT_e}{m_i}} \tag{2.195}$$

In case of finite ion temperature T_i it is shown in [11] that the Bohm velocity is given by

$$v_{Bohm} = \sqrt{\frac{k(T_e + T_i)}{m_i}} \tag{2.196}$$

A stable sheath can only be formed if the ion velocity at the sheath edge is above this critical value. This condition is called the Bohm criterion. In [16] and [11] it is shown that a non-physical singularity shows up for the neutral bulk plasma if the ion velocity increases above the Bohm velocity. This leads to the complementary criterion

$$v_{is} \leq v_{Bohm} \tag{2.197}$$

Hence, the ion velocity at the sheath edge has to be exactly equal to the Bohm velocity for a stable sheath

$$v_{is} = \sqrt{\frac{k(T_e + T_i)}{m_i}} \tag{2.198}$$

This high velocity cannot be provided by the thermal motion of the ions. A presheath electric field is needed to accelerate the ions up to the Bohm velocity. The presheath potential drop V_{ps} should be $kT_e/2q_e$ in the collisionless case. According to the Boltzmann relation (2.190) this leads to a corresponding drop of the plasma density with respect to the bulk density with a factor $\exp(-q_e V_{ps}/kT_e) \approx 0.6$. In case of collisions V_{ps} should be higher in order to reach the Bohm velocity in the presence of energy loss due to momentum transfer. Hence, the presheath potential drop and density drop increase with decreasing ion collision mean free path. The presheath is much thicker than the sheath. Typically the presheath thickness d_{ps} has the same order of magnitude as the ion collision mean free path or even as the plasma dimensions in case of a collisionless plasma. In [37] it is shown that the potential profile of the presheath often can be fitted successfully to

$$V(x) = V_s + V_{ps}\sqrt{\frac{|x - x_s|}{d_{ps}}} \tag{2.199}$$

Matching the sheath and the presheath regions requires the existence of a transition region. The electric field in this transition region often has a value of about kT_e/q_eL_D with L_D the Debye length [37].

Let us now go back to the sheath equation (2.193). This equation has to be integrated twice to get the potential profile and consequently also the electron and ion density profiles. The first integration can be performed analytically by multiplication with dV/dx. One then gets

$$\frac{1}{2}\left(\frac{dV}{dx}\right)^2 = \frac{n_s}{\epsilon_0}\left(kT_e \exp\frac{q_eV}{kT_e} + m_iv_{is}^2\sqrt{1 - \frac{q_eV}{\frac{1}{2}m_iv_{is}^2}} - kT_e - m_iv_{is}^2\right) \tag{2.200}$$

The integration constant was taken in accordance with the assumed disappearing electric field at the sheath edge. The second integration of the sheath equation can only be performed numerically. Two interesting limits will now be discussed. The first limit is that of an unbiased floating wall for which $q_e|V| << kT_e$. Neglecting higher order terms of q_eV/kT_e in (2.193) gives and exponentially decaying potential profile with as expected from the discussion in 2.3.1 the Debye length at the sheath edge as scaling length. This shows that the thickness of a low voltage sheath is of the order of the Debye length. The second limit is that of an electrode biased to a high negative voltage $q_e|V_b| >> kT_e$. If one uses $q_e|V| >> kT_e$ in (2.193) then also the second integration can be performed analytically resulting in

$$V(x) = -\left(\frac{9}{4}\frac{n_sq_e}{\epsilon_0}\sqrt{\frac{m_iv_{is}^2}{2q_e}}x^2\right)^{2/3} \tag{2.201}$$

In [11] it is shown that in a plasma the bias potential between two electrodes is almost completely taken up by the sheath at the negative electrode. At $x = d_s$ one should, therefore, recover the bias potential $V = -V_b$. Using this and the Bohm velocity for the ion velocity at the sheath edge one finds a relation between the sheath thickness d_s and the bias potential V_b

$$d_s = L_D\frac{\sqrt{2}}{3}\left(\frac{2q_eV_b}{kT_e}\right)^{3/4} \tag{2.202}$$

in terms of the Debye length in the bulk plasma L_D. So if the bias potential at an electrode is much higher than the electron temperature, then the sheath thickness at this electrode can be significantly larger than the Debye length. This can also be rewritten as the famous Child-Langmuir law that was derived first in the context of vacuum diodes to calculate the current density in the space-charge-limited regime

$$J = q_e n_s v_{is} = \frac{4}{9}\epsilon_0 \sqrt{\frac{2q_e}{m_i}} \frac{V_b^{3/2}}{d_s^2} \tag{2.203}$$

In case of a heated electron emitting electrode the sheath structure becomes more complicated. This situation is analysed in detail in [38]. It turns out, however, that the thickness of the sheath does not change much with respect to (2.202).

2.3.7 Langmuir probe theory

Langmuir probes have been used in plasma diagnostics since long time. Basically one simply has to insert a conducting object as a probe in the plasma and look at the collected current as function of the bias potential V_{pr}. It is not very difficult to fabricate such a Langmuir probe. Most crucial is that the probe is small enough not to disturb the plasma too much and that the probe can withstand the harsh environment. The analysis of the measured I-V characteristics is often, however, not straightforward. In this subsection the basics of Langmuir probe theory are introduced as a theoretical background for the Langmuir probe analysis software developed for VISIONI as will be discussed in 4.3. More detailed discussions can be found in [39], [40], [16] and [41].

The simplest and most instructive example of a Langmuir probe I-V characteristic is the ideal I-V curve of an isotropic Maxwellian plasma with one species of singly ionized ions and with probe dimensions much bigger than the sheath thickness. In this case the one dimensional planar approximation can be used and the electron velocity distribution function is given by a Maxwellian as discussed in 2.3.1. Inserting a probe in the plasma leads to the formation of a sheath and a presheath as explained in the previous subsection. The electron current collected by the probe depends on the probe biasing potential V_{pr} with respect to the plasma potential V_{pl}. If $V_{pr} > V_{pl}$ then the electrons are unhampered by the probe potential. They are collected by free diffusion towards the probe. If $V_{pr} < V_{pl}$ then the electrons experience the probe potential as a barrier. Only the electrons with normal velocity $v_z > v_{z,min} = \sqrt{\frac{2q_e(V_{pl}-V_{pr})}{m_e}}$ can be collected by the probe. Without loss of generality the normal velocity can be taken along the z-axis because of the assumed isotropy and the planar approximation. The collected electron current can then be calculated using the probe surface area A_{pr}, the plasma density at the sheath edge n_s and the Maxwellian velocity distribution (2.3) because it is not disturbed too much by the presence of the sheath.

$$I_e = q_e A_{pr} n_s \left(\frac{m_e}{2\pi k T_e}\right)^{3/2} \int_{-\infty}^{\infty} dv_x \int_{-\infty}^{\infty} dv_y \int_{v_{z,min}}^{\infty} dv_z v_z \exp\left(-\frac{m_e v^2}{2kT_e}\right) \tag{2.204}$$

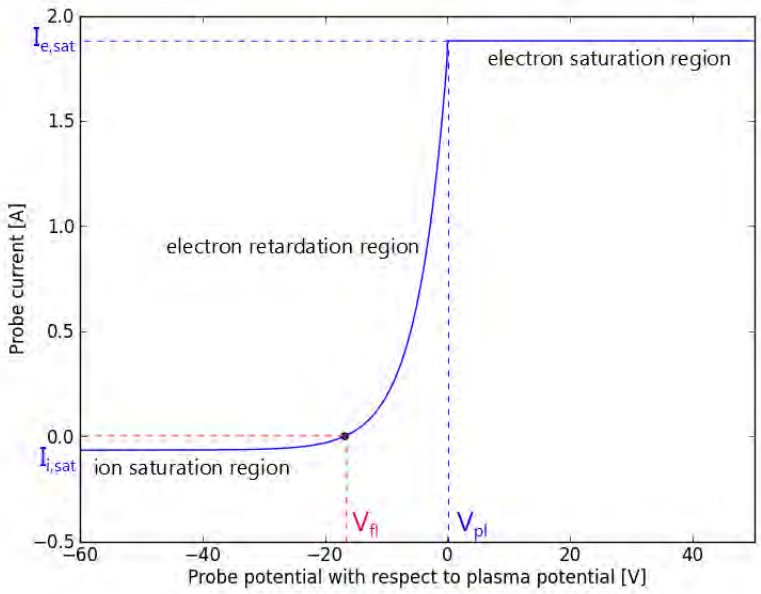

Figure 2.17: Ideal Langmuir probe I-V curve

Using the integral identities (5) and (6) one finds

$$I_e = \begin{cases} I_{e,sat} \exp\left(-\frac{q_e(V_{pl}-V_{pr})}{kT_e}\right) & \text{if } V_{pr} < V_{pl} \\ I_{e,sat} & \text{if } V_{pr} \geq V_{pl} \end{cases} \tag{2.205}$$

with $I_{e,sat}$ the electron saturation current given by

$$I_{e,sat} = \frac{1}{4} q_e A_{pr} n_s \sqrt{\frac{8kT_e}{\pi m_e}} \tag{2.206}$$

If the ion temperature is comparable to the electron temperature, one can perform a similar calculation for the collected ion current. Typically, however, one has $T_i << T_e$. The situation is then different. The ions can then not be considered as freely diffusing towards the probe. Their velocity is dominated by the directed flow due to acceleration in the presheath as explained in the previous subsection. Therefore, the ion saturation current $I_{i,sat}$ is now given by

$$I_{i,sat} = q_e A_{pr} n_s v_{Bohm} = q_e A_{pr} n_s \sqrt{\frac{k(T_e + T_i)}{m_i}} \tag{2.207}$$

This is the ion current collected by the probe if $V_{pr} < V_{pl}$. Due to the high ion to electron mass ratio the ion saturation current is much lower than the electron saturation current. For a H^+ plasma the ratio would be around 28. For $V_{pr} > V_{pl}$ the ions are repelled from the probe and the collected ion current decreases with increasing V_{pr}. In this region the electron current is highly dominant and the ion current can be neglected. Putting all this together the ideal I-V curve is characterized by three important regions. This is shown in figure 2.17 where the ideal I-V curve is plotted for a 1 cm radius disk probe in an isotropic Maxwellian H^+ plasma with $T_e = 5$ eV. Note that by convention the collected electron current is taken to be positive. For very negative probe potentials $q_e(V_{pl} - V_{pr})/kT_e >> 1$ all ions are collected and the electron contribution is negligible. This region is called the ion saturation region. For increasing probe potential the electron contribution increases exponentially. This region is called the electron retardation region. At the so called floating potential V_{fl} the electron current has paced up with the ion current and no net current is collected by the probe. By equating the expressions for the ion saturation current (2.207) and the electron current (2.205-2.206) the floating potential can be calculated to be given by

$$V_{fl} = V_{pl} - \frac{kT_e}{2q_e} \ln\left(\frac{1}{2\pi}\frac{m_i}{m_e}\left(1 + \frac{T_i}{T_e}\right)\right) \tag{2.208}$$

Hence, the floating potential is negative with respect to the plasma potential and the difference is proportional to the electron temperature and increases logarithmically with the ion to electron mass ratio. For a H^+ plasma one has approximately $V_{fl} = V_{pl} - 3kT_e$. Any object in contact with the plasma and not drawing any net current will eventually acquire the floating potential due to charging by impinging electrons. Eventually when the probe potential is increased up to the plasma potential, the electrons are then not repelled and the collected current saturates resulting in a sharp knee in the I-V curve. The region above the plasma potential is called the electron saturation region. Figure 2.17 is plotted with the plasma potential as reference potential. In reality the I-V curve will of course be measured with respect to one of the electrodes. Therefore, the curve will be shifted horizontally. The anode potential is typically a few kT_e/q_e negative with respect to the plasma potential, slightly above the floating potential in order to extract as much electrons as needed to sustain quasi-neutrality in the bulk plasma.

In case of the ideal I-V characteristic described above, it is easy to derive the plasma parameters. The plasma potential corresponds to the position of the knee, the electron temperature can be determined from the slope in the electron retardation regime and the plasma density can be determined

from the values of the ion or electron saturation current. Unfortunately, in reality the measured I-V curve can differ strongly from this ideal I-V curve. The most important non-ideal effects are discussed below.

- **Plasma fluctuations and electronic noise** lead to rounding of the knee. The plasma potential can then no longer be determined exactly. Emissive probes are better suited to determine the plasma potential.

- **Magnetic fields** influence the collection of electrons and ions if the probe dimensions are similar to or larger than the Larmor radius $R_{cycl} = mv_{\perp}/qB$. Hence, this effect is stronger for higher magnetic fields and particles with lower mass and lower energy. Direct collection of charged particles is only possible along the field lines intersecting the probe surface. Once these field lines are depleted, collection can only occur by cross field diffusion. This leads to lower saturation currents, a decreased slope in the electron retardation region and rounding of the knee. Hence, magnetic fields can complicate the calculation of the plasma potential, the plasma density and the electron temperature.

- **Collisions with neutrals** are important if the probe dimensions are similar to or larger than the collision mean free path λ. Hence, this effect is especially important at high neutral pressures. Collisions hamper the free diffusion towards the probe and lead to decreased saturation currents and to a rounding of the knee. Hence, collisions can complicate the calculation of the plasma potential and the plasma density.

- **Non-maxwellian EEDFs** are rather common for low density plasmas due to low collisionality. A lot of low density plasmas have for instance a bi-Maxwellian EEDF. Besides the cold bulk electron population with electron temperature T_{ec}, these plasmas have a fraction f_{eh} of the electrons belonging to a hot electron population with electron temperature T_{eh}. According to [42] the Bohm velocity should then be calculated using an effective electron temperature $T_{e,eff}$ given by

$$\frac{1}{T_{e,eff}} = \frac{1 - f_{eh}}{T_{e,c}} + \frac{f_{eh}}{T_{e,h}} \tag{2.209}$$

  Furthermore, the floating potential for these plasmas can be much more negative with respect to the plasma potential than indicated by (2.208). The floating potential can be calculated from the balance of electron and ion current with an additional term for the hot electron population. The parameters T_{ec}, T_{eh} and f_{eh} can be determined for instance by a multiparameter fit in the electron retardation region. Some plasmas are not even bi-Maxwellian. In principle one can then no longer speak about electron temperature. If the probe is convex

and the plasma isotropic, then one can derive the EEDF from the I-V characteristic with the Druyvenstein method [16]

$$f(E = q_e(V_{pl} - V_{pr})) = \frac{2}{A_{pr} q_e^2} \sqrt{\frac{2m_e(V_{pl} - V_{pr})}{q_e}} \frac{\partial^2 I_e}{\partial V_{pr}^2} (V_{pr}) \quad (2.210)$$

- **Secondary electron emission** from the probe surface by electron bombardment has to be subtracted from the collected electron current before calculating the plasma parameters. Using the secondary electron emission model from [43] and the data from [44], it can be shown that secondary electron emission from molybdenum or tungsten is important even below electron impact energies of 100 eV. Electron emission due to ion impact is negligible because even at ion impact energies of 1 keV the electron emission probability is typically less than 10% [44],[45]. Electron emission by photon bombardment can also be neglected because the radiation level of a typical laboratory plasma is too low. Thermionic electron emission requires probe temperatures as high as 2000 K to be significant. Field emission is also not significant at the low electric fields around Langmuir probes.

- **Sheath geometry and particle orbits** are influenced by the bias voltage and the shape of the probe. Therefore, the probe current in the electron and ion saturation regime is usually not constant. These effects are especially important for the high negative voltages in the ion saturation regime. The first theory developed to deal with this was the orbital motion limit (OML) theory of Mott-Smith and Langmuir [46]. This simple theory takes into account orbital motions of the charged particles based on energy and angular momentum conservation. However, it has a very restricted applicability. The sheath geometry is not taken into account. Therefore, the theory is only valid if the sheath is much larger than the probe dimensions. This is usually only true for very low density plasmas. The OML theory shows that in this case the square of the collected current is proportional to the bias potential. Later in the Allen-Boyd-Reynolds (ABR) theory [47] the sheath geometry was taken into account by solving the Poisson equation. But in this case the orbital motion of the charged particles was not taken into account. The first probe theory taking into account both sheath formation and orbital motion was derived by Bernstein and Rabinowitz [48] and further refined by Laframboise [49]. The calculations of this Bernstein-Rabinowitz-Laframboise (BRL) theory are very complicated. Fortunately the computed curves for the commonly used cylindrical probe geometry have been fitted to algebraic functions by Chen [50]. One first has to convert the probe voltage

Table 2.6: Parameters for computing the Bernstein-Rabinowitz-Laframboise curves [50]

	a	**b**	**c**	**d**	**f**
A	1.12	0.00034	6.87	0.145	110
B	0.50	0.008	1.50	0.180	0.80
C	1.07	0.95	1.01	-	-
D	0.05	1.54	0.30	1.135	0.370

V_{pr} and the collected ion current I_{ion} to the dimensionless quantities η and J according to

$$\eta = -\frac{q_e(V_{pr} - V_{pl})}{kT_e} \tag{2.211}$$

$$J = \frac{I_{ion}}{q_e A_{pr} n_e \sqrt{\frac{kT_e}{2\pi m_i}}} \tag{2.212}$$

The relation between the normalized voltage and ion current is then given by

$$\frac{1}{J^4} = \frac{1}{(A\eta^B)^4} + \frac{1}{(C\eta^D)^4} \tag{2.213}$$

The parameters A, B, C and D in this relation depend on the probe radius normalized to the Debye length $\xi = R_{pr}/L_D$ according to the relations

$$A = a + \frac{1}{\frac{1}{b\xi^c} - \frac{1}{d\ln(\xi/f)}} \tag{2.214}$$

$$B, D = a + b\xi^c \exp\left(-d\xi^f\right) \tag{2.215}$$

$$C = a + b\xi^{-c} \tag{2.216}$$

with the parameters a, b, c, d and f for these relations given in table 2.6. Fitting the relation 2.213 to the experimental data in the ion saturation region by varying n_e yields the plasma density. However, it is necessary to iterate the fitting because L_D and ξ depend also on n_e.

- **Plasmas with multiple ions** with different masses and charges give I-V characteristics that are very difficult to analyse.

- **The presence of the probe** unavoidably perturbs the bulk plasma. The probe surface is an additional particle sink influencing the particle balance, impurities can be introduced by sputtering of the probe surface and there can be a shadowing effect. These effects can be minimized by making the probe small enough. However, for very small probes the analysis becomes more complicated because one has to take into account the collection geometry.

2.4 Plasma-surface interaction

In a thermonuclear fusion device the plasma unavoidably interacts with the inner reactor materials. The magnetic field can never perfectly confine the plasma due to cross field diffusion and turbulences. Furthermore, it is necessary to have this interaction because of two reasons. Firstly, in the end the fusion energy has to be extracted from the vacuum vessel in order to produce electricity. Secondly, the helium ashes produced by the fusion reactions have to be exhausted to avoid fuel dilution.

The plasma-facing materials are continuously bombarded by ions, atoms, molecules, radicals and neutrons and are hereby also exposed to high heat loads. This can lead to safety issues and reduction of the lifetime of the materials due to a variety of detrimental effects such as crack formation, thermal fatigue, creep, melting, sublimation, evaporation, blistering, neutron induced defects, neutron activation, physical sputtering, chemical erosion, layer deposition, material mixing and tritium retention. An effective scientific programme for ITER can only be guaranteed if these effects are well understood and kept under control. The plasma-surface interaction will be even more important in future fusion power plants because safety and low cost are of primordial importance.

In this section only the plasma-surface interaction phenomena relevant for this work are treated. The first subsection deals with the emission of electrons from metals by heating and particle bombardment. The models presented here are important for the development of the VMCPT plasma simulation code for VISIONI discussed in 4.2, more in particular for the treatment of primary electron emission by the tungsten filaments and secondary electron emission by electron impact on the plasma chamber walls. The next subsections discuss the most important processes for material migration in thermonuclear fusion devices. These subsections are important for the update of the plasma-surface interaction database in ERO discussed in 4.1.2 and for the interpretation of the material migration experiments in TEXTOR and VISIONI presented respectively in chapters 5 and 7. The first two subsections discuss physical and chemical erosion processes under particle bombardment. In 2.4.4 it is shown how neutral fluxes released from surfaces and thus also erosion yields can be determined spectroscopically using so called inverse photon efficiencies. This concept is used for

the material migration studies in TEXTOR. In 2.4.5 it is explained how impinging energetic ions and neutrals can be reflected back into the plasma or implanted inside the material, while in 2.4.6 it is discussed how the implanted particles can be retained inside the material or recycled back into the plasma. In 2.4.7 it is shown that also thermal molecules and radicals can contribute to layer growth by sticking to the surface of the material. The last two subsections highlight the most important plasma-surface interaction issues for future thermonuclear fusion devices and discuss the most promising candidate plasma-facing materials.

2.4.1 Electron emission from metals

Metals are characterized by a sea of free electrons in the conduction band. These electrons cannot readily escape from the metal due to the presence of a potential energy barrier at the surface. Heating or particle bombardment of metal surfaces in contact with a plasma can, however, supply the free electrons with enough energy to overcome the surface barrier. These phenomena are important for simulating primary electron emission by the tungsten filaments and secondary electron emission by electron impact on the plasma chamber walls in VISIONI with the VMCPT code in 4.2. In principle electrons can also be extracted by applying very strong electric fields of more than $10^7 - 10^8$ V/cm to the metal. Quantum mechanical Fowler-Nordheim tunnelling through the potential energy barrier then becomes important [51], [52]. Such high fields are, however, not used in this work. Therefore, field emission will not be discussed here.

2.4.1.1 Electron velocity distribution function

To study electron emission from a metal over the surface potential energy barrier one first has to know the energy and velocity distributions of conduction electrons in a metal. Electrons are spin 1/2 fermions. The Pauli exclusion principle, therefore, dictates that only two electrons can occupy a momentum phase space element with volume h^3. The density of states in momentum phase space is then given by

$$D(\vec{p})d\vec{p} = \frac{2}{h^3}d\vec{p} \tag{2.217}$$

Furthermore, the occupation probability $P(E)$ of a fermion energy level E is governed by Fermi-Dirac statistics according to

$$P(E) = \frac{1}{1 + \exp\left(\frac{E-E_F}{kT}\right)} \tag{2.218}$$

At temperature $T = 0$ K all the electron energy levels below the Fermi energy E_F are occupied, while all the energy levels above E_F are empty. Hence, the Fermi energy of a metal is closely related to its conduction

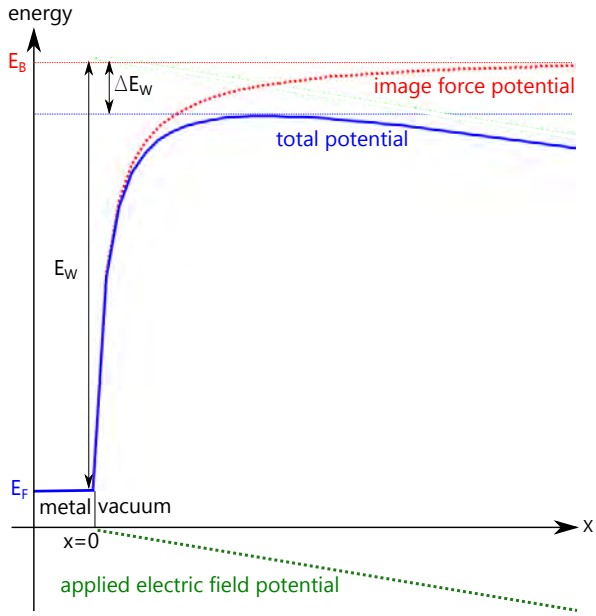

Figure 2.18: Shape of the surface potential energy barrier for electrons in metals

electron density. Combining (2.217) and (2.218), the density of electrons with Cartesian velocity components between v_x and v_x+dv_x, v_y and v_y+dv_y and v_z and v_z+dv_z is given by

$$n(v_x,v_y,v_z)dv_xdv_ydv_z = \frac{1}{1+\exp\left(\frac{m_e(v_x^2+v_y^2+v_z^2)/2-E_F}{kT}\right)}\frac{2m_e^3dv_xdv_ydv_z}{h^3} \quad (2.219)$$

2.4.1.2 Surface potential energy barrier

Let us now have a closer look at the surface potential energy barrier. Conduction electrons in metals trying to escape through the surface are pulled back by the positive charge of the fixed lattice ions. This leads to a potential energy barrier close to the surface. Figure 2.18 shows schematically that without an external electric field the barrier is infinitely thick and increases hyperbolically with the distance x from the surface up to the asymptotic value E_B according to the image force potential energy

$$U_{image}(x) = -\frac{q_e^2}{16\pi\epsilon_0 x} + E_B \quad (2.220)$$

The energy difference between the top of the barrier and the Fermi energy is called the work function E_W. It is the energy needed to remove one electron from the metal surface. For most metals the work function is about 4.5 eV [53]. The exact value depends not only on the material, but also on the temperature, the purity of the surface and for crystalline materials also on the crystal plane parallel with the surface. The work function of pure polycrystalline tungsten is about 4.55 eV [53]. Bringing two metals with different work functions E_{W1} and E_{W2} in contact with each other leads to a contact potential $V_{contact} = (E_{W1} - E_{W2})/q_e$ [54]. This has to be taken into account when two electrodes with different work functions are biased with respect to each other.

It can be seen in figure 2.18 that the height and the width of the potential energy barrier can be decreased by applying an external electric field E to extract the electrons from the metal. For a homogeneous electric field perpendicular to the surface the potential energy barrier can be described by

$$U_{barrier}(x) = -\frac{q_e^2}{16\pi\epsilon_0 x} - q_e E x + E_B \tag{2.221}$$

The maximum of the barrier is now not infinitely far away from the surface, but at a distance $x = \sqrt{q_e/16\pi\epsilon_0 E}$. The height of the barrier is decreased by the amount

$$\Delta E_W = \sqrt{\frac{q_e^3 E}{4\pi\epsilon_0}} \tag{2.222}$$

This barrier lowering is sometimes called the Schottky effect. For very strong electric fields the barrier becomes very thin and field emission due to quantum mechanical tunnelling according to the Fowler-Nordheim theory has to be taken into account [52].

2.4.1.3 Thermionic electron emission

From the previous paragraphs it is clear that if the metal is heated up to a non-zero temperature T some electrons will have a velocity component normal to the surface high enough to surmount the potential energy barrier with height E_B. An important quantity to characterize this thermionic electron emission is the emitted current density J. It can be calculated in a semi-classical way. Assume that the surface normal is along the z-axis. Only electrons with $v_z > \sqrt{2E_B/m_e}$ can overcome the surface barrier. The electron emission current density is then given by

$$J = \int_{-\infty}^{+\infty} \int_{-\infty}^{+\infty} \int_{\sqrt{2E_B/m_e}}^{+\infty} q_e v_z n(v_x, v_y, v_z) dv_x dv_y dv_z \tag{2.223}$$

Only electrons in the tail of the energy distribution function with $E >> E_F$ can escape. Therefore, the Fermi-Dirac factor from (2.218) can be approximated in the above integral by the Maxwell-Boltzmann factor

$$P(E) \approx \exp\left(\frac{E_F - E}{kT}\right) \tag{2.224}$$

Working out the integrals using integral identities (5) and (7) eventually gives the Richardson-Dushman equation

$$J = A_R T^2 \exp\left(-\frac{E_W}{kT}\right) \tag{2.225}$$

with the Richardson constant A_R given by

$$A_R = \frac{4\pi q_e m_e k^2}{h^3} = 1.20173 \cdot 10^6 A/m^2 K^2 \tag{2.226}$$

and the work function E_W as discussed above by

$$E_W = E_B - E_F \tag{2.227}$$

Hence, the thermionic current density increases exponentially with increasing temperature and decreasing work function. Experimentally the constant in front of the equation turns out to be only about half of the theoretical Richardson constant A_R. This is the case because the derivation above did not take into account quantum mechanical effects. Each electron with $v_z > \sqrt{2E_B/m_e}$ was assumed to contribute to the emitted current. Quantum mechanically, however, even these electrons have a finite probability of being reflected back into the material. The exact value of the constant depends on the material, the surface roughness, the crystal plane parallel with the surface and possible contaminants on the surface. Therefore, the Richardson constant A_R is typically replaced by $A = \lambda A_R$ with λ a correction factor around 0.5. For pure tungsten one has $\lambda = 0.517$ [55].

Thermionic electron emission is used in filament driven DC discharges. Most commonly one uses thin tungsten wires heated Ohmically up to temperatures of about 2500 K. Tungsten has the advantage that it can be heated up to very high temperatures due to its high melting temperature. Often tungsten is thoriated or coated with barium oxide in order to decrease the rather high work function. Other commonly used electron emitting materials are LaB_6 and BaSrO.

An important remark is that the current actually emitted by a heated filament is not always in agreement with the Richardson-Dushman equation. If the applied potential difference between the cathode and the anode is sufficiently high all emitted electrons can reach the anode. One is then operating in the so called emission limited or temperature limited regime. For too low potential differences the current collected at the anode is limited by the presence of negative space charge due to accumulation of electrons in

front of the cathode. For planar geometry the space charge limited current is given by the Child-Langmuir law derived in 2.3.6. Also in other geometries one has the typical $I \propto V^{3/2}$ dependence in the space charge limited regime. Space charge effects can also play a role in filament driven DC discharges. The injection of electrons by the hot filament into the surrounding sheath completely modifies the sheath structure with respect to the standard electropositive sheath discussed in 2.3.6. A double sheath is formed with an electronegative region close to the filament and an electropositive region close to the plasma. Space charge effects mitigate the electric field in the sheath. The current emitted by the filament cannot be increased indefinitely. There exists a maximum current for which the electric field at the cathode becomes zero [38]. A clear transition from a space charge limited to a temperature limited mode for increasing discharge potential can be observed in filament driven DC discharges [56]. The transition is characterized by a sudden increase of the discharge current and a drastic change of the plasma potential profile. In the space charge limited mode the plasma potential stays close to the cathode potential over most of the discharge volume and jumps to the anode potential only just in front of the anode. The electrons get only enough energy for ionization and excitation of the neutrals in the neighbourhood of the anode. This mode is, therefore, also called the anode glow mode. In the temperature limited mode the plasma potential stays close to the anode potential over most of the discharge volume and drops to the cathode potential only just in front of the cathode. Sometimes hysteresis is observed in the IV characteristic of a filament driven DC discharge [8].

2.4.1.4 Secondary electron emission by electron impact

Bombardment of the metal surface with energetic primary electrons from the plasma can also lead to electron emission. Kinetic energy from the projectile electrons is transferred to the conduction electrons in the metal. Some of these excited conduction electrons will subsequently move towards the surface. On their way they lose part of their energy mainly by electron-electron scattering. If they still have enough energy to overcome the surface potential energy barrier they can eventually be emitted from the surface. Energy loss during the transport to the surface limits the depth from which the secondary electrons can be ejected to a few nanometres.

An important quantity to characterize the secondary electron emission is the secondary electron emission yield δ, the average number of electrons returning from the surface after impact of one primary electron. It comprises both true secondary electrons and elastically reflected primary electrons. One can also define the more fundamental corrected secondary electron emission yield δ_c by correcting for the fraction f_r of the returning electrons that are actually reflected electrons. It is related to the uncorrected secondary electron emission yield by

Table 2.7: Secondary electron emission parameters δ_{cm} and E_m for relevant metals [45]

	δ_{cm}	E_m [**eV**]
W	1.4	650
Mo	1.25	375
stainless steel	1.22	400

$$\delta_c = \frac{\delta - \delta f_r}{1 - \delta f_r} \tag{2.228}$$

or the inverse relation

$$\delta = \frac{\delta_c}{1 - f_r + \delta_c f_r} \tag{2.229}$$

The corrected secondary electron emission yield gives the number of true secondary electrons emitted from the surface after impact of one primary electron penetrating the material without being reflected. It depends strongly on the impact energy E. At very low primary energies δ_c increases rapidly with increasing impact energy because more energy is available for excitation of secondary electrons. With increasing impact energy the primary electrons penetrate deeper into the material. After a while δ_c reaches a maximum $\delta_{cm} \approx 1-2$ for an impact energy E_m of a few 100 eV and eventually starts to decrease again slowly because the primary electrons penetrate too deep such that not all excited secondary electrons can make it to the surface with enough energy to overcome the barrier. In [43] it is shown that this energy dependence can be described quite accurately by

$$\delta_c(E) = \delta_{cm} \exp\left(-\frac{\left[\ln \frac{E}{E_m}\right]^2}{5.12} \right) \tag{2.230}$$

with δ_{cm} and E_m material dependent parameters. Table 2.7 lists these parameters for several relevant metals according to [45]. For increasing impact angles with respect to the surface normal the maximum of the curve increases slightly and shifts towards higher energies.

The reflected fraction f_r of the electrons returning from the surface also depends on the energy of the primary electrons. It decreases strongly for increasing impact energy and according to [43] it can be described by the universal function of the impact energy E in eV

$$f_r = \exp\left[1.59 + 3.75 \ln E - 1.37(\ln E)^2 + 0.12(\ln E)^3\right] \ \% \tag{2.231}$$

In [43] it is demonstrated that the true secondary electrons typically have energies about 5 eV. The experimentally observed secondary energy distributions could be successfully fitted by the function

$$f(E) \propto \exp\left(-\frac{\left[\ln\frac{E}{E_0}\right]^2}{2\tau^2}\right) \tag{2.232}$$

with the maximum E_0 and the width τ material dependent fitting parameters. For primary electrons impinging with 100 eV on stainless steel it turned out that $E_0 = 2.7$ and $\tau = 1.05$. In [57] it is shown that the angular distribution of the true secondary electrons can be approximated by a cosine distribution.

The above equations are very convenient for use in analytical and numerical models. Imagine that an electron impinges on the surface of the material with a certain energy. Using equation (2.230) with the appropriate values for E_m and δ_{cm} gives the corrected secondary electron emission yield δ_c. From equation (2.231) one can calculate the reflected fraction f_r. The uncorrected secondary electron emission yield δ can then be calculated according to equation (2.229). The average number of true secondary electrons is eventually given by $\delta(1 - f_r)$, while the reflection probability of the primary electron is given by δf_r.

2.4.1.5 Secondary electron emission by ion, neutral and photon impact

Impact by ions or neutrals can also lead to secondary electron emission. There are two possible mechanisms. The first mechanism is kinetic emission. This is the same as the one responsible for secondary electron emission by electron bombardment. For ions and excited neutrals potential emission is a second possible mechanism leading to electron emission. If one of the conduction electrons in the metal tunnels into a vacancy of the projectile, a second conduction electron can be ejected by the Auger process and if it has sufficient energy it may emerge from the metal surface. In contrast to kinetic emission there is no energy threshold for this process. Secondary electron emission by ion or neutral impact is, however, not important in this work. In [44] and [45] it is shown that the secondary electron emission yield for ions and or neutrals for the typical impact energies in this work below 100 eV are only a few percent at maximum. Also secondary electron emission due to photon impact, the photoelectric effect, can be neglected in this work because the flux of high energy photons from the plasma is very low.

2.4.2 Physical sputtering

Energetic ions, atoms, molecules or particle clusters impinging with fusion relevant energies on a material lose their energy primarily by nuclear collisions. If the projectile impact energy is high enough a collision cascade is initiated and defect creation inside the material and physical sputtering of atoms, ions and particle clusters may be observed. In principal also electrons and photons can lead to defect creation and physical sputtering by means of electron-phonon interactions. However, in practice this is rarely observed because electron-phonon interactions are very inefficient in transferring momentum to the atoms inside the material. Electron impact leads to physical sputtering only if the impact energy is above a few 100 keV, except for some specific insulators or very pure semi-conductors which can undergo sputtering by electrons already at lower energies between 5 and 100 eV. For photons sputtering only occurs for very high photon energies and very high intensities. Sputtering and defect creation due to electron and photon impact are not relevant for thermonuclear fusion and are, therefore, not discussed here. This subsection focuses on physical sputtering during impact of energetic ions or atoms with fusion relevant energies and is based mostly on [58], [59] and [60].

2.4.2.1 Collision dynamics

For a projectile impinging on a target material one can distinguish different interaction regimes based on the projectile impact energy. For very low impact energies below 10 eV the binding energy of the target particles and between the target particles and the projectile are comparable with the impact energy. Physical effects are then negligible and dominated by chemical effects. For some projectile-target combinations even at these low energies target particles can be eroded. This is called chemical erosion or chemical sputtering and is discussed in detail in 2.4.3. In the single knock-on regime for impact energies between 10 eV and 100 eV physical effects become more important. The kinetic energy of the projectile is usually lost already by one collision with a target atom. In the linear cascade regime for impact energies between 100 eV and 1 keV recoiling target atoms get enough energy from the projectile to created a cascade of nuclear collisions. The density of recoiling atoms is still very low such that collisions between moving target atoms are rare. In the spike regime with energies between 1 keV and 1 MeV the recoiling atom density is much higher and collisions between moving atoms become more important. For even higher impact energies above 1 MeV the projectile loses its kinetic energy primarily by means of electronic collisions instead of nuclear collisions and electron-phonon interaction becomes an important energy transfer mechanism inside the target material. However, in a thermonuclear fusion reactor the impact energy is usually not much higher than 1 keV and thus this regime is not relevant

here.

The theoretical foundations of nuclear collision effects upon particle bombardment were established by Sigmund [61]. He derived a complicated integrodifferential equation based on the general Boltzmann transport equation which he solved analytically for some simplified cases. This analytical approach is very instructive but has limited applicability due to the simplifications introduced in the model. Nowadays people usually resort to numerical simulations. In this field one can distinguish two different types of simulations. The first type of simulations is based on the binary collision approximation (BCA). In this case it is assumed that the nuclear collisions involve only two particles per collision. The trajectories of the particles are approximated by the asymptotic trajectories in between two nuclear collisions. The simultaneous interaction with the electrons in the material is treated as an independent energy loss mechanism not influencing the direction of propagation. The scattering angles and momentum transfer for the nuclear collisions are calculated using the classical collision theory that was discussed in 2.3.4. An important input in BCA codes is the interaction potential between projectile and target particles and between target particles. One can use an empirical potential or a more sophisticated quantum mechanically calculated potential. Usually one uses some kind of screened Coulomb potential. For amorphous target materials the impact parameters for the nuclear collisions are generated randomly using a Monte Carlo algorithm. TRIM [62] is a well known example of such a code. TRIM.SP [63] is the extended version of TRIM including physical sputtering. Tridyn [64] is the dynamical version of TRIM taking into account the effect of implanted projectiles. SDTrimSP [65] is the most recent extension of TRIM including both physical sputtering and projectile implantation. For crystalline materials the impact parameters for the nuclear collisions are calculated in a deterministic way using the predefined crystal lattice. MARLOWE [66] is a well known BCA code for crystalline materials. The BCA approximation is not always realistic. At impact energies below 100 eV, in the spike regime, for cluster and molecule impact and to simulate the release of clusters and molecules one should take into account the simultaneous interaction between multiple particles. In that case one has to resort to more realistic molecular dynamics (MD) simulations. Unfortunately MD simulations usually require four to five orders of magnitude longer CPU times in comparison with BCA simulations. Also the simulation volume is limited to approximately one million target particles. This limits the applicability. In an MD code the particles are tracked classically by integrating the equation of motion including a special potential taking into account the interaction with all other particles. These potentials are crucial in MD simulations and very difficult to construct because the impact of the projectile leads to a non-equilibrium situation. In principle one should calculate the potential quantum mechanically each time step using for instance density functional theory. This is, however, too time consuming. Therefore, approximations

have to be made also in MD codes.

2.4.2.2 Physical sputtering

Nuclear collisions induced by impact of an energetic projectile can cause a target atom to move towards the surface of the material. If the kinetic energy of this target atom along the surface normal is higher than the target surface binding energy E_{bt} then the target atom can be physically sputtered and leave the material. Usually E_{bt} is approximated by the sublimation energy. Physical sputtering occurs for all combinations of projectiles and targets. It requires momentum transfer from the projectile to the target atoms and reversal of the momentum back to the surface. Momentum transfer and thus also physical sputtering is most efficient for projectile and target atoms with similar masses because the maximum energy transfer fraction f for a head on collision given according to equation (2.130) by

$$f = \frac{4m_p m_t}{(m_p + m_t)^2} \tag{2.233}$$

is highest for $m_p = m_t$ and lowest for projectiles and targets with very different masses. The sputtered particles are mainly coming from the topmost surface layer with small contributions from the second and third atomic layer. The time between the impact of the projectile and the release of the sputtered particle is typically less than a picosecond. Most physically sputtered species are released as neutrals. Usually less than 5% is released as ions. Experiments and simulations have shown that the angular distribution of sputtered species for amorphous or polycrystalline samples can often well be approximated by a cosine distribution with respect to the surface normal. For crystalline samples the sputtered species are preferentially emitted in the direction of the close-packed crystal planes. It has also been found that the energy distribution of the sputtered particles peaks at $E = E_{bt}/2$ and decreases for very high energies according to $1/E^2$. The sputtered particle energy distribution is usually approximated by the Thompson distribution

$$n(E)dE \propto \frac{E}{(E + E_{bt})^3} dE \tag{2.234}$$

The maximum energy E_{max} with which a sputtered particle can be released due to a projectile impinging with an energy E_p is given by

$$E_{max} = f(1 - f)E_p - E_{bt} \tag{2.235}$$

with f the maximum energy transfer fraction given by (2.233). This corresponds to the situation where the projectile momentum is first reverted by a head on collision and then knocks a target atom from the surface by a head on collision. Therefore, the Thompsonian energy distribution is cut off at $E = E_{max}$.

2.4.2.3 Physical sputtering yield

Physical sputtering is usually quantified using the physical sputtering yield Y_{phys}. This is the average number of physically sputtered target atoms per impinging projectile. It depends on a lot of parameters such as projectile mass, impact energy, impact angle, target mass, target crystallinity, crystal orientation, surface binding energy, surface roughness and the possible presence of multiple materials or impurities in the interaction layer. Furthermore, during continuous bombardment the yield can also change in time due to change in surface topology and impurity content. This makes measuring of Y_{phys} very challenging. One has to be able to control very well all relevant parameters. Physical sputtering yields are usually measured using dedicated ion beam experiments. Numerous techniques can be used to determine the amount of sputtered particles such as SIMS, optical emission spectroscopy, profilometry, interferometry and mass change measurement. Another possibility is calculating the yield using BCA or MD codes.

Let us now focus on the case where a specific ion impinges on a specific pure amorphous target with a clean polished surface. In this case Y_{phys} only depends on the impact energy E_p and the impact angle θ_p of the projectile with respect to the surface normal. There exists a threshold energy, typically between 5 and 400 eV below which no sputtering occurs. This threshold energy depends primarily on the projectile mass, the target mass and the binding energy of the target atoms. At the threshold Y_{phys} increases at first dramatically for increasing E_p, but eventually reaches a broad maximum in the energy range between 0.2 and 150 keV. Beyond this maximum Y_{phys} starts to decrease again. This can be explained by the fact that for very high energies more and more of the projectile energy is deposited in deeper layers from which the recoiling target atoms can no longer reach the surface. Going from normal incidence towards grazing incidence Y_{phys} first increases up to an angle in the range 50-80^o because more energy is deposited in the surface layer. For very large θ_p the yield starts to decrease again because reflection of the projectile is strongly enhanced which results in a decrease of the energy deposited in the surface layer.

For long time people have been using the Bohdansky [67] and Yamamura [68] formulas to describe the dependence of Y_{phys} on E_p and θ_p. The Bohdanksy formula describes the dependence on E_p using a fitting formula based on Sigmund's analytical theory with some modifications in order to include the inelastic electronic energy loss and to extend the use of the formula to near threshold energies and low projectile mass. The Yamamura formula describes the dependence on θ_p using an empirical fitting formula. However, in [69] it is shown that the Bohdansky and Yamamura formulas have their limitations. Therefore, new formulas have been proposed in [70], [58] to describe the dependence on E_p and θ_p. In the new approach the E_p dependence is described using a nuclear stopping cross section based on an analytical fit to the more realistic krypton-carbon potential instead of

the Thomas-Fermi potential used in the Bohdansky formula. Furthermore, the factor to describe the threshold behaviour has been replaced by a new factor with two additional free parameters to get a better description of the threshold without influencing the high energy behaviour. Also the Yamamura formula has been adapted in order to get a better behaviour for low projectile to target mass ratio and near threshold sputtering. The formulas presented here are a little bit different from the formulas in [58] because they take into account the published errata. The energy behaviour for normal incidence is now given by

$$Y(E_p, \theta_p = 0) = q s_n^{KrC}(\epsilon_L) \frac{\left(\frac{E_0}{E_{th}} - 1\right)^{\mu}}{\frac{\lambda}{w(\epsilon_L)} + \left(\frac{E_0}{E_{th}} - 1\right)^{\mu}} \tag{2.236}$$

Here ϵ_L is the reduced energy defined as

$$\epsilon_L = E_p \frac{m_t}{m_p + m_t} \frac{4\pi\epsilon_0 a_L}{q_e^2 Z_p Z_t} \tag{2.237}$$

where a_L is the Lindhard screening

$$a_L = \left(\frac{9\pi^2}{128}\right)^{1/3} r_B \left(Z_p^{2/3} + Z_t^{2/3}\right)^{-1/2} \tag{2.238}$$

The function

$$w(\epsilon_L) = \epsilon_L + 0.1728\sqrt{\epsilon_L} + 0.008\epsilon_L^{0.1504} \tag{2.239}$$

was introduced to simplify the notation. $s_n^{KrC}(\epsilon_L)$ is the nuclear stopping given by

$$s_n^{KrC}(\epsilon_L) = \frac{0.5 \ln(1 + 1.2288\epsilon_L)}{w(\epsilon_L)} \tag{2.240}$$

Finally q, E_{th}, λ and μ are the fitting parameters. q fixes the magnitude of the yield, E_{th} defines the minimal energy for which sputtering occurs, λ triggers the onset of the decrease of Y at low energies towards the threshold and μ determines the strength of this decrease. The yield for θ_p different from zero can be calculated from the yield for normal incidence by multiplying with the appropriate correction factor according to

$$\frac{Y(E_p, \theta_p)}{Y(E_p, \theta_p = 0)} = \left\{\cos\left[\left(\frac{\theta_p}{\theta_0}\frac{\pi}{2}\right)^c\right]\right\}^{-f} \exp\left\{b\left(1 - \frac{1}{\cos\left[\left(\frac{\theta_p}{\theta_0}\frac{\pi}{2}\right)^c\right]}\right)\right\} \tag{2.241}$$

Here θ_0 is a normalization angle defined by

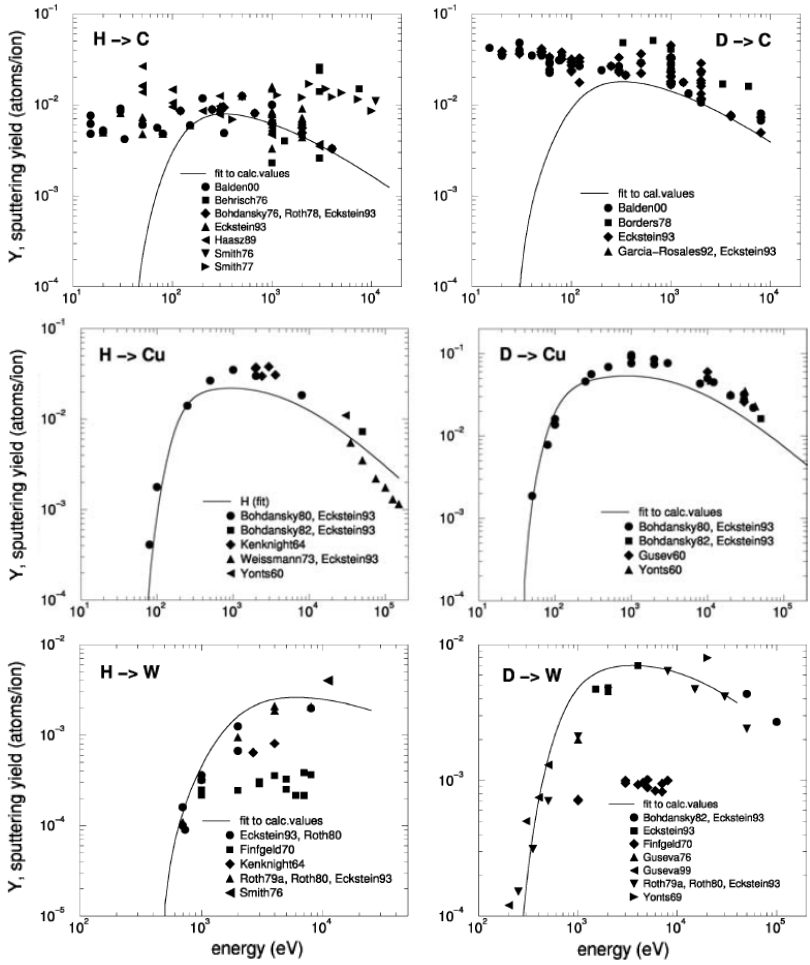

Figure 2.19: Impact energy dependence of the sputtering yield at normal incidence for several projectile-target combinations [58]

$$\theta_0 = \pi - \arccos\sqrt{\frac{1}{1 + E/E_{bp}}} \tag{2.242}$$

with E_{bp} the binding energy of the projectile to the surface of the target material. This normalization takes into account the fact that some projectiles may experience acceleration and refraction towards the surface normal due to attraction by the surface. b, c and f are the fitting parameters. A very nice data set has been compiled in [58]. The fitting parameters for

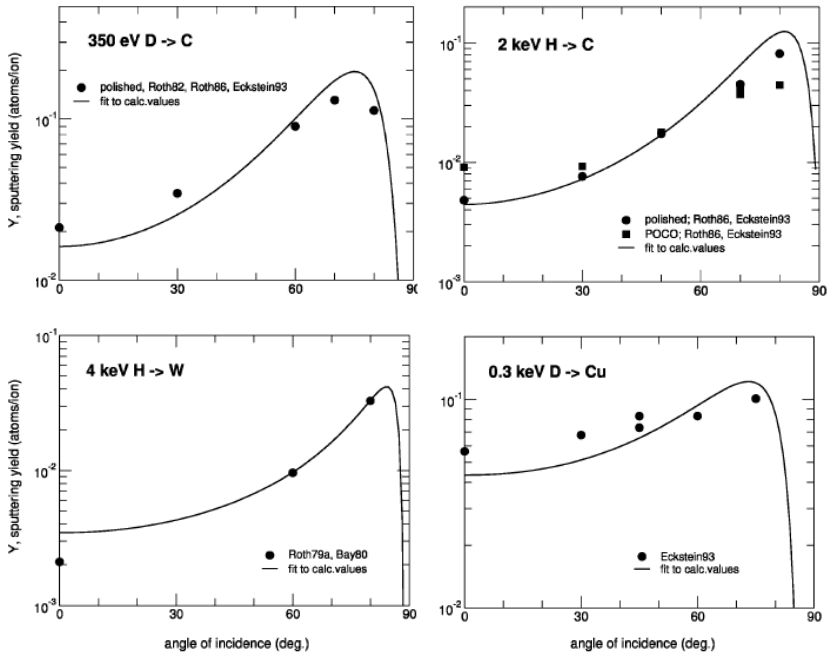

Figure 2.20: Impact angle dependence of the sputtering yield at a specific impact energy for several projectile-target combinations [58]

the energy and angular dependence for different projectile-target combinations have been determined using Bayesian probability theory on sputtering yields calculated with TRIM.SP and ACAT. The resulting curves are compared with experimental data found in literature. In general the agreement is very good. Figure 2.19 shows the dependence of Y_{phys} on E_p for some relevant projectile-target combinations. The full lines are the fits to the simulation results. The symbols are different experimental data sets. These examples exhibit the typical shape of the energy dependence of the sputtering yield with a clear threshold, a broad maximum and a slow decrease. The plots also illustrate that sputtering is easier for projectiles and targets with similar masses. Furthermore, the plots for hydrogen and deuterium impinging on a carbon target clearly show that the BCA simulation results and the experimental results disagree strongly for low impact energies due to additional chemical erosion and chemical sputtering as will be discussed in 2.4.3. Figure 2.20 shows some typical examples of the dependence of Y_{phys} on θ_p. Also here the agreement is rather good.

2.4.2.4 Radiation enhanced sublimation

Normally the physical sputtering yield does not depend on the surface temperature. However, for carbon it has been observed that at surface temperatures higher than about 1300 K, which is still well below the sublimation temperature of about 3200 K, the physical sputtering yield increases exponentially with temperature [71]. The sputtered particles also have a thermal velocity distribution instead of the Thompson distribution for real physically sputtered particles. This process has been called radiation enhanced sublimation. It is thought that this phenomenon is caused by the production of interstitials and vacancies by energetic projectile impact and the consequent diffusion of the interstitials to the surface where they can desorb into the gas phase.

2.4.3 Chemical erosion and chemical sputtering

In the previous subsection it was explained how nuclear collisions induced by energetic projectiles can lead to physical sputtering of target particles. In addition to these kinetic processes for some specific projectile-target combinations also chemical effects can cause erosion of target particles. Chemical interaction between projectile and target cannot only lead to the formation of stronger compounds such as oxides, carbides and nitrides but also to loosely bound volatile species that can be released thermally or by physical sputtering with a reduced threshold energy. In the context of thermonuclear fusion chemical erosion and chemical sputtering of carbon by hydrogen atoms and ions is very important. Both processes are discussed in detail in this subsection. This discussion is primarily based on [58] and [60]. Carbon can also be eroded by oxygen and nitrogen [58] and recently it turned out that also beryllium can be chemically eroded by deuterium forming BeD molecules [72].

2.4.3.1 Chemical erosion of carbon by thermal hydrogen atoms

Chemical erosion of carbon by hydrogen is the process in which reactive thermal hydrogen atoms impinging on the carbon surface interact chemically with the target atoms and lead to the formation and thermal release of volatile hydrocarbon species. In contrast to physical sputtering this phenomenon is a thermally activated chemical effect which requires no minimal impact energy.

The complicated chemical erosion cycle has been elucidated in detail by dedicated experiments [73] and is summarized in figure 2.21.

- Even at room temperature the graphitic sp^2 hybridized carbon atoms are hydrogenized by impinging hydrogen atoms to the sp^3 state via an intermediate radical sp^x state. This hydrogenation process is characterized by the cross section $\sigma_h = 4.5 \cdot 10^{-20}$.

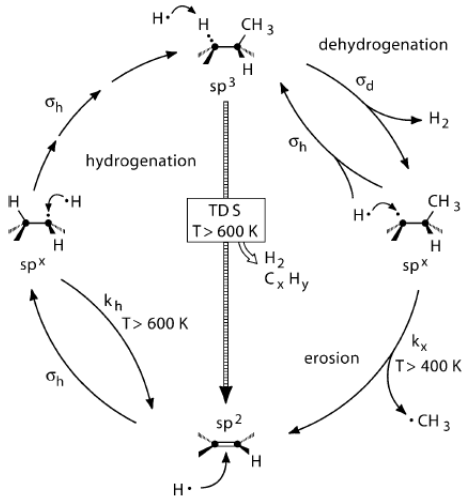

Figure 2.21: Chemical erosion cycle for thermal atomic hydrogen on carbon [73]

- Further irradiation with thermal atomic hydrogen leads to the formation and desorption of hydrogen molecules with cross section $\sigma_d = 0.05 \cdot 10^{-20}$ leaving a radical sp^x state with a broken bond in the hydrocarbon network
- For temperatures above 400 K chemical erosion can occur by desorption of a hydrocarbon complex attached to the hydrocarbon network in the neighbourhood of an sp^x radical which is then converted back to the basic graphitic sp^2 configuration. This process is characterized by the rate constant $k_x = 10^{13} \exp(-1.61/kT)$.
- Above 600 K incoming hydrogen atoms may recombine with adsorbed hydrogen atoms with rate coefficient $k_h = 10^{13} \exp(-1.73/kT)$ interrupting the hydrogenation processes and limiting the chemical erosion.

From the steady state rate equations it can then be calculated that according to this model the thermal chemical erosion yield Y_{therm} is given by

$$Y_{therm} = \frac{n_C \sigma_d k_x}{\sigma_h \Phi + \left(1 + \frac{\sigma_d}{\sigma_h^2} \frac{k_h}{\Phi}\right) k_x} \tag{2.243}$$

with $n_C = 2.3 \cdot 10^{19}$ m^{-2} the number density of carbon surface sites per unit area for graphite and Φ the atomic hydrogen flux impinging on the surface. The yield has a strong temperature dependence due to the competition

between chemical erosion and recombinative hydrogen desorption. At room temperature Y_{therm} is very small, while a maximum occurs around 600 K.

The actual yield depends strongly on the type of material. For an amorphous hydrocarbon layer (a-C:H) the yield can be up to two orders of magnitude higher than for pure graphite as illustrated in figure 2.22 [74]. Even at room temperature the chemical erosion yield is still about 0.01 for a-C:H. The reason for this dependence on the material is that impinging hydrogen atoms can only react with dangling bonds at the edge of graphitic planes. Hence, chemical erosion is also enhanced if the surface is simultaneously bombarded with energetic ions creating additional dangling bonds. If the ion fluence received by the surface is higher than about $10^{21} - 10^{22}$ m^{-2} the dependence on the original material disappears because the surface of all carbon based materials then becomes similar to an a-C:H layer with a saturation concentration of hydrogen of about 30% at room temperature decreasing with increasing temperature due to recombinative desorption of hydrogen molecules.

In contrast to physical sputtering the chemically eroded carbon is released mainly as CH_3, CH_4, C_2H_y and C_3H_y [75]. Each species has its own temperature maximum leading to different spectra at different temperatures. The energy distribution of the chemically eroded hydrocarbons can well be approximated by a Maxwellian distribution according to the surface temperature. So chemically eroded species have much lower energies than physically sputtered species. The emission angles are approximately distributed according to a cosine distribution.

2.4.3.2 Chemical sputtering of carbon by energetic hydrogen

If energetic hydrogen species bombard a carbon surface the resulting yield is higher than the sum of physical sputtering and chemical erosion. This is due to a complex synergy between kinetic effects and chemical interaction called chemical sputtering. The total chemical sputtering yield Y_{tot} depends on a lot of different parameters.

- **surface temperature:** The temperature dependence shows a clear maximum at a temperature in the range 800-900 K due to increasing reactivity with increasing temperature competing with enhanced recombinative hydrogen desorption at higher temperatures. The exact position of the maximum depends on the impinging hydrogen flux and impact energy.
- **impact energy:** Also the energy dependence exhibits a maximum. This is located in the range 300-1000 eV and shifts towards higher energies for higher surface temperatures. This is caused by similar knock-on effects as for physical sputtering.
- **surface state:** Chemical sputtering is enhanced for higher concentrations of dangling bonds due to increased chemical reactivity.

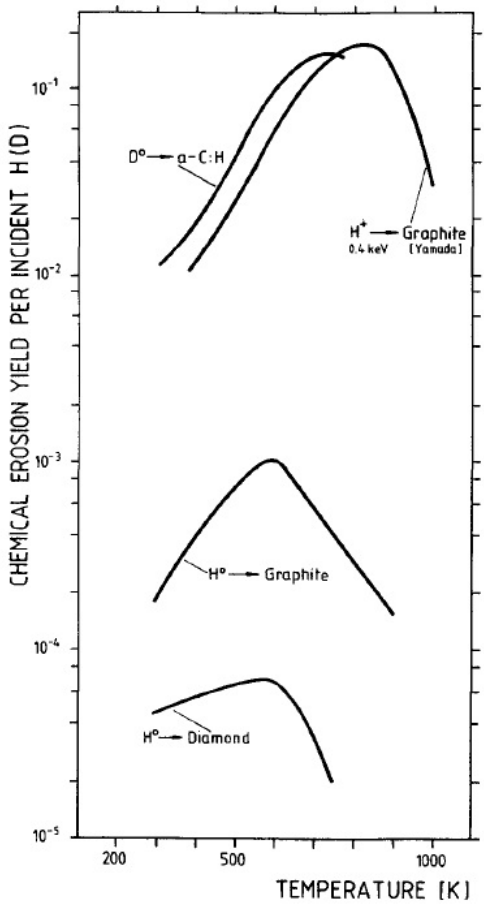

Figure 2.22: Chemical erosion yield for different carbon based materials as function of the surface temperature [74]

- **hydrogen flux:** The position of surface temperature maximum shifts towards higher temperatures with increasing ion flux. This leads to a slight decrease of the yield with increasing flux due to recombinative desorption of hydrogen and annealing of radiation damage at higher surface temperatures.
- **isotope:** The isotopic mass has a clear effect on the chemical sputtering due to the difference in momentum transfer. The yields for deuterium can be up to a factor of 7 higher than for hydrogen.
- **molecular species:** In some situations the surface is bombarded

with molecular species such as H_2^+ or H_3^+. Usually it is then assumed that this is equivalent to bombardment with respectively a two or three times higher flux of H^+ with half or one third of the impact energy. Above 100 eV experiments have shown that this is a good approximation. However, at lower energies it was found that the yield per atom for H_3^+ can be up to a factor two higher than for H^+ [76].

An empirical analytical model has been derived that successfully describes the most important dependencies [77]. In this model the chemical sputtering yield is given by

$$Y_{tot} = Y_{phys} + Y_{therm}(1 + DY_{dam}) + Y_{surf} \tag{2.244}$$

The first term simply represents the physical sputtering as discussed in the previous subsection. The second term describes the thermal chemical erosion. The thermal chemical erosion yield Y_{therm} here is given by

$$Y_{therm} = c^{sp^3} \frac{0.033 \exp(-E_{therm}/kT)}{2 \cdot 10^{-32}\Phi + \exp(-E_{therm}/kT)} \tag{2.245}$$

with c^{sp^3} the surface concentration of sp^3 sites according to

$$c^{sp^3} = C \frac{2 \cdot 10^{-32}\Phi + \exp(-E_{therm}/kT)}{2 \cdot 10^{-32}\Phi + \left[1 + \frac{2 \cdot 10^{29}}{\Phi} \exp(-E_{rel}/kT)\right] \exp(-E_{therm}/kT)} \tag{2.246}$$

These expressions are coming from the chemical erosion model [73] described above but with the cross sections and activation energies used as free parameters to fit the model to the experimental data. The factor

$$C = \frac{1}{1 + (\Phi/6 \cdot 10^{21})^{0.54}} \tag{2.247}$$

was added to take into account an additional decrease of the yield at higher fluxes as was observed experimentally [78]. During bombardment with energetic projectiles the chemical erosion is enhanced by near surface radiation damage created by kinetic energy transfer from the projectiles to the targets. This is taken into account by the enhancement factor $1 + DY_{dam}$. D is a constant depending on the isotope mass. Y_{dam} is the near surface damage yield which has a similar dependence on the projectile impact energy E_p as the physical sputtering yield but with a different threshold energy E_{dam}. In this model the old Bohdansky formula is used such that

$$Y_{dam} = QS_n \left[1 - \left(\frac{E_{dam}}{E_p}\right)^{2/3}\right] \left(1 - \frac{E_{dam}}{E_p}\right)^2 \tag{2.248}$$

Here Q is a fitting parameter determining the absolute value of the yield. The stopping power S_n is given by the expression

Table 2.8: Parameters for the empirical chemical sputtering formula [58]

Parameter	Hydrogen	Deuterium
E_{TF}	415 eV	447 eV
Q	0.035	0.1
E_{th}	31 eV	27 eV
E_{dam}	15 eV	15 eV
E_{des}	2 eV	2 eV
D	250	125
E_{rel}	1.8 eV	1.8 eV
E_{therm}	$\mu = 1.7$ eV, $\sigma = 0.3$ eV	$\mu = 1.7$ eV, $\sigma = 0.3$ eV

$$S_n = \frac{0.5 \ln(1 + 1.2288 E_p/E_{TF})}{E_p/E_{TF} + 0.1728\sqrt{E_p/E_{TF}} + 0.008(E_p/E_{TF})^{0.1504}} \tag{2.249}$$

with E_{TF} the Thomas-Fermi energy. The last term in (2.244) represents a surface effect. Weakly bound sp^3 CH_n groups at the surface can be physically sputtered by the impinging energetic projectiles with a yield Y_{surf} given by

$$Y_{surf} = c^{sp^3} \frac{Y_{des}}{1 + \exp\left(\frac{E_p - 65 \text{ eV}}{40 \text{ eV}}\right)} \tag{2.250}$$

Here c^{sp^3} is the surface concentration of sp^3 states given by (2.246). Y_{des} is the ion induced desorption yield defined as

$$Y_{des} = Q S_n \left[1 - \left(\frac{E_{des}}{E_p}\right)^{2/3}\right] \left(1 - \frac{E_{des}}{E_p}\right)^2 \tag{2.251}$$

in analogy with physical sputtering but with a different threshold energy E_{des}. The denominator in (2.250) limits the contribution of the surface effect to lower energies because for higher energies the projectiles release their kinetic energy too deep in the surface. The values for the fitting parameters in the above equations resulting from fitting the analytical model to experimental data are listed in table 2.8 for hydrogen and deuterium. The comparison between the model, experimental data and MD calculations for a flux $\Phi = 10^{20}$ $m^{-2}s^{-1}$ in figure 2.23 shows good agreement.

The majority of the chemically eroded species is released as CH_4 and higher hydrocarbons C_2H_y and C_3H_y [75]. The product spectrum changes with ion energy. At energies above 1 keV CH_4 dominates, but for lower energies the sum of the higher hydrocarbon product species is dominant.

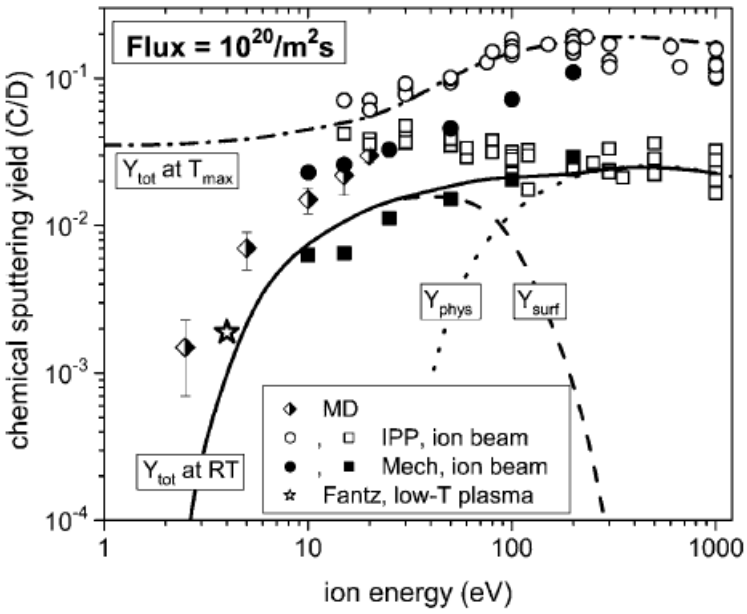

Figure 2.23: Comparison of MD calculations, analytical model and experimental data for the chemical sputtering of carbon by deuterium [58]

As for chemically eroded species the energy of the chemically sputtered particles is distributed according to a Maxwellian distribution at the surface temperature and the emission angles are distributed according to a cosine distribution.

2.4.4 Spectroscopic determination of neutral fluxes

Neutral fluxes released from surfaces and thus also physical and chemical erosion yields can be determined in-situ by means of optical emission spectroscopy. The spectroscopic technique is based on the so called D/XB and S/XB values also known as inverse photon efficiencies. To explain how this works first the most simple case will be considered. Imagine that a flux Φ_A of neutral particles A is released from a certain source into the plasma along a certain line of sight. Assume an ionizing plasma for which recombination can be neglected and in which the original neutrals are lost by electron impact dissociation or ionization with rate coefficient D long before they leave the plasma volume. The flux Φ_A can then be set equal to the loss flux as

$$\Phi_A = \int_{x_1}^{x_2} n_A(x) n_e(x) D(x) dx \tag{2.252}$$

where n_A is the density of the neutral species and the integration is along the line of sight. Besides dissociation and ionization electron impact can also lead to excitation of ground state species to species excited to the energy level j with rate coefficient X_j. Assume a low density plasma for which the excited species density is much lower than the ground state species density and for which collisional excitation is balanced by radiative decay according to the coronal equilibrium

$$n^*_{A,j} \sum_{i<j} A_{ji} = n_A n_e X_j \tag{2.253}$$

where $n^*_{A,j}$ is the density of excited species in the energy level j and A_{jk} the spontaneous radiative decay rate coefficient for the transition from energy level j to energy level k. The photon flux $\Phi_{ph,jk}$ emitted along the line of sight due to the transition from energy level j to energy level k can now be written as

$$\Phi_{ph,jk} = B_{jk} \int_{x_1}^{x_2} n_A(x) n_e(x) X_j(x) dx \tag{2.254}$$

with B_{jk} the branching ratio of the transition to the level k from the level j defined as

$$B_{jk} = A_{jk} / \sum_{i<j} A_{ji} \tag{2.255}$$

If one further assumes that the plasma is rather homogeneous equations (2.252) and (2.254) can be combined to get the following relation between the neutral particle flux and the photon flux

$$\Phi_A = \frac{D}{X_j B_{jk}} \Phi_{ph,jk} \tag{2.256}$$

The factor on the right hand side of this equation needed to multiply with the photon flux to get the neutral flux is often simply called the D/XB value. If the neutrals are atomic they can only be lost by ionization with rate coefficient S. The conversion factor is then called the S/XB value instead. In the above derivation several assumptions have been introduced to get the relation between Φ_A and $\Phi_{ph,jk}$. A similar relation can be written also in less restrictive cases. The conversion factor is then called the effective D/XB or S/XB value or inverse photon efficiency because it represents the number of released neutrals per emitted photon. The inverse photon efficiency can even be defined for transitions of dissociation products of the released neutrals. In case of methane for instance only electronic transitions in the dissociation

products CH, CH^+ and C result in photons in the visible or near UV range. In general the inverse photon efficiency can no longer simply be calculated as a reaction rate ratio. One has to use more sophisticated collisional-radiative models or calibrated injection experiments to determine the inverse photon efficiencies. Once the inverse photon efficiency is known, the neutral flux can easily be derived from the measured photon flux.

2.4.5 Reflection and implantation of energetic particles

Energetic projectiles hitting a material surface lose their energy by nuclear collisions and partly also by electronic collisions. Nuclear collisions can also redirect the velocity. The projectile is almost instantaneously neutralized. Eventually it can get thermalized and implanted inside the material at an interstitial site or it can be reflected out of the material.

Reflection and implantation can be quantified by defining the reflection probability R or the implantation probability which is of course just $1 - R$. The reflection probability depends on a lot of parameters such as projectile mass, impact energy, impact angle, target mass, target crystallinity, crystal orientation, surface roughness and the possible presence of multiple materials or impurities in the interaction layer. It is possible to measure R in dedicated ion beam experiments, but this is rare for fusion relevant impact energies. One can also use BCA and MD codes to calculate R.

A lot of reflection probability data calculated with TRIM have been compiled in [79]. It can be seen that R increases for increasing target to projectile mass ratio. This means that light projectiles are easily reflected on heavy targets. According to TRIM calculations R increases monotonically with projectile impact angle because at grazing incidence the projectile penetrates less deep into the material. Further TRIM simulations show that R is zero for low projectile impact energies around 10 eV, then increases with energy until it reaches a maximum at a few 100 eV and starts to decrease again for higher energies due to deeper penetration of the projectiles into the material. The behaviour at very low impact energies is not realistic. For such low energies MD simulations are more appropriate because chemical effects are then dominant. MD simulations show a non-zero reflection probability for very low impact energies especially for grazing incidence [80], [81]. Also for molecular projectiles MD simulations are more appropriate.

2.4.6 Retention and recycling

In the previous subsection it was explained how energetic particles impinging on a material are eventually either reflected back into the plasma or implanted inside the material. If the particle is implanted it is usually not just staying where it was originally implanted. Figure 2.24 shows schematically the recycling and retention processes that can occur. These processes are briefly discussed in this subsection. For thermonuclear fusion the most

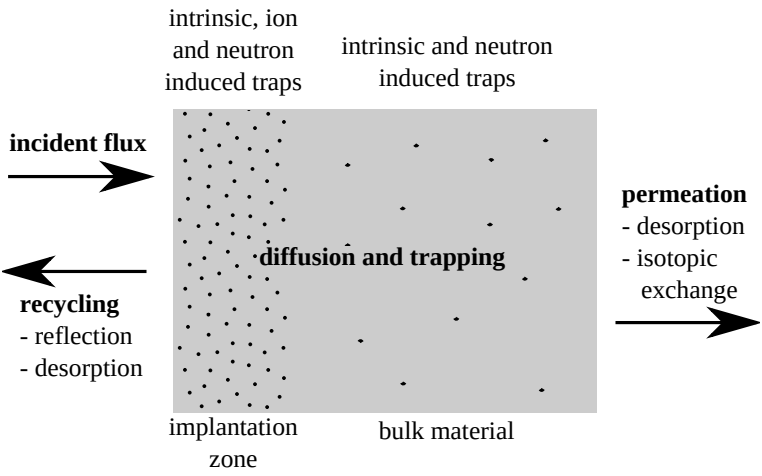

Figure 2.24: Scheme of the important hydrogen recycling and retention processes

important situations to look at are hydrogen from the fuel and helium produced by the nuclear fusion reaction implanted in fusion relevant materials like tungsten, beryllium and carbon. For this work it is only relevant to discuss hydrogen in graphite. More details on recycling and retention in the context of thermonuclear fusion can be found in [82], [83] and [44].

Once an impinging hydrogen atom becomes thermalized inside the lattice of the target material it is usually located at an interstitial position. The hydrogen atom is then said to be in the solute state. A material has only a finite amount of solute sites for hydrogen. Therefore, if the hydrogen fluence is too high the implantation zone between the surface and the maximum implantation range gets saturated and the hydrogen atoms are driven out of the material or into a separate phase.

A hydrogen atom can hop from one solute site to the other. As can be seen in figure 2.25 on the one dimensional sketch of the potential energy landscape the hydrogen atom perceives this requires an amount of energy E_D which can be provided thermally. The random walk resulting from the thermally activated hopping between solute sites is called diffusion. Diffusion is promoted by increasing the temperature.

During diffusion a hydrogen atom can get trapped by defects such as vacancies, voids and grain boundaries. As shown in 2.25 at such trapping sites the hydrogen atoms are more strongly bound with an energy E_T. Detrapping requires increase of the temperature as is done for instance in thermal desorption spectroscopy. Some traps are intrinsically present in the material due to manufacturing. Additional traps can be created by neutron or ion irradiation. Neutron irradiation leads to a homogeneously distributed

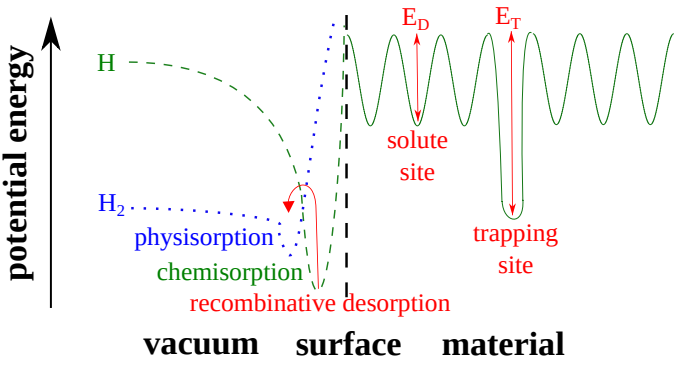

Figure 2.25: Scheme of the hydrogen potential energy landscape near a surface

trap concentration. Ion irradiation leads to an increased trap concentration in the implantation zone. Agglomeration of hydrogen at traps can lead to bubbles or to blisters if the trap is just below the surface.

It is also possible that a hydrogen atom manages to diffuse to the surface of the material where it becomes chemisorbed. These hydrogen atoms can eventually be desorbed by ion, electron or photon impact or by heating to very high temperatures. As can be seen in figure 2.25 it is energetically favourable for hydrogen atoms to recombine at the surface. Two chemisorbed hydrogen atoms can meet each other to recombine by surface diffusion or an impinging hydrogen atom from the plasma can recombine with a chemisorbed hydrogen atom. This gives rise to the possibility for recombinative desorption which requires only little activation energy that can easily be provided thermally even at low temperatures.

For graphite it has been observed experimentally that very rapidly a hydrogen saturated implantation layer is formed. The saturation concentration decreases with increasing temperature. For room temperature one typically has $H/C = 0.4 - 0.5$ [83]. This layer has an important effect on recycling of hydrogen fuel because once the layer is saturated almost all impinging hydrogen is immediately recycled back into the plasma. At room temperature almost all hydrogen is released as molecular hydrogen. At 800 K also hydrocarbons form an important contribution and for temperatures above 1800 K atomic hydrogen dominates the spectrum [83]. At low temperatures the diffusion of hydrogen in graphite is primarily along the internal porosities and grain boundaries. At temperatures above 1000 K transgranular diffusion becomes important. For graphite with very high porosity hydrogen penetration in the material up to tens of millimetres has been observed even at room temperature [83].

2.4.7 Sticking of thermal molecules and radicals

Although only energetic projectiles can be implanted, thermal species can also be deposited by adsorption at the target surface. The surface target atoms are not fully surrounded by other atoms and have free bonding sites. Two mechanisms are possible. The first mechanism is physisorption. In this case a weak van der Waals bond with a binding energy of less than 0.5 eV is formed. The second mechanism is chemisorption. In this case a stronger covalent bond is formed with a binding energy of a few electronvolts. The adsorption probability depends on the projectile-target combination, the surface structure and the surface temperature. Adsorbed species can be desorbed thermally, by impact of energetic projectiles or by photons.

In the context of thermonuclear fusion the most important situation is that of hydrocarbon molecules and radicals impinging on an a-C:H surface because hydrocarbons produced by chemical erosion of carbon can lead to the formation of substantial a-C:H layers, especially at remote areas. Sticking of thermal hydrocarbons species depends strongly on the presence of dangling bonds to which radicals can stick. These can be created by ion bombardment [84] or by hydrogen abstraction due to impinging hydrogen atoms [85].

The sticking probability S for hydrocarbon species is difficult to measure. Several studies have used the cavity technique to determine the surface loss probabilities of reactive hydrocarbon species [86], [87], [88]. The surface loss probability is the probability that a reactive particle either sticks to the surface or is reflected as a non-reactive volatile particle. Hence, the surface loss probability is an upper limit for the sticking probability. With the cavity technique hydrocarbons from the plasma can enter the cavity in a remote area through a narrow slit. This results in a deposition pattern inside the cavity which can be analysed after the experiment. Using analytical calculations or Monte Carlo simulations it is possible to deduce the surface loss probability from the deposition pattern inside the cavity. The experiments have clearly shown that the surface loss probability depends strongly on the hybridization state of the hydrocarbon species and increases from sp^3 to sp^2 to sp.

As an alternative one can also use MD simulations to calculate the sticking probabilities of the hydrocarbon species. The simulations in [89] and [90] show that the sticking probability of hydrocarbons increases with the number of unpaired electrons in CH_y and with the hybridization state of carbon in C_2H_x from sp^3 to sp^2 to sp. This is in perfect agreement with the cavity experiments. The simulations further show that the sticking probability also increases with the impact energy and that the sticking probability is lower for hard plasma-exposed surfaces than for soft plasma-shadowed redeposited layers. In [91] it is shown that also the hybridization state of the carbon surface itself, which depends on the ion flux impinging on the surface, influences the reflection. Exposure to a higher flux leads to more sp^2

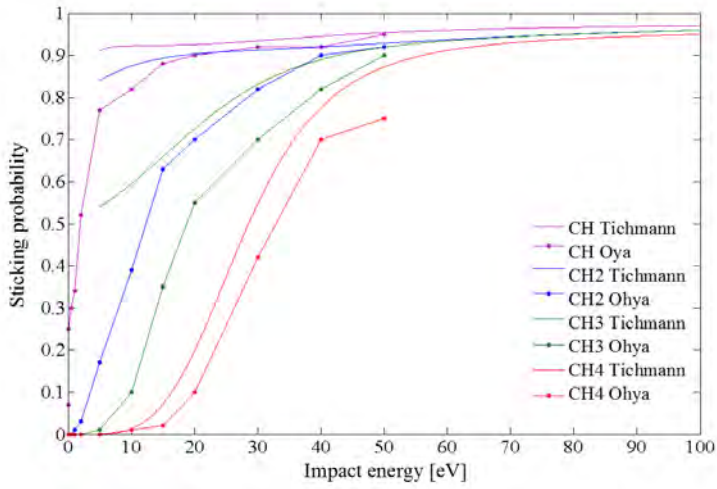

Figure 2.26: MD hydrocarbon sticking probabilities as function of impact energy for normal incidence [92],[80]

hybridization and less reflection.

Recently extensive MD data on hydrocarbon sticking have been published by Tichmann [92]. Classical MD simulations with the Brenner potential were performed to study the sticking of different hydrocarbons on an a-C:H surface with 40% hydrogen for various impact angles and energies. The covered energy range was 5-100 eV. Interpolation between the data points was done by means of a third order rational Bezier-spline surface. In this way the sticking probability S can be calculated as function of impact energy and angle according to

$$S(E,\theta) = \frac{\sum_{i=0}^{3}\sum_{j=0}^{3} P_{ij} w_{ij} B_i(E) B_j(\theta)}{\sum_{i=0}^{3}\sum_{j=0}^{3} w_{ij} B_i(E) B_j(\theta)} \tag{2.257}$$

with the basis functions B_i derived from the Bernstein polynoms as

$$B_i(x) = B_{i,3}\left(\frac{x - x_{min}}{x_{max} - x_{min}}\right) \tag{2.258}$$

$$B_{i,3}(t) = \binom{3}{i} t_i (1-t)^{3-i} \tag{2.259}$$

where x_{min} and x_{max} are the boundaries of the studied parameter space, respectively 5 eV and 100 eV for the impact energy and 0^o and 89^o for the

impact angle. P_{ij} and w_{ij} are matrices of fitting parameters. At normal incidence S increases monotonically with increasing impact energy to a value of almost 1 at energies above 50 eV. For lower energies S depends strongly on the type of hydrocarbon species. This is very different from BCA simulation results where below 50 eV the sticking probability goes to 1. MD simulations seem to be more reliable because the very high reflection probabilities for CH_4 and CH_3 are in very good agreement with the experimental observations in [87] and [88]. The sticking of CH_y is lower for higher values of y which also corresponds with experiments. This is probably due to fewer binding possibilities. S decreases monotonically with increasing impact angle which is in agreement with BCA simulations. Ohya performed similar studies in [80]. The MD code used in this work is also based on the Brenner potential. The hydrogen content of the surface was taken to be 30%. The covered energy range was 0.01-50 eV. The MD hydrocarbon sticking probabilities for normal incidence simulated by Tichmann and Ohya are compared in figure 2.26. Qualitatively the results are in perfect agreement. Also quantitatively the agreement is reasonable except for the fact that at lower impact energies the sticking probabilities are systematically lower in the simulations by Ohya. This can be caused by the difference in hydrogen content in the simulations.

2.4.8 Plasma-surface interaction issues

Plasma-surface interaction in thermonuclear fusion devices affects both the plasma-facing components and the fusion plasma. Operating scenarios and plasma-facing components have to be optimized in order to limit adverse effects. The most crucial issues with respect to plasma-surface interaction in thermonuclear fusion devices are addressed in detail in [93], [94] and [95]. This subsection gives a short overview.

First of all physical sputtering, chemical erosion and chemical sputtering lead to removal of particles from the plasma-facing components. Part of these particles is pumped out via the divertor. However, the majority of the eroded particles eventually gets redeposited. The redeposition is not necessarily at the same location as the erosion. This leads to regions of net erosion and regions of net deposition. The erosion can be enhanced by the formation of material mixtures with different properties as the original material. If a significant fraction of the plasma-facing component has been eroded it should be replaced. This limits the availability of the fusion power plant and increases the cost of the produced electricity.

Part of the eroded particles will manage to penetrate into the core plasma. This diminishes the fusion power in two ways. Firstly, the fusion fuel will be diluted. A tokamak is characterized by an upper limit for the plasma density, the so called Greenwald limit, beyond which the plasma becomes unstable leading to a disruption with complete loss of confinement. Hence, the presence of impurities implies a decrease of the fusion

fuel density and hereby of the fusion power. Secondly, the impurities lead to cooling of the plasma. In the relatively cool plasma edge the impurities will be only partly ionized. The remaining electrons of the impurities can then be excited by collisions with plasma particles and subsequently dissipate the excitation energy by radiative decay. In the hot plasma core the impurities are highly charged. This leads to strong acceleration of the surrounding plasma electrons which hereby lose part of their kinetic energy by means of Bremsstrahlung. The kinetic energy lost by line radiation and Bremsstrahlung cools the plasma and thus also reduce the fusion power. This radiative cooling is most important for high Z impurities.

Another very important issue is dust formation. Dust in a fusion reactor can be produced for instance by agglomeration of eroded carbon atoms in the plasma, flaking of redeposited layers or blister rupture. In case of a leak radioactive or toxic dust could be released in the environment. Furthermore, in case of a cooling water leakage hot beryllium dust could react with steam producing hydrogen which in combination with oxygen is very explosive. Therefore, one has to impose a safety limit for the in vessel content of mobilizable dust in order to guarantee that even in case of an accident evacuation of nearby living people is not needed.

Also retention of fuel and especially of tritium is an important issue. Retention and recycling determines the fuelling efficiency. Furthermore, as in case of dust one has to impose also a safety limit for the total in-vessel tritium inventory due to its radioactivity. Tritium accumulation by adsorption and implantation saturates and represents only a small fraction of the total inventory. For low Z plasma-facing materials which are significantly eroded the tritium retention is dominated by codeposition of tritium in remote areas and gaps. For high Z plasma-facing materials it is dominated by diffusion and trapping of tritium in the bulk of the material.

If the safety limits for dust or tritium inventory are exceeded operation of the reactor has to be stopped and the vessel has to be cleaned with dedicated techniques which are still under development. This of course limits the availability of the power plant and increases also the cost of the produced electricity.

2.4.9 Candidate plasma-facing materials

For next generation fusion reactors basically three materials are envisaged: carbon based materials such as carbon-fibre composites (CFC) and graphite, beryllium and tungsten. The pros and cons of these materials are summarized in table 2.9. CFC was originally foreseen for the vertical divertor target plates in ITER during the non-active deuterium-deuterium phase. It would be replaced by tungsten cassettes during the active deuterium-tritium phase because the use of carbon would result in unacceptably high tritium retention due to codeposition. However, recently it was decided to start already in the non-active phase with the tungsten cassettes in order

Table 2.9: Pros and cons of the main candidate plasma-facing materials

carbon	
pros	low Z material giving only limited radiative cooling
	no melting and high sublimation temperature of 3200 K
	good thermal shock and thermal fatigue resistance
cons	high chemical erosion under hydrogen bombardment
	strong degradation under neutron irradiation
	strong build-up of tritium inventory in codeposits
beryllium	
pros	low Z material giving only limited radiative cooling
	good oxygen getter reducing the oxygen impurity level
	good thermal conductivity
	in-situ repair possible by plasma spraying
	low hydrogen solubility
cons	low melting temperature of 1560 K
	high physical sputtering yield
	toxic
	degradation and tritium production under neutron irradiation
tungsten	
pros	very low physical sputtering yield and no chemical erosion
	high melting temperature of 3695 K
	good thermal conductivity
	in-situ repair possible by plasma spraying
	low hydrogen solubility
cons	high Z material giving substantial radiative cooling
	high ductile-to-brittle transition temperature
	surface degradation, cracking, embrittlement for high heat loads

to reduce the cost. Also for the remaining parts of the divertor (baffles and dome) tungsten will be used. The ITER first wall will be covered with beryllium tiles. For the demonstration fusion power plant DEMO one foresees tungsten both for the divertor and the first wall.

Figure 2.27 shows the expected number of ITER discharges before the safety limits for erosion, dust generation and tritium retention are reached for different choices of plasma-facing materials according to [93]. A full carbon ITER will very rapidly reach the safety limit for tritium retention. A full tungsten ITER gives the largest number of discharges. However, the flexibility with respect to disruptions is very limited in this case. Therefore, in the original ITER design it was envisaged to use the low Z materials CFC for the high heat flux regions of the divertor and beryllium for the first wall. This limits the number of discharges but gives the opportunity to explore

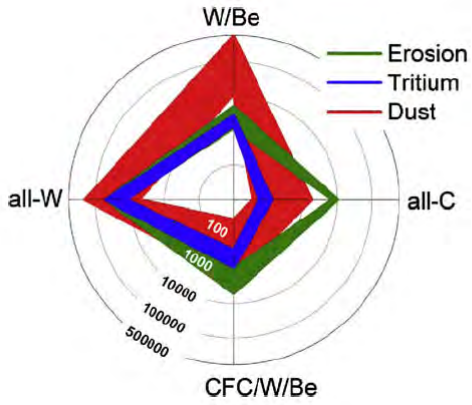

Figure 2.27: Comparison of the number of ITER discharges before the safety limits for erosion, dust and tritium retention are reached for different material choices [93]

different more operating scenarios. As explained above the CFC divertor target plates cannot be used during the active phase and should be replaced by tungsten cassettes. To reduce the cost the initial CFC divertor target plates will not be used which will of course limit the explorable parameter space of operating scenarios.

Chapter 3

Experimental facilities

3.1 TEXTOR tokamak

The first part of this work involved modelling of material migration experiments in the TEXTOR tokamak. The general characteristics of the TEXTOR tokamak are described in the first subsection. The next two subsections discuss in more detail two specific experiments modelled in this work.

3.1.1 General description

TEXTOR was a medium sized tokamak dedicated to plasma-surface interaction studies at Forschungszentrum Jülich. The name is an acronym for "tokamak experiment for technology oriented research". Operation of the machine started in 1983. It has been decommissioned end 2013. The design has been described in detail in [96] and [97]. TEXTOR has a major radius $R = 1.75$ m, a toroidal magnetic field $B_T \leq 3$ T, a toroidal plasma current $I_{plasma} \leq 0.8$ MA and a typical plasma pulse length of a few seconds. The cross section is circular and the minor plasma radius can be varied between 410 mm and 480 mm by positioning of the toroidal belt limiter or the poloidal limiters at the top and bottom of the vessel. The panorama photo in figure 3.1 shows the inside of the vacuum vessel with the different limiters. Already in the eighties the device was converted from a metallic wall machine to a low Z machine by changing the limiter material from steel to graphite and by introducing low Z wall coatings. The distance between the last closed flux surface and the wall components was about 10 cm and the boundary could easily be accessed by different diagnostics. This was very advantageous for the study of plasma-surface interaction. In addition to Ohmic heating the plasma could by heated by means of the 4 MW neutral beam injection system, the 4 MW ion cyclotron heating system and the 1 MW electron cyclotron heating system.

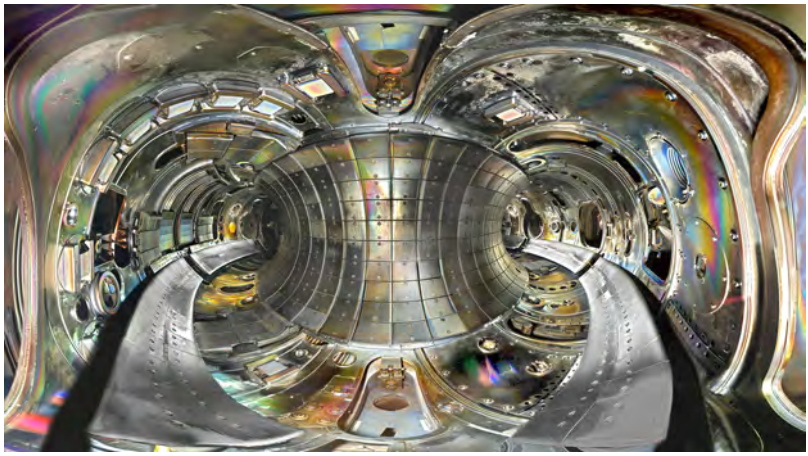

Figure 3.1: Panorama photo inside the TEXTOR vacuum vessel [98]

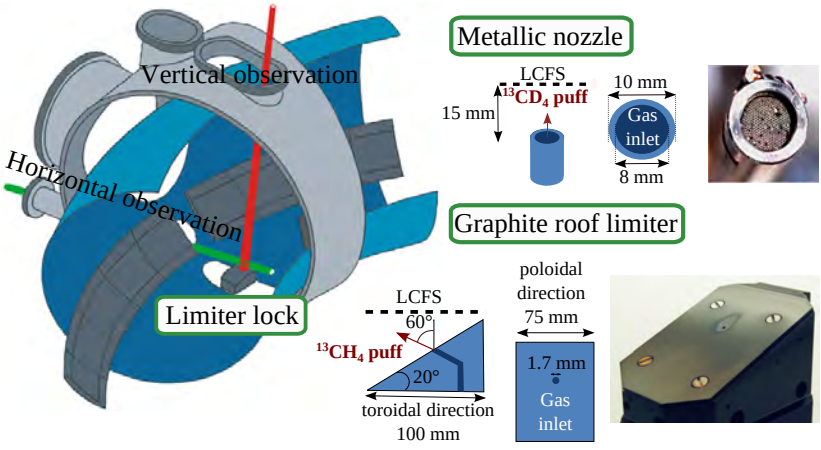

Figure 3.2: Schematic view of the TEXTOR limiter lock system with the metallic nozzle and the graphite roof limiter for the methane injection experiments

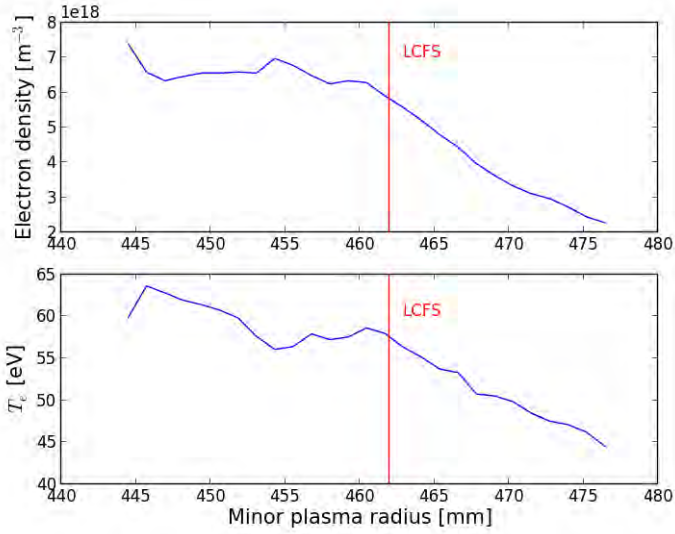

Figure 3.3: Radial electron density and temperature profiles during the TEXTOR nozzle experiment from neutral helium beam emission spectroscopy

Of particular interest for plasma-surface interaction studies was the special limiter lock system in TEXTOR [99]. It allowed mounting test limiters or diagnostic tools with dimensions of about 10 cm without breaking the vacuum within about one hour. The test limiters could be rotated with respect to the toroidal magnetic field and moved in the radial direction. Electrical isolation allowed biasing and a gas supply system made it possible to inject a tracer gas into the plasma. As shown schematically in figure 3.2 good vertical and horizontal access allowed detailed optical observation by means of a large number of optical and spectroscopic systems from VUV to IR with high spatial and temporal resolution.

3.1.2 Nozzle experiment

During one of the experimental campaigns in TEXTOR a cylindrical metallic nozzle with gas inlet was mounted at the limiter lock system as shown in figure 3.2. This experiment was described in detail in [100] and [101]. The surface of the nozzle was positioned 15 mm outside of the last closed flux surface which was located at a minor plasma radius of 462 mm. The nozzle had an outer radius of 5 mm and an inner radius of 4 mm. The surface area at the top consisted only of an annulus with 1 mm thickness. This

limited the light emission caused by recycled, reflected or eroded species. The gas inlet in the centre was used to inject tracer methane molecules with an injection rate of about $1.75 \cdot 10^{19} s^{-1}$. In order to be able to spectroscopically distinguish light emitted by hydrogen dissociation products from the injected methane and by hydrogen from the plasma the methane molecules were marked with deuterium and injected in a protium plasma. 2D light emission images were recorded from the top and the side using intensified CCD cameras equipped with interference filters for the CD Gerö band, the C_2 Swan band, the CD^+ Douglas-Herzberg band and several hydrogen Balmer lines. Methane itself has no electronic transitions in the visible or near UV range. Additionally a set of spectrometer systems was responsible for the integral observation of the light emission cloud due to the injected species. The effective D/XB values for electronic transitions of dissociation products from the injected hydrocarbon molecules were determined experimentally by dividing the total number of injected hydrocarbons by the total number of observed photons. The uncertainty on the effective D/XB values determined in this way was estimated to be below 20%. Radial electron density and electron temperature profiles at the plasma edge were measured at the low field side of the tokamak with neutral helium beam emission spectroscopy by using the line ratio of three neutral helium lines [102]. These profiles are shown in figure 3.3. The measurement error due to uncertainties in the atomic model is about 30% for the electron temperature and about 10% for the electron density. Local Langmuir probe and Balmer line ratio measurements have shown that an electron temperature decrease of up to 15% can be expected around the gas inlet due to disturbance of the plasma by the injected hydrocarbons.

3.1.3 Roof limiter experiment

During another experimental campaign a roof-like test limiter covered with a 2 mm thick polished graphite plate was mounted at the TEXTOR limiter lock system as shown in figure 3.2. The experiment was described in detail in [103] and used basically the same set-up as in previous studies described in [104]. The tip of the test limiter was located at the last closed flux surface at a minor plasma radius of 460 mm. The graphite plate was inclined at an angle of 20^o with respect to the toroidal direction. The dimensions of the roof-like test limiter were 100 mm in the toroidal direction and 75 mm in the poloidal direction. A small circular gas inlet 15 mm behind the last closed flux surface with radius 0.85 mm allowed injection of methane. The direction of injection made an angle of 40^o with respect to the surface normal. The methane injection rate was about $1.5 \cdot 10^{19}$ s^{-1}. As in the nozzle experiment described above the volume around the test limiter was spectroscopically observed in detail. The set-up of the spectroscopic diagnostics was discussed in detail in [105]. The test limiter surface was analysed ex-situ after the experimental campaign. The thickness of

the transparent amorphous hydrocarbon layer deposited locally around the injection hole as visible in figure 3.2 was determined from the colours of the interference fringes by means of colorimetry [106]. The injected methane molecules were marked with ^{13}C to distinguish the injected carbon from the intrinsic carbon present in TEXTOR due to erosion of carbon based plasma-facing materials. The ratio $^{13}C/^{12}C$ in the deposited layers was determined using SIMS. The plasma pulses during this experimental campaign were Ohmic discharges with toroidal magnetic field $B_T = 2.25$ T, toroidal plasma current $I_{plasma} = 350$ kA and pulse duration $\Delta t \approx 5.5$ s. The plasma parameters at the last closed flux surface were $T_e = 54$ eV, $T_i = 81$ eV and $n_e = 1.9 \cdot 10^{18}$ m^{-3}. The surface temperature of the graphite plate was about 520 K. The ion flux on the plate was around 10^{22} m^{-2}s^{-1} and the average ion impact energy due to thermal motion and acceleration in the sheath and presheath was about 250 eV.

3.2 VISIONI plasma simulator

The second part of this work involved experiments and modelling for the VISIONI plasma simulator. The first subsection discusses the experimental program of the device. The next subsections discuss the plasma generation mechanism, the magnetic confinement, the sample holder, the vacuum system and the diagnostics. The last subsection lists some typical values for the most important plasma parameters in VISIONI.

3.2.1 Testbed for ITER first wall materials

The VISIONI plasma simulator was originally a tool to study hydrogen isotope recycling in the ETHEL tritium laboratory at the EC-JRC Ispra research site in Italy [107]. After the shut down of ETHEL it was decided in 2007 to transfer the machine to the Belgian Nuclear Research Center SCK-CEN and to refurbish it. The plasma simulator was named VISIONI. This is an acronym for "versatile instrument for the study of ion interaction". It is now dedicated to plasma-material interaction studies in the context of thermonuclear fusion [108].

Small disk shaped samples with a diameter of 11.3 mm and a thickness of 4 mm can be exposed to continuous ion bombardment for several hours or even days with an ion flux density $\Phi_i \leq 10^{21}$ m^{-2}s^{-1} and an ion impact energy $E_i \leq 400$ eV. Most samples in VISIONI are exposed to a deuterium plasma in order to distinguish the effects of plasma exposure from the background hydrogen present already before exposure. For specific studies it is sometimes decided to work with H_2, Ar, He, CH_4, N_2 or mixtures of these elements.

It has been proposed to install the device in glove boxes in order to have the combined capability to work with tritium, beryllium and low-activated

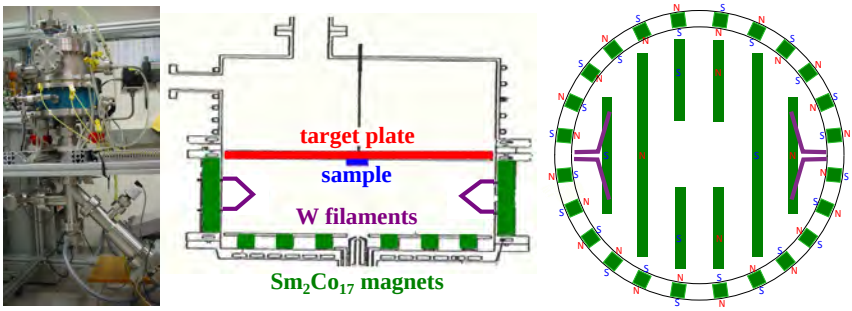

Figure 3.4: Schematic view of the VISIONI plasmatron

neutron irradiated samples. Together with the in-house facilities for neutron irradiation and post-mortem sample analysis this would allow us to study the synergistic effects of tritium loading of the sample, ITER relevant material mixing and neutron induced defects. Understanding this synergy is indispensable for making reliable predictions for the effects of plasma-material interaction on the inner reactor materials in next step fusion devices like ITER.

A comparison with other plasma simulators in the fusion community is shown in figure 3.5. It can be seen that the exposure conditions in VISIONI are very similar to the conditions expected at the ITER first wall, while other plasma simulators can go up to higher ion fluxes relevant for the ITER divertor. Within the Trilateral Euregio Cluster (TEC) there is now a strong focus on plasma-material interaction studies in such plasma simulators due to their flexibility in comparison with tokamaks [109]. In addition to MAGNUM-PSI at FOM in the Netherlands and PSI-2 at Forschungszentrum Jülich in Germany, the new JULE-PSI is now being built at Forschungszentrum Jülich and will be able to operate with beryllium and neutron activated materials. There are several other plasma simulators spread around different laboratories all over the world such as PISCES-B in the US and NAGDIS-II in Japan [110].

3.2.2 Filament driven DC discharge

Figure 3.4 shows the core of VISIONI formed by a vertically mounted cylinder with 29 cm outer diameter, 25 cm inner diameter and 40 cm height. An insulating Al_2O_3 ring and the target plate at a height of 9.1 cm divide the cylinder in two parts. The top part contains the electrical connections and the feedthroughs of the conditioning and cooling system. The bottom part is the actual plasma chamber. The schematic views in figure 3.4 indicate the main parts of the plasma chamber. The bottom and side wall are made of

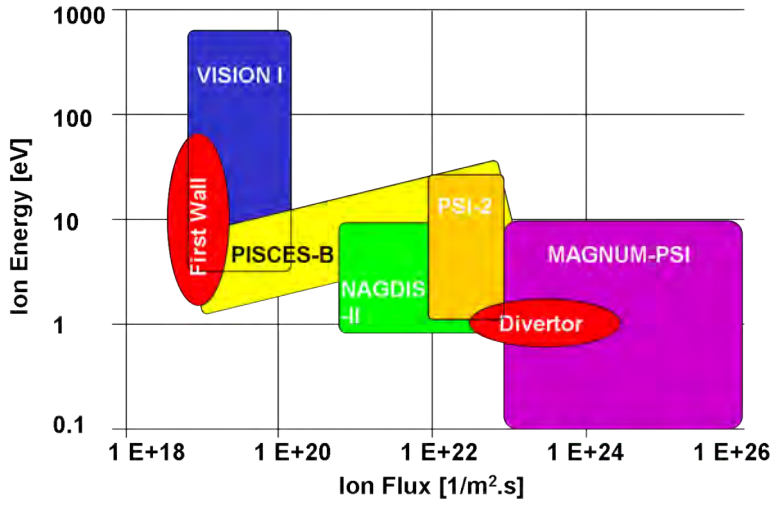

Figure 3.5: Comparison of VISIONI with other plasma simulators [108]

SS304 stainless steel. The target plate at the top is made of SS316 stainless steel. The whole chamber wall is actively cooled by means of a cooling fluid circuit. Two pairs of triangularly shaped 1 mm diameter tungsten filaments are mounted opposite to each other at the side wall. The two filament power supply units allow circulating an electric current $I_f \leq 120$ A through the filaments with a potential difference $V_f \leq 12$ V. In this way the filaments can be heated Ohmically to a temperature $T_f \approx 2400$ K. This leads to thermionic emission of the primary electrons. The discharge power supply unit allows to bias the filaments negatively with respect to the plasma chamber bottom plate and side wall with a potential difference $V_{ac} \leq 250$ V. The negative pole of the discharge power supply unit is connected to the negative poles of the filament power supply units as indicated in figure 3.6. The primary electrons are then accelerated by the high voltage sheath around the filaments up to energies above the electron impact ionization threshold of the filling gas and initiate the discharge. Additionally also the target plate can be biased negatively with respect to the plasma chamber bottom plate and side wall with a potential difference $V_{at} \leq 400$ V. By choosing $V_{at} > V_{ac}$ the primary electrons are shielded from the target plate, while the ions are accelerated towards it by the high voltage sheath and presheath. As will be explained in 3.2.4 an exchangeable sample can be mounted at the centre of the target plate. The impact energy of the ions on the sample can be regulated by adapting the sample bias potential V_{st} with respect to the target plate.

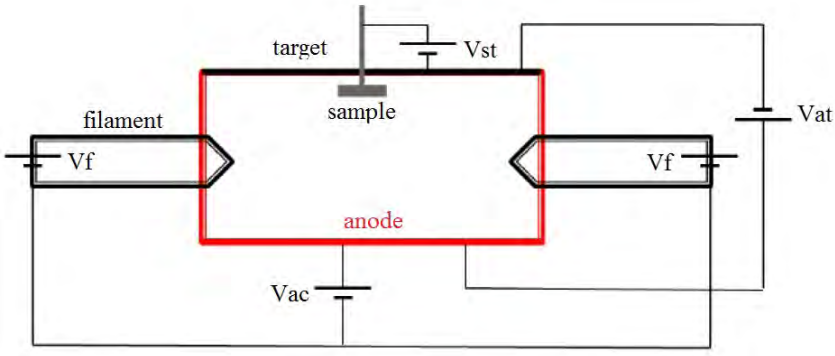

Figure 3.6: Electric circuit diagram of VISIONI

3.2.3 Multidipole magnetic field configuration

The bottom plate and side wall of the plasma chamber in VISIONI are lined by strong permanent magnets with alternating polarity. The positions of these magnets are shown in the side and top views of the plasma chamber in figure 3.4. Multidipole magnetic field configurations were first proposed and tested in the early seventies by Limpaecher and MacKenzie [111]. Presently it is a commonly used set-up for ion sources in ion beam litography, particle accelerators, ion implantation systems, proton therapy instruments and neutral beam injectors for tokamaks [112]. The magnetic field in VISIONI is about 0.2 T at the wall in front of the magnets, but decreases very rapidly towards the field free centre of the chamber as will be discussed in 6.1. The field lines are directed mainly parallel with the chamber wall. Only right in front of the magnets one has the so called cusps where the magnetic field lines intersect perpendicularly with the wall. These cusps are the major loss regions of charged particles because of the strongly inhibited perpendicular diffusion in a magnetic field, especially for electrons in a low density plasma with limited collisionality [30]. Even charged particles heading towards one of the cusps can be reflected back into the chamber by the magnetic mirroring force if they are outside of the loss cone as explained in 2.3.3. The presence of a multidipole magnetic field has two important effects.

- The plasma density is typically increased by two orders of magnitude. This is mainly due to better confinement of the ionizing primary electrons and in lesser amount due to the increased path length of gyrating ionizing primary electrons and better confinement of ions and secondary electrons [113].
- The plasma uniformity of the field free region in the centre is strongly enhanced. This has two reasons [114]. Firstly, the strongly inhibited

cross-field diffusion at the vessel walls leads to steepening of the density gradient at the plasma edge. Secondly, also ionization is localized at the edge because the primary ionizing electrons are trapped by the local magnetic field lines around the filaments.

The volume of the uniform field free region can be increased by increasing the number of magnets. This leads, however, also to an increase of the loss area at the cusps and a corresponding decrease of the plasma density. Therefore, one has to make a compromise between plasma density and plasma volume.

All magnets in VISIONI are permanent Sm_2Co_{17} samarium-cobalt magnets. This compound consists of 2 parts of the rare earth element samarium and between 13 and 17 parts of a mixture of transition metal elements, mainly cobalt and in lesser amounts also iron and copper. Traces of zirconium and hafnium are added to enhance heat treatment response. Light rare earth elements such as samarium are strongly ferromagnetic due to the numerous unpaired electrons in the f-shell. The Curie temperature, which for pure rare earth elements is smaller than room temperature, can be increased significantly by compound formation with cobalt. Furthermore, the resulting compound is highly anisotropic. After neodymium magnets, samarium-cobalt magnets are the strongest rare earth magnets. The advantages of samarium-cobalt magnets over neodymium magnets are their higher coercivity and higher temperature ratings. The Curie temperature of samarium-cobalt is as high as 1100 K. Below this temperature the magnetic field is reduced only by about 3.5% for a 100 K temperature rise [115]. This is a very beneficial property in VISIONI because the walls can be heated significantly by the plasma and the radiation from the tungsten filaments, even with the active cooling. More detailed information on permanent magnets can be found in [116].

3.2.4 Sample holder

The samples exposed in VISIONI are placed in a special sample holder which is depicted schematically in figure 3.7. The sample is supported by a tungsten-lanthanum ring protruding 1 mm with respect to the surface of the sample. Tungsten was chosen because it is not expected to be sputtered by hydrogen or deuterium ions below 400 eV impact energy. The lanthanum was added because it strongly improves the machinability. The sample supported by the tungsten ring is electrically isolated from the target plate by a macor ring such that they can be biased with respect to each other. Macor is a machinable glass-ceramic made up of fluorphlogopite mica in a borosilicate glass matrix. It contains fluorine, oxygen, silicon, magnesium, aluminium, potassium and boron. It was chosen because of its good electrical and thermal isolation. The sample temperature can be controlled by means of the cold finger. An air cooled copper element is pressed onto

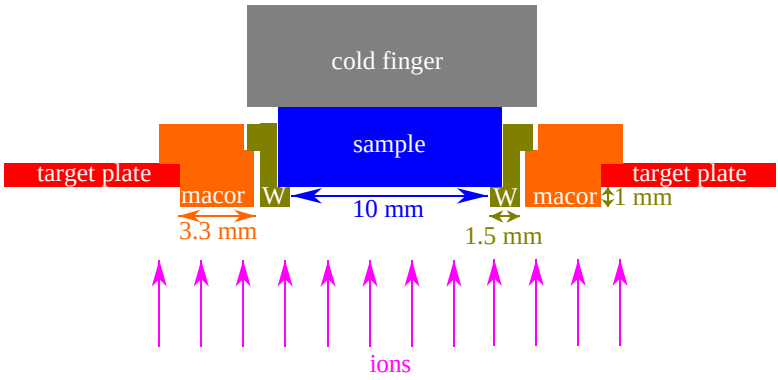

Figure 3.7: Schematic representation of the sample holder with the cold finger in VISIONI

the back of the sample with a force of about 100 N. A pyrolytic highly orientate graphite sheath with a thickness of 70 μm ensures good thermal coupling between the copper element and the sample. The sample temperature can be modified by tuning the gas flow rate through the cold finger. The sample temperature is measured by means of a thermocouple in the copper element 2 mm above the interface between the copper element and the pyrolytic graphite sheath.

3.2.5 Vacuum system

Figure 3.8 shows that the major part of VISIONI consists of a system of multiple oil free pumps to provide Ultra High Vacuum. The primary vacuum system is made up of a diaphragm pump coupled with a molecular drag pump and a turbo molecular pump with magnetic bearings. Ultra High Vacuum is provided by two getter pumps. These are effective in adsorbing impurities irreversibly, while hydrogen isotopes are pumped reversibly. The system is first brought at a base pressure of $10^{-6} - 10^{-5}$ Pa in order to limit impurities as much as possible. Afterwards the appropriate filling gas is injected up to a neutral gas pressure $p \approx O.3$ Pa by a combination of valves, pressure sensors and control units.

3.2.6 Diagnostics

3.2.6.1 Overview spectrometer

The AvaSpec-2048-USB2 compact overview spectrometer from Avantes is used in this work to study the light emission from the plasma and the tungsten filaments. The spectrometer can observe in the range 250-770 nm

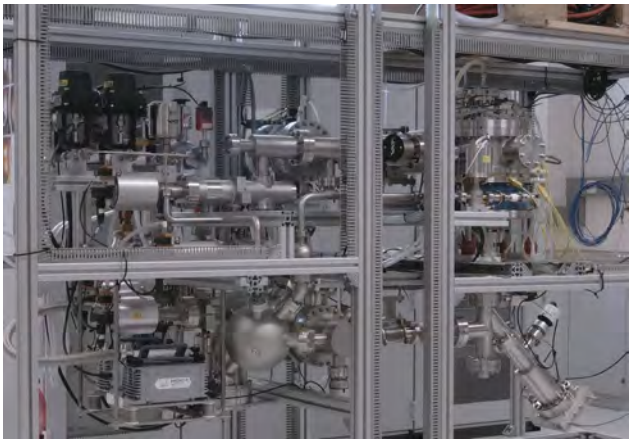

Figure 3.8: VISIONI plasmatron and its vacuum system

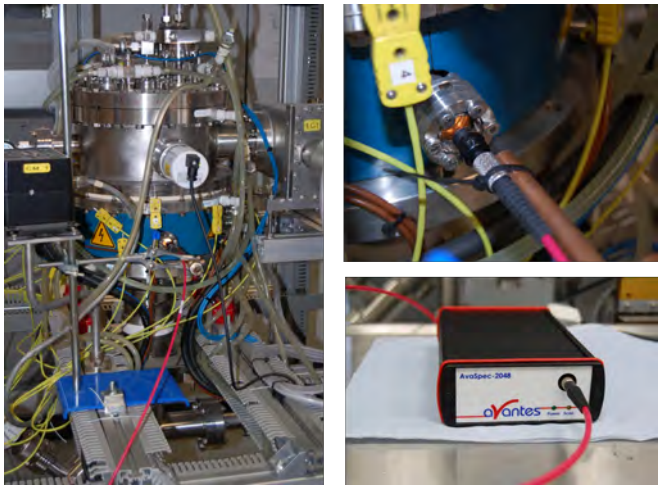

Figure 3.9: Experimental setup for the spectroscopic measurements in VISIONI

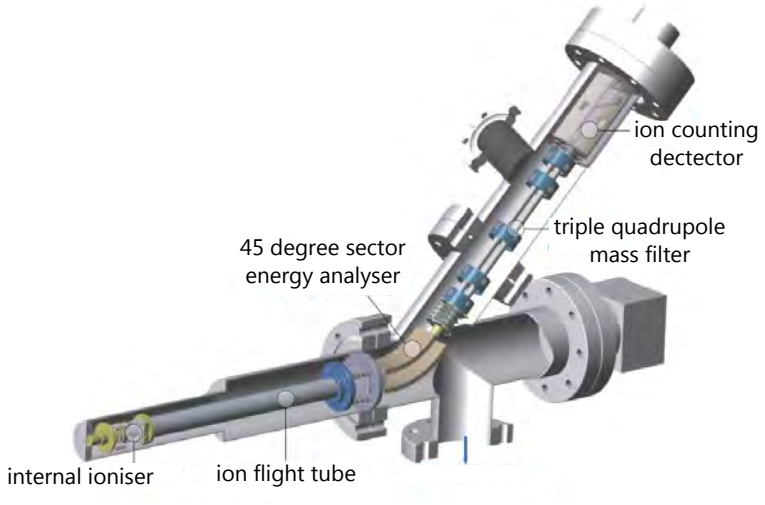

Figure 3.10: Scheme of the mass and energy analyzer at the VISIONI bottom plate [117]

with a spectral resolution of 0.1 nm. As shown in figure 3.9 the spectrometer is coupled with the plasma chamber by means of an optical fiber with a lens in front of the kodial glass window at the side of the vessel. A relative intensity calibration for the spectrometer-fiber-lens system was performed using an Oriel calibration source for the wavelength range 250-900 nm. The window has no effect on the relative calibration because the kodial glass transmission curve has a fairly constant plateau for the wavelength range 350-2000 nm.

3.2.6.2 Mass and energy analyzer

The Hiden Analytical EQP1000 [118] is coupled to VISIONI to perform mass and energy scans of ions and neutrals in the plasma with sub ppm detection. It can be seen in figure 3.4 installed below the plasma chamber. A schematic view of the device is shown in figure 3.10. The sampling orifice is located at the centre of the plasma chamber bottom plate. Behind the orifice an internal electron impact ionizer provides the possibility to analyse not only ions, but also neutrals. By tuning the energy of the ionizing electrons it is even possible to study the excitation state of the neutrals using appearance potential spectra. A 45 degree sector field energy analyser is followed by a triple quadrupole mass filter. This allows one to perform a mass scan for a certain energy or an energy scan for a certain mass.

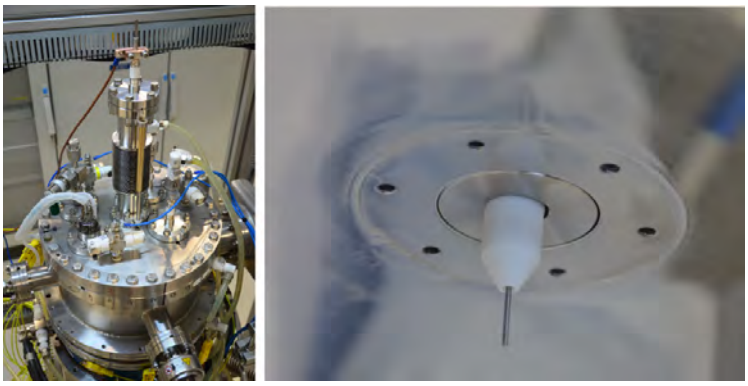

Figure 3.11: Insertion of a Langmuir probe through the VISIONI target plate

3.2.6.3 Langmuir probe

Due to the limited amount of diagnostics available in VISIONI and the need for decent characterization of the plasma, a movable Langmuir probe has been manufactured during this work. From a simple IV scan with such a probe one can estimate plasma parameters such as plasma density, plasma potential and electron energy distribution function. As shown in figure 3.11 the probe can be inserted through the centre of the target plate where normally the sample holder is installed. By means of a bellow one can perform a vertical scan along the central axis of the plasma chamber up to 3 cm above the bottom plate. During operation the probe is heated very rapidly, especially in the electron saturation regime. Therefore, a water cooled molybdenum pin is used. The pin with radius 0.5 mm is inserted into a ceramic tube to insulate it from the plasma except for an exposed length of 10.3 mm. At the end of the ceramic tube the edges are not in direct contact with the pin in order to avoid that the effective probe area would increase due to deposition of a conductive coating on the ceramic in contact with the pin.

3.2.7 Typical plasma parameters

Plasma physics is a very complex topic. It is almost never possible to perform exact calculations. It is important to have a good idea about the order of magnitude of the plasma parameters in order to be able to use the appropriate approximations in the calculations. The plasma parameters in VISIONI are determined by

- the temperature of the tungsten filaments $T_f \approx 2400$ K

Table 3.1: Some typical numbers for the VISIONI plasmatron

	hot electrons	**cold electrons**	**ions**	**neutrals**
T **[eV]**	20-25	1-2	0.025	0.025
n **[m^{-3}]**	10^{15}	10^{17}	10^{17}	10^{20}
λ_c **[cm]**	100	10	1	
τ_c **[s]**	10^{-7}	10^{-7}	10^{-7}	
R_{cycl} **[mm]**	$0.1 - 20$	$0.02 - 3$	$0.2 - 40$	
τ_{cycl} **[s]**	$10^{-10} - 10^{-8}$	$10^{-10} - 10^{-8}$	$10^{-7} - 10^{-5}$	

- the neutral gas pressure $p \approx 0.3$ Pa
- the discharge potential difference $V_{ac} \approx 80$ V

The limited variation of these operational parameters during a normal discharge, however, do not change the plasma parameters drastically. This subsection summarizes the order of magnitude of the most important numbers for a deuterium plasma in VISIONI. The elaborate justification of these numbers is given later in 6.3 based on analytical calculations, numerical simulations and measurements. Table 3.1 lists some important numbers used throughout this work.

The most commonly used parameters to characterize a plasma are the density and the energy distribution of the different plasma particles. For a deuterium plasma in VISIONI the neutrals are primarily molecules with a negligible fraction of atoms. The deuterium molecules are at room temperature and their density can simply be determined from the neutral gas pressure and the ideal gas law. The ionization degree during normal operation is below 0.1%. The electrons have a bi-Maxwellian energy distribution. The majority of the electrons belong to a cold population with a temperature of about 1-2 eV. A small fraction of about 1-2% of the electrons belong to a hot population with a temperature of about 20-25 eV. The ions are dominated by D_3^+ and D_2^+ with a negligible fraction of D^+ and D^-. The ion temperature is around room temperature due to the very inefficient energy transfer between light electrons and much more massive ions. But the energy of the ions can be of the order of 1 eV due to acceleration in the presheath of the negatively biased target plate. Ions hitting the target plate get an additional acceleration in the thin high voltage sheath close to the target plate. This leads to an increase of their energy with an amount $q_e V_{ac}$. The typical densities and temperatures of the different particles in VISIONI are summarized in table 3.1.

Several important length scales exist in a plasma. First of all one has the size of the plasma chamber. In VISIONI the plasma chamber is cylindrical with 25 cm diameter and 9.1 cm height. Another important length scale in a plasma is the Debye length L_D. This is the length scale over which the

quasi-neutrality of a plasma can be violated. The effect of an electric charge immersed in a plasma is limited to a few Debye lengths due to shielding by the charged plasma particles. The low voltage sheath at the side wall and bottom plate of the plasma chamber is, therefore, only a few Debye lengths thick. The high voltage sheaths around the target plate, the sample and the filaments have a larger thickness of about 15 Debye lengths, as can be calculated from equation (2.202). Using equation (2.15) and the values from table 3.1 one finds that for VISIONI

$$L_D \approx 0.02 - 0.10 \text{ mm} \tag{3.1}$$

The next important numbers are the collision mean free path λ_c and the corresponding collision time τ_c. In VISIONI collisions with neutrals dominate due to the low ionization degree. Therefore, λ_c and τ_c can be calculated from the neutral density and the collision cross sections and reaction rates as was explained in 2.3.4.5. The relevant cross section data can be found in [119], [120], [121], [122], [123] and [124]. The resulting values for λ_c and τ_c are summarized in table 3.1. The plasma in VISIONI is magnetized by the permanent samarium-cobalt magnets. The magnetization is characterized by the cyclotron or Larmor radius R_{cycl} and the associated cyclotron period τ_{cycl} that can be calculated according to the formulas in 2.3.3. Table 3.1 summarizes the typical values for R_{cycl} and τ_{cycl} for hot electrons, cold electrons and ions for the magnetic field range between 0.001 T in the central field free region and 0.2 T in the edge right in front of the pole of one of the samarium-cobalt magnets.

During exposure of a sample to the plasma the crucial parameters are the ion impact energy and the ion flux. The ion impact energy is determined by the potential difference between the sample and the plasma. The plasma is slightly positive with respect to the anode due to charging of the walls. However, this potential difference is of the order of the electron temperature and thus negligible with respect to the much higher potential difference V_{as} between the sample and the anode. Therefore, the ion impact energy is given in good approximation by $q_e V_{as}$ which is typically around 100 eV. The ion flux impinging on the sample can easily be determined from the measurement of the electric current collected by the sample. It can also be calculated based on the plasma parameters listed in table 3.1. According to the theory in 2.3.6 and 2.3.7 the ion velocity at the sheath edge is given by the Bohm velocity and the plasma density is decreased in the presheath by a factor of about 0.6. The ion flux is thus given by

$$\Phi_i \approx 0.6 n_e \sqrt{\frac{kT_e}{m_i}} \approx 10^{19} - 10^{20} \text{ ions/m}^2\text{s} \tag{3.2}$$

Chapter 4

Numerical tools

4.1 ERO material migration code

An important part of this work deals with modelling of material migration in fusion relevant devices with the ERO code. Modelling with ERO allows more detailed interpretation of the experimental results. The ERO code is briefly described in the first subsection. The next two subsections discuss the code developments in ERO performed during this work. Subsection 4.1.2 describes the update of the plasma-surface interaction database in ERO, while subsection 4.1.3 explains how a new version of ERO was developed for simulating material migration experiments in VISIONI.

4.1.1 Description of the code

The ERO code was developed to simulate erosion, transport and deposition of impurities in fusion relevant devices in 3D. The majority of the physical phenomena are simulated by means of a Monte Carlo algorithm in combination with an extensive database of the most recent atomic and molecular data for plasma chemistry and plasma-surface interaction. The code is well established and widely used within the fusion community. ERO development started already in 1993 to simulate material migration in JET [125]. Presently the default version is used to simulate material migration in TEXTOR [126]. By means of conditional compilation directives also versions for simulating material migration in JET [127], ITER [128], PISCES-B [129], [130], PILOT-PSI [131] and AUG [132] have been implemented in ERO.

Setting-up a simulation for a specific experiment requires input of the plasma-facing materials geometry and composition and routines for calculating plasma parameters such as plasma flow, electron temperature, ion temperature, electron density, ion density, impurity concentrations, electric field and magnetic field at any location inside the simulation volume.

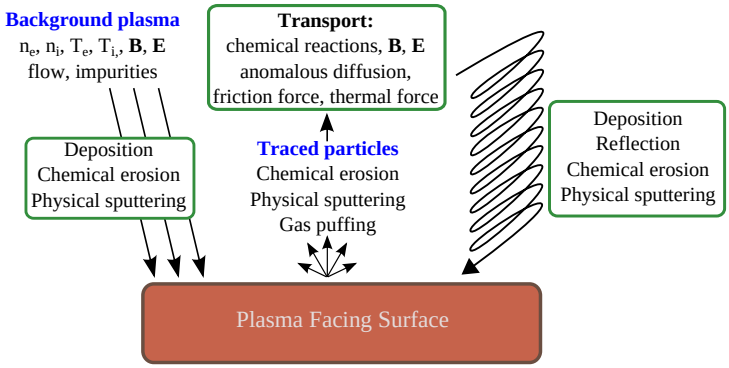

Figure 4.1: Scheme of the physics simulated by the ERO code

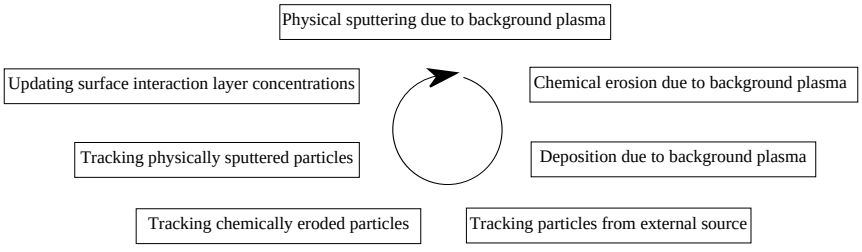

Figure 4.2: One time step in the ERO code

These routines can be based on an analytical model as was done for TEXTOR [126], on measurements as was done for PISCES-B [129] and PILOT-PSI [131] or on plasma simulations as was done for JET [127] and ITER [128]. It is implicitly assumed that these plasma parameters remain constant throughout the whole simulation. This means that ERO simulations are only appropriate in case the plasma is not significantly influenced by eroded or externally injected impurities.

During the simulation ERO keeps track of the time evolution of the plasma-facing materials surface composition. After each simulation time step the surface composition is updated. The composition is calculated on a user specified surface mesh by assuming that erosion and deposition occur in a homogeneous interaction layer with a user specified thickness. The simulation time step has to be chosen small enough such that the eroded fraction of the interaction layer is small.

The physics simulated by ERO is depicted schematically in figure 4.1. The work flow in ERO will now be discussed in more detail by following the code during one simulation time step Δt as shown also schematically in figure 4.2.

1. ERO calculates for each surface cell, for each plasma species and for each surface species the number of physically sputtered atoms N_{phys} according to

$$N_{phys} = cfS\Delta t \cos\beta \frac{n_e}{Z_{eff}} \sqrt{\frac{k(T_e + T_i)}{m}} < Y_{BY} > (T_i, T_e, Z) \quad (4.1)$$

   with c the concentration of the surface species, f the fraction the plasma species contributes to the total ion flux, S the surface cell area, β the angle between the magnetic field and the surface cell normal, Z_{eff} the average ion charge and m the mass of the plasma species. Y_{BY} is the Bohdansky-Yamamura sputtering yield or the recently implemented Eckstein sputtering yield averaged according to the Abramov approach. The yield is averaged over the angle and energy distributions of the impinging ions by assuming that the energy of the impinging plasma species can be described by a Maxwellian distribution with ion temperature T_i and a shift due to acceleration in the sheath potential drop depending on electron temperature T_e and the plasma species charge state Z [133]. The average sputtering yields were precalculated and stored in data files for different plasma species, charge states, surface species, ion temperatures and electron temperatures.

2. ERO calculates for each surface cell the number of chemically eroded carbon atoms N_{chem} by impact of hydrogen or oxygen ions from the

plasma according to

$$N_{chem} = cfS\Delta t \cos\beta \frac{n_e}{Z_{eff}} \sqrt{\frac{k(T_e + T_i)}{m}} Y_{chem} \tag{4.2}$$

This calculation is very similar to the one for physical sputtering in the first part. The only difference is the erosion yield. The chemical erosion yield Y_{chem} is usually a constant user defined value deduced from experiments. For hydrogen on carbon it is also possible to use the analytical model described in 2.4.3. Recently also chemical erosion of beryllium has been implemented in the code.

3. ERO calculates for each surface cell and for each plasma impurity ion the number of deposited ions N_{dep} according to

$$N_{dep} = fS\Delta t \cos\beta \frac{n_e}{Z_{eff}} \sqrt{\frac{k(T_e + T_i)}{m}} (1 - R) \tag{4.3}$$

with R the effective reflection probability. The reflection probabilities were precalculated with the TRIM binary collision code [62] and stored in data files for different plasma impurity ions, surface species, impact energies and impact angles. The effective reflection probability R is calculated by averaging over the different surface species and by using an appropriate mean impact angle and a mean impact energy taking into account the thermal energy of the ions and their acceleration in the presheath and the sheath.

4. In case an external impurity source injects impurity particles into the plasma with a certain rate R_{source} ERO tracks these particles. The number of simulation particles N_{sim} starting each time step Δt from the source is defined by the user. Typically the number of real particles injected per time step $N_{real} = R_{source}\Delta t$ is huge. Thus simulation particles are super-particles representing N_{real}/N_{sim} real particles. The distributions of the starting positions and starting velocities of the externally injected particles can be specified by the user. ERO allows to inject atoms, hydrocarbon molecules and recently also BeD has been implemented.

   The life of such a tracked particle is depicted schematically in figure 4.3. The motion of the particle is followed with a time step small enough to resolve the gyromotion in the magnetic field. For a neutral particle the trajectory is a straight line in between possible collisions with the neutral gas particles. Each time step it is checked whether a chemical reaction occurred due to electron or ion impact from the plasma. For atoms and atomic ions Maxwellianly averaged reaction rate coefficients are provided from the ADAS database [134] or according to the Lotz formula [135]. For hydrocarbon molecules and

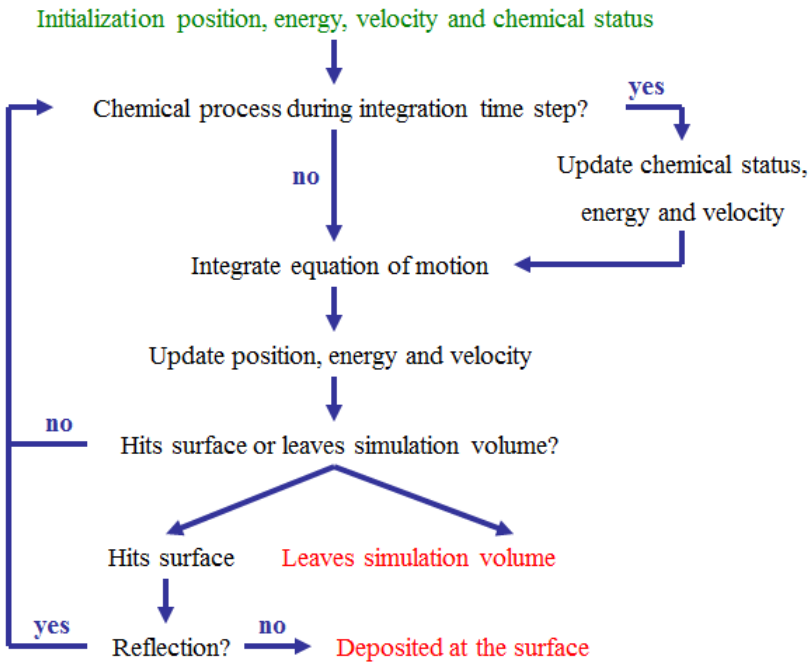

Figure 4.3: Life of a tracked particle in the ERO code

molecular ions the rate coefficients are provided from the HYDKIN database [136] described in [137]. If a reaction occurred the chemical status, the energy and the velocity of the particle are updated. ERO can also keep track of light emission due to tracked particles corresponding to specific transitions. This is calculated using photon emission rate coefficients which are also provided from the ADAS database for atoms and the HYDKIN database for molecules.

Once the tracked particle is ionized its trajectory deviates from a straight line due to electric and magnetic fields. Cyclotron motion around the magnetic field lines, acceleration along the magnetic field lines and perpendicular drifts are implicitly taken into account by integrating the equation of motion with the Boris-Leapfrog particle pusher with an integration time step sufficiently small in comparison with the cyclotron time. Anomalous diffusion perpendicular to the magnetic field can be taken into account by specifying a perpendicular diffusion coefficient or by using the Bohm diffusion coefficient. Also a friction force due to the plasma flow is taken into account by means of the Focker-Planck method based on Spitzer relaxation times.

This method results from solving the Boltzmann equation with the Coulomb collision term. ERO also includes higher order effects of the friction force by considering a thermal force due to gradients in electron and ion temperature. The position, energy and velocity of the particle are updated each integration time step.

After each integration time step it is checked whether the particle has hit the surface of the plasma-facing materials. If the particle hits the surface it can be either reflected or deposited. As the impact angle and impact energy of a particle is known the reflection probability for atoms and atomic ions can easily be interpolated from the precalculated TRIM data. Reflected atoms and atomic ions are re-emitted as neutrals with an angle and energy sampled from the appropriate distributions as precalculated also with TRIM. They are then tracked further. For molecules and molecular ions the reflection probability and the angle distributions, energy distributions and chemical status of reflected species have to be specified by the user. These data should be based on experimental findings or MD simulations. Deposited particles are no longer tracked. If a tracked particle hits the surface it can also lead to physical sputtering. The number of sputtered particles can easily be calculated using the Bohdansky-Yamamura or Eckstein formula. Particles can also leave the simulation volume. They are then no longer tracked. Therefore, the simulation volume should be large enough such that tracked particles leaving the volume have negligible chance of coming back to the surface of the plasma-facing materials.

5. ERO tracks for each surface cell the particles physically sputtered by the plasma ions during this simulation time step and by the tracked particles in the previous simulation time step. The number of simulation particles released per surface cell is specified by the user. The particles are released as neutrals with a Thompson energy distribution around the surface binding energy and a cosine angle distribution around the surface cell normal. They are tracked as described above.

6. ERO tracks for each surface cell the methane molecules chemically eroded by the plasma hydrogen ions during this simulation time step. The number of simulation particles released per surface cell is specified by the user. The particles are released with a Maxwellian energy distribution for the surface temperature and a cosine angle distribution around the surface cell normal. They are tracked as described above.

7. Before going to the next simulation time step the concentrations of the interaction layer are updated for all surface cells by taking into account physically sputtered, chemically eroded and deposited particles.

Presently it is also possible to use a coupled version of ERO with the

SDTrimSP binary collision code to treat reflection, deposition and physical sputtering in a more realistic way [138]. Coupling ERO with a MD code would be even more realistic. Unfortunately this is computationally too demanding [139]. An alternative is of course using MD databases in ERO instead of the TRIM databases. However, presently only limited data are available.

During ERO simulations a lot of output is generated. Most important are the 2D erosion/deposition and 3D light emission patterns because they can directly be compared with experimental results. With ERO it is also possible to separate the effects of different phenomena such as prompt redeposition of eroded particles, chemical erosion, physical erosion, tracked particle effects and plasma effects. This is information that cannot easily be obtained experimentally. It can be used to improve our understanding of the complex interplay of different material migration processes.

4.1.2 Updated plasma-surface interaction database

During this work the plasma-surface interaction database in ERO was updated. As will be explained in chapter 5 the aim was to check whether this improved model would be able to explain the need for enhanced reerosion of redeposited particles in previous ERO studies of the roof-limiter methane injection experiments in TEXTOR. The improved model involves three main changes and a few minor corrections which are discussed below.

4.1.2.1 Erosion due to hydrogen from injected methane

An important class of experiments simulated with ERO involves injection of methane from an external source into the plasma. The injected methane gives rise to different hydrogenic species by dissociation under influence of electron and proton impact in the plasma. In the past ERO did not track these hydrogenic species. However, chemical erosion and physical sputtering of the plasma-facing materials by these hydrogenic species can be significant. Therefore, tracking of hydrogenic species has been implemented in ERO.

The processes taken into account for usual tracked particles are now also taken into account for the hydrogenic species. Electron impact reaction rates for hydrogen molecules were taken from the HYDKIN database [136]. Proton impact reactions were found to be negligible for the conditions in the TEXTOR scrape-off layer. The values for kinetic energy release ΔE_{kin} during the different dissociative reactions were taken from [140]. Each of the dissociation products gets hereby an additional kinetic energy E_i depending on its mass m_i according to

$$E_i = \frac{\mu}{m_i} \Delta E \tag{4.4}$$

with μ the reduced mass of the dissociation products which can be calculated as

$$\frac{1}{\mu} = \sum_{i=1}^{N} \frac{1}{m_i} \tag{4.5}$$

The dissociation products are emitted in a random direction uniformly distributed over a sphere. The ionization and Balmer line emission rate coefficients were taken from the ADAS database [134]. Reflection probabilities for hydrogen atoms and atomic ions were calculated as function of impact angle and impact energy with the TRIM binary collision code [62]. The molecular hydrogen reflection probabilities are discussed in 4.1.2.3. In addition to the physical sputtering, which is covered in 4.1.2.2, carbon can also be chemically eroded by hydrogen. This process is, however, very complex and as explained in 2.4.3 depends on a variety of parameters such as surface temperature, surface composition, impact angle, impact energy and flux. It is very difficult to take into account all these dependencies correctly and, therefore, a simplified model has been used. H, H^+, H_2 and H_2^+ are assumed to cause chemical erosion of carbon with a constant yield of 2%. This is a typical value observed for chemical erosion by hydrogen ions by means of light emission spectroscopy during similar Ohmic TEXTOR discharges with surface temperature of the roof limiter around 250^{o}C, ion impact energy around 250 eV and ion flux around 10^{18} ions/cm^{2}s. These TEXTOR experiments also showed that deposited amorphous hydrocarbon layers typically contain about 50% of hydrogen. Therefore, the hydrogen in excess of 50% is released thermally as hydrogen molecules.

4.1.2.2 New Eckstein formula for physical sputtering

In the past physical sputtering yields for the background plasma and tracked particles were calculated in ERO with the Bohdansky-Yamamura formula. However, as discussed in 2.4.2 this formula performs badly around the threshold energy and for self-sputtering. Therefore, the more realistic Eckstein fitting formulas (2.236) and (2.241) for the energy and angle dependence of the sputtering yield have been implemented in ERO. However, in ERO the formulas are used with fitting parameter values different from the values listed in [58]. The presence of hydrogen in the surface layer has an influence on the physical sputtering yield. Therefore, the Eckstein formulas have been fitted to SDTrimSP simulation results for a carbon surface with 50% hydrogen content. In these simulations the carbon surface binding energy was kept unchanged at the value of 7.4 eV, while for hydrogen a surface binding energy of 1 eV was assumed. The Eckstein formulas are used directly for tracked species in ERO. For CH_x and CH_x^+ the bounded hydrogen atoms are neglected and the same formulas as for carbon are used. For hydrogen molecules the fitting formula for the hydrogen sputtering yield

is used. It is sufficiently realistic to assume that the yield of H_2 is the same as that of two hydrogen atoms with half of the H_2 energy as was discussed in 2.4.2. For the background plasma, the sputtering yields were averaged over the angle and energy distributions of the plasma ions. These distributions were determined with ERO. As usually background species are not followed in ERO, special ERO runs have been performed with injection of background species into the plasma. The species were followed up to arrival at the limiter surface. This is a more realistic approach than the Abramov averaging used before.

4.1.2.3 Tichmann MD hydrocarbon sticking probabilities

Reflection of atoms and atomic ions is treated in ERO according to precalculated data from TRIM binary collision simulations. This approach cannot be used for molecular species because chemical effects are not taken into account in TRIM. Due to the lack of relevant experimental or modelling data, the ERO approach used to be very simplified. The molecular reflection probabilities were constant and defined by means of an input parameter. Usually, for neutral hydrocarbons total reflection was assumed. Ions typically had a smaller reflection probability of 0.1. Considering their acceleration by the sheath potential, they penetrate deeper into the surface and have smaller chance of escape. However, variations of these reflection coefficients also have been studied.

As discussed in 2.4.7 new MD results were published recently by Tichmann [92] and Ohya [80] for hydrocarbons impinging on amorphous hydrocarbon layers. The very convenient formulas from Tichmann were implemented in ERO to calculate the reflection probability of tracked hydrocarbons as function of their impact angle and energy. The Tichmann formulas are also used for carbon atoms and ions because MD simulations are assumed to be more realistic than BCA simulations for energies below 100 eV which are typical for tracked particles in ERO for TEXTOR and VISIONI. The studies performed by Tichmann were in the impact energy range between 5 and 100 eV. The studies performed by Ohya were only at normal incidence, but for impact energies as low as 0.01 eV. Therefore, for impact energies below 5 eV the reflection probability is interpolated from the Ohya data and multiplied with the angular dependence factor from Tichmann for an impact energy of 5 eV. For hydrogen molecules the former assumption of reflection probability 1 for neutrals and 0.1 for ions is still used due to lack of relevant data.

4.1.2.4 Some minor corrections

Apart from the main improvements described above, some minor corrections have been applied in ERO. Before, tracked particles were always released from the surface starting at the centre of a surface cell. Now reflected

particles start from the exact location where they hit the surface. Externally injected particles start uniformly distributed over the surface of the injection hole. Sputtered particles start uniformly distributed over the whole surface cell. Before, externally injected particles could be emitted directly into the surface. They are emitted according to a cosine distribution centred around the injection direction. If the injection direction does not correspond with the surface normal, as for the TEXTOR roof limiter experiment, this leads to particles hitting the surface immediately upon release. This is now avoided by sampling a new velocity for such particles until they are no longer emitted directly into the surface. Before, particles returning to the surface at the location of the injection hole were either reflected or deposited. Now they are re-injected into the plasma as a neutral with a velocity sampled from a Maxwellian with a cosine angle distribution centred around the injection direction.

4.1.3 ERO-VISIONI

During this work a new version of ERO was developed to simulate the experimental campaign in VISIONI discussed in 7.3 during which graphite samples biased at -80 V with respect to the side and bottom of the plasma chamber were exposed to a deuterium plasma with simultaneous injection of trace amounts of $^{13}CH_4$. The first important change in ERO was of course the geometry. The target plate and the graphite sample in the centre are represented by a disc as this is one of the standard geometries that can be specified in the ERO parameter file. The composition of the stainless steel target plate is taken to be pure iron, while the graphite sample is taken to be pure carbon. The protruding macor and tungsten-lanthanum rings of the sample holder are not taken into account. Tracked particles can also be reflected or deposited on the side wall and bottom plate of the VISIONI plasma chamber. For hydrocarbon molecules and carbon the Tichmann sticking probabilities discussed in 4.1.2.3 are used as the side and bottom in VISIONI are observed to be net deposition areas where amorphous hydrocarbon layers are formed due to the magnetic field shielding these walls from the impinging ions. Re-erosion of species deposited on the side wall or bottom plate is not taken into account as this would require a more sophisticated surface mesh and a drastic increase of the needed CPU time. Furthermore, re-erosion from the side wall and bottom plate is not expected to be an important effect because ions can only hit the side wall and bottom plate at the poles of the permanent magnets and their energy is typically only a few electron volts. Impinging neutrals also do not lead to erosion because the surface temperature of the walls of about 310 K is too low for thermally activated chemical erosion. The external source for the injection of $^{13}CH_4$ is located at the side window 90^o rotated with respect to the tungsten filaments at 4.1 cm above the bottom plate.

Another important change in ERO considers the spatial dependence of

the electromagnetic field. The magnetic field of VISIONI is read from a data file with magnetic field values precalculated according to the analytical equations deduced in 6.1. This approach drastically reduces the needed CPU time in comparison with direct use of the analytical equations. The electric field in VISIONI could be characterized only with limited precision as discussed in 6.3.4.4. The Langmuir probe measurements along the central axis of the plasma chamber showed that the electric potential increases about 1 eV from the sheath edge at the target plate towards the centre of the plasma chamber. The plasma simulations with the VMCPT code could not be used to calculate the electric field self-consistently. The simulations only indicated that the sheath potential drop at the side and bottom of the plasma chamber is of the order of 2.5 eV. Therefore, only a simplified electric field spatial dependence could be implemented in ERO. The presheath caused by the strongly negatively biased target plate is approximated by the 1D profile of equation (2.199) with a potential drop of 1 eV and a width of 5 cm in accordance with the Langmuir probe measurements. The sheath at the target plate is approximated by the Child-Langmuir sheath in equation (2.201) with a potential drop of 82.5 eV in accordance with the VMCPT simulations. So the electric field in ERO only has a vertical component.

The spatial dependence of the plasma parameters had to be adapted as well. The spatial dependencies of the plasma density, the ion flux on the target plate and the electron energy distribution function were calculated with the VMCPT code as will be explained in 6.3.4. The calculated values were stored in data files and are read from these files when starting an ERO simulation. As explained in 6.3.2 the electron energy distribution function in VISIONI is not Maxwellian but bi-Maxwellian with a cold and a hot electron population. Therefore, the reactions probabilities in ERO are calculated for VISIONI by taking the weighted average of the Maxwellian rate coefficients for the cold and the hot electron population. As the ions in VISIONI are not heated the ion temperature was taken equal to room temperature.

The ion flux on the target plate read from the data file is used directly to calculate the amount of particles sputtered, reflected and deposited at each surface cell of the target plate and the sample. As explained in 6.3.3 for standard operating conditions the ions are dominated by D_3^+ ions. For carbon the physical sputtering yield is calculated according to the Abramov averaged Eckstein sputtering yield as before assuming that the yield for a D_3^+ ion with energy E is equal to three times the yield for a D^+ ion with energy $E/3$. The chemical sputtering yield per impinging D_3^+ ion was taken to be equal to 0.14 which corresponds to the average value deduced from the experimental campaign presented in 7.2 when the target and the sample are biased negatively with respect to the side and bottom of the plasma chamber with a potential difference of 80 V. This value takes into account the observed enhancement of the chemical sputtering which is probably caused by molecular ion effects. Sputtering of the iron from the target plate

is not taken into account as the impact energy per deuteron of about 30 eV is too low to cause significant sputtering of iron.

Due to the low ionization degree and the low plasma density in VISIONI other processes are important in comparison with TEXTOR. It is important for VISIONI to include also recombination of tracked ions and collisions of tracked species with the neutral gas. These processes were already implemented in ERO for other devices and simply had to be switched on in the parameter file. The friction force experienced by the tracked ions was not taken into account because the spatial dependence of the ion flow velocity is not accurately known in VISIONI. However, as the plasma density in VISIONI is very low, this is not expected to be an important effect. Finally, tracked species hitting the target plate can be lost through a 1 mm gap at the edge of the target plate. This takes into account the neutral gas flow along the edge of the target plate in VISIONI which leads to continuous refreshing of the neutral gas.

4.2 VMCPT code

The VISIONI plasma simulator was described in detail in 3.2. The limited amount of diagnostics available in the device could not provide all plasma properties required as input for the new version of the ERO code for VISIONI. Therefore, it was decided to develop a plasma simulation code to simulate hydrogen plasmas in VISIONI in detail. The first subsection discusses the choice of the most appropriate simulation technique for VISIONI. The details of the code are explained in the subsequent subsections. More technical details concerning compiling and running of the code and a short description of the different parts are given in appendix F.

4.2.1 Simulation technique

The most commonly used plasma simulation techniques were introduced in 2.3.2. It was shown that fluid simulations are very convenient to obtain spatially resolved information on plasma composition, plasma density and self-consistent electromagnetic field. Fluid simulations require certain assumptions for the velocity distributions of the plasma species in order to close the infinite series of moments of the Boltzmann equation. However, the collisionality between the charged particles in VISIONI is limited due to the low ionization degree of about 0.1%. Thus it is expected that the velocity distributions are far from Maxwellian. Furthermore, the applied electric fields are rather strong. Therefore, it is important to include non-equilibrium effects. Fluid simulations are thus ruled out for VISIONI.

Non-equilibrium effects can be taken into account with PIC-MCC simulations. In VISIONI the presence of the primary electron emitting tungsten filaments and the magnets break the cylindrical symmetry of the plasma

chamber. Hence, 3D simulations are necessary. Unfortunately, in the framework of this work it was not possible to develop a 3D PIC-MCC code for the scale of VISIONI. This is computationally extremely demanding and, if even possible, requires the development of a very sophisticated massively parallelized PIC-MCC code and the use of a very powerful supercomputer. The bottleneck is the self-consistent calculation of the electric field on a 3D grid resolving the Debye length of about 0.1 mm in VISIONI. This requires solving Poisson's equation every time step on a grid with about 10^9 grid points.

It was decided to develop a Monte Carlo charged particle tracking code without self-consistent calculation of the electromagnetic field. The code was named VMCPT, which stands for VISIONI Monte Carlo Charged Particle Tracker. The simulation scheme is shown in figure 4.4. It is based on that of PIC-MCC in figure 2.10, but the time consuming self-consistent electromagnetic field calculation step is eliminated by using approximations for the electromagnetic field as will be explained in detail below. The simulation starts with a uniform, time-independent neutral fluid with a Maxwellian energy distribution. Then a loop is iterated each time step until steady state is reached. The loop has four parts. Firstly, the heated tungsten filaments thermionically emit new electrons. These energetic primary electrons drive the discharge by electron impact ionization. Next, the equation of motion is integrated for all charged particles and their positions and velocities are updated. The charged particle motion is determined by the electromagnetic field. Collisions with the wall are treated using the Monte Carlo method. Charged particles hitting the wall are either absorbed or reflected and can lead to the emission of secondary electrons. This is an important sink and source of charged particles. Finally, the charged particles are allowed to collide with each other and with the neutrals by means of a Monte Carlo scheme. Particles can be created or destroyed and the change in energy and velocity is taken into account. For the generation of pseudo-random numbers in the Monte Carlo algorithms the code makes use of the RANLUX library [141]. The most important aspects of the VMCPT code will be elaborated in more detail in the next subsections.

Similar Monte Carlo codes have been developed for other filament driven multicusp discharges [142], [143], [144]. There are also several reports on global model simulations with a finite difference electron Boltzmann solver for the electron energy distribution function [23], [145], [146], [147]. Such simulations are often used to study negative hydrogen production. In that case a global model is perfect because a lot of chemical reactions and vibrationally excited species have to be taken into account. However, in VISIONI negative hydrogen is not important. Furthermore, a global model cannot explicitly take into account electromagnetic fields and does not provide spatial information. Therefore, a Monte Carlo charged particle tracker was considered to be the best option for this work.

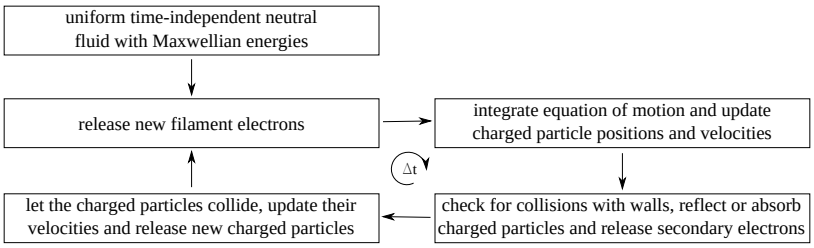

Figure 4.4: Basic steps of the VISIONI Monte Carlo charged particle tracker code

4.2.2 Charged particle tracking

A hydrogen plasma can generally contain electrons, H^+, H_2^+, H_3^+, H^-, H_2 and H. Electrons, H_2^+ and H_3^+ are tracked particles in VMCPT. As explained in 6.3.3 H^+ and H^- are not important in VISIONI. Therefore, they are usually not tracked. If desired H^+ can be tracked. For H^- this is not possible because it requires taking into account a lot of additional reactions and vibrationally excited species which are not implemented in the code. Neutrals are very important in VISIONI due to the low ionization degree of about 0.1%. It is, however, not needed to track the neutrals. It is realistic to treat the neutral gas as an unchangeable uniformly distributed background fluid with a Maxwellian energy distribution. The temperature of the gas can be adapted in the input file and is usually taken to be equal to the ambient temperature. The neutral density decrease due to ionization and the fraction of excited neutrals are negligible because of the low ionization degree. As explained in 6.3.3 the dissociation degree of the H_2 gas is very low and the presence of H can also be neglected. H atoms are, therefore, only taken into account in case H^+ tracking is activated. The main sources of H atoms [148] are then taken into account: dissociative recombination of H_3^+ impinging on the wall [149], thermal dissociation of H_2 impinging on the hot surface of the tungsten filaments with a probability around 20-30% [150] and electron impact dissociation of H_2 by excitation to the dissociative $b^3\Sigma_u^+$ state or one of the higher triplet states followed by radiative decay to the $b^3\Sigma_u^+$ state as will be explained in 4.2.6.1. Also the main loss of H atoms [148] is taken into account: recombination at the stainless steel walls of the plasma chamber with a probability of about 10% [151].

4.2.3 Thermionic primary electron emission

For the thermionic emission of primary electrons from the heated tungsten filaments one has to specify in the input file the filament heating current I_f, the discharge potential difference V_{ac}, the potential drop over one

filament V_f, the primary electron emission rate R_{pe} and the number of super-electrons emitted per time step in the simulation N_{es}. The filament temperature T_f is then calculated by the code according to the empirical relation

$$T_f = 862.64 + 16.87 I_f \tag{4.6}$$

from a linear fit to pyrometer measurements in VISIONI in the absence of plasma. In principle R_{pe} can also be calculated from the Richardson-Dushman equation (2.225). However, this equation has an exponential dependence on T_f and the work function of the filament surface E_W, two parameters that are known only with a limited precision. T_f can significantly deviate from the empirical relation (4.6) measured in vacuum due to the additional discharge current extracted by the negative lead of the filaments during plasma operation [152]. Also E_W can deviate from the theoretical value of about 4.55 eV for pure polycrystalline tungsten due to the possible presence of absorbants. Therefore, it was decided to specify R_{pe} as an independent parameter in the input file. The primary electrons are tracked in VMCPT as super-particles. The weight of one super-particle is determined by R_{pe}, N_{es} and the length of the time step.

The starting position $\vec{r}$ and velocity $\vec{v}$ of an emitted primary electron are determined with a Monte Carlo algorithm. $\vec{r}$ is picked from a uniform distribution over the surface of the filaments. It is explained in 2.4.1 that $\vec{v}$ is distributed in good approximation according to a Maxwellian distribution with temperature T_f. As discussed in 2.3.1 this is equivalent to picking three orthogonal velocity components independently from each other from a Gaussian distribution with mean zero and standard deviation $\sqrt{kT_f/m_e}$. The velocity component normal to the filament surface v_n has a lower limit $\sqrt{2E_W/m_e}$ in order to guarantee that the electron can overcome the surface potential barrier. Lower velocities can efficiently be rejected with the Marsaglia algorithm as discussed in appendix E.6. To take into account the energy lost by surmounting the surface potential energy barrier with height E_W and the energy gained due to acceleration in the sheath potential drop around the tungsten filament v_n is immediately increased with a value dv_n according to the relation

$$\frac{1}{2} m_e (\vec{v} + dv_n \vec{e}_n)^2 = \frac{1}{2} m_e \vec{v}^2 - E_W + q_e (V_{ac} - f V_f) \tag{4.7}$$

Here $\vec{e}_n$ is the unit vector normal to the filament surface. The sheath potential drop is taken to be equal to the discharge potential V_{ac} diminished by a fraction f of the potential drop over the filament V_f. This fraction f depends on the exact starting location of the considered electron. It increases linearly with the distance from the end of the negative lead of the filament from 0 up to 1.

4.2.4 Electromagnetic field

Calculating the electromagnetic field in VISIONI self-consistently is computationally too demanding as was explained in 4.2.1. Therefore, the fields in VMCPT are predefined. For the magnetic field this does not involve drastic approximations. The magnetic field created by the permanent samarium-cobalt magnets was calculated analytically and verified by means of Hall probe measurements as explained in 6.1. The magnetic field due to the heating current I_f running through the tungsten filaments was calculated analytically as well. The magnitude of this field is proportional to the value of I_f specified in the input file. The magnetic field created by the currents due to the charged particles in the low density plasma of VISIONI is much weaker. The plasma current integrated over the whole target plate typically sums up to about 2 A, while the current through the 1 mm diameter tungsten filaments is usually around 80 A. The calculations and measurements in 6.1 will show that the permanent samarium-cobalt magnets have an equivalent surface current density of about 10^6 A/m. Therefore, the magnetic field induced by the weak plasma currents can safely be neglected with respect to the magnetic field of the tungsten filaments and the permanent samarium-cobalt magnets. The code has two options to calculate the magnetic field. The first option is to calculate the magnetic field at runtime using the equations derived in 6.1.1. The second option is to interpolate the magnetic field from a 3D grid. A grid spacing of 0.9 mm was chosen as a compromise between precision and CPU time. The magnetic field values on this grid are read at the beginning of the simulation from a data file containing precalculated magnetic field values. This method is less precise due to the finite grid spacing, but it leads to a drastic reduction of the CPU time.

For the electric field the situation is more complicated. In the absence of the plasma it is rather straightforward to calculate the electric field with for instance a finite difference calculation as shown in 6.2. However, the space charge effects in a plasma modify the electric potential completely. This was explained in detail in 2.3.6. The potential in the core of the plasma is slightly above the anode potential and the majority of the potential variation is concentrated in very thin sheath layers with a thickness of less than 1 mm at the filaments, the target plate and the anode surfaces. The potential variation in the bulk plasma is only of the order of kT_e/q_e, typically a few volts. So, the electric field in the bulk plasma is much weaker than the electric field in the sheath layers. Therefore, it was decided to take into account only the sheath potential drops in VMCPT. The magnitude of the potential drops at the negatively biased filaments and target plate are taken to be equal to respectively the potential difference V_{ac} between the anode and the filaments and the potential difference V_{at} between the anode and the target, both specified in the input file. The potential drop at the anode is calculated self-consistently by a feedback mechanism ensuring global quasi-

neutrality of the plasma. All sheaths are assumed to be infinitely thin. Primary electrons emitted by the filaments are accelerated instantaneously by the electric field in the sheath as explained in 4.2.3. Electrons hitting the anode are reflected if their kinetic energy along the surface normal is too low to overcome the potential energy barrier of the anode sheath layer. Electrons hitting the filaments or the target plate are all reflected because the amount of electrons having enough energy to overcome the large potential barrier of the filament or target plate sheath layers is negligible. Reflection in the sheath layer is simply implemented by reverting the electron velocity component along the surface normal.

What is the effect of neglecting the bulk electric field in VMCPT on the simulation results? The bulk electric field is expected to be rather weak due to the shielding effect of the plasma as was confirmed by the plasma potential profile measured along the central axis of the plasma chamber with the Langmuir probe which is shown in figure 6.32. The plasma potential varies over only a few volts. Therefore, the effect of the bulk electric field on the primary electrons with an energy of tens of electronvolts is not expected to be significant and the simulated trajectories of the primary electrons will not deviate strongly from the real trajectories.

However, the bulk electric field has an important effect on the ions which are created by ionization of the neutral gas with an energy of about 0.025 eV only. As discussed in 2.3.6 they are accelerated significantly in the presheath electric field such that they reach the Bohm velocity at the edge of the sheaths surrounding the plasma chamber walls. Hence, the bulk electric field strongly enhances the wall losses of the ions which significantly reduces the equilibration time of the plasma and has an important effect on the steady state plasma parameters as well. This was confirmed by the first test runs with VMCPT. Due to the absence of a bulk electric field the ions remained thermal and the equilibration time of the plasma was of the order of 1 ms. Furthermore, the plasma parameters simulated with VMCPT deviated significantly from the measured plasma parameters. The primary electron emission rate was fitted to reproduce the experimentally measured target current as will be discussed in 6.3.1. The electron temperature simulated in this way was too low, while the simulated plasma density was too high. This could be resolved by taking into account the acceleration of the ions by the bulk electric field artificially. Imposing a predefined electric field accelerating the ions towards the walls resulted in spurious ion density profiles because the effect of the plasma space charges on the electric field could not be taken into account. Therefore, it was decided to mimic the effect of the bulk electric field by giving the ions an initial energy of the order of the average electron temperature kT_e. It was found that an initial ion energy of $0.3kT_e$ gave the best agreement with measurements for standard operating conditions with a target current of 2 A, a discharge potential difference of 80 V and a neutral pressure of 0.3 Pa. This reduced the equilibration time by one order of magnitude. The obtained value of $0.3kT_e$ agrees well with

the expected presheath potential drop in a plasma of the order of kT_e.

The bulk electric field also has an important effect on the cold electrons produced by ionization, secondary electron production at the plasma chamber walls and energy degradation of primary electrons due to collisions. These electrons have an energy of only a few electronvolts and are thus significantly influenced by the bulk electric field. They are slowed down by the ambipolar electric field forcing them to diffuse at the same pace as the ions in order to guarantee local quasi-neutrality in the plasma as explained in 2.3.5. Global quasi-neutrality is guaranteed in VMCPT by the self-consistent sheath potential drop at the side and bottom of the plasma chamber. However, local quasi-neutrality is not assured as the absence of the bulk electric field leads to non-ambipolar diffusion. Hence, one cannot expect the cold electron density distribution simulated by VMCPT to correspond with reality. The simulated ion density will be much more representative as the massive slow ions can be considered as immobile with respect to the cold electrons which will adapt to the ion density by means of ambipolar diffusion to guarantee local quasi-neutrality of the plasma. Thus the simulated ion density distribution is expected to be close to the real ion and cold electron density distribution, while the simulated cold electron density distribution is expected to be unrealistic.

4.2.5 Charged particle movement

The motion of charged particles in an electromagnetic field is governed by the Newton-Lorentz equation of motion

$$m\frac{d^2\vec{r}}{dt^2} = q\left(\vec{E}(\vec{r}) + \vec{v}\times\vec{B}(\vec{r})\right) \tag{4.8}$$

This second order differential equation can easily be transformed into an equivalent set of first order differential equations

$$\begin{cases} \frac{d\vec{v}}{dt} &= \frac{q}{m}\left(\vec{E}(\vec{r}) + \vec{v}\times\vec{B}(\vec{r})\right) \\ \frac{d\vec{r}}{dt} &= \vec{v} \end{cases} \tag{4.9}$$

Numerical integration requires this set of differential equations to be approximated by a set of finite difference equations. The leapfrog algorithm is a commonly used second order finite difference method in plasma particle simulations [20]. It represents a good compromise between accuracy and computational effort, which is important due to the huge number of tracked particles in VMCPT. In the leapfrog algorithm the position $\vec{r}$ and the velocity $\vec{v}$ are discretized on staggered time grids. The position is defined on the integral time steps $n\Delta t$, while the velocity is defined on the half time steps $n\Delta t/2$. So the velocity of newly started particles has to be shifted back half a time step before starting the leapfrog algorithm. Then the velocity and

the position consequently jump over each other to proceed in time. Hence, the name leapfrog algorithm.

For the Newton-Lorentz equation of motion one gets the following set of finite difference equations with the leapfrog algorithm

$$\begin{cases} \frac{\vec{v}_{t+\Delta t/2}-\vec{v}_{t-\Delta t/2}}{\Delta t} & = \frac{q}{m}\left(\vec{E}(\vec{r}_t) + \frac{\vec{v}_{t+\Delta t/2}+\vec{v}_{t-\Delta t/2}}{2} \times \vec{B}(\vec{r}_t)\right) \\ \frac{\vec{r}_{t+\Delta t}-\vec{r}_t}{\Delta t} & = \vec{v}_{t+\Delta t/2} \end{cases} \tag{4.10}$$

where the time centred average velocity is used in the magnetic field term on the right hand side of the first equation. The second equation is straightforward to solve. The first equation, however, seems to require substantial computational effort because the new velocity appears not only on the left hand side of the equation but also in the vector product on the right hand side. Fortunately, with the Boris method [153] this equation can be solved very elegantly and efficiently.

Firstly, the electric field can be eliminated from the equation by substituting $\vec{v}_{t-\Delta t/2}$ and $\vec{v}_{t+\Delta t/2}$ by $\vec{v}\,'_{t-\Delta t/2}$ and $\vec{v}\,'_{t+\Delta t/2}$ defined as

$$\vec{v}\,'_{t-\Delta t/2} = \vec{v}_{t-\Delta t/2} + \frac{q\Delta t}{2m}\vec{E}(\vec{r}_t) \tag{4.11}$$

$$\vec{v}_{t+\Delta t/2} = \vec{v}\,'_{t+\Delta t/2} + \frac{q\Delta t}{2m}\vec{E}(\vec{r}_t) \tag{4.12}$$

This substitution shows that numerically the electric field can be taken into account independently from the magnetic field by splitting the acceleration due to the electric field in two parts. First only half of the acceleration is added to the velocity. Then the velocity vector is rotated by the magnetic field as will be explained below. Finally also the second half of the acceleration by the electric field is added to the velocity.

Now we turn our attention to the effect of the magnetic field. With the substitutions (4.11-4.12) the first equation in (4.10) becomes

$$\frac{\vec{v}\,'_{t+\Delta t/2} - \vec{v}\,'_{t-\Delta t/2}}{\Delta t} = \frac{q}{m}\frac{\vec{v}\,'_{t+\Delta t/2} + \vec{v}\,'_{t-\Delta t/2}}{2} \times \vec{B}(\vec{r}_t) \tag{4.13}$$

Taking the scalar product of this equation with $\vec{v}\,'_{t+\Delta t/2} + \vec{v}\,'_{t-\Delta t/2}$ shows that the magnitudes of $\vec{v}\,'_{t+\Delta t/2}$ and $\vec{v}\,'_{t-\Delta t/2}$ are equal. Hence, equation (4.13) represents a rotation of $\vec{v}\,'_{t-\Delta t/2}$ to $\vec{v}\,'_{t+\Delta t/2}$ in the plane perpendicular to the magnetic field. The sketch in figure 4.5 shows the projection of the velocity vectors $\vec{v}\,'_{t-\Delta t/2}$ and $\vec{v}\,'_{t+\Delta t/2}$ in the plane perpendicular to the magnetic field. Using some simple trigonometry it can be shown that the rotation angle θ can be expressed as function of the velocity components perpendicular to the magnetic field as

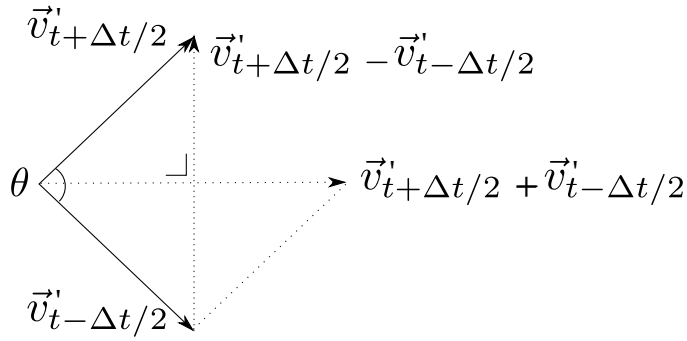

Figure 4.5: Sketch to calculate the velocity rotation angle due to the magnetic field

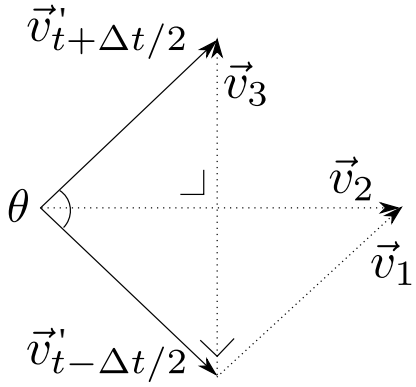

Figure 4.6: Intermediate velocity vectors in the Boris algorithm

$$\tan\frac{\theta}{2} = \frac{|\vec{v}\,'_{t+\Delta t/2} - \vec{v}\,'_{t-\Delta t/2}|_\perp}{|\vec{v}\,'_{t+\Delta t/2} + \vec{v}\,'_{t-\Delta t/2}|_\perp} \tag{4.14}$$

The velocity $\vec{v}\,'_{t+\Delta t/2}$ is, however, still unknown. Therefore, by taking the component of equation (4.13) perpendicular to the magnetic field the right hand side in equation (4.14) can be replaced by $qB(\vec{r}_t)\Delta t/2m$. One can then write θ as function of the magnetic field as

$$\tan\frac{\theta}{2} = \frac{qB(\vec{r}_t)\Delta t}{2m} \tag{4.15}$$

With this expression for θ the velocity $\vec{v}\,'_{t+\Delta t/2}$ can now be calculated from the velocity $\vec{v}\,'_{t-\Delta t/2}$ using three intermediate vectors $\vec{v}_1$, $\vec{v}_2$ and $\vec{v}_3$ as shown

in figure 4.6. Vector $\vec{v}_1$ is taken perpendicular to both $\vec{v}\,'_{t-\Delta t/2}$ and $\vec{B}(\vec{r}_t)$. Its magnitude is chosen such that $\vec{v}\,'_{t-\Delta t/2} + \vec{v}_1$ gives a vector bisecting $\vec{v}\,'_{t-\Delta t/2}$ and $\vec{v}\,'_{t+\Delta t/2}$. This bisecting vector is defined as $\vec{v}_2$. Vector $\vec{v}_3$ eventually is taken perpendicular to both $\vec{v}_2$ and $\vec{B}(\vec{r}_t)$. Its magnitude is chosen such that $\vec{v}\,'_{t-\Delta t/2} + \vec{v}_3$ gives the desired new velocity $\vec{v}\,'_{t+\Delta t/2}$. This gives the following algorithm to determine $\vec{v}\,'_{t+\Delta t/2}$ from $\vec{v}\,'_{t-\Delta t/2}$.

$$\vec{v}_1 = \frac{q\Delta t}{2m}\left(\vec{v}\,'_{t-\Delta t/2} \times \vec{B}(\vec{r}_t)\right) \tag{4.16}$$

$$\vec{v}_2 = \vec{v}\,'_{t-\Delta t/2} + \vec{v}_1 \tag{4.17}$$

$$\vec{v}_3 = \frac{\frac{q\Delta t}{m}}{1 + \left(\frac{qB(\vec{r}_t)\Delta t}{2m}\right)^2}\left(\vec{v}_2 \times \vec{B}(\vec{r}_t)\right) \tag{4.18}$$

$$\vec{v}\,'_{t+\Delta t/2} = \vec{v}\,'_{t-\Delta t/2} + \vec{v}_3 \tag{4.19}$$

We now have a very efficient algorithm to update both the velocity and the position of a particle. The new velocity $\vec{v}_{t+\Delta t/2}$ can be calculated from the old velocity $\vec{v}_{t-\Delta t/2}$ using the equations (4.11-4.12) and (4.16-4.19). The new position $\vec{r}_{t+\Delta t}$ can be calculated from the old position $\vec{r}_{t-\Delta t}$ using equation the second equation in (4.10) and the new velocity $\vec{v}_{t+\Delta t/2}$.

4.2.6 Collisions

Collisions are a very important aspect in the code because they strongly influence both the energy and the particle balance of the plasma. The first part of this subsection discusses the reactions that are taken into account in VMCPT. The second part of this subsection explains which Monte Carlo techniques are used to take these reactions into account.

4.2.6.1 Relevant reactions

A hydrogen plasma in VISIONI is dominated by H_2 molecules, electrons, H_3^+ ions and H_2^+ ions as will be demonstrated in 6.3.3. Therefore, H atoms, H^+ ions and H^- ions can safely be neglected in VMCPT. The symbol H and the word hydrogen is used here for any of the three hydrogen isotopes. It is assumed that all colliding particles start from their electronic ground state. This is a good approximation in a weakly ionized plasma because the fraction of excited species is very low. Further it is assumed that the colliding hydrogen molecules also start from their vibrational ground state. This is not a very good approximation because H_2 does not possess a permanent dipole moment and, therefore, vibrationally excited molecules do not spontaneously decay radiatively. It would, however, make things very complicated to take into account also the vibrational state of the hydrogen molecules. Furthermore, the cross section data on vibrationally excited

Table 4.1: Reactions taken into account in the VMCPT code with indication of the inelastic energy loss and the reaction type

	reaction	ΔE_{inel} **[eV]**	**type**
1	$e^- + H_2 \rightarrow e^- + H_2$	-	elastic [123]
2	$e^- + H_2 \rightarrow e^- + H_2(J > 0)$	0.01	rotational [123]
3	$e^- + H_2 \rightarrow e^- + H_2(v = 1)$	0.516	vibrational [120]
4	$e^- + H_2 \rightarrow e^- + H_2(v = 2)$	1.003	vibrational [120]
5	$e^- + H_2 \rightarrow e^- + H_2(B^1\Sigma_u^+)$	12.754	electronic [120]
6	$e^- + H_2 \rightarrow e^- + H_2(B'^1\Sigma_u^+)$	14.85	electronic [120]
7	$e^- + H_2 \rightarrow e^- + H_2(B"^1\Sigma_u^+)$	15.47	electronic [120]
8	$e^- + H_2 \rightarrow e^- + H_2(C^1\Pi_u)$	13.29	electronic [120]
9	$e^- + H_2 \rightarrow e^- + H_2(D^1\Pi_u)$	14.996	electronic [120]
10	$e^- + H_2 \rightarrow e^- + H_2(D'^1\Pi_u)$	15.555	electronic [120]
11	$e^- + H_2 \rightarrow e^- + H_2(EF^1\Sigma_g^+)$	13.13	electronic [120]
12	$e^- + H_2 \rightarrow e^- + H_2(H\bar{H}^1\Sigma_g^+)$	14.98	electronic [120]
13	$e^- + H_2 \rightarrow e^- + H_2(GK^1\Sigma_g^+)$	14.816	electronic [120]
14	$e^- + H_2 \rightarrow e^- + H_2(I^1\Pi_g)$	14.824	electronic [120]
15	$e^- + H_2 \rightarrow e^- + H_2(a^3\Sigma_g^+)$	11.72	electronic [120]
16	$e^- + H_2 \rightarrow e^- + H_2(b^3\Sigma_u^+)$	7.93	electronic [120]
17	$e^- + H_2 \rightarrow e^- + H_2(c^3\Pi_u)$	11.72	electronic [120]
18	$e^- + H_2 \rightarrow e^- + H_2(d^3\Pi_u)$	13.6	electronic [120]
19	$e^- + H_2 \rightarrow e^- + H_2(e^3\Sigma_u^+)$	13	electronic [120]
20	$e^- + H_2 \rightarrow 2e^- + H_2^+$	15.42	ionization [120]
21	$e^- + H_2 \rightarrow 2e^- + H_2^+(X^2\Sigma_g^+)$ $H_2^+(X^2\Sigma_g^+) \rightarrow H^+ + H$	18.15	dissociative ionization [120]
22	$e^- + H_2 \rightarrow 2e^- + H_2^+(B^2\Sigma_u^+)$ $H_2^+(B^2\Sigma_u^+) \rightarrow H^+ + H$	30.6	dissociative ionization [120]
23	$H_2^+ + H_2 \rightarrow H_3^+ + H$	-1.7	proton transfer [120]
24	$H_2^+ + H_2 \rightarrow H_2 + H_2^+$	-	charge exchange [120]
25	$H_2^+ + H_2 \rightarrow H_2^+ + H_2$	-	elastic [154]
26	$H_3^+ + H_2 \rightarrow H_3^+ + H_2$	-	elastic [154]
27	$e^- + e^- \rightarrow e^- + e^-$	-	elastic
28	$e^- + H_2^+ \rightarrow H + H$	-	recombination [120]
29	$e^- + H_2^+ \rightarrow e^- + H + H^+$	-	dissociation [120]
30	$e^- + H_3^+ \rightarrow H + H + H$	-	recombination [120]
31	$e^- + H_3^+ \rightarrow H^+ + H + H$	14	dissociation [120]

molecules are rather limited. Fortunately, it was shown in [147] that the presence of vibrationally excited molecules in multidipole discharges has no critical effect on the plasma parameters.

The reactions taken into account in VMCPT are listed in table 4.1 together with the inelastic energy loss ΔE_{inel} and the reaction type. The Monte Carlo methods used to take these reactions into account require the collision cross sections σ_c of these reactions as function of impact energy,

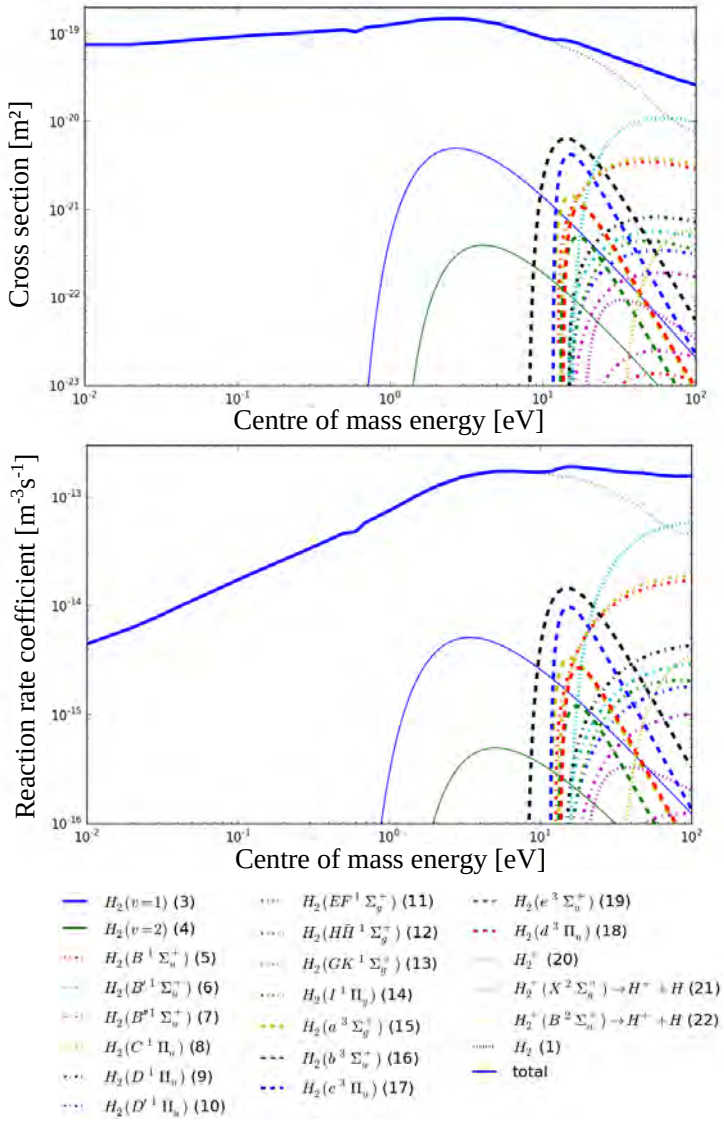

Figure 4.7: Cross sections and reaction rate coefficients for electron-H_2 reactions [120],[123]

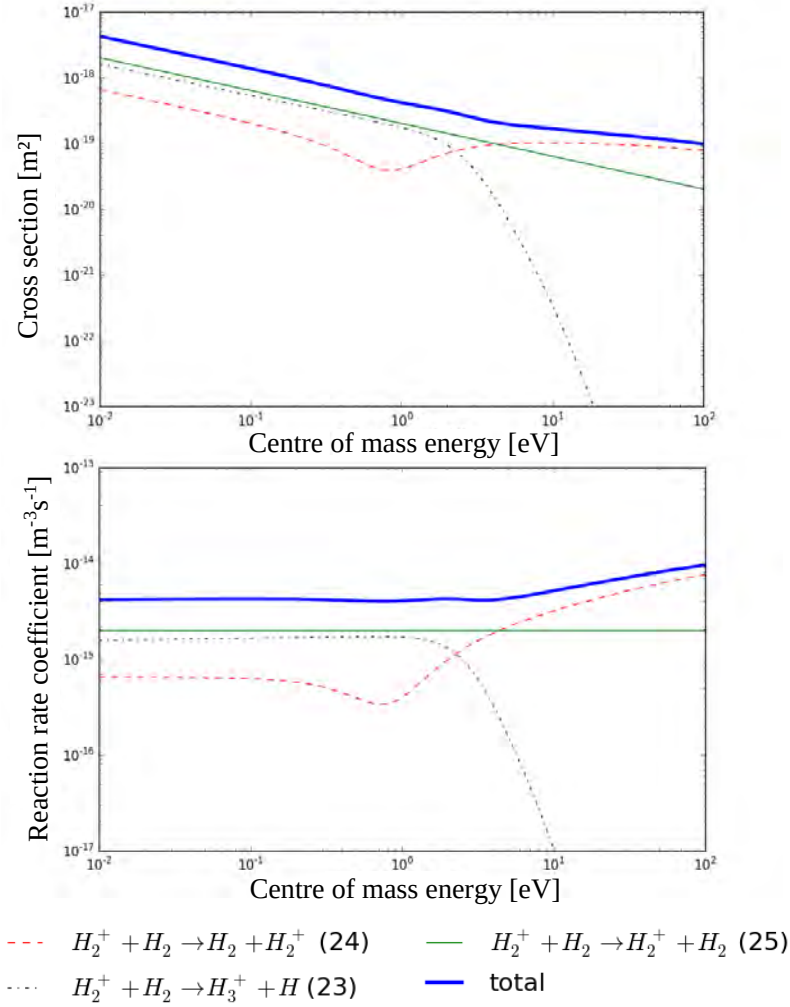

Figure 4.8: Cross sections and reaction rate coefficients for H_2^+-H_2 reactions [120],[154]

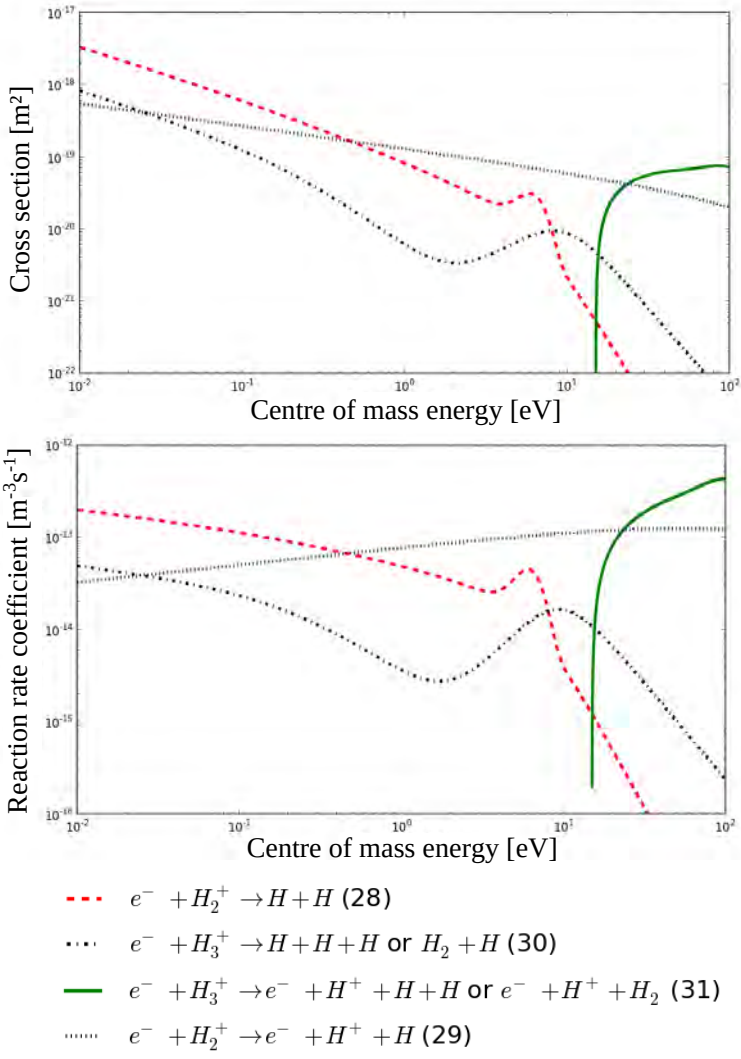

Figure 4.9: Cross sections and reaction rate coefficients for electron-ion reactions [120]

thus not averaged over a Maxwellian distribution as is often done. These cross sections are shown in figures 4.7-4.9 together with the reaction rate coefficients $R = \sigma_c v$. Most cross sections were taken from [120]. For elastic scattering of electrons by molecules the cross sections were taken from [123]. For elastic collisions of H_2^+ and H_3^+ with hydrogen molecules the cross sections were taken from [154]. The same cross sections are used for hydrogen or deuterium. In [155] it is shown that most cross sections are very similar for hydrogen and deuterium. For vibrational excitation there is possibly, however, a significant difference between hydrogen and deuterium. Due to the lack of cross section data for deuterium also for vibrational excitation the same cross sections as hydrogen are used in VMCPT.

Collisions with hydrogen molecules are dominant in VISIONI due to the low ionization degree. As in the atomic case a molecule can exist in different electronic states related to the electron motion. The energy separation between the different electronic states is of the order of 10 eV. In a molecule each electronic state additionally has a substructure of vibrational states with a separation of the order of 0.1 eV related to the movement of the nuclei about their equilibrium positions and rotational states with a separation of the order of 0.001 eV related to the rotation of the molecule as a whole. In case of the homonuclear diatomic hydrogen molecule the states are labelled as ${}^{2S+1}\Lambda_{g/u}^{+/-}$. Here S is the total intrinsic spin of the electrons and $2S+1$ the associated multiplicity. The projection l_z of the orbital angular momentum along the symmetry axis of the molecule is denoted by the quantum number Λ which can take the values Σ, Π, Δ and Φ corresponding respectively to $l_z = 0$, 1, 2 and 3. The letters g and u come from the German 'gerade' and 'ungerade' and indicate respectively that the electronic wave function does or does not change sign for inversion with respect to the centre of symmetry. The symbols + and − indicate respectively that the wave function does or does not change sign for reflection with respect to a plane through the symmetry axis of the molecule. More details on the molecular structure can be found for instance in [156].

For electrons it can be seen in figure 4.7 that for energies below 1 eV the collisions with H_2 are dominated by elastic collisions. Rotational electron impact excitations are included in the elastic electron impact collisions because of the limited energy resolution of the electron beam measurements used to determine the cross sections. At higher energies in the range 1-10 eV also vibrational excitations play a significant role. Vibrational excitation to the two lowest lying excited states is taken into account in VMCPT. At energies in the range 10-100 eV the electronic excitation and ionization reactions become important. Excitation to singlet states is followed by radiative decay to the $X^1\Sigma_g^+$ ground state. Excitation to triplet states is followed by radiative decay to the $b^3\Sigma_u^+$ anti-bonding state and leads eventually to the dissociation of the hydrogen molecule. There are three important ionizing reactions. The most probable ionizing reaction is direct ionization to

H_2^+. For ionizing reactions into the vibrational continuum of H_2^+ or into the $B^2\Sigma_u^+$ first excited state or higher excited states of H_2^+ the H_2^+ ion dissociates and H and H^+ are formed. Above 70 eV the direct ionization reaction becomes the most probable reaction.

H_2^+ and H_3^+ ions in VISIONI do not have enough energy to cause excitation or ionization of H_2 molecules. The collisions between H_2^+ and H_2 are dominated by elastic collisions, charge exchange and proton transfer as shown in figure 4.8. For collisions between H_3^+ and H_2 only elastic collisions are important.

Finally one also has to consider the collisions between charged particles. Electron-electron Coulomb collisions are important because they allow the electron energy distribution to equilibrate. Also recombination between electrons and ions has to be taken into account because it can significantly contribute to the loss of ions and low energy electrons. Elastic electron-ion collisions are considered to be unimportant. The energy transfer in such collisions is very small due to the large difference in electron and ion mass as can be seen from equation (2.130). Hence, elastic electron-ion collisions only lead to momentum redirection of the electrons which is strongly dominated by elastic collisions with H_2. Similarly inelastic electron-ion collisions are also neglected because the inelastic energy loss is dominated by inelastic collisions with H_2. Ion-ion collisions are not considered at all. Elastic ion-ion collisions have an important effect on the ion energy distribution function. However, VMCPT is not capable of properly predicting the ion energy distribution function. The ion energy is dominated by acceleration in the bulk electric field, which is not taken into account in VMCPT as explained above.

4.2.6.2 Null collision method

Collisions between charged particles and hydrogen molecules are taken into account in VMCPT using the Monte Carlo approach. From the theory in 2.3.4.5 it can be seen that the probability for a charged particle to undergo a certain reaction i with a hydrogen molecule during a time step Δt can be expressed as

$$P_i(v) = n_{H_2}\sigma_{c,i}(v)v\Delta t \tag{4.20}$$

with n_{H_2} the particle density of the hydrogen molecules, $\sigma_{c,i}$ the cross section for reaction i and v the relative velocity. This reaction probability is clearly a function of v, both directly and through the collision cross section. The total reaction probability is then given by

$$P_{tot}(v) = n_{H_2}\sigma_{c,tot}(v)v\Delta t \tag{4.21}$$

with $\sigma_{c,tot}$ the sum of the collision cross sections for all possible reaction mechanisms. For each particle it can be determined whether it did undergo

a collision by generating a random number R uniformly distributed between 0 and 1. A reaction has taken place if

$$R \leq P_{tot}(v) \tag{4.22}$$

In case a reaction did take place it can also be determined which one of the reactions took place according to the following criteria

$$\begin{aligned}
R &\leq \frac{P_1}{P_{tot}} && \text{reaction 1} \\
\frac{P_1}{P_{tot}} < R &\leq \frac{P_1 + P_2}{P_{tot}} && \text{reaction 2} \\
\frac{P_1 + P_2}{P_{tot}} < R &\leq \frac{P_1 + P_2 + P_3}{P_{tot}} && \text{reaction 3} \\
&\vdots
\end{aligned} \tag{4.23}$$

It is implicitly assumed here that more than one reaction per particle per time step is not possible. Therefore, the time step has to be chosen such that the probability for more than one collision is indeed negligible. This procedure has to be performed for each particle. This is computationally very demanding due to the huge number of particles used in VMCPT. The computational effort can, however, drastically be reduced by using the equivalent but much more efficient null collision method [22]. In this case an additional fictitious collision is introduced with a collision cross section $\sigma_{c,f}(v)$ such that $P_{tot}(v)$ becomes equal to its maximum value $P_{tot,max}$ for all values of v. The number of particles N that will undergo a collision during the time step is then known in advance and given by

$$N = n_{H_2} \left[\sigma_{c,tot}(v) v\right]_{max} \Delta t \tag{4.24}$$

Therefore, one can now randomly select N particles and neglect all other particles. This drastically reduces the computational time. For the N selected particles the criteria in (4.23) can again be used to determine which reaction took place. If the fictitious collision is determined to occur, it means that the particle did not undergo a real physical collision. Hence, the name null collision method. The null collision method is also used for electron-ion collisions. For simplicity it is assumed that the ions are uniformly distributed over the whole volume.

In case a collision happens the energy and velocity of the colliding particles are updated using the kinematic formulas in 2.3.4.3. These formulas require first the knowledge of the scattering angles. The azimuthal scattering angle ϕ is always taken from a uniform distribution between 0 and 2π due to the axial symmetry of the scattering geometry. For ion-neutral collisions it is assumed that the hard sphere model is sufficiently realistic and the scattering angles are determined according to the Monte Carlo

algorithm described in E.3 for a uniform distribution over a sphere. For collisions between electrons and hydrogen atoms the approach from [157] is used. It is assumed that the interaction potential between the electron and the atom can be approximated by the screened Coulomb potential. Using the first Born approximation for the quantum mechanical calculation of the scattering angle distribution it is then found that the polar scattering angle θ can be calculated from the impact energy E and a random number R uniformly distributed between 0 and 1 according to

$$\cos\theta = 1 - \frac{2R}{1 + \frac{8E}{27.21\ \mathrm{eV}}(1-R)} \tag{4.25}$$

The collisions between electrons and hydrogen molecules are also treated according to [157] by using a generalization of (4.25). In this case θ is calculated according to

$$\cos\theta = 1 - \frac{2R(1-\xi(E))}{1 + \xi(E)(1-2R)} \tag{4.26}$$

with R again a random number uniformly distributed between 0 and 1 and $\xi(E)$ given by the implicit equation

$$\frac{\sigma_{c,mom}(E)}{\sigma_{c,tot}(E)} = \frac{1-\xi}{2\xi^2}\left((1+\xi)\ln\frac{1+\xi}{1-\xi} - 2\xi\right) \tag{4.27}$$

where $\sigma_{c,mom}(E)$ is the momentum transfer cross section and $\sigma_{c,tot}(E)$ the total collision cross section for electron impact on a hydrogen molecule with impact energy E. The cross section data for calculating $\xi(E)$ was taken from [123].

For recombination reactions the original particles are removed because neutrals are not tracked in VMCPT. For ionization reactions a new electron and a new ion are being released. The secondary electron energy E_{sec} can be calculated from the impact energy E after subtraction of the ionization energy E_{ion} and a random number R uniformly distributed between 0 and 1 according to

$$E_{sec} = 8.3\tan\left[R\arctan\left(\frac{E-E_{ion}}{2\cdot 8.3\ \mathrm{eV}}\right)\right]\ \mathrm{eV}; \tag{4.28}$$

following the approach from [158] and using the form factor 8.3 for hydrogen [159]. The velocity direction is determined from momentum conservation. For the new ion the energy and velocity are picked from a Maxwellian distribution at room temperature in accordance with the assumption that the neutral background gas is in thermal equilibrium at room temperature.

4.2.6.3 Binary collision method

The electron-electron collisions are treated with the binary collision method [160]. The simulation volume is first divided in a predefined number of cells in cylindrical coordinates. The number of cells should be a compromise between spatial resolution and good statistics and is usually around 125. Each time step the electrons are randomly paired per cell. All electron pairs are assumed to undergo a Coulomb collision. The azimuthal scattering angle ϕ is taken from a uniform distribution between 0 and 2π. The polar scattering angle θ is taken from a Gaussian distribution with mean zero and variance

$$< \theta^2 >= \frac{n q_e^4 Z_1^2 Z_2^2 \ln \Lambda \Delta t}{2\pi \epsilon_0^2 m_r^2 v^3} \tag{4.29}$$

in accordance with the theory from 2.3.4.6. With the scattering angles now determined, the velocities and energies of the electrons can be updated using the kinematic formulas in 2.3.4.3.

4.2.7 Plasma-wall interaction

During each time step of the integration of the equation of motion it is checked whether the tracked charged particle has collided with the plasma chamber walls or the tungsten filaments. Electrons hitting the tungsten filaments or the target plate are instantaneously reflected by the high potential barrier in the thin sheath layer. This is simply done by inverting the component of the electron velocity normal to the surface. Electrons hitting the side or bottom of the plasma chamber can really collide with the wall if the energy component normal to the surface is high enough to overcome the relatively low potential barrier in the thin sheath layer. Reflection, implantation and secondary electron emission is then treated according to the model discussed in 2.4.1.4. Secondary electron emission at the chamber walls is an important effect in multidipole discharges as was found already for instance in [161]. An ion hitting the plasma chamber walls or the filaments is either absorbed or reflected as a neutral. There is no potential barrier for positively charged ions. As neutrals are not tracked in VMCPT the ion is then considered to be lost. Sputtering is not included in VMCPT as the effect of sputtered impurities on the plasma properties is assumed to be negligible.

4.2.8 Time steps

The choice of the time steps in VMCPT is critical. For the integration of the equation of motion it is important that the gyration due to the magnetic field is well resolved and that the particle does not travel too far in comparison with the dimensions of the plasma chamber during one time step. In table

3.1 it can be seen that the shortest gyration period for electrons is around 10^{-10} s at the poles of the permanent samarium-cobalt magnets where the field is around 0.2 T. Therefore, the integration time step Δt_e for the electron equation of motion was chosen to be inversely proportional with the magnetic field according to $\Delta t_e = \frac{0.2\ T}{B} 10^{-12}$ s. In this way it is guaranteed that each gyration is covered by about 100 integration time steps. In regions where the magnetic field is very low the time step Δt_e is never taken above 10^{-10} s such that the electrons never travel more than 1 mm during a time step. Ions have a much longer gyration period and are also moving much slower. By a similar reasoning as for the electrons it can be shown that it suffices to use an integration time step Δt_i for the ion equation of motion according to $\Delta t_i = \frac{0.2\ T}{B} 10^{-9}$ s with an upper limit of 10^{-7} s.

Another consideration is the time step Δt_c required for the Monte Carlo collision algorithm. The null collision scheme explained above only works properly in case the probability that a particle undergoes more than one collision during one time step is negligible. From table 3.1 it can be seen that the collision time in VISIONI is comparable for all charged particles and around 10^{-7} s. Therefore, a time step $\Delta t_c = 10^{-9}$ s has been chosen. Consequently it was also required to lower the value for Δt_i to 10^{-9} s.

Eventually the main time step in VMCPT has a value of 10^{-9} s. According to the scheme in figure 4.4 during each main time step new primary electrons are released, all charged particles are advanced in time by integrating the equation of motion and collisions are taken into account with the Monte Carlo algorithm. For electrons the integration of the equation of motion requires taking multiple substeps because the integration time step is smaller than the main time step. For the ions only one step has to be taken during the integration because the integration time step is equal to the main time step.

4.2.9 Parallelization

The amount of super-particles used in the simulation has to be chosen such that the statistics allow determination of the plasma parameters with the desired spatial resolution and resolving of the high energy tail of the electron energy distribution function. Simulations have shown that at least ten primary electron super-particles have to be emitted per main time step to resolve the high energy tail of the electron energy distribution function. This results then eventually in a few million super-particles in steady state and relatively long CPU times of more than one month on one processor of the Fermi cluster at SCK-CEN. The CPU time is dominated by the integration of the equation of motion for the electrons. Therefore, it was decided to parallelize VMCPT using the MPI standard [162], [163] by distributing the super-particles over different cores for integrating the equation of motion. In this way the computational time can be reduced to a few days for eight cores on the Fermi cluster at SCK-CEN or the HPC clusters at Ghent Uni-

Table 4.2: Parameters required in the VMCPT input file

parameter name	**description**
real_electron_number	primary electrons emitted per second
simulation_electron_number	primary electron super-particles emitted per time step
max_particle_number	maximum number of super-particles
output_steps	number of main time steps before output
total_time	total simulation time
H2_pressure	neutral hydrogen pressure
Tn	neutral hydrogen temperature
mh	isotopic mass
Vb_fil	discharge potential
V_fil	potential drop over the filaments
I_fil	filament heating current
elastic_scattering_electrons	switch on or off elastic electron scattering
elastic_scattering_ions	switch on or off elastic ion scattering
vibrational_excitation	switch on or off vibrational excitation
electronic_excitation	switch on or off electronic excitation
ionization	switch on or off ionization
h3_creation	switch on or off H_3^+ creation
recombination	switch on or off recombination
ee_collisions	switch on or off electron-electron collisions
magnetic_field	switch on or off the magnetic field
magnetic_field_from_file	magnetic field from data file or real time calculation
wall_electrons	switch on or off secondary electron emission from wall
restart	number of data file from which to restart the simulation

versity [164]. Further reduction of the computational time by using multiple nodes is limited due to slow inter-node communication.

4.2.10 Code input and output

Running VMCPT requires only the executable, the magnetic field data file and the input file. In the input file one can specify the simulation parameters listed in table 4.2. This allows to change the operational parameters such as neutral pressure, neutral temperature, isotopic mass of the working gas, filament heating current, primary electron emission rate and discharge potential without having to recompile the code. It is also possible to modify some more technical parameters such as the number of primary electron super-particles emitted per main time step, the total simulation time, the number of main time steps before output files are being generated and optionally the number of the output file from which to restart a previously stopped simulation. Furthermore, one can also switch on or off different processes in order to study their effect on the simulation results. In case it is specified in the input file that the magnetic field should be read from a data file executing the code also requires a data file with the precalculated magnetic field in VISIONI on a 3D grid with 0.9 mm grid spacing.

After the number of main time steps specified in the input file the code generates new output files. There is an output file for each type of charged particle listing for all particles their origin, position, velocity, energy and age. Additionally there is an output file showing the time evolution of the

charged particle densities and the magnitude of the sheath potential drop at the side and bottom of the plasma chamber. Finally there is also an output file listing for each process how many times it happened since the previous output was generated. This is a lot of information. A python [165] script has been developed to process the data automatically and generate more visual output. It produces pie charts to compare different processes and plots showing the plasma density scan along the central axis, horizontal and vertical projections of the charged particle positions, energy probability distribution functions and the time evolution of the charged particle densities and the sheath potential drop at the side and bottom of the plasma chamber.

4.3 Langmuir probe I-V analyser

During this work a cylindrical 1 mm diameter molybdenum Langmuir probe was fabricated for VISIONI. A description of the probe was given in 3.2.6.3. This section discusses the analysis program that was developed during this work to extract the plasma parameters automatically from the measured IV curves. The program can read the IV characteristic directly from the VISIONI log files, performs the analysis and generates an output file with the most important plasma parameters and some graphs showing the fits to the IV curve. The program is written in python [165] and is provided with a GUI using the *EasyGui* python package [166]. It is also compiled into a Windows executable using py2exe [167]. This makes it possible to run the code also on Windows systems without a python installation.

The Langmuir probe theory relevant for the analysis is discussed in 2.3.7. The list below summarizes the most important assumptions used in the code to calculate the plasma parameters.

- Ion collection can be described by the BRL theory for cylindrical probes. Hence, the plasma density n can be determined by fitting the Chen BRL functions to the measured ion saturation current.
- Collisions are negligible in the analysis of the IV characteristic in VISIONI because the typical collision mean free paths given in table 3.1 are much larger than the probe dimensions.
- Typical Larmor radii in VISIONI are given in table 3.1. At the central axis of the plasma chamber where $B = 0.001$ T only the cold electrons have a Larmor radius R_{cycl} that is comparable to the probe radius R_{pr}. Laframboise and Rubinstein have calculated the electron saturation current for a cylindrical probe at plasma potential in a magnetic field for different angles between the magnetic field and the probe axis and for different ratios R_{pr}/R_{cycl} [168]. As shown later in figure 6.9 the magnetic field in VISIONI is perpendicular to the probe surface. The

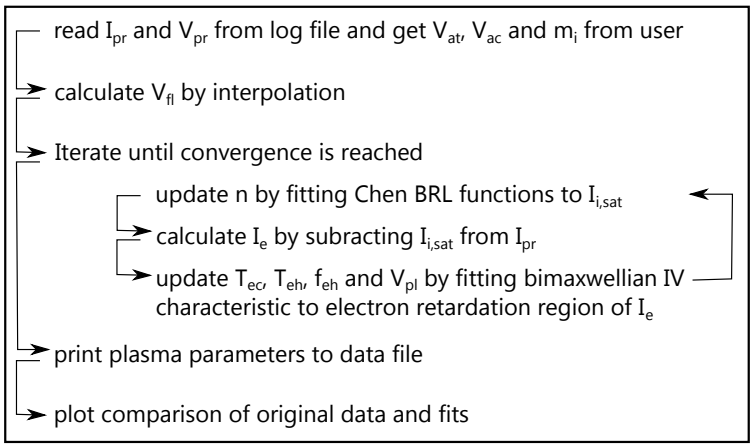

Figure 4.10: Algorithm of the automatic IV characteristic analysing program

ratio R_{pr}/R_{cycl} for cold electrons in VISIONI is about 0.17. Figure 3 in [168] shows that the effect of the magnetic field in VISIONI gives a reduction of only 2% for I_e. Therefore, the effect of the magnetic field in VISIONI can safely be neglected during the analysis of the IV characteristic.

- The EEDF in VISIONI is assumed to be bi-Maxwellian. The cold electron temperature T_{ec}, the hot electron temperature T_{eh}, the hot electron fraction f_{eh} and the plasma potential V_{pl} can then be determined by fitting an ideal bi-Maxwellian IV characteristic to the electron retardation region.

- Secondary electron emission at the probe surface due to electron impact is significant in VISIONI due to the presence of the hot electron population. Therefore, the secondary electrons have to be subtracted from the electron current before fitting an ideal bi-Maxwellian IV characteristic to the electron retardation region.

- It is assumed that the plasma has only one type of ions. Otherwise the analysis would be very complicated.

The algorithm used by the code is shown schematically in figure 4.10. The program starts by reading the probe current I_{pr} and the probe potential V_{pr} data from the log file. The anode-target potential difference V_{at}, the anode-cathode potential difference V_{ac} and the ion mass m_i are requested from the user. The floating potential V_{fl} can be calculated immediately by interpolation of the $I_{pr}V_{pr}$ data at the zero crossing. Then an iteration

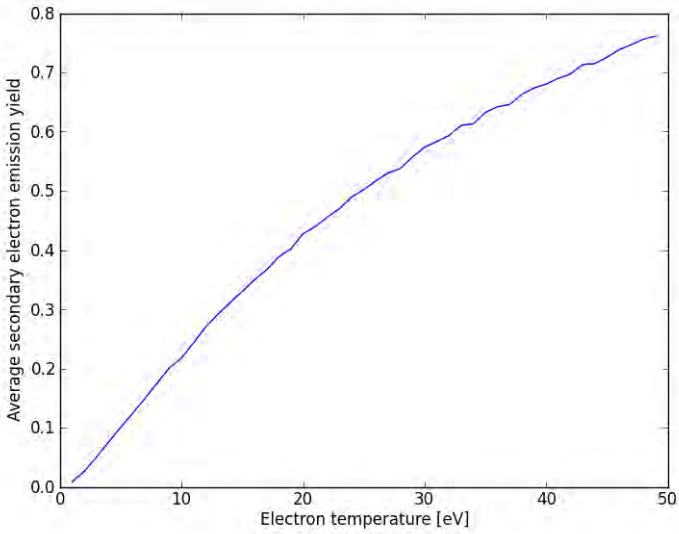

Figure 4.11: Mo secondary electron emission yield as function of electron temperature

loop starts to determine n, T_{ec}, T_{eh}, f_{eh} and V_{pl} starting from an initial guess. First the program looks at the ion saturation current. Only the $I_{pr}V_{pr}$ data points for which $V_{pr} < -V_{ac}$ are taken into account because in this region all electrons are repelled and I_{pr} is completely determined by ion collection. The Chen BRL fitting functions are then fitted to these data points by varying n. This gives an updated value for n. The fitted ion saturation curve is eventually subtracted from I_{pr} to get only the electron current I_e. Next the program looks at I_e in the electron retardation region. Only the data points with V_{pr} higher than $-0.6V_{ac}$ and below the value of V_{pr} for which the derivative of I_e with respect to V_{pr} reaches its maximum value are taken into account. The lower limit reduces errors due to a not well subtracted ion saturation current, while the upper limit reduces errors due to rounding of the knee below the plasma potential. These data points are fitted to the bi-Maxwellian electron retardation characteristic

$$\begin{aligned} I_e(V_{pr}) =& \frac{1}{4} q_e A_{pr} n (1 - f_{eh}) \left[1 - < \delta_{Mo} > (V_{pl} - V_{pr}, T_{ec})\right] \sqrt{\frac{8kT_{ec}}{\pi m_e}} \exp\left(-\frac{V_{pl} - V_{pr}}{kT_{ec}}\right) \\ &+ \frac{1}{4} q_e A_{pr} n f_{eh} \left[1 - < \delta_{Mo} > (V_{pl} - V_{pr}, T_{eh})\right] \sqrt{\frac{8kT_{eh}}{\pi m_e}} \exp\left(-\frac{V_{pl} - V_{pr}}{kT_{eh}}\right) \end{aligned} \tag{4.30}$$

by varying T_{ec}, T_{eh}, f_{eh} and V_{pl}. The function $< \delta_{Mo} > (V_b, T)$ is the average secondary electron emission coefficient for a molybdenum surface biased negatively with respect to the plasma with a potential difference V_b for a Maxwellian electron distribution with a temperature T. It can be calculated according to

$$< \delta_{Mo} > (V_b, T) = \frac{\int_{-\infty}^{+\infty} \int_{-\infty}^{+\infty} \int_{v_{z,min}}^{+\infty} dv_x dv_y dv_z \exp\left(-\frac{m_e v^2}{2kT}\right) v_z \delta_{Mo}(\frac{1}{2}\frac{m_e v^2}{q_e} - V_b)}{\int_{-\infty}^{+\infty} \int_{-\infty}^{+\infty} \int_{v_{z,min}}^{+\infty} dv_x dv_y dv_z \exp\left(-\frac{m_e v^2}{2kT}\right) v_z} \tag{4.31}$$

with $v_{z,min} = \sqrt{2q_e V_b/m_e}$ the minimum normal velocity electrons should have to overcome the potential barrier and $\delta_{Mo}(E_{imp})$ the secondary electron emission coefficient for molybdenum as function of the electron impact energy in eV which can be calculated according to the model from Scholtz discussed in 2.4.1.4. The integral in the numerator cannot be calculated analytically. Therefore, Monte Carlo sampling is used to calculate the average secondary electron emission coefficient. The velocities v_x, v_y and v_z of a Maxwellian velocity distribution have to be sampled from a Gaussian with mean 0 and standard deviation $\sqrt{kT/m_e}$. For v_z there is additionally the lower limit $v_{z,min}$. This sampling can be done with the Marsaglia algorithm described in appendix E. The Monte Carlo sampling calculation takes quite some time. Therefore, the average secondary electron emission coefficients have been precalculated for multiple values of V_b and T and are read from a data file during analysis of the IV characteristic. It turns out that the variation with V_b is negligible. The variation with T is plotted in figure 4.11. It shows that the effect of the secondary electrons is only important in case of high negative biasing when hot electrons are dominant. The multiparameter fitting is done with the *lmfit* package [169] using the Levenberg-Marquardt algorithm. Eventually one then gets updated values for T_{ec}, T_{eh}, f_{eh} and V_{pl}. The iteration converges already after a few cycles.

Chapter 5

Enhanced re-erosion of redeposited carbon in TEXTOR

Multiple studies in fusion relevant devices have shown that redeposited species appear to be eroded more easily than original species under ion bombardment. The responsible mechanism behind this phenomenon is not yet fully clear. As the observed enhancement factors are sometimes as large as 50, the enhanced re-erosion of redeposited species is a crucial issue for predicting the erosion/deposition balance in future fusion devices. Therefore, deeper investigation is definitely required. This chapter starts with a review of the literature on enhanced re-erosion of redeposited species in fusion relevant devices. The next two sections present ERO modelling studies of methane injection experiments in TEXTOR with the updated plasma-surface interaction database implemented during this work as described in 4.1.2. The aim of these studies was to investigate further this enhanced re-erosion. Section 5.2 discusses the simulation of the deuterium Balmer line emission in the nozzle experiment described in 3.1.2. The aim of this study was to check whether the transport and chemistry implemented in ERO during this work for tracking of hydrogenic species from the dissociation of injected methane is realistic. Section 5.3 discusses the simulation of the ^{13}C deposition in the roof limiter experiment described in 3.1.3. With this study it was checked whether the enhanced re-erosion of redeposited carbon is still needed with the updated plasma-surface interaction database to get agreement with the experimental observations. The last section summarizes the main conclusions from this chapter.

5.1 Enhanced re-erosion in literature

A commonly used technique to study material migration in fusion relevant devices is tracer injection. Tracer gases such as SiH_4, CH_4, C_2H_4 and WF_6 are injected into the plasma. The amount of injected species should be small enough such that the plasma is not disturbed too much but also large enough such that one can study their transport in the plasma in-situ by means of optical emission spectroscopy and their erosion/deposition behaviour on plasma-facing surfaces ex-situ by means of surface analysis.

Such studies have extensively been performed in TEXTOR [103], [170], [171], [104]. During the experimental campaign described in 3.1.3 methane has been injected into the plasma through a 1.7 mm diameter hole in the surface of a roof-like test limiter covered with a graphite plate to study the transport and local erosion/deposition behaviour of carbon. The methane was marked with ^{13}C to distinguish injected carbon from carbon intrinsically present in TEXTOR due to erosion of carbon based plasma-facing materials. In-situ optical emission spectroscopy showed a light emission cloud due to methane break-up products close to the injection hole. ERO simulations could well reproduce this light emission pattern which indicates that the impurity transport and chemistry in ERO is described realistically. Ex-situ analysis of the amorphous hydrocarbon deposit on the graphite plate by means of colorimetry and SIMS showed that only about 0.3% of the injected ^{13}C eventually gets deposited on the surface. ERO simulations, however, gave about two orders of magnitude higher deposition efficiencies and a more localized deposition pattern. The experimental deposition pattern could be reproduced with ERO only by assuming zero sticking for hydrocarbon molecules and ions such that only atomic and ionic carbon contribute to the layer formation. These sticking probabilities are not in agreement with measurements and calculations. Therefore, it was thought that these sticking probabilities represent an effective sticking taking into account self re-erosion of the deposits formed by hydrocarbons due to the incorporated hydrogen. Even with these extreme assumptions for hydrocarbon sticking the deposition efficiency simulated by ERO was still about a factor of six higher than the experimentally observed 0.3%. Therefore, it was speculated that redeposited carbon has a higher erosion yield than carbon from the graphite plate. With an enhancement factor of 5 for chemical re-erosion of redeposited carbon in addition to the assumption of zero sticking for hydrocarbons one can eventually reproduce the very low experimentally observed ^{13}C deposition efficiencies. The same conclusion was obtained from studies with the more realistic coupled version of ERO with SDTrimSP [138].

Indications of enhanced re-erosion of redeposited species have popped up also in other studies. Methane injection experiments in the divertor of the AUG [132] and the JET tokamak [127] have indicated that enhanced re-erosion of redeposited carbon in ERO is also needed to reproduce experimental deposition efficiencies in other machines. Simulations with the

EDDY material migration code have shown that the need for enhanced re-erosion of redeposited carbon is also needed in other material migration codes [172]. Furthermore, the enhanced re-erosion of redeposited species seems to occur not only for carbon. ERO modelling of a WF_6 injection experiment in TEXTOR has shown that tungsten exhibits the same behaviour [171]. Experimental observations in PISCES-B have indicated that the physical sputtering yield of redeposited beryllium is almost a factor 10 higher than that of the original beryllium [173]. All these studies show that enhanced re-erosion of redeposited species in fusion relevant devices is an important issue that should be studied in more detail.

5.2 Nozzle experiment

As explained in 4.1.2 one of the improvements implemented in ERO during this work is the tracking of hydrogenic species produced during dissociation of injected methane molecules. It was decided to test first the atomic and molecular data used for the hydrogen tracking such as electron impact collision rates and photon emission rates. Modelling of the nozzle methane injection experiment described in 3.1.2 was perfect for this purpose. The surface area at the top of the nozzle was very small. This strongly limited the light emission due to recycled, reflected or eroded species. Furthermore, there were no graphite surfaces in the observation volume of the optical spectrometers and CCD cameras. This was confirmed by the fact that no significant intrinsic atomic or molecular carbon light emission was detectable before the methane injection was started. The methane was marked with deuterium and injected into a protium plasma. This allowed to spectroscopically distinguish light emission due to hydrogen produced by dissociation of the injected methane and due to hydrogen from the plasma.

Figure 5.1 shows the hydrogen Balmer α line emission pattern. The top picture shows the pattern observed by the intensified CCD camera with the appropriate interference filter. The bottom picture shows the pattern simulated with the ERO code. In both pictures the nozzle surface is indicated with a black line. The comparison shows that qualitatively the emission patterns look relatively similar. A small light emission blob occurs just in front of the gas inlet. However, it can be seen that the experimental pattern is broader and slightly shifted away from the nozzle in comparison with the simulated pattern. This was also observed in [100] for the CD Gerö band emission. Therefore, the observed deviation is probably not caused by uncertainties in the reaction rates and emission coefficients for hydrogen but by uncertainties in the reaction rates for hydrocarbon break-up.

A more detailed comparison of the emission patterns can be made by plotting the emission profile along the central axis of the nozzle normalized to its maximum as in the top graph of figure 5.2. The full green curve represents the experimental profile after subtraction of the background light

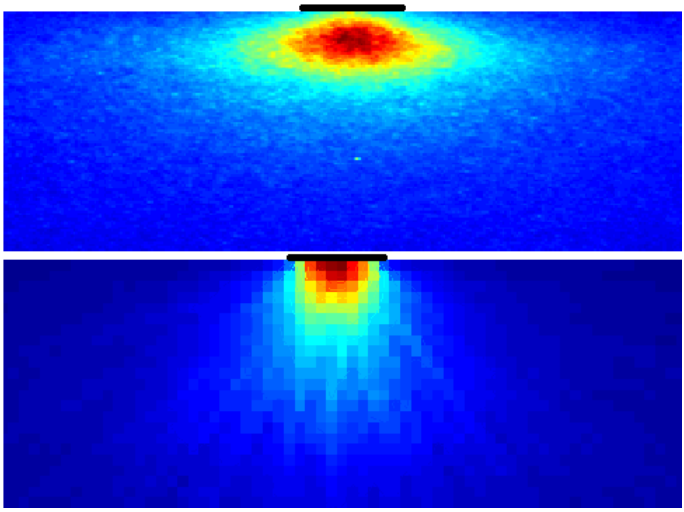

Figure 5.1: Hydrogen Balmer α line emission pattern in the TEXTOR nozzle experiment observed experimentally (top) and simulated by ERO (bottom). The nozzle surface is indicated with a black line.

emission due to the plasma itself taken just before the methane injection started. The other curves represent the profiles simulated by ERO for different assumptions. The first assumption concerns the electric sheath around the nozzle. Due to the presence of the gas inlet in the centre the electric sheath will deviate from the Debye sheath normal to a simple circular surface. The correct electric field configuration can only be calculated by means of sophisticated PIC simulations. This was outside the scope of this work. Therefore, two extreme cases were tested. The first case was the complete absence of a sheath potential drop around the nozzle denoted in the legend as "sheath off". The second case was a sheath configuration equal to that for a simple circular surface denoted in the legend as "sheath on". The second assumption concerns the fate of tracked particles hitting the top surface of the nozzle. Three cases were tested. The first case was that these particles are neutralized and reinjected into the plasma with the same velocity distribution as the injected methane molecules. This case is denoted in the legend as "neutral repuffing". The second case was that the particles are again reinjected into the plasma but now without being neutralized. This case is denoted in the legend as "repuffing". The third case was that particles are not neutralized and reflected without changing their energy. This case is denoted in the legend as "total reflection". In all cases it is assumed that no particles stick to the nozzle because after the experiments no deposition was found on or inside the nozzle. The comparison of the

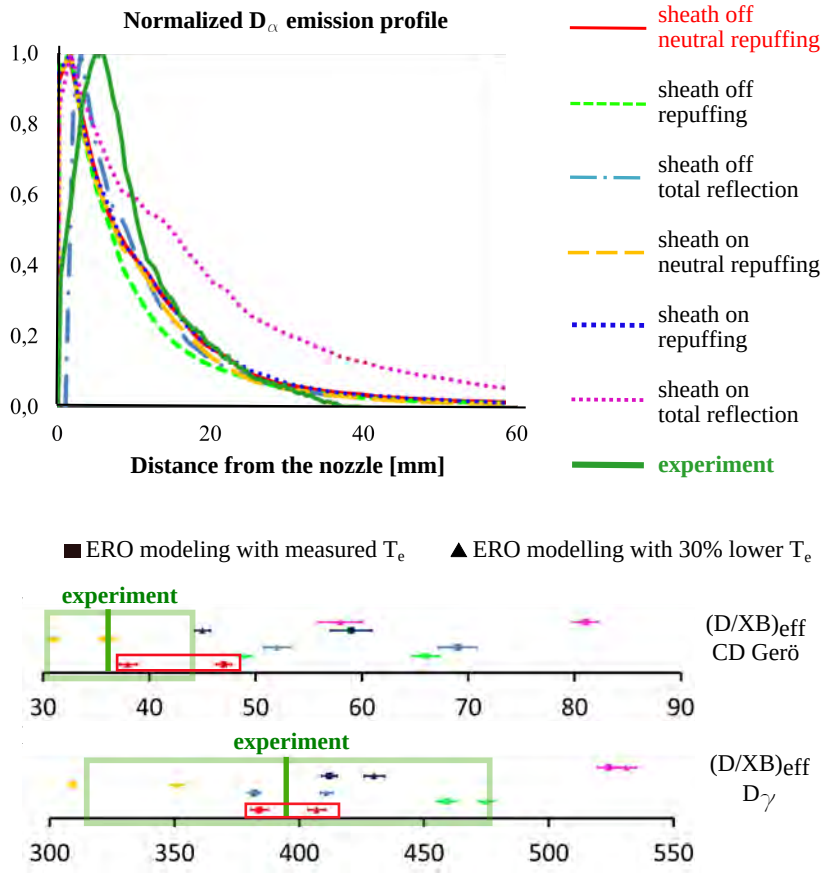

Figure 5.2: Dα Balmer line emission profiles (top) and effective D/XB values (bottom) in the TEXTOR nozzle experiment simulated with ERO versus experimental results

different profiles shows that all simulated profiles look rather similar except for the one with sheath on and total reflection which is significantly broader. The agreement between the other simulated profiles and the experimental profile is reasonable. The main difference is the fact that the peak position is significantly closer to the nozzle for the simulated profiles. Variations of 30% in electron density and electron temperature in the ERO simulations could not cause a significant shift in the peak position as the reaction rates and photon emission probabilities are not very sensitive to such variations. Simulations showed that also variations in the perpendicular diffusion coefficients do not have a significant influence on the simulated profiles. The peak position could only be shifted further away from the nozzle surface by

increasing the injection energy of the methane molecules, but the required injection energy of about 1 eV was too high to be realistic and gave a strong deviation from experiment for the effective D/XB value. The disagreement could be simply due to the fact that the determination of the position of the nozzle surface in the CCD images is rather cumbersome. Shifting the experimental profile a few millimetres gives already a much better agreement. As discussed above it can also be caused by the uncertainties in the reaction rates for hydrocarbon break-up.

A more quantitative comparison between ERO simulations and the experiment can be made by looking at the effective D/XB values. As explained in 2.4.4 these values can be calculated by dividing the total number of injected methane molecules by the total number of photons for a specific electronic transition in one of the break-up products of the methane molecules. The plot at the bottom in figure 5.2 shows a comparison between ERO simulations and the experiment for the CD Gerö band and the Dγ Balmer line. The comparison for the CD Gerö band has already been studied in [100]. A similar analysis was performed in this work to check whether the new ERO simulations give the same result for the CD Gerö band effective D/XB value. The green bar with the light green box denotes the experimental values with the 20% measurement error. The colored data points represent the results from ERO simulations with different assumptions. The color code is the same as for the emission profiles in the top graph. The error bars represent the statistical spread inherent to the ERO Monte Carlo simulations. They were calculated by repeating the same simulation several times but each time with a different seed for the random number generator and then calculating the standard deviation on the effective D/XB values. The square data points represent the ERO simulations using the measured electron temperature, while the triangular data points represent the ERO simulations with a 30% lower electron temperature. The simulations with lower electron temperature were performed because it was shown by local Langmuir probe measurements that the methane injection can decrease the local electron temperature [101]. The comparison for the Balmer γ line shows that the agreement between the ERO simulations and the experiment is reasonable. The best agreement is obtained for the simulations without electric sheath and with neutralization and reinjection of particles hitting the nozzle top surface. The same conclusion was obtained by looking at the effective D/XB values for the Balmer δ line. For the CD Gerö band the deviation between simulations and experiment is larger. The simulation results are shifted towards higher effective D/XB values. This was also observed in [100] and is probably due to uncertainties in the photo-emission coefficients for the CD Gerö band.

The comparison between ERO simulations and the experiment for the normalized Balmer α emission profiles and for the effective D/XB values for the Balmer γ and δ lines shows a reasonable agreement. The best agreement is obtained for the case without sheath electric field around the nozzle and

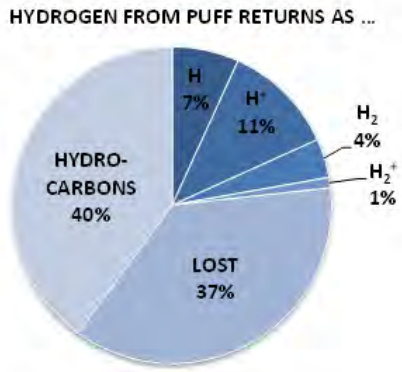

Figure 5.3: Pie chart showing how hydrogenic species from the injected methane returns to the surface in the TEXTOR roof limiter experiment

with neutralization and reinjection of tracked particles hitting the nozzle top surface. This agreement gives confidence that the transport and chemistry of the tracked hydrogenic species is simulated realistically.

5.3 Roof limiter experiment

As explained above previous ERO modelling studies of ^{13}C deposition in the TEXTOR roof limiter experiment described in 3.1.3 always required the assumption of strongly enhanced re-erosion of redeposited carbon to reproduce the very low experimental deposition efficiencies. However, the erosion of carbon by hydrogen species produced during dissociation of injected methane was not taken into account in these studies. This additional erosion was proposed as a possible explanation for the very low experimental ^{13}C deposition efficiencies. Therefore, the tracking of hydrogenic species from the dissociation of injected methane has been implemented in ERO to take into account this additional erosion. The ERO PSI model has also been updated by implementing the more realistic physical sputtering yields from Eckstein and hydrocarbon reflection probabilities from Tichmann. These changes in ERO are discussed in detail in 4.1.2. The effects on the modelling of the TEXTOR roof limiter experiment are discussed in this section.

5.3.1 Hydrogen returning to the limiter surface

As illustrated by the pie chart in figure 5.3 ERO simulations show that about 63% of the hydrogen from the break-up of injected methane returns to the limiter surface. A significant fraction of about 23% returns as H, H^+, H_2 or H_2^+. One can, therefore, expect a significant amount of chemical erosion due

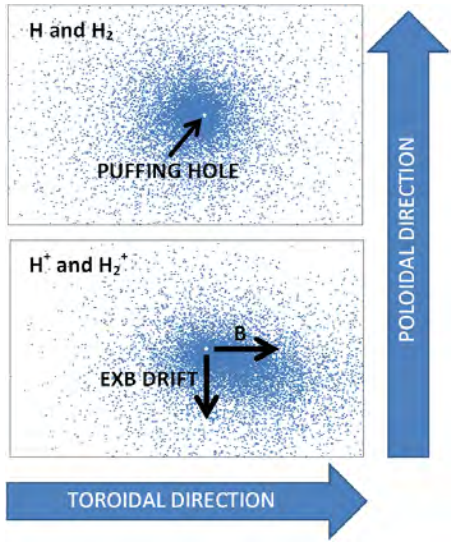

Figure 5.4: Pattern of hydrogenic neutrals and ions from the injected methane returning to the surface in the TEXTOR roof limiter experiment

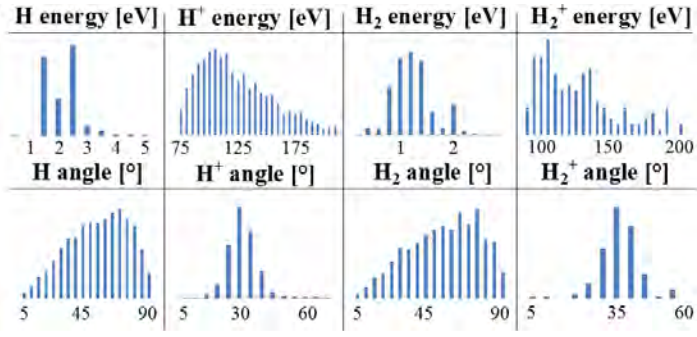

Figure 5.5: Angle and energy distributions of the hydrogenic species from the injected methane returning to the surface in the TEXTOR roof limiter experiment

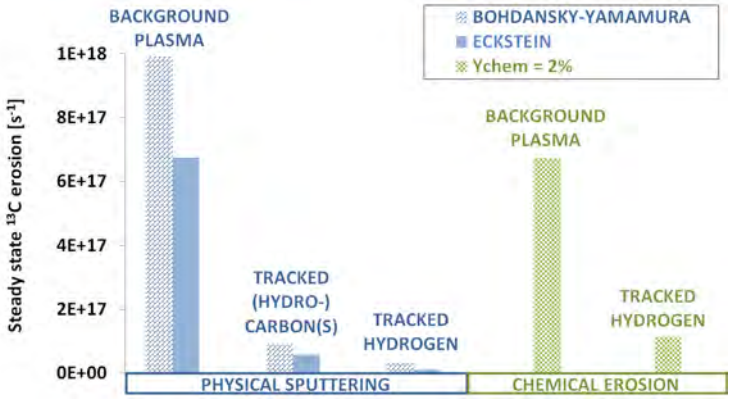

Figure 5.6: Comparison of the contributions to the re-erosion of redeposited ^{13}C in the TEXTOR roof limiter experiment

to these species. This was previously neglected by ERO. The remaining 40% of the returning hydrogen comes back as hydrocarbons. ERO kept account of the impact positions of the returning hydrogenic species. Figure 5.4 shows that the patterns of neutrals and ions look very different. For the neutrals the pattern is almost symmetric around the injection hole. The small shift to the left is probably due to the 40^o angle between surface normal and methane injection direction. The elongated pattern of the ions is clearly caused by the movement along the magnetic field lines together with the $E \times B$ drift. Also the impact energies and angles of the hydrogenic species were stored by ERO. The distributions are shown in figure 5.5. H and H_2 have energies in the range $1 - 2$ eV and have a broad angular distribution. H^+ and H_2^+ have a Boltzmann-like energy distribution with a maximum around 120 eV. This agrees well with the expected $3kT_e$ sheath potential drop at the puffing hole where T_e is around 40 eV. The angular distribution is peaked with maxima at 30^o and 35^o with respect to the surface normal for H^+ and H_2^+ respectively.

5.3.2 Contributions to re-erosion of redeposited ^{13}C

Figure 5.6 compares the different contributions to the steady-state re-erosion of redeposited ^{13}C at the roof limiter surface during the injection of $^{13}CH_4$ in ERO. The left side shows physical sputtering. A distinction is made between the effects of the background plasma and the tracked particles produced by break-up of the injected methane. The results are given both for the old BohdanskyYamamura and the new Eckstein sputtering yields. It can be seen that both for the background plasma and the tracked particles

the average sputtering yields for the new Eckstein data are significantly lower than for the old Bohdansky−Yamamura data. The use of the new data will, therefore, increase the simulated ^{13}C deposition efficiency. One can also see that the contribution of physical sputtering by the tracked hydrogenic species is negligible for the conditions of the roof limiter experiment in TEXTOR. This is caused by the fact that the flux of hydrogen ions from the background plasma averaged over the roof limiter is almost two orders of magnitude higher than that of the hydrogenic species from the injected methane. Only very locally around the injection hole the flux of hydrogen ions from the background plasma and the methane injection are comparable. Further, hydrogen ions from the background plasma on average have higher impact energies of about 300 eV in comparison with 120 eV for hydrogen ions from the injected methane. This leads to about five times higher physical sputtering yields for the background plasma ions in comparison with the hydrogen ions from the injected methane. On the right hand side chemical erosion is given. A constant chemical erosion yield of 2% was assumed both for background and tracked hydrogen according to spectroscopic measurements. Also here a distinction is made between background plasma and tracked particles. One can see that due to the equal chemical erosion yield for background and tracked hydrogenic species the contribution of chemical erosion by the tracked hydrogenic species is not negligible. Taking this additional erosion into account will decrease the simulated ^{13}C deposition efficiency.

5.3.3 Hydrocarbon reflection probabilities

Table 5.1 shows the new reflection probabilities for the different hydrocarbon molecules according to Tichmann's formulas. The probabilities were averaged over the angle and energy distribution of the respective molecules returning to the roof limiter surface as simulated by ERO. It can be seen that the results are very similar to the reflection probabilities of 0.1 and 1.0 that were previously assumed for respectively ions and neutrals. The reflection probabilities averaged over all species according to the number of species returning to the roof limiter surface are 0.29 and 0.19 respectively for Tichmanns formulas and the old approach. Therefore, one can expect a smaller simulated ^{13}C deposition efficiency with Tichmanns formulas.

5.3.4 ^{13}C deposition

Table 5.2 lists the ^{13}C deposition efficiencies for different ERO simulations. In the first simulation the old approaches were used for physical sputtering yields and molecular reflection probabilities. Additional chemical erosion by tracked hydrogen from the break-up of injected methane was not taken into account. The next three simulations were performed to look at the effect of the new Tichmann molecular reflection data, the new Eckstein sputtering

Table 5.1: Tichmann reflection probabilities averaged by ERO for the hydrocarbons returning to the surface in the TEXTOR roof limiter experiment

Species	Ion	Neutral
$\mathbf{CH_4}$	0.12	-
$\mathbf{CH_3}$	0.08	0.99
$\mathbf{CH_2}$	0.06	0.98
CH	0.05	0.70

Table 5.2: ERO ^{13}C deposition efficiencies for the TEXTOR roof limiter experiment

ERO run	Deposition efficiency
Old run	53.9%
Tichmann reflection	53.7%
Eckstein sputtering	57.3%
Hydrogen tracking	50.9%
All three improvements	53.4%
All three improvements with enhancement factor 50	0.5%
Experimental	0.3%

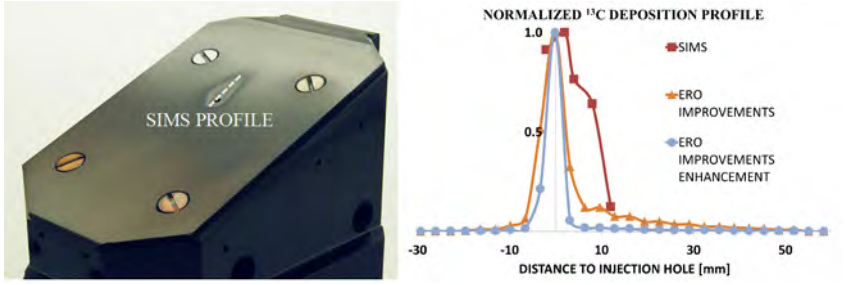

Figure 5.7: Comparison of the ^{13}C deposition profiles in the TEXTOR roof limiter experiment simulated by ERO and measured by SIMS

data and the addition of chemical erosion by tracked hydrogen from the break-up of injected methane. As expected the use of Tichmanns molecular reflection probabilities leads to a very small decrease of the deposition efficiency. The Eckstein sputtering data increases the deposition efficiency by 3%. The addition of chemical erosion by tracked hydrogen from the break-up of injected methane lowers the deposition efficiency with 3%. If all improvements are switched on, the resulting ^{13}C deposition efficiency is 53.4%. This is very close to the original value of 53.9% and much larger than the typical experimentally observed values around 0.3%. Only with an enhancement factor of about 50 for both physical and chemical re-erosion of redeposited carbon, the low experimental values could be reproduced. This shows that the update of the PSI database in ERO has only a very small effect on the simulated ^{13}C deposition efficiency and confirms the need for enhanced re-erosion of redeposited carbon to get agreement between ERO modelling and experimental observations.

Finally, also the spatial distribution of the deposited ^{13}C has been studied. On the left hand side in figure 5.7 the direction of the considered ^{13}C deposition profile along the centre of the deposition pattern is shown. On the right hand side a comparison is given between the normalized profiles from a SIMS measurement and an ERO run with all improvements included, without and with enhancement factor 50 for the re-erosion of redeposited carbon. The agreement of the shapes is reasonable, though not perfect. Both profiles are strongly peaked around the puffing hole, but as in previous studies the SIMS profile is somewhat broader than the simulated profile. As was found already in the previous studies the width of the profile depends strongly on the assumed hydrocarbon reflection probabilities. One can easily get agreement with the experiment by increasing the hydrocarbon reflection probabilities and decreasing the enhancement factor for re-erosion of redeposited carbon. This is because the enhanced re-erosion is thought to be an in-situ effect caused by too many species trying to stick to the surface while being bombarded by a large flux of energetic ions. The species are then eroded before they can manage to properly stick to the surface. Thus it is something in between an enhanced re-erosion and an enhanced reflection. Therefore, it is required to combine enhancement factors for the re-erosion and increased reflection probabilities to get agreement between experiments and simulations for both the deposition efficiency and the deposition profile.

5.4 Conclusions

- Literature shows clear indications for an enhanced re-erosion mechanism for redeposited species in different fusion relevant machines and for different materials both in purely experimental studies and in modelling studies with different material migration codes.
- The ERO plasma-surface interaction model was improved during this

work by implementing tracking of hydrogenic species produced by dissociation of injected methane, new Eckstein physical sputtering yields and new Tichmann hydrocarbon reflection probabilities.

- ERO modelling of the hydrogen Balmer line emission due to hydrogen produced by dissociation of injected methane in the TEXTOR nozzle experiment has shown that the transport and chemistry of the tracked hydrogenic species implemented during this work is simulated realistically in ERO.

- ERO modelling of the ^{13}C deposition from the methane injected in the TEXTOR roof limiter experiment with the improved plasma-surface interaction model implemented during this work shows that the improvements have only a small effect on the simulated ^{13}C deposition efficiency. This study confirms the need to assume enhanced re-erosion of redeposited carbon to reproduce with ERO the very small ^{13}C deposition efficiencies observed experimentally in the TEXTOR roof limiter experiment.

- The main conclusion of this chapter is that enhanced re-erosion of redeposited species is a very important issue that strongly influences the erosion/deposition balance in fusion relevant devices. As to the current understanding it is caused by too many species trying to stick to the surface while being bombarded by a large flux of ions. The sticking species are then eroded before they manage to stick properly to the surface. It is of primordial importance to get a better understanding of the phenomenon in order to be able to make reliable predictions for the erosion/deposition balance in future fusion devices.

Chapter 6

Characterization of the VISIONI plasma simulator

The main objective of the second part of this work was the start-up of material migration studies in VISIONI by means of dedicated experiments and ERO simulations to further study the enhanced re-erosion of deposited species. As explained in 4.1 ERO modelling requires the input of the geometry, the electric field, the magnetic field and the plasma parameters of the modelled device. From the experimental point of view it is also important to have a good understanding of the dependence of the plasma parameters on the operational parameters. Therefore, an important part of this work considers the detailed characterization of VISIONI by means of analytical calculations, numerical simulations and measurements. The characterization of the magnetostatic field is treated in the first section of this chapter. The next section deals with the characterization of the electrostatic field. The third section discusses the characterization of the plasma. The fourth section describes the study performed to investigate the feasibility of an optical emission spectroscopy system for VISIONI as an aid to study material migration. The main conclusions of this chapter are summarized in the last section.

6.1 Characterization of the magnetic field

As explained in 3.2.3 and shown again in figure 6.1 the side wall and bottom plate of the VISIONI plasma chamber are lined with permanent Sm_2Co_{17} magnets in a multidipole configuration. The magnetic field in VISIONI strongly influences the path of the charged plasma particles. Therefore, the magnetic field as a function of the location in the plasma chamber is an important input for the ERO code and the VMCPT code. In the first subsection the magnetostatic field in VISIONI is calculated analytically.

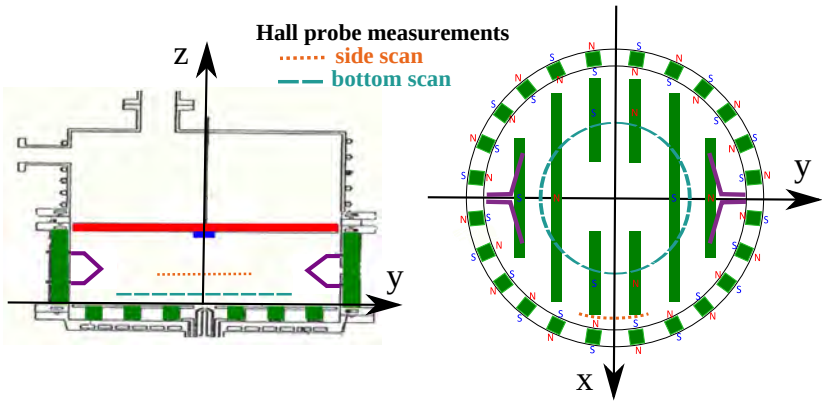

Figure 6.1: Location of the Hall probe scans in the VISIONI plasma chamber

In the second subsection the analytical calculations are benchmarked and verified by means of Hall probe measurements. The last subsection discusses the results.

6.1.1 Analytical calculation

For the analytical calculation it is assumed that all permanent Sm_2Co_{17} magnets are magnetized homogeneously along their north-south axis with the same strength and that the SS304 stainless steel between the magnets and the inside of the plasma chamber does not significantly influence the magnetic field. With these assumptions it suffices to derive an analytical expression for the magnetic field generated by a single rectangular bar magnet. For each magnet in VISIONI this expression then has to be modified by a coordinate transformation to go from the local coordinate system of the magnet indicated in figure 6.2 to the global coordinate system of VISIONI shown in figure 6.1. The total magnetic field in VISIONI can then be obtained by adding the contributions from all magnets together. Therefore, we now concentrate on the case of one rectangular bar magnet.

The local x, y and z-axis are taken along three edges of the magnet with the z-axis pointing towards the northern magnetic pole parallel with the north-south axis as shown in figure 6.2. The macroscopic magnetic field is created by atomic-level magnetic dipoles related to the electron orbits around the nuclei and the electron spins. These dipoles can be regarded as being created by microscopic electric current loops. Neighbouring current loops in the bulk of the magnets cancel each other out because the magnetization is assumed to be homogeneous. The only net current is located at the surface of the magnets. Therefore, a permanent rectangular magnet that is magnetized homogeneously along one of its axes is equivalent

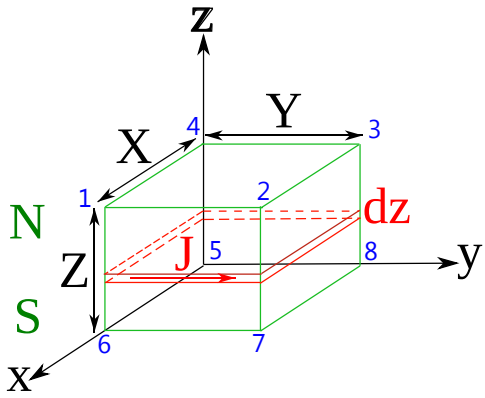

Figure 6.2: Sketch for the magnetic field calculation for a rectangular permanent magnet

to an infinitely closely wound rectangular solenoid with an electric current homogeneously distributed over its surface in the direction corresponding to the right-hand-rule. This equivalence can also be proven more rigorously starting from Maxwell's equations. This is shown briefly in appendix B. The derivation can be found in more detail in [174]. With this picture in mind, the magnetic field generated by a single magnet can be calculated by appropriately integrating Biot-Savart's law. According to this law the magnetic field $d\vec{B}$ as function of the location $\vec{r_p} = (x_p, y_p, z_p)$ due to an infinitesimal current carrying element positioned at position $\vec{r} = (x, y, z)$ can be calculated from

$$d\vec{B} = \frac{\mu_0}{4\pi} \frac{I d\vec{l} \times (\vec{r_p} - \vec{r})}{|\vec{r_p} - \vec{r}|^3} \tag{6.1}$$

where I is the current running through the infinitesimal element and $d\vec{l}$ an infinitesimal vector in the direction of the current. To get the magnetic field $\vec{B} = (B_x, B_y, B_z)$ at location $\vec{r_p}$ due to the complete rectangular magnet, this equation has to be integrated first over a rectangular current loop corresponding to the cross section of the magnet in the xy-plane and then over the height of the magnet along the z-axis. This tedious calculation is elaborated in appendix C. The resulting equations are

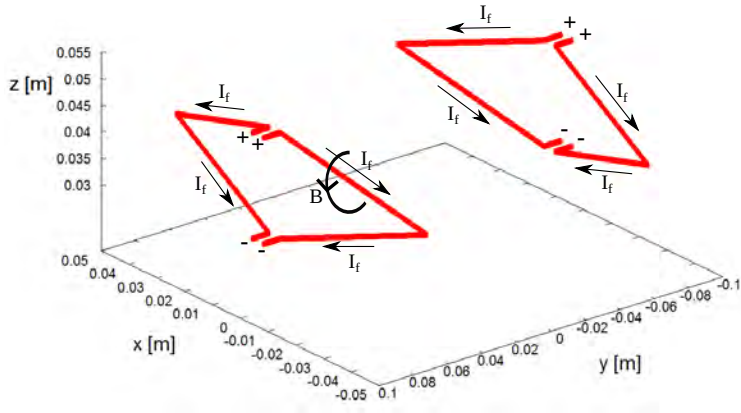

Figure 6.3: Magnetic field due to the heating current through the tungsten filaments

$$B_x = \frac{\mu_0 J_s}{4\pi} \sum_{i=1}^{8} (-1)^i \ln\left(-(y_p - y_i) + \sqrt{(x_p - x_i)^2 + (y_p - y_i)^2 + (z_p - z_i)^2}\right)$$

$$B_y = \frac{\mu_0 J_s}{4\pi} \sum_{i=1}^{8} (-1)^i \ln\left(-(x_p - x_i) + \sqrt{(x_p - x_i)^2 + (y_p - y_i)^2 + (z_p - z_i)^2}\right)$$

$$B_z = \frac{\mu_0 J_s}{4\pi} \sum_{i=1}^{8} (-1)^i \arctan\left(\frac{(x_p - x_i)(y_p - y_i)}{(z_p - z_i)\sqrt{(x_p - x_i)^2 + (y_p - y_i)^2 + (z_p - z_i)^2}}\right)$$

The summations are over the 8 corners of the magnet at the positions $\vec{r_i} = (x_i, y_i, z_i)$. Hence, each corner of the magnet can be regarded as having its own contribution to the total magnetic field. As can be seen from the numbering in figure 6.2 the signs of these contributions are opposite for neighbouring corners. J_s is the so called equivalent surface current density. This is the surface current density of the infinitely closely wound rectangular solenoid equivalent with the rectangular magnet and has units A/m. As deduced in appendix B it is related to the remanent magnetic field or remanence B_r of the magnet by the equality $\mu_0 J_s = B_r$.

These results are confirmed by similar calculations in literature. The calculations in [175] are also based on the electric current point of view. The resulting equations are equivalent to the equations found above, but they were not further simplified as in appendix C. The calculations in [176] are based on the concept of magnetic charges and result in the same equations as found above.

During plasma operation a heating current I_f in the range $70 - 90$ A is running through the tungsten filaments from the positive leads at the top

to the negative leads at the bottom as shown in figure 6.3 in the global coordinate system. This relatively strong electric current creates an additional magnetic field. It can easily be calculated analytically by integrating Biot-Savart's law (6.1) along the filaments. Actually this has already been done for a straight wire in appendix C as a first step in calculating the field generated by a rectangular permanent magnet. From this calculation it follows that the field at the location $\vec{r_p}$ due to a straight wire of length L centred on the origin along the z-axis is given by

$$
\begin{aligned}
B_x &= \frac{\mu_0 I}{4\pi}\left(\frac{y_p(z_p-\frac{L}{2})}{(x_p^2+y_p^2)\sqrt{x_p^2+y_p^2+(z_p-\frac{L}{2})^2}}-\frac{y_p(z_p+\frac{L}{2})}{(x_p^2+y_p^2)\sqrt{x_p^2+y_p^2+(z_p+\frac{L}{2})^2}}\right)\\
B_y &= \frac{\mu_0 I}{4\pi}\left(\frac{x_p(z_p+\frac{L}{2})}{(x_p^2+y_p^2)\sqrt{x_p^2+y_p^2+(z_p+\frac{L}{2})^2}}-\frac{x_p(z_p-\frac{L}{2})}{(x_p^2+y_p^2)\sqrt{x_p^2+y_p^2+(z_p-\frac{L}{2})^2}}\right)\\
B_z &= 0
\end{aligned}
$$

For each straight segment of the filaments these equations then have to be modified by a coordinate transformation to go from the local coordinate system of the filament segment to the global coordinate system shown in figures 6.1 and 6.3. The contributions from all filament segments have to be added to the magnetic field of the permanent magnets. The field due to the filaments is weak compared to the field of the permanent magnets. The maximum filament field is only about 0.05 T compared to 0.2 T for the permanent magnets. However, locally around the filaments this field is about one order of magnitude higher than the permanent magnet field. Therefore, the filament field is dominant in this region and has to be taken into account.

6.1.2 Hall probe measurements

The equivalent surface current density J_s in the equations for the magnetic field was initially an unknown parameter because the remanence of the magnets was not accurately known. In order to determine J_s, a magnetic field measurement of at least one component of the magnetic field on at least one location had to be performed in absence of the filament magnetic field. Even more desirable was a spatial scan of the magnetic field to check also whether the assumptions made to come to the analytical equations are really valid.

The magnetic field measurements in the VISIONI plasma chamber were performed with a Honeywell SS94A2D Hall sensor. The experimental set-up for the Hall probe measurements is shown in figure 6.4. The sensor was mounted on a rod allowing the sensor to be moved vertically, radially and circularly. The rod could also be rotated locally over 90° such that the

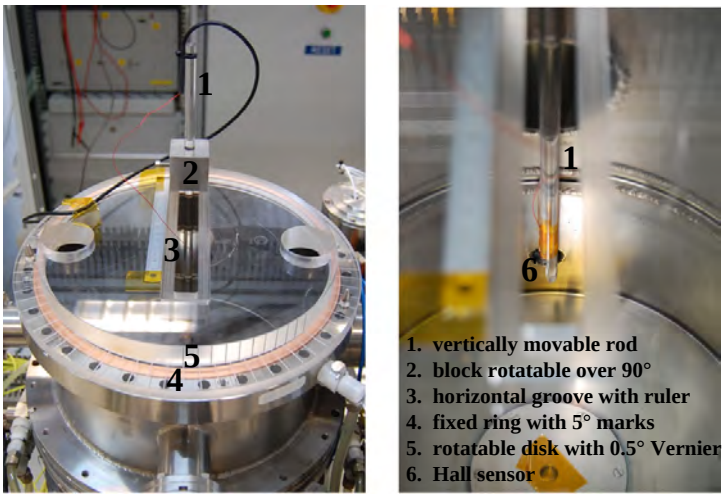

Figure 6.4: Setup for the Hall probe measurements in VISIONI

active area of the sensor was aligned either parallel with or perpendicular to the plasma chamber side walls. Various spatial scans of both magnetic field components were made to determine J_s and to verify the approximations made during the calculation.

6.1.3 Results and discussion

Figure 6.5 shows the results for the two measurement scans indicated with the dotted and dashed lines in figure 6.1. The field due to the filaments was not taken into account in these calculations because the heating current was switched of during the measurements. The left side of figure 6.5 shows the result of the side magnetic field scan along a 30° circle segment 4 cm above the bottom of the vessel and 1 cm away from the vacuum vessel side walls with the side magnets (dotted line in figure 6.1). The measured magnetic field components *Bpar* parallel with and *Bper* perpendicular to the vessel walls are compared with the analytical calculations. By fitting the calculation to the measurements a value of $\mu_0 J_s = 1.12\ T$ was obtained for the initially unknown equivalent surface current density J_s. The order of magnitude is in agreement with typical tabulated values for the remanence $B_r = \mu_0 J_s$ of Sm_2Co_{17} magnets [115]. The error bars on the measurement arise from the 5% error in the reading of the Hall sensor and the uncertainty in the sensor position. A very good agreement can be observed between measurements and calculations for both magnetic field components. The right side of figure 6.5 shows similar results for the bottom scan along a full circle 5 cm away from the vessel walls and 1 cm above the bottom of

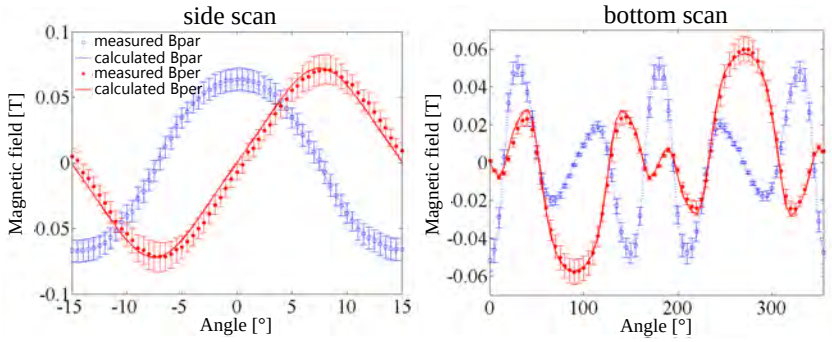

Figure 6.5: Comparison of measurements and calculations of the VISIONI magnetic field

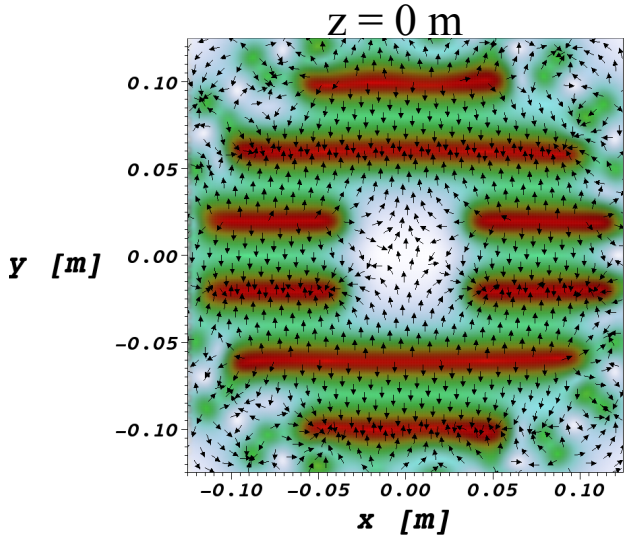

Figure 6.6: Horizontal cross section of the magnetic field in VISIONI at the bottom of the plasma chamber

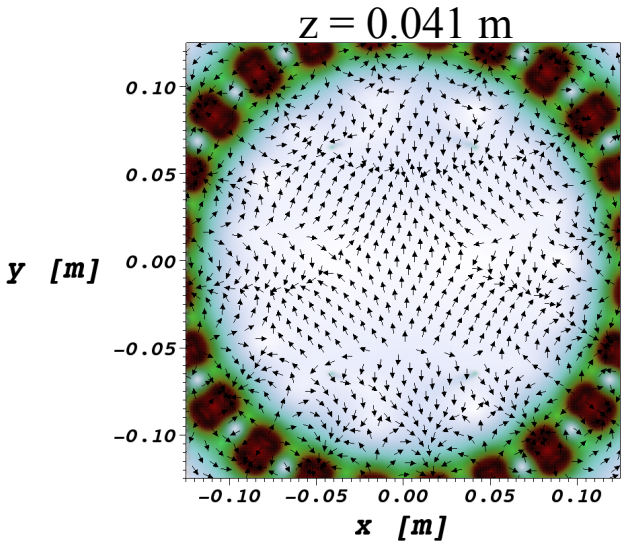

Figure 6.7: Horizontal cross section of the magnetic field in VISIONI at the centre of the plasma chamber

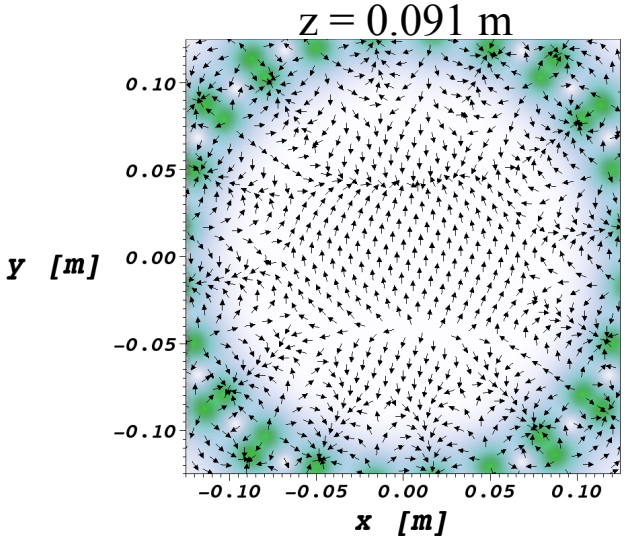

Figure 6.8: Horizontal cross section of the magnetic field in VISIONI at the top of the plasma chamber

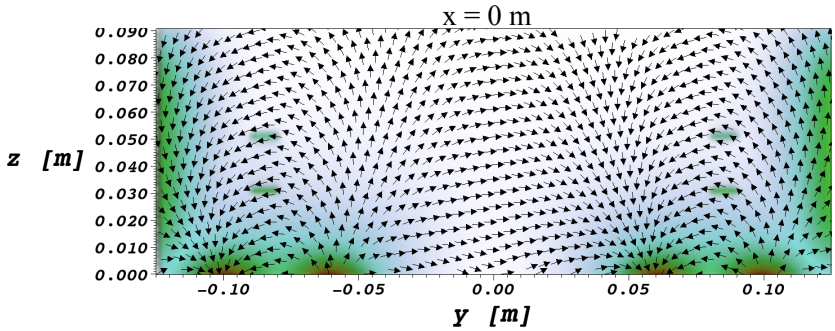

Figure 6.9: Vertical cross section of the magnetic field in VISIONI through the centre of the plasma chamber

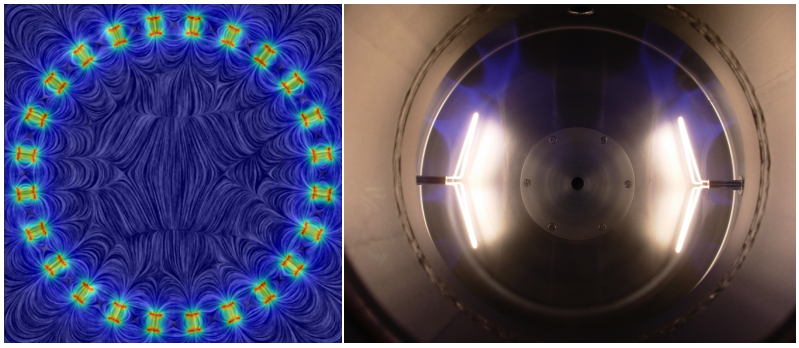

Figure 6.10: Horizontal cross section of the magnetic field lines in VISIONI at the centre of the plasma chamber in comparison with the visible light emission during plasma operation

the vessel with the bottom magnets (dashed line in figure 6.1). The same value $\mu_0 J_s = 1.12\ T$ was used. Again there is very nice agreement between measurements and calculations. Additionally also the perpendicular magnetic field component was measured in front of all 24 side magnets to check whether they all have the same strength as was assumed in the calculations. The deviation from the calculation was never more than 2% and, hence, within the error bars of the measurement.

The magnetic field in VISIONI has been calculated on three horizontal and one vertical cross section. The results are given in figures 6.6-6.9. The arrows show the direction of the magnetic field, while the colours correspond to the magnetic field intensity. The structure of the magnetic field can be seen more easily in figure 6.10. It shows at the left a projection of the

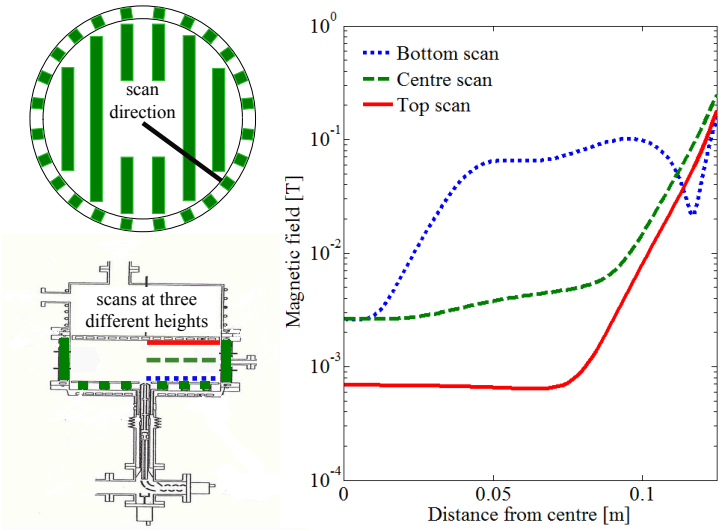

Figure 6.11: Radial profiles of the VISIONI magnetic field strength

magnetic field lines on a horizontal cross section through the centre of the plasma chamber. This picture was made with the JAVA tool [177] based on the Line Integral Convolution technique [178]. One can distinguish the typical cusps of a multidipole magnetic field. These are also clearly visible in the light emission of the plasma shown in the visible light photograph at the right of figure 6.10. To get a better impression of how fast the magnetic field drops when moving away from the magnets, figure 6.11 shows calculated radial profiles of the magnetic field strength. The profiles were taken from the axis of the plasma chamber towards one of the side magnets at three different heights. Close to the side magnet the magnetic field was calculated to be about 0.2 T, which is in perfect agreement with the measurements performed earlier in VISIONI [107]. Towards the centre of the plasma chamber the field drops rapidly over about two orders of magnitude. The central part of the chamber, especially around the sample, can be considered as a field-free region.

6.2 Characterization of the electrostatic field

As explained in 3.2.2 and shown in figure 6.12 the tungsten filaments and the target plate in VISIONI are biased negatively with respect to the rest of the plasma chamber. The filaments are typically at -80 V with respect to the chamber walls. The target plate is typically at -100 V with respect to the chamber walls. These two applied potential differences lead to a

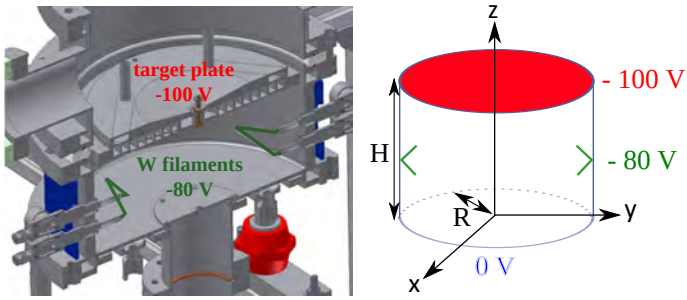

Figure 6.12: Applied potential differences in VISIONI

strong electrostatic field inside the device. During operation this field is of course modified by plasma space charges. In this section the electrostatic field is calculated in absence of the plasma. The effect of the plasma on the electrostatic field will be discussed in the next section.

To calculate the electrostatic field in VISIONI we start from Gauss's law

$$\vec{\nabla} \cdot (\overleftrightarrow{\epsilon} \cdot \vec{E}) = \rho. \tag{6.2}$$

In vacuum the permittivity tensor $\overleftrightarrow{\epsilon}$ can be set equal to the scalar vacuum permittivity $\epsilon_0 = 8.8541 \cdot 10^{-12}$ F/m. In absence of plasma $\rho = 0$. In the electrostatic case $\vec{\nabla} \times \vec{E} = 0$ and the electric field can be written in terms of the electric potential as $\vec{E} = -\vec{\nabla} V$. Gauss's law is then transformed into Laplace's equation

$$\nabla^2 V = \frac{\partial^2 V}{\partial x^2} + \frac{\partial^2 V}{\partial y^2} + \frac{\partial^2 V}{\partial z^2} = 0. \tag{6.3}$$

This equation has to be solved in combination with the appropriate boundary conditions in accordance with figure 6.12

$$V(x, y, 0) = 0 \quad , \text{ for all } (x, y) \tag{6.4}$$
$$V(x, y, z) = 0 \quad , \text{ for all } z \text{ and } x^2 + y^2 = R^2 \tag{6.5}$$
$$V(x, y, H) = -100 \quad , \text{ for all } (x, y) \tag{6.6}$$
$$V(x, y, z) = -80 \quad , \text{ for } (x, y, z) \text{ on the filaments} \tag{6.7}$$
$$\frac{\partial V}{\partial y}(0, y, z) = 0 \quad , \text{ for all } (y, z) \tag{6.8}$$
$$\frac{\partial V}{\partial x}(x, 0, z) = 0 \quad , \text{ for all } (x, z). \tag{6.9}$$

The conditions (6.4-6.7) are Dirichlet boundary conditions fixing the applied potential differences. Due to symmetry only one quarter of the system with

$x \geq 0$ and $y \geq 0$ has to be calculated. (6.8) and (6.9) are Neumann boundary conditions expressing this two-fold mirror symmetry of the system.

The presence of the filaments breaks the cylindrical symmetry and makes it impossible to solve the problem analytically. Therefore, a simple finite difference code has been written. In such a code all functions and equations are discretized on a grid with spacing h. The function $V(x, y, z)$ is replaced by the discrete version

$$V_{i,j,k} = V(ih, jh, kh)$$

with i,j and k integral numbers. By Taylor expansion one can prove that

$$\frac{\partial^2 V}{\partial x^2}(ih, jh, kh) = \frac{V_{i+1,j,k} - 2V_{i,j,k} + V_{i-1,j,k}}{h^2} + O(h^2). \tag{6.10}$$

With this result Laplace's equation (6.3) can be replaced by the finite difference equation

$$V_{i,j,k} = \frac{V_{i+1,j,k} + V_{i-1,j,k} + V_{i,j+1,k} + V_{i,j-1,k} + V_{i,j,k+1} + V_{i,j,k-1}}{6} \tag{6.11}$$

The Dirichlet boundary conditions (6.4), (6.5), (6.6) and (6.7) are easily translated into their discrete equivalents. Using the discrete version of Laplace's equation (6.11) and

$$\frac{\partial V}{\partial x}(ih, jh, kh) = \frac{V_{i+1,j,k} - V_{i-1,j,k}}{2h} + O(h^2).$$

from Taylor expansion, the Neumann boundary conditions (6.8) and (6.9) become

$$V_{0,j,k} = \frac{2V_{1,j,k} + V_{0,j+1,k} + V_{0,j-1,k} + V_{0,j,k+1} + V_{0,j,k-1}}{6} \text{ for all } (j,k) \tag{6.12}$$

$$V_{i,0,k} = \frac{V_{i+1,0,k} + V_{i-1,0,k} + 2V_{i,1,k} + V_{i,0,k+1} + V_{i,0,k-1}}{6} \text{ for all } (i,k) \tag{6.13}$$

The discrete version of Laplace's equation (6.11), the discrete Dirichlet boundary conditions and the discrete Neumann boundary conditions (6.12) and (6.13) form a set of coupled algebraic equations. It can be solved either by matrix inversion or iteratively. In this case it was chosen to solve the problem iteratively because it was easiest to implement and did not take too much computational time.

To check the finite difference code for bugs, the electric potential was calculated first for the case without the filaments. This case has an analytical solution. The calculation is given in appendix D. The electric potential is given by

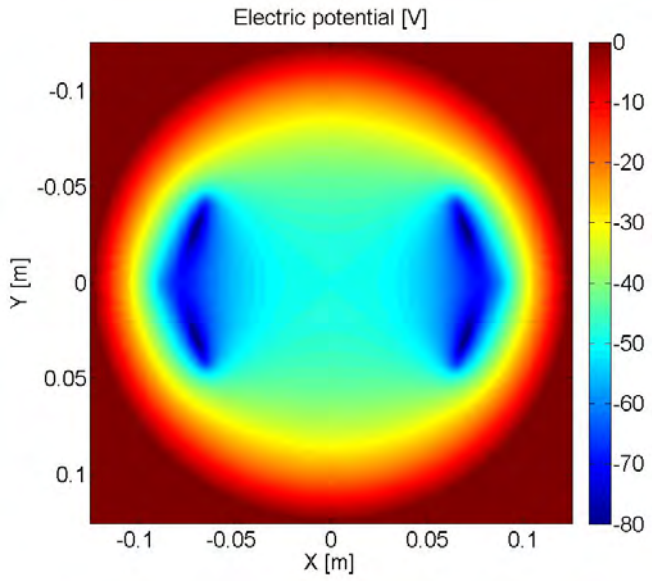

Figure 6.13: Horizontal cross section of the electrostatic field in VISIONI without plasma

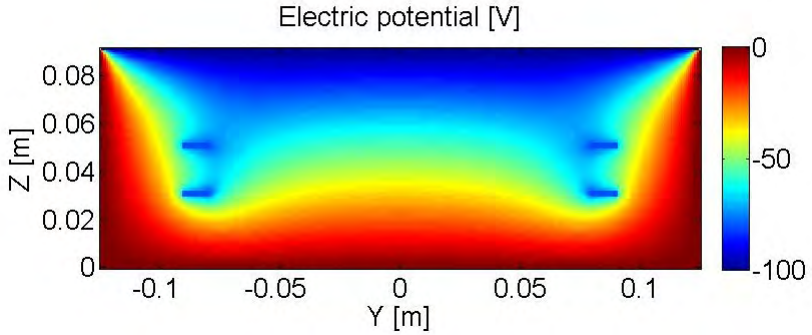

Figure 6.14: Vertical cross section of the electrostatic field in VISIONI without plasma

$$V(r,z) = \sum_{n=0}^{n=+\infty} -\frac{200 J_0\left(\frac{\chi_{0n}}{R} r\right) \sinh\left(\frac{\chi_{0n}}{R} z\right)}{\chi_{0n} J_1(\chi_{0n}) \sinh\left(\frac{\chi_{0n}}{R} H\right)}.$$

Cylindrical coordinates are used because of cylindrical symmetry. J_0 is the 0^{th} Bessel function and χ_{0n} is the n^{th} zero of this function. The finite difference calculation was in perfect agreement with this analytical solution and, therefore, proven to work correctly. An impression of the electric potential calculated by the finite difference code with the filament field included is shown on the horizontal and vertical cross sections in figures 6.13 and 6.14. The electric field can of course easily be calculated by taking the negative gradient of the electric potential.

6.3 Characterization of the plasma

This section focusses on the properties of a deuterium plasma in VISIONI. Most of the results come from simulations with the VMCPT plasma simulation code. This code was developed from scratch during this work as discussed in detail in 4.2. The simulation results are compared with measurements. Most measurements were performed with the movable Langmuir probe. This probe was specially designed and developed for VISIONI during this work. The design of the probe was discussed in 3.2.6.3. The theory behind Langmuir probe measurements was briefly treated in 2.3.7. The automatic analysis software that was developed during this work to derive the plasma parameters from the IV characteristic was described in 4.3. The ion and neutral composition in the plasma chamber was measured with the quadrupole mass and energy analyser that was described in 3.2.6.2.

The first subsection explains which free parameters are governing the plasma properties in VISIONI and the VMCPT code and how the VMCPT code was benchmarked against the experimental results. The next subsection describes the characteristics of the electron energy distribution function. In 6.3.3 the plasma composition is discussed. The spatial dependence of the plasma properties is treated in 6.3.4. The effect of variations of the free parameters on the plasma properties is studied in 6.3.5. The last subsection discusses the importance of different processes in the plasma.

6.3.1 Free parameters in VISIONI and VMCPT

Three free parameters can be used to tune the plasma in VISIONI: the filament heating current I_f, the discharge potential difference V_{ac} and the neutral gas pressure p. The first parameter is the heating current I_f running through the tungsten filaments. This current is used to regulate the filament temperature T_f and thus also the primary electron emission rate R_{pe}. This requires some more elaboration.

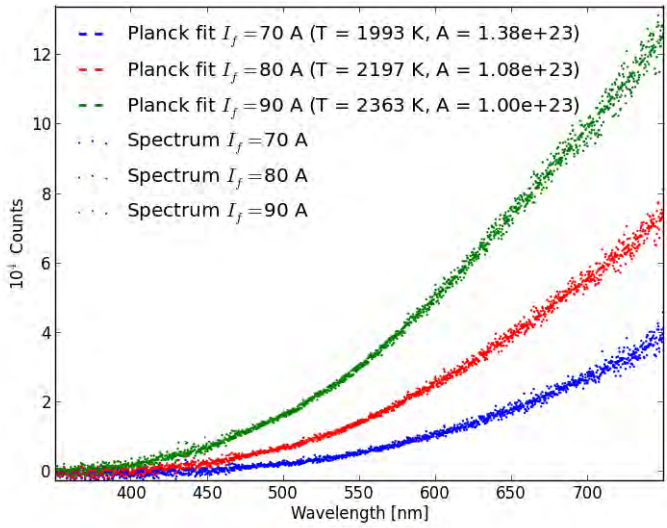

Figure 6.15: Planck fitting of the tungsten filament light emission spectra in VISIONI

The relation between I_f and T_f was investigated by means of optical emission spectroscopy with the AvaSpec-2048-USB2 compact overview spectrometer as described in 3.2.6.1. The spectral emissivity of tungsten in the wavelength range of the spectrometer is about 0.4 with a variation of only about 10% [179]. Figure 6.15 shows that the optical emission spectra of the tungsten filaments indeed can be fitted successfully by Planck black body radiation curves of the form

$$\Phi(\lambda; A, T_f) = \frac{A}{\lambda^5} \frac{1}{\exp\left(\frac{hc}{\lambda T_f}\right) - 1} \tag{6.14}$$

with λ the wavelength, h the Planck constant, c the speed of light and as fitting parameters the filament temperature T_f and the normalization coefficient A depending on the collection optics. The multiparameter fitting was done with the *lmfit* package [169] using the Levenberg-Marquardt algorithm. In this way it was found that T_f varies in the range 2000-2400 K for I_f in the typical range 70-90 A. This is in good agreement with the linear relation

$$T_f(I_f) = 16.875 I_f + 862.64 \tag{6.15}$$

which resulted from a fit to previous pyrometer measurements in VISIONI.

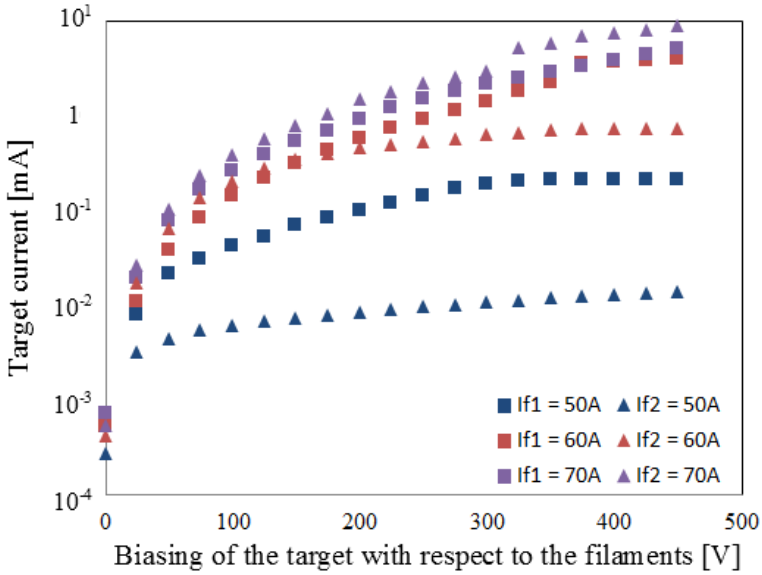

Figure 6.16: Target current measured in VISIONI as a function of the target biasing for different filament heating currents in order to determine the primary electron emission rate

The filament temperatures expected according to this relation for some typical heating currents are listed in table 6.1.

Let us now have a look at the relation between T_f and R_{pe}. As discussed in 2.4.1 for the typical values of the potential difference V_{ac} between the tungsten filaments and the side and bottom of the plasma chamber around 80 V Schottky barrier lowering and Fowler-Nordheim tunnelling can be neglected. Therefore, R_{pe} can be calculated from T_f according to the Richardson-Dushman equation

$$R_{pe} = \frac{A_f \lambda A_R}{q_e} T_f^2 \exp\left(-\frac{E_W}{kT_f}\right) \tag{6.16}$$

with $A_f = 1.4 \cdot 10^{-3}$ m^2 the surface area of the tungsten filaments, A_R the Richardson constant, $\lambda = 0.517$ the correction factor to A_R for tungsten and $E_W = 4.55$ eV the work function for tungsten. The expected primary electron emission rates for the tungsten filaments at both sides of the plasma chamber together for some typical heating currents are also listed in table 6.1 and are typically in the range $10^{17} - 10^{19}$ s^{-1}.

This relation between T_f and R_{pe} was verified also experimentally in VISIONI. For this experiment the target plate was exceptionally biased

Table 6.1: Expectations for the tungsten filament temperature, the saturation current, the saturation voltage and the primary electron emission rate according to (6.15-6.17) for different values of the tungsten filament heating current

I_f [**A**]	T_f [**K**]	I_{sat} [**mA**]	V_{sat} [**V**]	R_{pe} [$\mathbf{s^{-1}}$]
50	1706	0.05	13	$6.33 \cdot 10^{14}$
60	1875	0.99	96	$1.23 \cdot 10^{16}$
70	2043	11.91	506	$1.45 \cdot 10^{17}$
80	2213	99.63	2087	$1.24 \cdot 10^{18}$
90	2381	623.57	7089	$7.78 \cdot 10^{18}$
100	2550	3090.60	20608	$3.86 \cdot 10^{19}$

positively with respect to the tungsten filaments with a biasing potential V_{tc} up to 500 V, while the side and bottom of the plasma chamber were kept floating such that the majority of the electrons was collected by the target plate. Furthermore, the experiment was performed at UHV conditions with a neutral gas pressure below 10^{-4} Pa in order to avoid significant ionization. Only one tungsten filament was heated at a time. The primary electron current collected by the target plate was then measured as function of V_{tc} for different values of I_f. The results are shown in figure 6.16. For low values of V_{tc} the collected current increased with increasing V_{tc}. As explained in 2.4.1.3 this is due to space charge effects. For sufficiently high biasing $V_{tc} \geq V_{sat}$ the emission limited regime is reached. In this regime the collected current is equal to the saturation current $I_{sat} = q_e R_{pe}$ with R_{pe} calculated according to the Richardson-Dushman equation (6.16). The critical biasing potential V_{sat} can be estimated from the one dimensional Child-Langmuir law

$$I_{sat} = \frac{4}{9} A_f \epsilon_0 \sqrt{\frac{2q_e}{m_e}} \frac{V_{sat}^{3/2}}{d^2} \tag{6.17}$$

with A_f the surface area of the tungsten filaments and $d = 0.04$ m the approximate distance between the tungsten filaments and the target plate. Table 6.1 lists the expected values for I_{sat} and V_{sat} for some typical values of I_f. In order to allow comparison with the measurements, these values are for the case that only the tungsten filaments at one side of the plasma chamber are activated at a time. The measured and predicted values for I_{sat} are in reasonable agreement with each other. Deviations from the predicted values and deviations between the two tungsten filaments are probably caused by aging effects as discussed below. Saturation could not be obtained for biasing up to 500 V for I_f above 70 A as could be expected from the predicted values for V_{sat} in table 6.1 which are largely above 500 V.

Space charge effects are not expected to limit the primary electron emission rate in VISIONI during plasma operation. The plasma potential profile was measured during operation along the central axis of the plasma chamber with the Langmuir probe as shown in figure 6.32. The plasma potential is a few volts positive with respect to the anode. As discussed in 2.4.1.3 this clearly indicates that VISIONI is operated in the temperature limited mode where the primary electron emission from the tungsten filaments is not limited by space charge effects.

Based on the above considerations one can calculate the primary electron emission rate R_{pe} from the applied filament heating current I_f by using the empirical formula (6.15) to calculate T_f from I_f and the Richardson-Dushman equation (6.16) to calculate R_{pe} from T_f. However, this approach has its limits. It was found that T_f can significantly deviate from the empirical relation (6.15). Firstly, the relation between T_f and I_f can change significantly during the lifetime of the filaments due to changes in crystallinity, impurity content and thickness. It was observed experimentally that the heating current needed to obtain a target current of 2 A decreases significantly during aging of the filaments from 90 A up to 70 A. Secondly, the discharge current running through the tungsten filaments leads to additional heating. This was confirmed during the optical emission spectroscopy measurements. It was found that the value of T_f determined by fitting of a Planck spectrum just after plasma operation was about 100 K higher than just before plasma operation, although I_f was kept constant during the whole experiment. This higher value of T_f in turn leads to a higher value of R_{pe} and thus also to a higher discharge current which leads then to further increase of T_f. This runaway effect was confirmed experimentally by the fact that during plasma operation the target current I_t is observed to increase gradually for constant I_f. Based on these findings it was decided for further experiments to adapt I_f such that I_t stays at a constant value. Only in this way constant plasma properties can be assured. Hence, I_f is not the value that one should refer to for specifying the plasma conditions. One should only use I_f as a parameter to regulate I_t which is a more significant parameter for characterizing the plasma conditions.

The other two free parameters in VISIONI are more straightforward to discuss. The second free parameter is the potential difference V_{ac} applied between the anode and the tungsten filaments. This parameter fixes the initial energy of the primary electrons emitted by the tungsten filaments because in the temperature limited operating regime the potential drop is concentrated in a thin sheath around the tungsten filaments as was discussed in 2.3.6 and 2.4.1.3.

The last free parameter is the neutral gas pressure p which is regulated by the pressure control valve. The neutral pressure determines the collisionality as collisions with neutrals are dominant in VISIONI due to the low ionization degree of the plasma. The standard operating conditions in VISIONI are characterized by a target current $I_t = 2$ A, a discharge potential

difference $V_{ac} = 80$ V and a neutral pressure $p = 0.3$ Pa.

The VMCPT code basically has the same free parameters as VISIONI. It was decided to specify the primary electron emission rate R_{pe} directly in the input file because the theoretical relations between I_f, T_f and R_{pe} can only be used to make a rough guess as was discussed in detail above. Hence, R_{pe} should be used as a fitting parameter tuned to get agreement between the simulated and measured target current I_t. Also the potential difference between the anode and the tungsten filaments V_{ac} and the neutral pressure p are specified directly in the input file. Of course these parameters should be set equal to their experimental counterparts. As explained in 4.2.4 the initial ion energy is an additional free parameter that was introduced in VMCPT to mimic the effect of the bulk electric field on the ions. Fitting of this parameter to get the best agreement between simulated and measured electron temperature and ion density was done for standard operating conditions and resulted in an initial ion energy of $0.3kT_e$. In principal this fitting should be done for each simulated operating condition. This is, however, very time consuming. Therefore, it was decided to use the value $0.3kT_e$ also for the other operating conditions simulated in the free parameter variation study presented in 6.3.5.

6.3.2 Electron energy distribution function

The electron energy distribution function or EEDF is a very important plasma property as it strongly determines the reaction rate coefficients. Figure 6.17 shows the fitting results for a Langmuir probe IV characteristic measured in VISIONI at standard operating conditions. The top plot shows how the ion contribution is removed from the total current by making a fit in the ion saturation region and subtracting this fit from the IV characteristic. The bottom plot shows that the electron current characteristic obtained in this way agrees very well with the assumption of a bi-Maxwellian EEDF. On the left side of the electron saturation region one can clearly distinguish two straight segments reflecting two Maxwellian electron populations. Apparently, the electron population in VISIONI consists of a cold bulk electron population with a temperature $T_{ec} = 2$ eV and a small fraction $f_{eh} = 0.02$ of hot electrons with a temperature $T_{eh} = 25$eV.

These findings contrast strongly with previous measurements obtained by using the sample as a Langmuir probe [180]. These measurements indicated a fully Maxwellian EEDF with a very high electron temperature in the range 5-10 eV. A combination of two effects is probably responsible for these deviating results. Firstly, the magnetic field has an important effect on the IV characteristic obtained with the sample. As shown in figure 6.9 the magnetic field at the sample is parallel to the sample surface. The parallel magnetic field strongly reduces the collection of cold electrons as their Larmor radius is comparable to the dimensions of the sample. The hot electron collection is less influenced by the magnetic field due to their

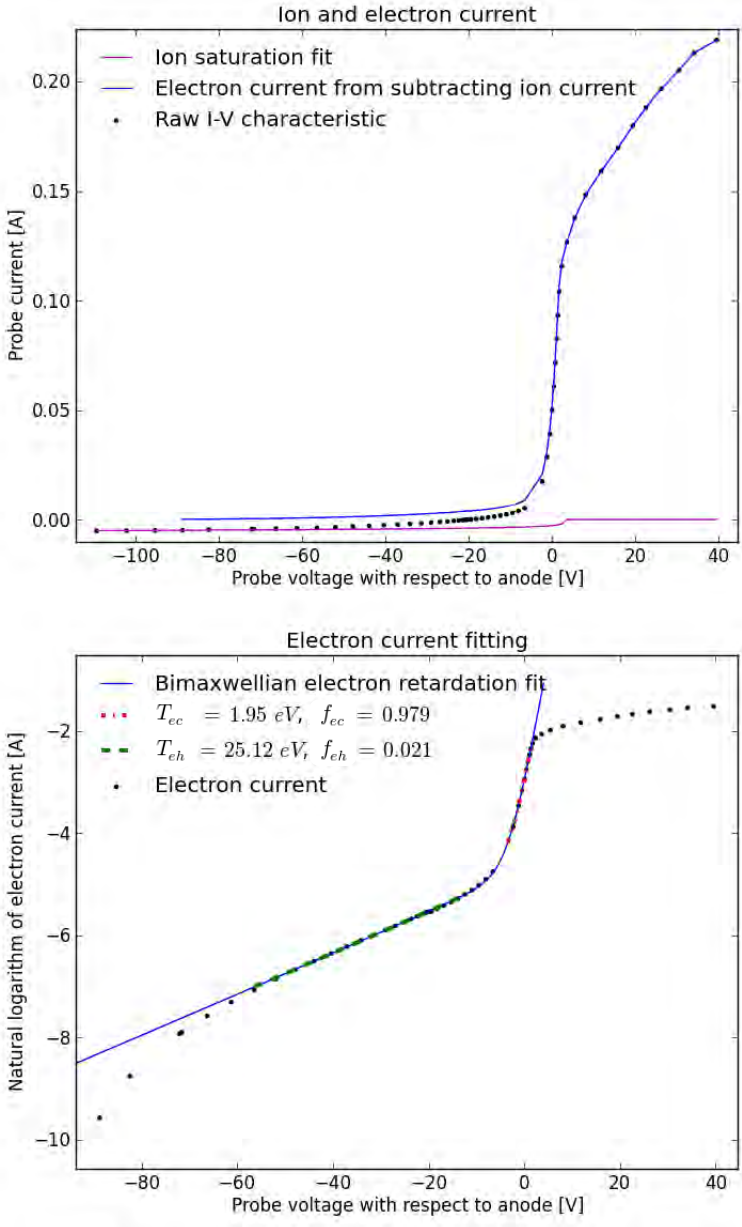

Figure 6.17: Fitting results for a Langmuir probe IV characteristic measured in VISIONI at standard operating conditions

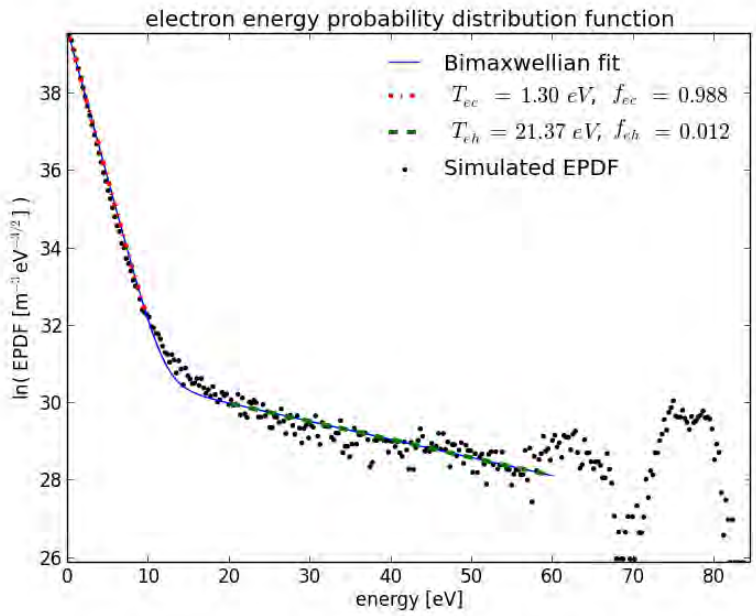

Figure 6.18: Fitting results for an electron energy probability distribution function simulated by VMCPT for standard operating conditions

larger Larmor radius. Therefore, with the sample as Langmuir probe one measures preferably the hot electrons. This effect is much smaller for the cylindrical Langmuir probe as the magnetic field is perpendicular to the surface of the collecting pin. Secondly, the sample is located inside the sheath created by the strongly biased target plate which reflects electrons with low energies. This again enhances the collection of hot electrons with respect to cold electrons. Thus by using the sample as a Langmuir probe one looks preferentially at the hot electron population in the tail of the EEDF, which explains the unexpectedly high electron temperatures measured before.

Simulations with VMCPT for standard operating conditions gave results very similar to the Langmuir probe measurements. Figure 6.18 shows the simulated electron energy probability distribution function or EPDF on a logarithmic scale. As explained in 2.3.1 the EPDF is the EEDF divided by the square root of the energy in order to eliminate the density of states in energy space from the EEDF. Based on this definition one expects for a Maxwellian EPDF on a logarithmic scale a simple straight line. Therefore, the two straight segments in the simulated EPDF clearly show the bi-Maxwellian character of the electron population.

Despite the qualitative agreement between the simulations and the measurements, the simulated values $T_{ec} = 1.3$ eV, $T_{eh} = 21.4$ eV and $f_{eh} = 0.012$ are somewhat lower than their measured counterparts. There are several possible explanations for this deviation. Firstly, although the magnetic field is perpendicular to the collecting surface for the cylindrical Langmuir probe, it can still slightly enhance the collection of hot electrons with respect to cold electrons and thus lead to an experimental overestimation of T_{ec}, T_{eh} and f_{eh}. Secondly, VMCPT simulations have shown that the uncertainty in the vibrational excitation cross sections for deuterium has an important effect on the simulated values for T_{ec}, T_{eh} and f_{eh}. Due to the lack of data for deuterium all collision cross sections used in VMCPT are actually for hydrogen. For most processes the isotopic effect is very small. However, it has been shown that for vibrational excitation the cross sections for deuterium might be significantly lower than for hydrogen [181]. Switching off vibrational excitation during the VMCPT simulations gave the increased values $T_{ec} = 1.7$ eV, $T_{eh} = 25$ eV and $f_{eh} = 0.013$. Thus using the vibrational excitation cross sections for hydrogen in VMCPT can lead to a significant underestimation of T_{ec}, T_{eh} and f_{eh}. Thirdly, VMCPT simulations with different values for the initial ion energies mimicking the ion acceleration by the neglected bulk electric field have shown that T_{ec} is also very sensitive to this initial ion energy. For higher initial ion energies and thus higher ion wall loss rates and lower equilibration times T_{ec} increases significantly because less time is available for energy relaxation. Therefore, the uncertainty in the simulated equilibration time due to the absence in VMCPT of the self-consistent bulk electric field governing the ion wall loss rate is another possible explanation for the deviation between the experimental and simulated values for T_{ec}. Finally, one also has to take into account that usually an uncertainty of about 20% is ascribed to plasma parameters derived from Langmuir probe IV characteristics and that the values determined for T_{eh} and f_{eh} by bi-Maxwellian fitting of the measured IV characteristic and the simulated EPDF are very sensitive to the fitting procedure as the hot electron population is very small.

How can we understand the bi-Maxwellian character of the EPDF in VISIONI? The discharge is initiated by primary electrons emitted from the tungsten filaments with energies uniformly distributed in the range 73-80 eV due to the discharge potential difference of 80 V applied between the filaments and the side and bottom of the plasma chamber and the potential drop of about 7 V over the length of the filaments. The primary electrons that did not yet undergo a collision lead to the peak in the range 70-80 eV which is slightly broadened by electron-electron Coulomb collisions. Figure 4.7 shows that in this energy range the energy loss is dominated by the ionization electron impact reaction with a threshold energy of 15 eV. The second peak in the range 58-65 eV is caused by primary electrons that experienced one such collision. Further peaks at lower energies are no longer visible because they are smeared out by further electron-electron collisions

and by different electronic excitation reactions with threshold energies in the range 10-15 eV which become important at lower energies. The two peaks could not be distinguished in the Langmuir probe IV characteristics due to the limited number of data points and the very low electron current in this region. The ionization and electronic excitation reactions lead to further energy degradation. The gradually decreasing reaction probability for electronic excitation and ionization reactions with decreasing energy leads to accumulation of the electrons at lower energies and thus to an EPDF which increases slightly with decreasing energy. This part of the EPDF resembles a Maxwellian EPDF. However, in reality the hot electrons are not in local thermal equilibrium. The energy degradation takes place very rapidly. The primary electrons have not enough time to fully equilibrate by means of electron-electron collisions. This is clearly illustrated by the fact that the EPDF in figure 6.18 sharply drops beyond 80 eV. Also the Langmuir probe IV characteristic in figure 6.17 drops significantly with respect to the Maxwellian fit below -80 V. The accumulation of electrons really starts to become important below 10 eV as then only vibrational excitations and elastic collisions are energetically possible. Furthermore, electrons with less than about 3 eV cannot escape from the plasma chamber as they are reflected by the sheath potential barrier at the side and bottom of the plasma chamber. They can only be lost by recombination with an ion which has a low probability due to the low ionization degree of the plasma. Therefore, the cold electrons have much more time to equilibrate by means of electron-electron collisions and are able to reach a real Maxwellian distribution. Secondary electrons created by ionization or electron collisions with the plasma chamber walls undergo the same kind of energy degradation but start typically with a much lower energy of only a few electronvolts. Hence, secondary electrons contribute mostly to the cold electron population. The important role of electron-electron collisions was confirmed by VMCPT simulations. By artificially increasing the electron-electron collision probability it was possible to obtain a full Maxwellian EPDF, while by artificially decreasing the electron-electron collision probability a non-Maxwellian EPDF with a lot of bumps was obtained.

The observations discussed in this subsection are in good agreement with results obtained in other studies. bi-Maxwellian electron probability distribution functions were found for similar sources by numerically solving the Boltzmann equation and Langmuir probe measurements in [146], [147], [145] and by simulations with similar codes in [144], [142], [143].

6.3.3 Plasma composition

A hydrogen plasma can contain different species such as electrons, H_2 molecules, H atoms, H^+ ions, H^- ions, H_2^+ ions and H_3^+ ions. It is important to have a good idea about the plasma composition in VISIONI because it determines what particles impinge on the surface of the exposed

samples. In this subsection it is first discussed what one could expect for the plasma composition based on literature. These expectations are then compared with results from VMCPT simulations and measurements with the quadrupole energy and mass analyser.

Negative hydrogen ions are not expected to be important. As explained in [182] and [183], H^- can be created in two ways. The first way is dissociative electron attachment

$$e^-(E \leq 1 \text{ eV}) + H_2(v \geq 5) \rightarrow H^- + H \tag{6.18}$$

This process is only significant for electrons with energies below 1 eV impinging on vibrationally excited molecules with $v \geq 5$. Such highly vibrationally excited molecules can be created by collisions with electrons with energies higher than 20 eV via excitation to a singlet state followed by radiative decay

$$\begin{aligned} e^-(E \geq 20 \text{ eV}) + H_2(X, v = 0) &\rightarrow e^- + H_2^*(B, C, \cdots) && (6.19) \\ H_2^*(B, C, \cdots) &\rightarrow H_2(X, v \geq 5) + h\nu && (6.20) \end{aligned}$$

These high energy electrons are, however, also very efficient in destroying H^- by electron detachment collisions. Therefore, a H^- source based on the two-step process explained above requires a separation of the plasma chamber into a region with high energy electrons where the vibrationally excited hydrogen molecules are created and a region with low energy electrons were H^- is produced by dissociative electron attachment. In the commonly used tandem source this is accomplished by means of a magnetic filter. A second method to create negative hydrogen ions consists of using metal surfaces with a very low work function such as cesium. A negative hydrogen ion can then be directly produced by double electron capture of hydrogen atoms impinging on the surface. In VISIONI there is neither cesium nor a magnetic filter separating the high energy electrons emitted by the tungsten filaments from the low energy plasma electrons. Therefore, one can expect that H^- will not be present in VISIONI.

Also H atoms and H^+ ions are expected to be negligible. As explained in [184] the dissociation degree of the neutral gas in a weakly ionized hydrogen plasma is determined by a balance between electron impact dissociation of H_2 molecules and recombination of H atoms at the walls of the plasma chamber. Recombination of two H atoms requires a third particle due to energy and momentum conservation. Three-body recombination in the gas phase is only significant for pressures above 100 Pa, but at the surface of the plasma chamber walls there are usually numerous adsorbed H atoms available for the recombination process. Let us now make a simple estimate for the dissociation degree. In steady state there is a balance between production of H atoms by electron impact dissociation of H_2 molecules and recombination of H atoms at the walls. The neutral pressure and thus also

the neutral particle density n_n in VISIONI is kept constant. The balance equation then becomes

$$n_e(1 - f_H)n_n R_{dis} = \frac{f_H n_n \gamma}{\tau_W} \tag{6.21}$$

giving for the atomic fraction f_H of the neutrals

$$f_H = \frac{n_e R_{dis}}{n_e R_{dis} + \gamma/\tau_W} \tag{6.22}$$

with R_{dis} the production rate coefficient of H atoms by electron impact dissociation of H_2 molecules, γ the recombination probability of H atoms at the wall and τ_W the typical time a H atom travels before hitting the wall. In [185] R_{dis} has been calculated as function of T_e and n_e by means of a collisional-radiative model. In VISIONI $n_e \approx 10^{17}$ m^{-3} and the EEDF is bi-Maxwellian with a cold bulk electron population with $T_{ec} \approx 2$ eV and a fraction of a $1 - 2\%$ of the electrons belonging to a hot electron population with $T_{eh} \approx 20 - 25$ eV. For these plasma conditions the data from [185] give $R_{dis} \approx 2.5 \cdot 10^{-15}$ m$^3 s^{-1}$. For a stainless steel surface measurements have shown that $\gamma \approx 0.1$ [151]. H atoms are typically produced during dissociation with an energy of the order of 1 eV [140]. The typical time before such an atom hits the wall can then be estimated to be around $5 \cdot 10^{-6}$ s by taking 5 cm as the typical distance to the wall. Elastic collisions with other neutrals have been neglected in this estimation because the collision mean free path is of the order of 10 cm at a neutral pressure of 0.3 Pa. Inserting all numbers in (6.22) gives an atomic fraction of about 1% only. H^+ can be produced by dissociative ionization of H_2 molecules. The cross section for this reaction is, however, almost two orders of magnitude lower than that of non-dissociative ionization [119]. H^+ can also be produced by ionization of H atoms, but as shown above they contribute only about 1% to the neutrals. This leads to the expectation that both H atoms and H^+ ions are neglgible in VISIONI.

We are now left with H_2^+ and H_3^+ ions. H_2^+ is produced by ionization of H_2 molecules. It is mainly destroyed by collisions with the plasma chamber walls and by the very efficient conversion process

$$H_2^+ + H_2 \rightarrow H_3^+ + H \tag{6.23}$$

creating H_3^+. Destruction of the H_3^+ ions is mainly due to collisions with the plasma chamber walls and recombination with electrons. So in the weakly ionized plasma in VISIONI the H_3^+ ions are not easily destroyed. Therefore, it is expected that H_2^+ dominates at low pressures, while H_3^+ should dominate at high pressures as was also found in [186]. The transition from the H_2^+ to the H_3^+ dominated regime is expected at a pressure of about 0.1 Pa because for this pressure the mean free path for H_2^+ to H_3^+ conversion

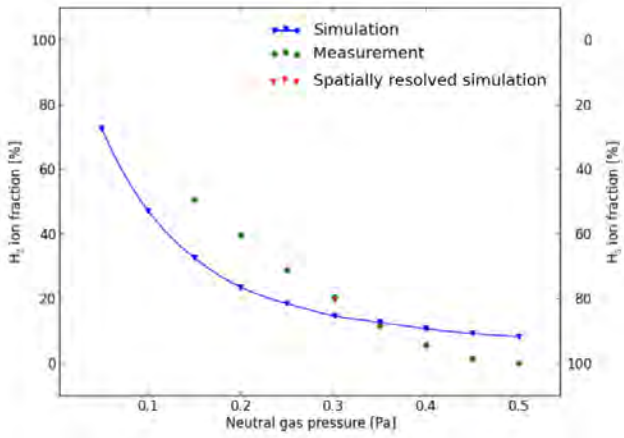

Figure 6.19: H_2^+ and H_3^+ ion fraction in VISIONI as function of neutral gas pressure measured with the quadrupole mass and energy analyser and simulated with VMCPT

is about 5 cm [119] and thus comparable with the dimensions of the plasma chamber.

The composition of the plasma and the neutral gas was measured during a deuterium plasma in VISIONI by means of the quadrupole mass and energy analyser described in 3.2.6.2. The above expectations were all confirmed. The ion composition was determined by integrating over the full energy distribution for each mass. H^+ ions formed a contribution of only about 0.1%, while H^- ions could not be observed. Figure 6.19 shows that H_2^+ ions dominate at low pressures, while H_3^+ ions dominate at high pressures. At a pressure of about 0.15 Pa the contributions of H_2^+ and H_3^+ were equal. This is in good agreement with the measurements performed in VISIONI when it was still at ETHEL [107]. A pressure scan of the neutral gas composition showed that only the signal of H_2 increases linearly with pressure. The small signal of H stayed constant at the same level as impurities such as water.

The same conclusions were obtained from VMCPT simulations. H^- ion creation and tracking were not implemented in VMCPT because this would require the implementation of a lot of additional reactions, while it was demonstrated experimentally that H^- ions are as expected not present in VISIONI. The first VMCPT simulations were performed with tracking of H^+ ions and H atoms. These simulations showed that the H^+ ions contribute only about 0.5% to the total ion content, while the dissociation degree of the neutral gas is even below 0.1%. It was concluded that the levels of

H^+ and H are sufficiently low to neglect these species in future simulations. Hence, only H_2^+ and H_3^+ ions are tracked in VMCPT. The ion composition as function of the neutral gas pressure simulated by VMCPT is also shown in figure 6.19. One can again clearly see that H_2^+ ions dominate at low pressures, while H_3^+ ions dominate at high pressures. However, there is a significant deviation between the measured and simulated H_2^+ ion fractions. There are two possible explanations for this deviation. Firstly, the simulated H_2^+ fraction was an average over the whole volume of the plasma chamber, while the measured H_2^+ fraction is a local sampling close to the centre of the bottom plate. For standard operating conditions with a neutral gas pressure of 0.3 Pa a simulation with very good statistics was performed. This allowed a study of the spatial dependence of the plasma parameters. This simulation resulted in a H_2^+ fraction around the centre of the bottom plate of 20% which is in much better agreement with the measured value as can be seen in figure 6.19. Secondly, VMCPT simulations have shown that the H_2^+ fraction is very sensitive to the assumed initial ion energy. As explained in 6.3.1 the initial ion energy is increased in order to mimic the acceleration of the ions by the bulk electric field neglected in the code. Increasing the initial ion energy leads to higher ion wall loss rates and thus as expected also to a higher H_2^+ ion fraction. Hence, the absence of the much more realistic self-consistent bulk electric field calculation in VMCPT is another possible explanation for the difference between the measured and simulated H_2^+ fraction.

6.3.4 Spatial dependence of the plasma parameters

It is not only important to have an idea about the global plasma parameters. Especially for the ERO simulations it is also indispensable to know how the plasma parameters change over the volume of the plasma chamber. This subsection discusses subsequently the spatial dependence of the plasma density, the charged particle fluxes to the plasma chamber walls, the EEDF and the plasma potential for standard operating conditions. These spatial dependencies were calculated with the VMCPT code. This was done by performing a simulation with a large amount of super-particles, splitting the simulation volume in a number of cells and calculating the plasma properties in each of these cells. The simulation results are compared with the Langmuir probe measurements along the central axis of the plasma chamber.

6.3.4.1 Plasma density

Figure 6.20 shows a horizontal and vertical cross section through the centre of the plasma chamber for the H_2^+ ion density, the H_3^+ ion density, the total ion density and the H_2^+ ion fraction as simulated by VMCPT. Figure 6.21 compares the simulation results with the Langmuir probe measurements on

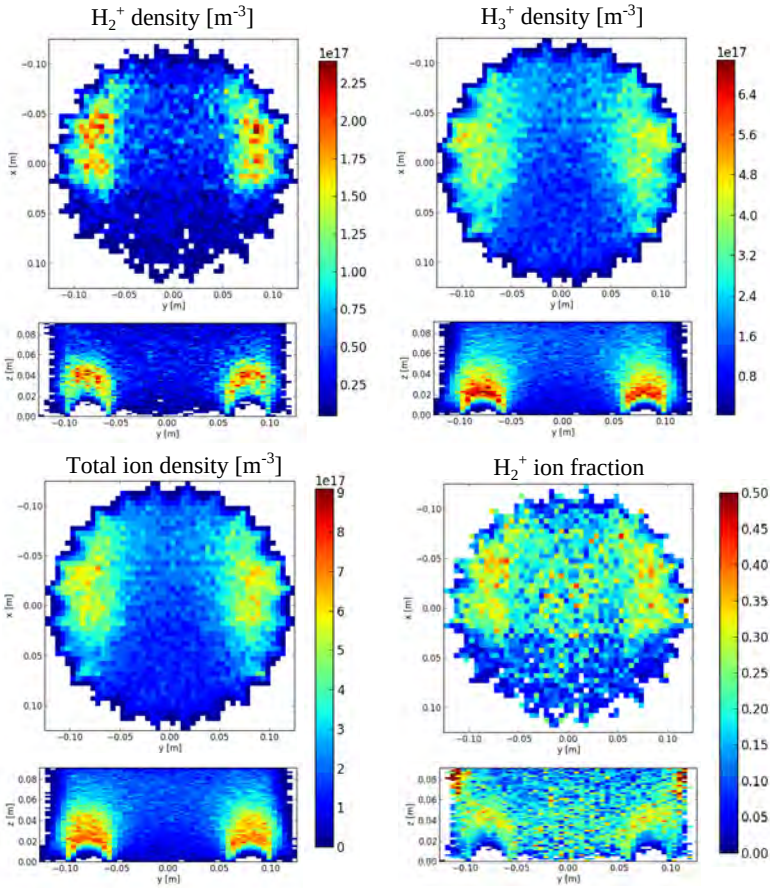

Figure 6.20: 2D plots of the ion densities on a vertical and horizontal cross section through the centre of VISIONI as calculated by VMCPT

a profile along the central axis of the plasma chamber. The ion density in this plot was normalized to the target current to correct for the effect of the slight drift of the plasma parameters during the Langmuir probe measurements. The horizontal and vertical error bars on the Langmuir probe data points take into account respectively that the collecting pin of the Langmuir probe has a finite length of 1 cm and that plasma parameters derived from a Langmuir probe I-V characteristic have an uncertainty of about 20%. The agreement between measurements and simulations is reasonable. The deviation is largest for the positions deeper inside the plasma chamber. This could be due to the increased disturbing effect of the Langmuir probe on the plasma characteristics when it is inserted further into the plasma.

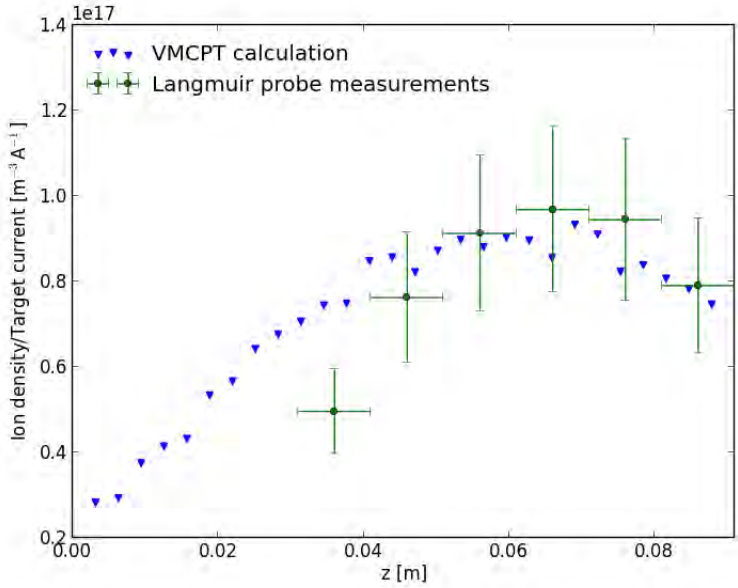

Figure 6.21: Comparison of the ion density to target current ratio profile along the central axis according to VMCPT simulations and Langmuir probe measurements

Most striking on the plots in figure 6.20 is the increased plasma density at the edge and the asymmetry for mirroring with respect to the y axis. This can be explained by looking at the trajectories of the primary electrons emitted by the tungsten filaments. As explained in 6.3.2 these primary electrons are the dominant source of ionizing electrons. Therefore, their trajectories determine where the ions are created and thus how the ion density is distributed over the plasma chamber.

A typical trajectory of such a primary electron calculated by VMCPT is shown in figure 6.22. It can be explained in terms of the drift and mirroring motion discussed in 2.3.3. Figure 6.11 shows that the gradient of the magnetic field in VISIONI is very high. However, in the edge of the plasma chamber the magnetic field is also very strong such that the magnetic field in the edge does not vary too much over one Larmor radius. Therefore, the concepts of drift and mirroring motion are valid in the edge of VISIONI. The diagrams in figure 6.23 show how the trajectory in figure 6.22 can be understood in terms of mirroring and drift motion. Most of the primary electrons emitted by the tungsten filaments are immediately captured by the magnetic field lines between the two outer bottom magnets. The initial

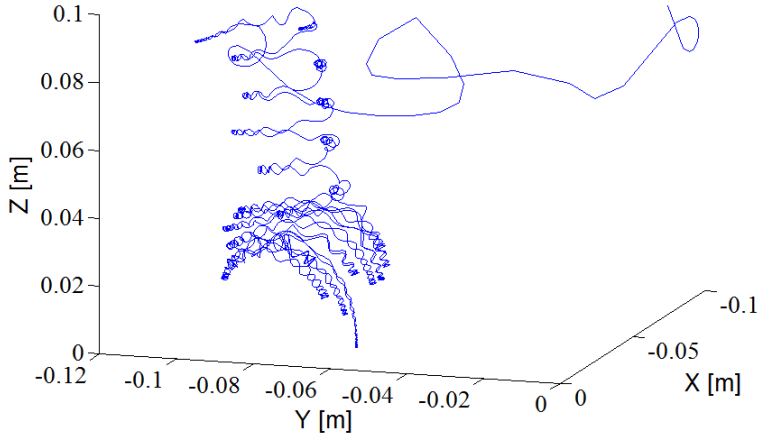

Figure 6.22: Typical trajectory of a primary electron emitted by the tungsten filaments in VISIONI exhibiting mirroring motion and grad B drifts

motion of such a primary electron is composed out of the cyclotron motion around these magnetic field lines, a mirroring motion in the y direction between the two bottom magnets and a drift in the negative x direction as shown in the top plots of figure 6.23. This drift is the combination of a $\vec{\nabla}B$ drift and a centrifugal drift given respectively by the equations (2.55) and (2.63). Taking into account the negative charge of an electron, these equations show that both drifts are directed along the $\vec{\nabla}B \times \vec{B}$ direction which corresponds with the negative x direction. Using the same reasoning it can be shown that the drift at the tungsten filaments at the other side of the plasma chamber is also in the negative x direction. During this drift the primary electron gets at a certain moment captured by the magnetic field lines between two of the side magnets. The motion is then composed out of the cyclotron motion around these magnetic field lines, a mirroring motion between the two side magnets and a drift in the z direction as shown in the bottom plots of figure 6.23. The drift is again the combination of a $\vec{\nabla}B$ drift and a centrifugal drift in the $\vec{\nabla}B \times \vec{B}$ direction which now corresponds with the z direction. If the primary electron would have been captured by the magnetic field lines between a neighbouring pair of side magnets, the drift would have been in the negative z direction. Eventually the primary electron is scattered into the central field free volume due to collisions with the neutral gas and succeeds to escape at the pole of one of the side magnets.

Another drift that could play an important role in the primary electron trajectories is the $\vec{E} \times \vec{B}$ drift. In [152] it is shown that the combination of the strong electric field in the sheath around the tungsten filaments and the magnetic field created by the heating current through the filaments can

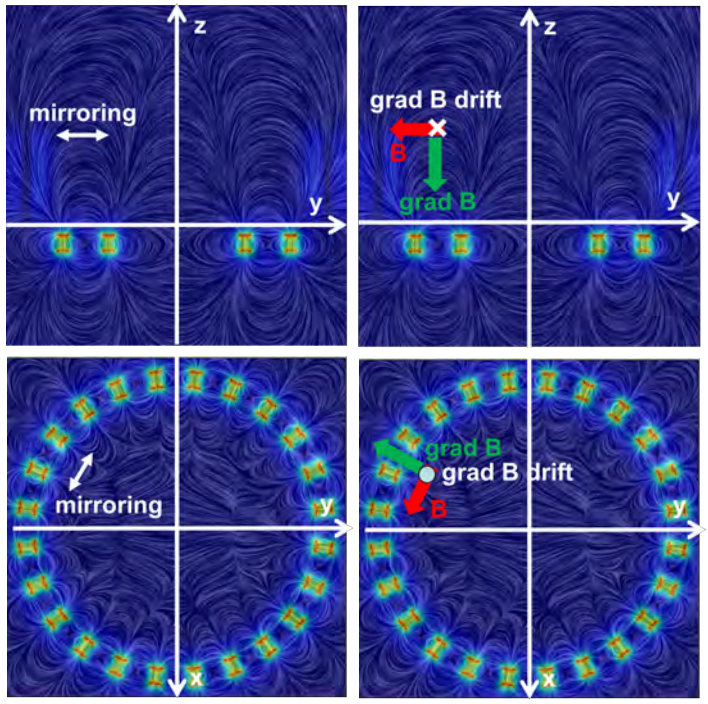

Figure 6.23: Schematic view of the magnetic field induced mirroring and drift motion experienced by the primary electrons emitted by the tungsten filaments in VISIONI

lead to a very characteristic primary electron trajectory where the electrons travel along the surface of the filaments until they encounter a sharp twist. As the electric field is not properly taken into account in VMCPT this possible effect was investigated by introducing artificially a realistic sheath electric field profile around the filaments. It turned out that the effect described in [152] is mitigated in VISIONI due to the presence of a significant contribution of the permanent magnets at the edge to the magnetic field around the filaments. The trajectories were not influenced too much by the additional electric field as it extends only less than 1 mm into the plasma. Hence, it was concluded that the sheath electric field does not play an important role for the primary electron trajectories in VISIONI.

The plots in figure 6.24 show the projection of the ionizing electron positions in the horizontal and vertical plane as simulated by VMCPT. The asymmetries in these plots clearly reflect the typical primary electron trajectories discussed above. Similar asymmetries can be observed experimentally.

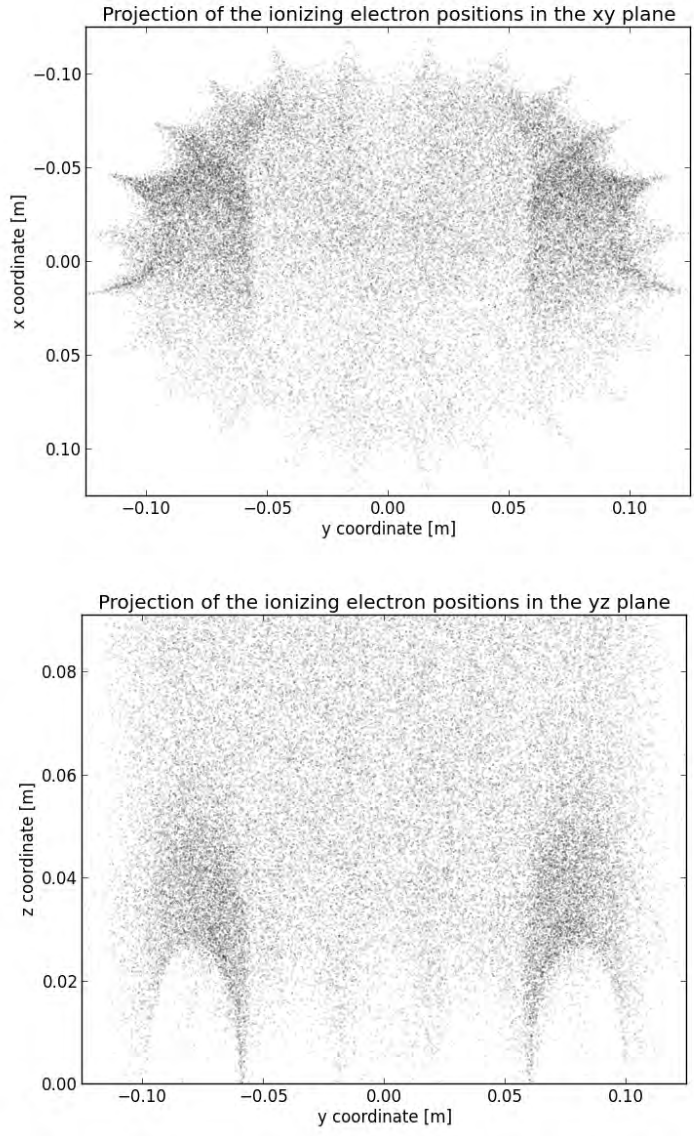

Figure 6.24: Scatter plots of the ionizing electron positions in VISIONI projected in the xy and xz planes as simulated by VMCPT

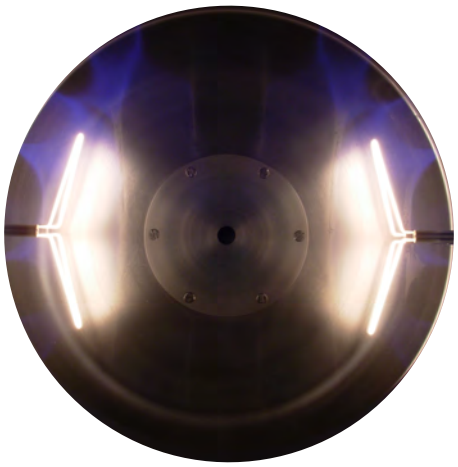

Figure 6.25: Photograph of the visible light emission pattern during an argon plasma in VISIONI reflecting the strong inhomogeneity of the ionizing electron density

Figure 6.25 shows a photograph of the light emission by an argon plasma in VISIONI. The light emission pattern is very similar to the ionizing electron density pattern as the ionizing electrons are also the electrons that are able to excite the neutral argon atoms which leads to light emission. The ionizing electron position plots are also very similar to the ion density plots in figure 6.20. Hence, it can be concluded that the asymmetry in the ion density distributions is caused by the drifts experienced by the primary electrons. One can see that the asymmetry for mirroring with respect to the y axis is somewhat less pronounced for the H_3^+ ions. This can be explained as follows. The ions are of course also charged particles and due to their positive charge they experience $\vec{\nabla}B$ and centrifugal drifts in the direction opposite to the primary electron drift direction. However, equations (2.55) and (2.63) show that the drifts are proportional to the kinetic energy of the charged particles. Therefore, the drift of the ions is much slower than the drift of the primary electrons. This explains why the ion density of the H_2^+ ions, which are rapidly converted into H_3^+ ions, looks very similar to the primary electron position plots. On the other hand, the H_3^+ ions have a much longer residence time in the plasma chamber and thus have more time to drift in the opposite direction. This explains why the asymmetry for mirroring with respect to the y axis is somewhat less pronounced for the H_3^+ ions.

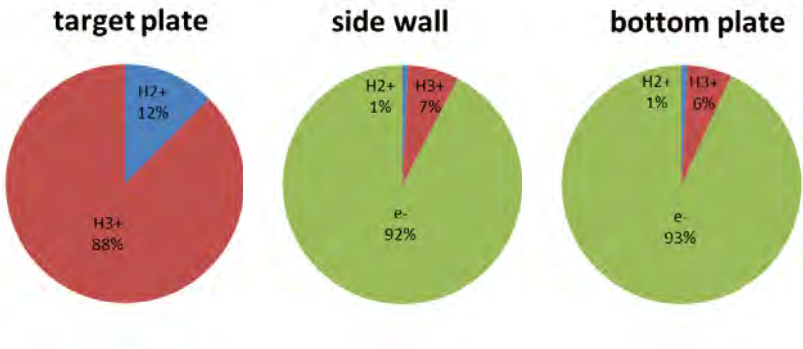

Figure 6.26: Relative contributions of the different charged particles to the fluxes on the plasma chamber walls in VISIONI as simulated by VMCPT

6.3.4.2 Ion fluxes to the walls

The ion fluxes to the plasma chamber walls are very important for this work as they determine the amount of erosion and deposition. Figure 6.26 shows the relative contributions of the different charged particles to the fluxes on the plasma chamber walls as simulated by VMCPT. Electrons can only escape through the side wall and the bottom plate because the target plate is biased negatively in order to repel even the most energetic electrons. Therefore, the electrons are absent in the target plate pie chart, while they dominate the pie charts for the side wall and the bottom plate. The ratio between the H_2^+ ion flux and the H_3^+ ion flux is similar for the three pie charts and also comparable with the density ratio in the plasma.

Figure 6.27 shows a plot of the ion flux hitting the target plate and scatter plots for the impact positions of ions on the bottom plate and a small part of the side wall as simulated by VMCPT. The ion flux on the target plate clearly reflects the asymmetry in the ion density discussed above. The scatter plots show that ions can escape through the bottom plate and side wall only around the poles of the magnets as could be expected from the magnetic field line structure shown in figure 6.10.

These simulation results were also confirmed experimentally. The photographs in figure 6.27 show the amorphous hydrocarbon layers deposited on the target plate, the bottom plate and part of the side wall in VISIONI after an experimental campaign with mixed deuterium-methane plasmas. The colour patterns of the transparent amorphous hydrocarbon layers are due to interference effects depending on the layer thickness. The regions with significant impact of ions according to the VMCPT simulations clearly correspond with the regions where no amorphous hydrocarbon layers were

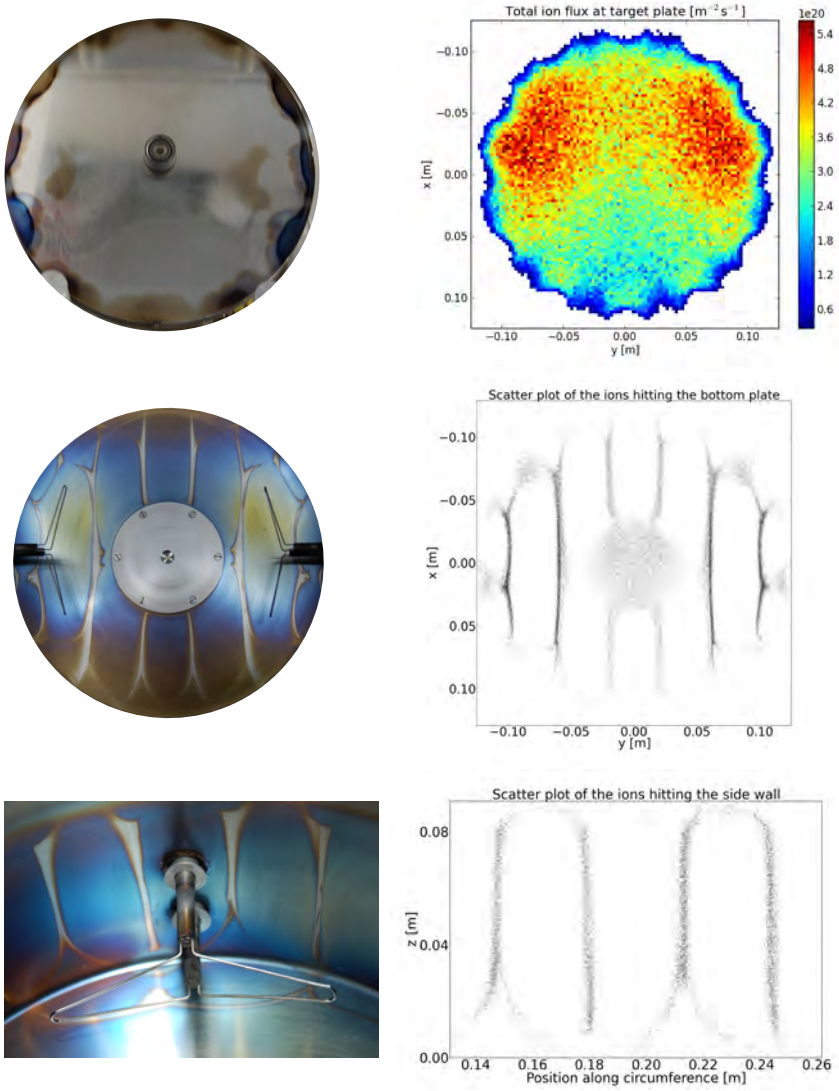

Figure 6.27: Photograph of the amorphous hydrocarbon layer deposition in VISIONI after a methane plasma in comparison with the hydrogen ion flux patterns as calculated by VMCPT

observed experimentally. This can be understood as follows. The deposition of the amorphous hydrocarbon layers is mainly due to neutral hydrocarbon radicals created by electron impact reactions with the methane. These neutral species are not affected by the magnetic field and can reach all regions of the plasma chamber. However, the amorphous hydrocarbon layers in the regions with strong ion bombardment are removed by physical and chemical sputtering much faster than they are built up. This very nice agreement shows that the simulated ion fluxes are very realistic.

6.3.4.3 Electron energy distribution function

As discussed in 6.3.2 the EEDF in VISIONI can be approximated by a bi-Maxwellian. Therefore, it can be characterized by three parameters: the cold electron temperature T_{ec}, the hot electron temperature T_{eh} and the hot electron fraction f_{eh}. Figure 6.28 shows the 2D plots of T_{ec}, T_{eh} and f_{eh} on a vertical and horizontal cross section through the centre of the plasma chamber as calculated by VMCPT. The tungsten filaments are indicated in purple. The resolution is very poor in comparison with the ion density plots in figure 6.20. This is because at least several tens of thousands of simulation electrons are needed in order to resolve the hot electron tail of the EEDF. Therefore, the amount of cells in which the simulation volume could be split for calculating T_{ec}, T_{eh} and f_{eh} was limited. A central cylinder with radius 4 cm was sliced into ten equally thick slices. The surrounding edge region was sliced in seven equally thick slices. The bottom two edge slices were added together because the electron density in the bottom slice was very low. All edge slices were additionally cut into twenty segments with an opening angle of 18^o. As VISIONI is symmetric for mirroring with respect to the xz plane, the corresponding segments on both sides of the xz plane were considered together for the calculation of the EEDF parameters. The 2D plots clearly show that T_{ec}, T_{eh} and f_{eh} are higher close to the tungsten filaments. The effects of the primary electron drifts in the negative x direction and along the z axis induced by the magnetic field gradient are also reflected in these plots.

The simulated profiles of T_{ec}, T_{eh} and f_{eh} along the central axis of the plasma chamber are compared with the Langmuir probe measurements in figures 6.29-6.31. The measured values are systematically above the simulated values. Possible explanations for this deviation were already discussed in 6.3.2. The Langmuir probe measurements show a slight increase of T_{eh} and f_{eh} when moving from the top towards the centre of the plasma chamber. This increase was not observed in the simulation results. The increase observed during the measurements could be caused by the increase of the primary electron emission rate as the Langmuir probe was moved downwards due to the drift of the filaments temperature discussed in 6.3.1. The deviation between the simulations and the measurements could also be due to the fact that the bulk electric field is not taken into account in VMCPT.

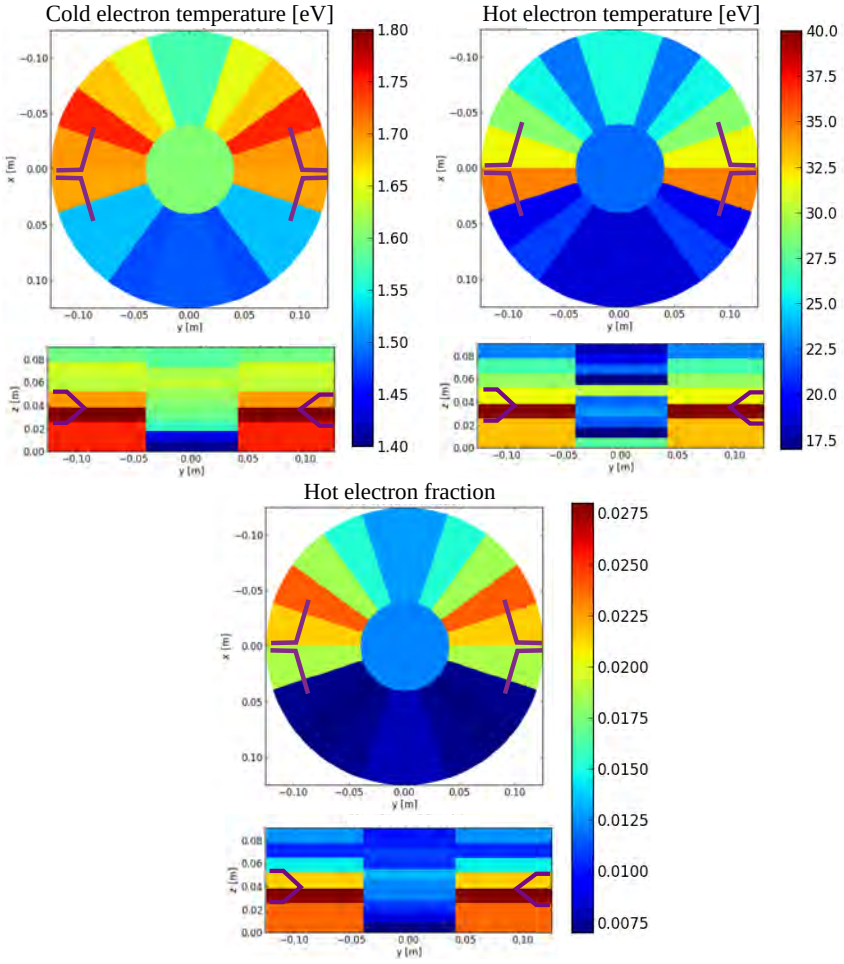

Figure 6.28: 2D plots of the cold electron temperature, hot electron temperature and hot electron fraction on a vertical and horizontal cross section through the centre of the VISIONI plasma chamber as calculated by VM-CPT

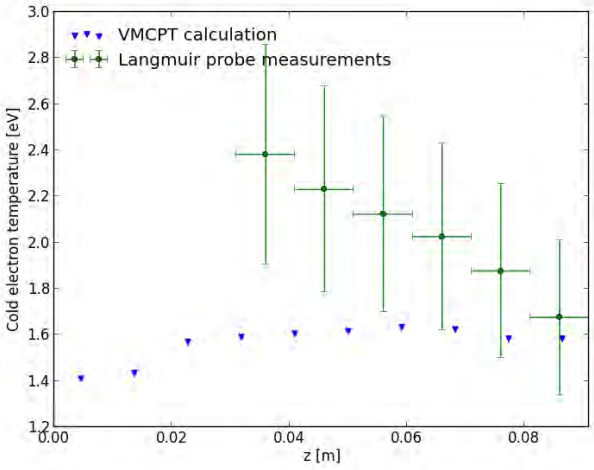

Figure 6.29: Comparison of the cold electron temperature profiles along the central axis according to VMCPT simulations and Langmuir probe measurements

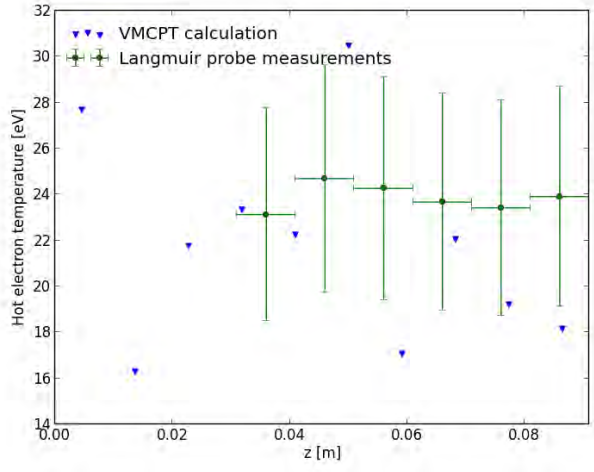

Figure 6.30: Comparison of the hot electron temperature profiles along the central axis according to VMCPT simulations and Langmuir probe measurements

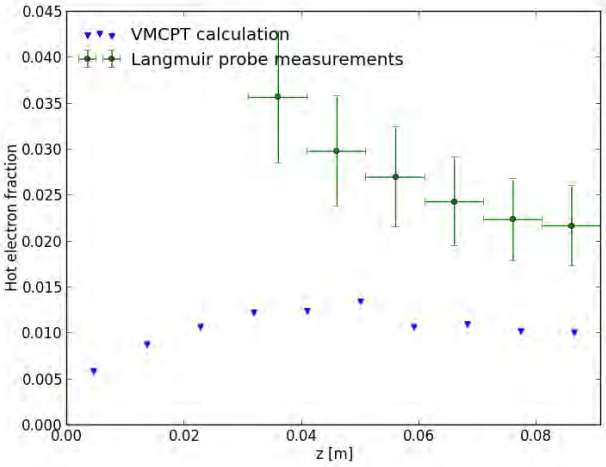

Figure 6.31: Comparison of the hot electron fraction profiles along the central axis according to VMCPT simulations and Langmuir probe measurements

As discussed in 4.2.4 the bulk electric field has an important effect on the trajectories of the cold electrons. The order of magnitude of T_{eh} obtained from the simulations is in good agreement with the measurements. However, the simulated values fluctuate quite a lot. This is caused by the limited statistics for the high energy tail of the EEDF in the simulations.

6.3.4.4 Plasma potential

The spatial dependence of the plasma potential and the bulk electric field is an important input for the ERO code. As the bulk electric field is neglected in VMCPT it was not possible to simulate the spatial dependence of the plasma potential. Only the sheath potential drop at the side and bottom of the plasma chamber was simulated self-consistently by VMCPT. This potential drop corresponds to the potential difference between the edge of the plasma and the anode. For standard operating conditions the simulations gave a value of about 2.4 V for the sheath potential drop. Due to the additional presheath potential drop of the order of kT_e/q_e it is expected that the plasma potential increases a few volts towards the centre of the plasma chamber.

These expectations are in good agreement with the Langmuir probe measurements. Figure 6.32 shows that the plasma potential with respect to the anode increases from 3 V close to the target plate up to 4.5 V in the

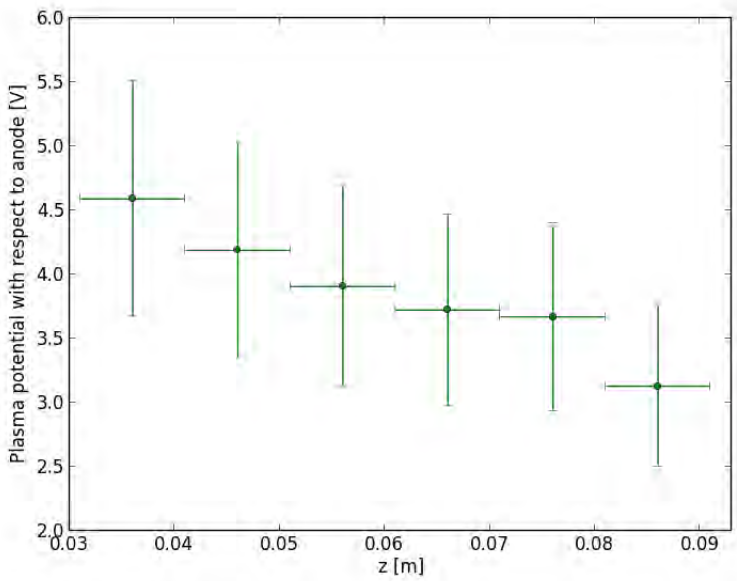

Figure 6.32: Vertical profile of the plasma potential with respect to the anode in VISIONI as measured by the movable Langmuir probe

centre of the plasma chamber. However, the determination of the plasma potential by means of a Langmuir probe is rather inaccurate due to the rounding of the knee in the IV characteristic. A more precise measurement of the plasma potential should be performed by means of for instance an emissive probe.

6.3.5 Free parameter variations

As discussed in 6.3.1 the plasma properties in VISIONI can be influenced by three operational parameters: the filament heating current I_f which determines the primary electron emission rate R_{pe}, the neutral gas pressure p and the potential difference V_{ac} applied between the tungsten filaments and the side and bottom of the plasma chamber. A parameter study was performed to assess the variation of the most important plasma parameters such as the cold electron temperature T_{ec}, the hot electron temperature T_{eh}, the hot electron fraction f_{eh}, the fraction of H_2^+ ions f_{H_2}, the plasma potential V_{pl}, the anode current I_a, the plasma density n_i and the target current I_t. This was done both with VMCPT simulations and Langmuir probe measurements. The simulated values for T_{ec}, T_{eh}, f_{eh} and f_{H_2} are values

averaged over the whole simulation volume as only for standard operating conditions a simulation was performed with enough statistics to determine the spatial dependence of these plasma properties. The simulated values for V_{pl} correspond with the self-consistent sheath potential drop at the side and bottom of the plasma chamber. As the self-consistent bulk electric field is not taken into account in VMCPT the presheath could not be taken into account. The simulated values for n_i correspond with the local plasma density on the central axis averaged over a cylinder with a radius of 0.02 m and a central axis between $z = 0.07$ m and $z = 0.08$ m. The Langmuir probe measurements of these parameters were performed with the probe positioned at the central axis of the plasma chamber with the molybdenum tip between $z = 0.07$ m and $z = 0.08$ m. As can be seen in figure 6.21 this position corresponds with the maximum of the plasma density profile along the central axis of the plasma chamber. Each Langmuir probe data point was obtained by averaging five measurements. The standard deviation of these measurements was very low in comparison with the variation of the plasma parameters. However, plasma parameters derived from a Langmuir probe I-V characteristic have an uncertainty of about 20%. The results are shown in figures 6.33-6.35. The red dashed lines indicate standard operating conditions: $R_{pe} = 2 \cdot 10^{19}$ s^{-1}, $p = 0.3$ Pa and $V_{ac} = 80$ V.

In general the agreement between the simulations and the measurements is reasonable. The measured values for T_{ec}, T_{eh} and f_{eh} are systematically higher than the simulated values. Possible explanations for this deviation were already discussed in 6.3.2. Also the measured values for V_{pl} are systematically higher than the simulated values. This was expected as the measured values include the sheath and presheath potential drop, while the simulated values take into account the sheath potential drop only. The measured values for I_a are systematically lower than the simulated values. The simulated values for I_a could only be decreased with respect to n_i and I_t by giving the ions an initial velocity directed towards the target plate. However, this results in a too large ratio I_t/n_i. Thus the deviation between simulations and measurements for the ratios between n_i, I_a and I_t is probably due to the fact that giving the ions just a higher initial energy to mimic the acceleration by the presheath electric field does not take into account the fact that the ions can be accelerated towards the side, top or bottom of the plasma chamber with a preference for the top as the contact area of the plasma at the target plate is much larger than at the side and bottom due to the absence of permanent magnets at the target plate. The agreement between the simulated and measured values for n_i and I_t is very good, especially for conditions close to the standard operating conditions. The deviations for operating conditions further away from standard operating conditions is probably caused by the fact that the value for the initial ion energy to mimic the acceleration of the ions in the presheath electric field was fitted to the experimental results at standard operating conditions only as was discussed in 6.3.2. Besides the absence of a self-consistent electric

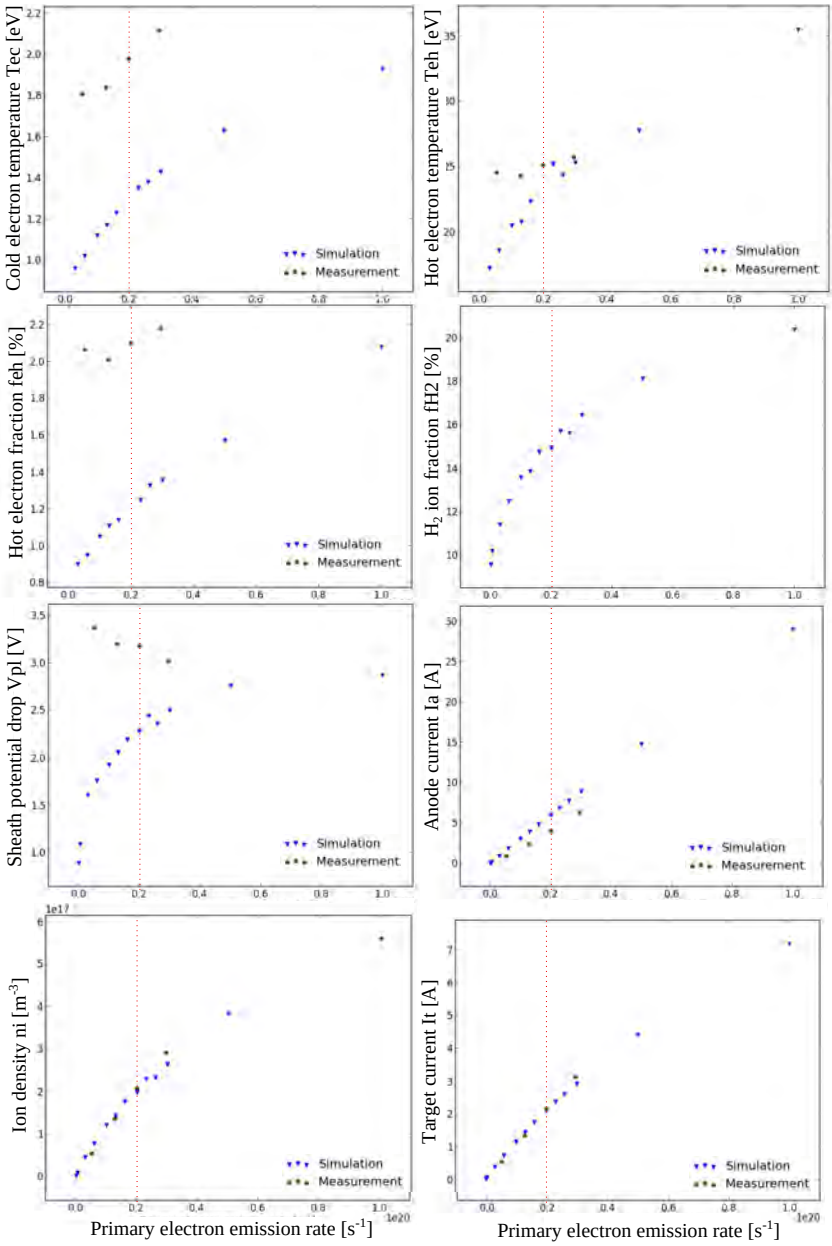

Figure 6.33: Dependence of the plasma parameters in VISIONI on the primary electron emission rate according to the VMCPT simulations and Langmuir probe measurements. The primary electron emission rate for standard operating conditions is indicated with the dashed red line.

field calculation another important factor that might explain the deviations between measurements and simulations is the drift of R_{pe} discussed in 6.3.1. This drift is unavoidable during a parameter scan. It is not possible to use the strategy used for other experiments where I_t is kept constant by adapting I_f as I_t is expected to change during the parameter variations. Thus R_{pe} will always increase during the parameter scan even though I_f is kept constant. This complicates of course the interpretation of the measured parameter dependencies.

The plots in figure 6.33 show the variation of the plasma parameters with the primary electron emission rate R_{pe}. For the experimental data the value of R_{pe} was calculated for each value of the filament heating current I_f by fitting to the VMCPT simulation results. The relationship between I_f and R_{pe} obtained in this way was in very good agreement with the theoretical relations discussed in 6.3.1. The simulations were performed for R_{pe} in the range $(0.05 - 1) \cdot 10^{20}$ s^{-1}. The measurements were performed for R_{pe} in the range $(0.05 - 0.2) \cdot 10^{20}$ s^{-1}. It can be seen that n_i increases in the range $(8.6 \cdot 10^{15} - 5.5) \cdot 10^{17}$ m^{-3} for increasing R_{pe}. This is logical as an increase in the primary electrons emission rate leads to an increase in the ionization rate. The increase slows down for higher R_{pe} as recombination becomes more and more important. Similarly, also I_a and I_t increase respectively in the ranges 0.15-30 A and 0.07-7 A for increasing R_{pe}. The increase of I_a is steeper as the hot electrons which are not significantly subjected to recombination form an important contribution to this current. The increased plasma density also has its effect on the EEDF. It is clear that T_{ec} increases from 1 eV to 2 eV with increasing R_{pe}. This increase can be explained by the enhanced recombination rate at higher plasma densities leading to a shorter lifetime and thus to a shorter energy relaxation time of the cold electron population. Also T_{eh} increases from 15 eV to 35 eV with increasing R_{pe}. This increase is probably caused by a more efficient energy transfer from the primary electrons due to the enhanced electron-electron collision rate at higher plasma densities. Further, also f_{eh} increases from 0.009 to 0.02 with increasing R_{pe}. The hot electron fraction is increased because enhanced recombination reduces the cold electron fraction. The increasing energy of the electrons for increasing R_{pe} also explains why V_{pl} increases in the range 1-2.9 V for increasing R_{pe}. If the electrons are more energetic a higher potential barrier is required to ensure quasi-neutrality of the plasma. Finally, f_{H_2} is observed to increase in the range $10 - 20\%$ for increasing R_{pe}. This is because recombination of H_2^+ ions becomes more important with respect to the conversion reaction to H_3^+ ions, which reduces the production rate of H_3^+ ions. Furthermore, enhanced recombination of H_3^+ ions also increases the loss rate of H_3^+ ions.

The plots in figure 6.34 show the variation of the plasma parameters with the neutral gas pressure p. The simulations were performed for p in the range 0.05-0.5 Pa. The measurements were performed for p in the range 0.15-0.5 Pa. The main effect of an increase of the neutral gas pressure is the

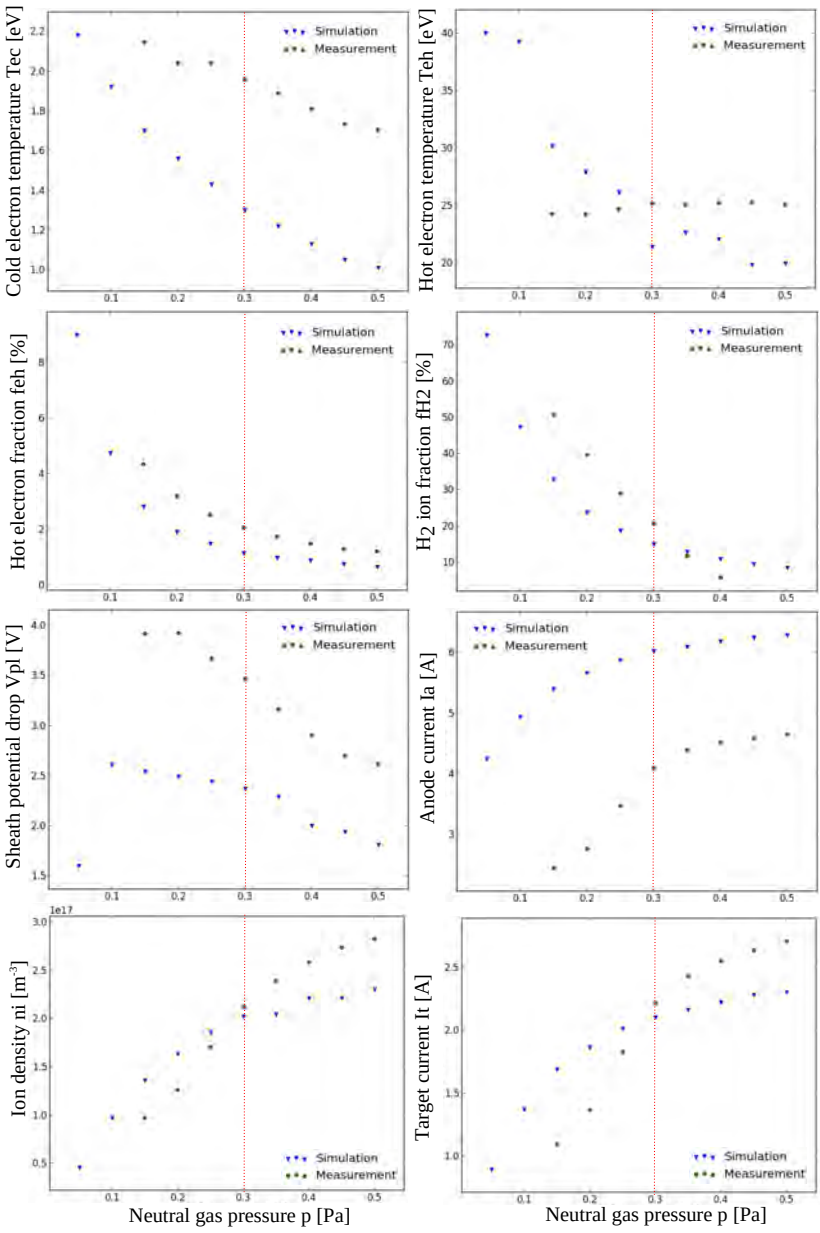

Figure 6.34: Dependence of the plasma parameters in VISIONI on the neutral pressure according to the VMCPT simulations and Langmuir probe and quadrupole mass and energy analyser measurements. The neutral pressure for standard operating conditions is indicated with the dashed red line.

increase of the collision rates of the charged particles with the neutrals. It can be seen that T_{ec} decreases from 2.2 eV to 1 eV for increasing p. This is caused by an increase of the vibrational excitation rate. Also T_{eh} decreases from 40 eV to 20 eV for increasing p due to enhanced electronic excitation and ionization rates. Further, a decrease of f_{eh} from 0.09 to 0.005 is observed for increasing p. This can be explained by an increase of the ionization rate and an enhanced energy relaxation of the hot electrons leading to an increase of the cold electron population with respect to the hot electron population. As expected the decrease of the electron energy with increasing p leads also to a decrease of V_{pl} such that quasi-neutrality of the plasma remains guaranteed. The values of n_i, I_t and I_a increase for increasing p respectively in the ranges $(0.7-2.7)\cdot 10^{17}$ m^{-3}, 1-2.7 A and 4.4-7 A. These increases are due to the enhanced ionization rates experienced by the primary electrons. The increase is limited as the available energy per primary electron is limited by the value of V_{ac}. Finally, as was discussed already in 6.3.3 the value of f_{H_2} decreases very strongly with increasing p due to the enhanced H_2^+ to H_3^+ conversion rate.

The plots in figure 6.35 show the variation of the plasma parameters with the potential difference V_{ac} applied between the tungsten filaments and the bottom and side of the plasma chamber. The simulations were performed for V_{ac} in the range 40-120 V. The measurements were performed for V_{ac} in the range 60-120 V. The value of V_{ac} clearly does not have a significant impact on T_{ec}. However, T_{eh} increases strongly in the range 10-40 eV for increasing V_{ac}. This is logic as V_{ac} determines the initial energy of the primary electrons. The value of f_{eh} decreases from 0.03 to 0.01 for increasing V_{ac}. This can be explained by the fact that primary electrons are lost more easily, while creation of cold electrons due to ionization is promoted due to the higher starting energy of the primary electrons. As T_{ec} is not influenced significantly by V_{ac} also V_{pl} does not vary a lot with V_{ac}. The values of n_i, I_t and I_a increase for increasing V_{ac} respectively in the ranges $(0.5-2.3)\cdot 10^{17}$ m^{-3}, 0.9-2.3 A and 4-6 A. These increases are due to the increased energy of the primary electrons which is available for ionization. The increase is limited as the increased energy of the primary electrons also leads to a more rapid loss. Finally, the value of f_{H_2} increases slightly with increasing V_{ac} due to the enhanced recombination which decreases the production rate of H_3^+ ions and at the same time increases the loss rate of H_3^+ ions.

6.3.6 Investigation of the effects of different processes

In addition to measurable plasma parameters the VMCPT code can also provide information which is not accessible experimentally. It is possible to study in detail the complex interplay of the different processes playing a role in the plasma.

Figure 6.36 for instance shows the contributions of electrons from ion-

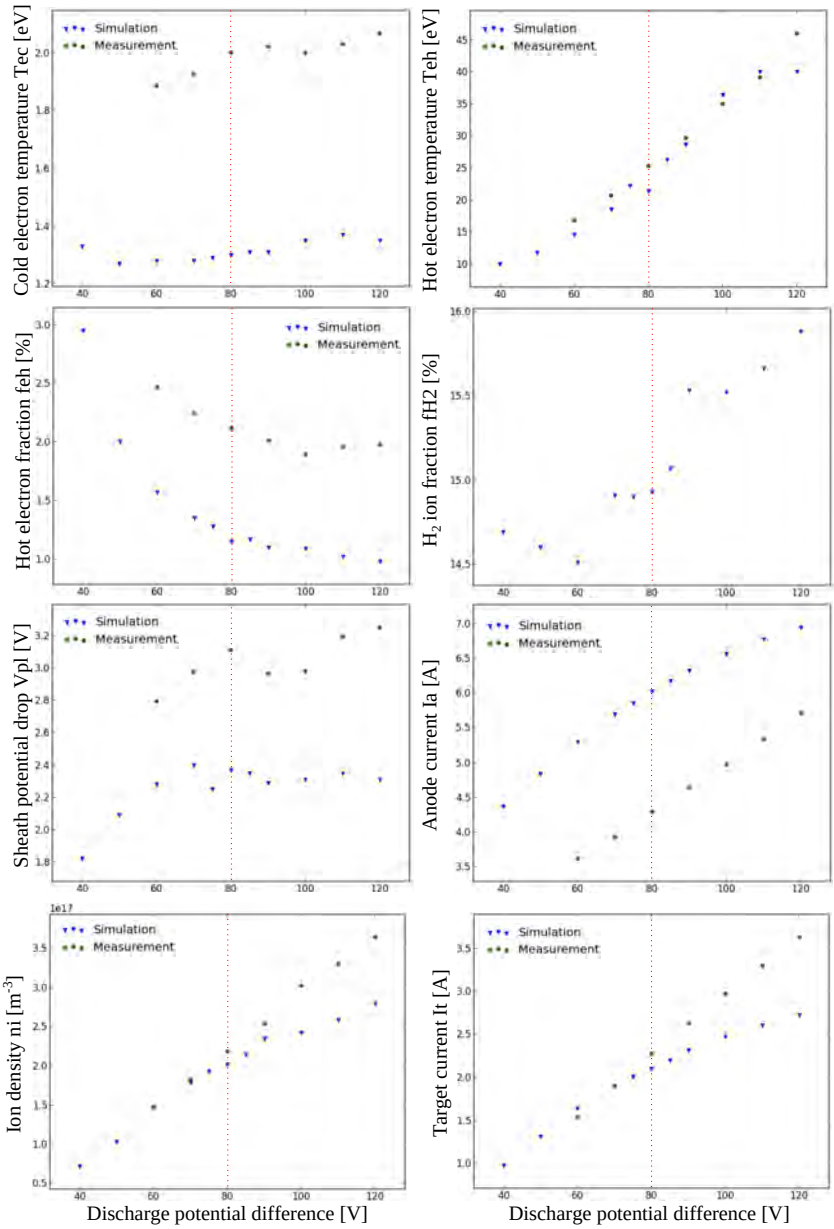

Figure 6.35: Dependence of the plasma parameters in VISIONI on the discharge potential difference according to the VMCPT simulations and Langmuir probe measurements. The discharge potential difference for standard operating conditions is indicated with the dashed red line.

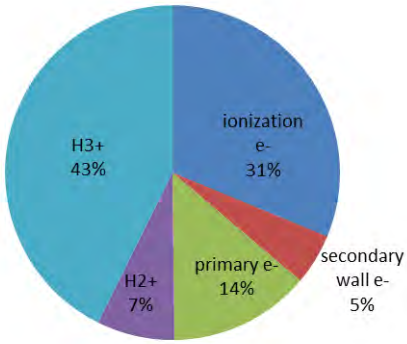

Figure 6.36: The contributions of different charged particles to the total charged particle inventory in VISIONI according to VMCPT simulations

ization, electrons knocked out of the plasma chamber walls and primary electrons to the plasma. This pie chart learns us that more than 60% of the electrons in the plasma are due to ionization. Secondary electrons ejected by the wall due to electron impact form only a small contribution of about 10%. The remaining 30% are primary electrons. As discussed already in 6.3.2 these primary electrons are the main source of hot electrons. However, only a small fraction of the primary electrons belongs to the hot electron population. Most of the primary electrons experienced several inelastic collisions and belong to the cold electron population.

The pie charts in figure 6.37 show the contributions of different loss processes to the total loss of the different charged particles in the plasma. The H_3^+ ions are lost mainly at the plasma chamber walls. Due to the absence of permanent magnets at the target plate about 71% of all H_3^+ losses are at the target plate. Losses at the side of the plasma chamber, losses at the bottom plate and losses due to recombination each contribute about 10% each to the total H_3^+ losses. For H_2^+ ions the losses are clearly dominated by the very efficient conversion process to H_3^+ ions. Also recombination is an important loss process contributing about 16% to the total H_2^+ losses. The wall losses contribute in total only about 10%. For electrons the losses are clearly dominated by wall losses. Losses at the side and bottom of the plasma chamber contribute respectively 42% and 53% to the total electron losses. Electrons cannot be lost at the target plate due to the high negative biasing. The remaining 5% of the electron losses are due to recombination.

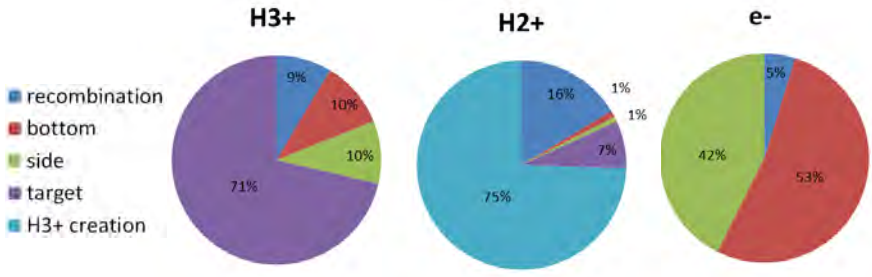

Figure 6.37: The contributions of different processes to the charged particle loss in VISIONI according to VMCPT simulations

6.4 Optical emission spectroscopy feasibility study for VISIONI

Optical emission spectroscopy is a valuable tool for material migration studies. It can be used to study the migration of eroded and externally injected particles. Therefore, the feasibility of an optical emission spectroscopy system for VISIONI was investigated. Due to the limited accessibility of the plasma chamber only the side port can be used for optical access. In principle optical emission spectroscopy could also be performed via the hole in the bottom plate, but this would require the removal of the energy and mass analyser. The first subsection discusses the IR heat load from the tungsten filaments on the side port. This is important because for too high heat loads it is necessary to use more expensive mirror instead of lens optics. The second subsection discusses an experiment in which a mixed deuterium-methane plasma was inspected with an overview spectrometer to investigate how well hydrocarbons can be observed by means of optical emission spectroscopy in VISIONI.

6.4.1 Estimation of the IR heat load on the side port

As discussed in 6.3.1 the optical emission of the tungsten filaments can well be approximated by a Planck spectrum. At standard operating conditions the temperature of the tungsten filaments T_f is about 2400 K. According to [179] the emissivity ϵ of tungsten in the relevant wavelength range is about 0.4. The power P_{rad} radiated by the tungsten filaments with a surface area A_f can then be calculated according to the Stefan-Boltzmann law

$$P_{rad} = A_f \epsilon \sigma T_f^4 = 951 \text{ W} \tag{6.24}$$

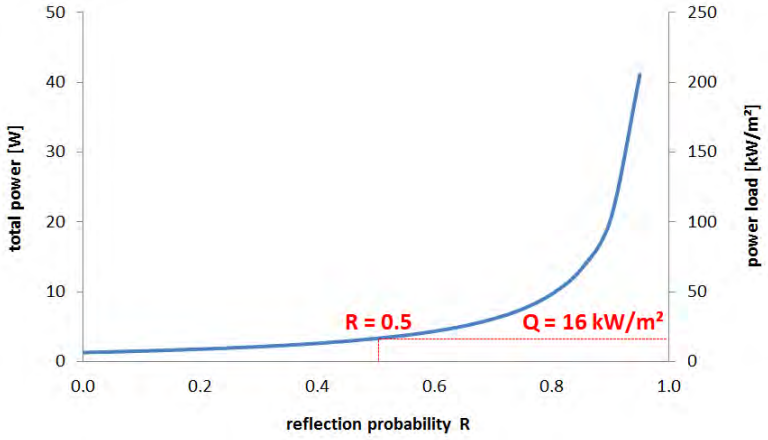

Figure 6.38: The power load and total power on the side port in VISIONI as function of the IR reflection probability of the stainless steel vacuum vessel walls as calculated by the Monte Carlo code

with σ the Stefan-Boltzmann constant. As the electric power put into the tungsten filaments amounts to about 2500 W, this means that about 40% of the input power is transformed into radiation.

Two different methods were used to estimate how much of this radiated power eventually ends up at the side port. For the first method a simple Monte Carlo photon tracking code was used. The calculation starts with the release of 10^7 semi-photons, each carrying a fraction 10^{-7} of the total radiated power P_{rad}. The starting positions of the semi-photons are uniformly distributed over the surface of the tungsten filaments. The starting velocities are for simplicity uniformly distributed over a full sphere. The semi-photons describe straight tracks until they hit the stainless steel walls of the plasma chamber. When hitting the wall, the photon is reflected with a power fraction R equal to the average IR reflection probability of stainless steel. The reflection angles were distributed according to a cosine distribution. The semi-photons were tracked as long as the carried power was greater than a fraction 10^{-12} of P_{rad}. The power carried by the semi-photons hitting the side port was considered fully absorbed and added up in order to estimate the heat load on the port. Figure 6.38 shows the results of this calculation. The plot shows the IR power load and the total IR power on the side port as a function of the IR reflection probability of the stainless steel vacuum vessel walls. The unknown IR reflection probability introduces an uncertainty. For an average reflection probability of 0.5 the power load on the side port P_{port} was calculated to be 16 kW/m^2.

The heat load on the side port was also estimated experimentally by

inserting a thermocouple into the plasma chamber through a pinhole in a copper insert positioned in the side port such that only 1 cm of the thermocouple was actually exposed to the IR heat load in the plasma chamber. The IR heat load P_{port} on the side port was then calculated from stating that the IR heat load absorbed by the exposed part of the thermocouple should in steady state be equal to the sum of the heat load conducted away by the thermocouple according to Fourier's law and the heat load radiated by the thermocouple according to the Stefan-Boltzmann law. This can be expressed as

$$(1 - R)A_{te}P_{port} = k_t A_{tc}\frac{T_{in} - T_{out}}{L_t} + A_{te}\sigma T_{in}^4 \tag{6.25}$$

where R is the average IR reflection probability of the stainless steel coating of the thermocouple, A_{te} the exposed surface area of the thermocouple, k_t the heat conduction coefficient of the thermocouple, A_{tc} the cross section area of the thermocouple, T_{in} the temperature of the end point of the thermocouple inside the plasma chamber, T_{out} the temperature of the end point of the thermocouple outside the plasma chamber and L_t the length of the thermocouple. If again a value of 0.5 is taken for the average IR reflection probability on stainless steel, the calculated value for P_{port} was in perfect agreement with the value of 16 kW/m^2 calculated with the Monte Carlo code.

From the estimated heat load of 16 kW/m^2 it can be concluded that it will be safer to use mirrors for the optics in VISIONI. This will make the system of course more expensive. Furthermore, an additional issue is that the mirrors could rather soon be covered with a deposit from the plasma. This will make it necessary to regularly clean the mirrors.

6.4.2 Spectroscopy of a deuterium-methane plasma

In order to investigate how well traces of impurities in the plasma will be observable by means of optical emission spectroscopy it was decided to study a deuterium plasma with a variable concentration of methane with the AvaSpec-2048-USB2 compact overview spectrometer as described in 3.2.6.1.

Figure 6.39 shows the optical emission spectra for a deuterium plasma with 1% of methane and a full methane plasma after taking into account the wavelength dependent relative sensitivity factor and subtracting of the background due to the IR emission of the tungsten filaments. Most prominent in both spectra are the hydrogen Balmer lines. Both spectra show a weak band at 430 nm which is most probably the CH band. The full methane spectrum also shows two weak lines at about 463 nm and 493 nm which might be neutral carbon lines.

From the two spectra it is clear that it is possible to observe trace amounts of impurities in the plasma. However, the signals due to these impurities are very weak. This is due to the rather low plasma density in

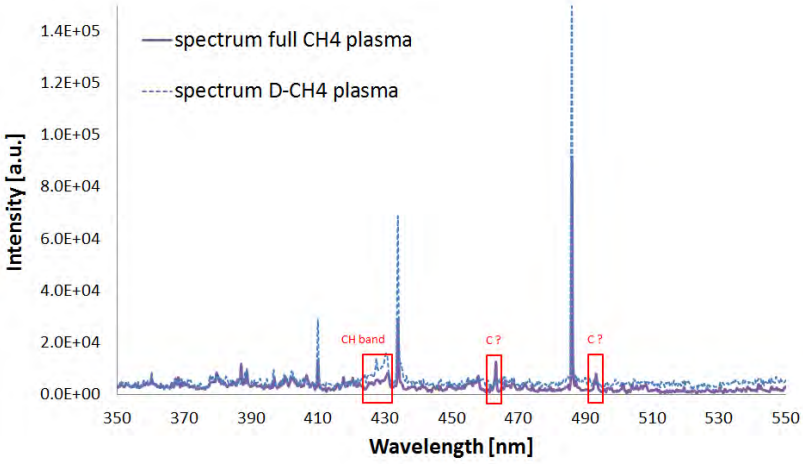

Figure 6.39: Optical emission spectra observed during mixed deuterium-methane and full methane plasmas in VISIONI

VISIONI. Therefore, especially for spatially resolved measurements, a very sensitive optical emission spectroscopy system will be needed.

6.5 Conclusions

- Analytical expressions were derived for the magnetostatic field created by the permanent Sm_2Co_{17} magnets and the heating current running through the tungsten filaments in VISIONI. The expressions for the magnetostatic field created by the permanent Sm_2Co_{17} magnets were benchmarked and verified by means of Hall probe measurements. The agreement between the calculations and the measurements was very good. A value of $\mu_0 J_s = 1.12\ T$ was found for the initially unknown equivalent surface current density J_s. As expected for a multidipole magnetic field configuration the magnetic field has a very strong gradient at the edge of the plasma chamber and drops over about two orders of magnitude when moving towards the centre. At the poles of the magnets the field has a strength of about 0.2 T, while in the centre of the plasma chamber the field has a magnitude of only about 0.002 T. The analytical expressions are very convenient for direct use in computer simulation codes.

- A simple iterative finite difference code was developed to calculate the electrostatic field in VISIONI in the absence of plasma by solving Laplace's equation. This code was first tested by calculating the an-

alytically solvable case without biasing of the tungsten filaments. For this case perfect agreement was found between the finite difference calculation and the analytical solution. Then biasing of the filaments was implemented as well. Additionally the possibility of solving Poisson's equation for a given charge distribution was implemented in the finite difference code.

- The VISIONI Monte Carlo Charged Particle Tracking or shortly VMCPT code was developed from scratch to simulate the plasma in VISIONI. It takes into account the thermionic emission of electrons by the tungsten filaments, the motion of the charged particles in the magnetostatic field and collisions of the charged particles with other charged particles, neutrals and the walls of the plasma chamber. The most important approximation in the VMCPT code is the fact that the bulk electric field is neglected. In principal the finite difference Poisson solver could be used in the VMCPT code to solve the electric field in the plasma self-consistently. However, this would require an unrealistically large amount of CPU time. Solving the electric field in VISIONI self-consistently could become possible in the future by using a much more efficient electric field solver, massive parallelization and a state of the art High Performance Computing system. This would eliminate the most important approximations in the VMCPT code and thus greatly improve the quality of the simulations.

- The deuterium plasma in VISIONI was characterized in detail by means of VMCPT simulations, Langmuir probe measurements and quadrupole mass and energy analyser measurements. In general the agreement between the simulations and the measurements was rather good. The observed deviations are probably caused by the uncertainty in the deuterium collision cross sections and the absence of a self-consistent electric field calculation in VMCPT. The acceleration of the ions by the potential drop in the presheath was introduced artificially in VMCPT by giving the ions a higher starting energy. This starting energy was chosen as a given fraction of the electron temperature as also the presheath potential drop is proportional to the electron temperature. This fraction of the electron temperature was treated as an additional free parameter that had to be calculated by fitting of the simulation results and the measurements. This fitting was only performed for standard operating conditions as it requires a large set of time consuming simulations. An initial ion energy $E_{in} = 0.3kT_e$ gave the best agreement between simulation results and measurements for standard operating conditions. Other possible explanations for the deviations between the simulations and the measurements are the inherent uncertainties on the plasma parameters derived from Langmuir probe measurements and the disturbance of the Langmuir probe IV

characteristic by the magnetic field and the presence of the probe itself.

- The plasma properties in VISIONI are determined by three free parameters. The first free parameter is the heating current I_f running through the tungsten filaments. It determines the filament temperature T_f and thus also the primary electron emission rate R_{pe}. Empirical and theoretical relations between I_f, T_f and R_{pe} were derived. However, the applicability of these relations is limited due to aging effects of the tungsten filaments and the additional discharge current running through the tungsten filaments during plasma operation. Therefore, it was decided to use I_f simply as a tuning parameter to keep the target current I_t at the desired value. In the VMCPT code R_{pe} can be specified directly in the input file and is treated as a fitting parameter tuned to get agreement between the simulated and measured values for I_t. The second free parameter is the potential difference V_{ac} between the tungsten filaments and the side and bottom of the plasma chamber. As the potential drop is concentrated in a very thin sheath layer around the tungsten filaments, V_{ac} determines the initial energy of the primary electrons. The third free parameter is the neutral gas pressure p which is regulated by the pressure control valve and determines the collisionality. The values for V_{ac} and p in VMCPT are directly specified in the input file and should be taken equal to their experimental counterparts.

- The combination of VMCPT simulations and Langmuir probe measurements showed that the EEDF for a deuterium plasma in VISIONI is bi-Maxwellian. About $98-99\%$ of the electrons belong to the cold bulk electron population with a temperature of about $1-2$ eV, while a small fraction of about $1-2\%$ of the electrons belong to a hot electron population in the tail of the EEDF with a temperature of about $20-25$ eV. The cold electron population consists mainly of secondary electrons created by ionization and electron ejection by electron impact on the plasma chamber walls with a smaller contribution from the primary electrons that lost most of their energy by collisions with the neutral gas molecules. The hot electron population consists mainly of primary electrons that experienced only a few collisions with a smaller contribution from the secondary electrons. The bi-Maxwellian EEDF is a result of the limited collisionality between the charged particles in the low density plasma of VISIONI. Especially the energetic primary electrons have not enough time to equilibrate.

- VMCPT simulations and quadrupole mass and energy analyser measurements showed that H_2^+ ions, H_3^+ ions, electrons and H_2 molecules are the dominant species for a deuterium plasma in VISIONI. This is in good agreement with theoretical expectations. H^- ions could not

be observed, while H^+ ions were found to contribute less than 1% to the total ion content. H_2^+ ions and H_3^+ ions dominate at respectively low and high pressures with a transition at about 0.15 Pa. This is due to the very efficient conversion reaction in which H_2^+ ions can be transformed into H_3^+ ions by collisions with H_2 molecules. The dissociation degree of the neutral gas was found to be below 0.1%.

- The ion density, the ion flux to the target plate and the hot electron population are strongly increased at the edges of the plasma chamber around the tungsten filaments. Furthermore, an asymmetry was observed for mirroring with respect to the y axis. These effects can be explained by the typical trajectories described by the primary electrons emitted from the tungsten filaments under influence of the magnetostatic field created by the permanent magnets at the side and bottom of the plasma chamber.

- Variations of the free parameters R_{pe}, p and V_{ac}, switching on and off different processes and generating specific data that cannot be accessed experimentally with the VMCPT code gave a deeper understanding of the important processes in VISIONI.

- A study was performed to investigate the feasibility of an optical emission spectroscopy system for VISIONI. From this study it was concluded that the high IR heat load from the tungsten filaments implies the use of mirrors instead of lenses for the collection optics. Further, it was shown that due to the low plasma density a very sensitive system will be needed to observe trace impurities in the plasma spectroscopically.

Chapter 7

Material migration studies in VISIONI

This chapter presents the results of the first experimental material migration campaigns performed in VISIONI. The first section discusses a campaign in which copper samples were exposed to a deuterium plasma. The aim of this campaign was to investigate physical sputtering and to check whether VISIONI is an appropriate tool to study erosion yields. The next section discusses a study in which graphite samples were exposed to a deuterium plasma. This allowed to look at additional chemical erosion. The third section deals with an experimental campaign in which graphite samples were again exposed to a deuterium plasma in VISIONI, but now with simultaneous injection of $^{13}CH_4$ to investigate the transport, deposition and especially the re-erosion behaviour of the injected ^{13}C. The last section summarizes the main conclusions of this chapter.

7.1 Physical sputtering of copper

7.1.1 Description of the experimental campaign

The aim of the first experimental material migration campaign in VISIONI was to study physical sputtering caused by the impact of molecular deuterium ions from the plasma and to investigate whether VISIONI is an appropriate tool to study erosion yields. Therefore, a material undergoing significant physical erosion under the impact of molecular deuterium ions with an impact energy of the order of 100 eV was needed. To start with the most simple case, it was further demanded that the material does not undergo chemical erosion by deuterium impact. Taking into safety and practical issues related to the use of several other candidate materials it was eventually decided to use copper. Disc shaped samples with a radius

Table 7.1: The exposure conditions and the post-mortem mass loss analysis of the copper samples exposed to a deuterium plasma in VISIONI

	conditions			**mass loss**		
	E_i **[eV]**	**p [Pa]**	I_t **[A]**	Δ**m [mg]**	Δ**t** [μ**m**]	**Y**
Cu1	334	0.30	2	6.7	9.7	0.0787
Cu2	204	0.30	2	0.8	1.1	0.0096
Cu3	259	0.30	2	1.8	2.6	0.0215
Cu4	334	0.05	1	3.1	4.4	0.0440
Cu5	224	0.05	1	1.3	1.9	0.0174
Cu6	279	0.05	1	2.0	2.9	0.0254
Cu7	334	0.30	2	1.8	2.6	0.0215
Cu8	384	0.30	2	3.1	4.4	0.0335
Cu9	384	0.30	2	5.3	7.6	0.0587

$r_s = 5.65$ mm and a thickness $t_s = 4$ mm were cut from a block of pure polycrystalline copper with a density $\rho_{Cu} = 8.909$ g/cm^3. Before exposure the surface of the copper samples was polished until a smooth highly reflective surface was obtained. This was done by wet polishing for a few minutes using subsequently the Struers MD-Piano 2000, the Struers MD-Piano 4000 and Struers FEPA P4000 SiC paper. The surface roughness after this treatment was determined to be about 3 μm by means of white light profilometry.

After the surface treatment the copper samples were exposed to a deuterium plasma in VISIONI. As explained in 3.2.4, due to the geometry of the sample holder only a circular area with radius $r_{se} = 5$ mm was actually exposed to the plasma. An annulus with thickness $dr = 0.65$ mm remained unexposed. To study the dependence of the physical sputtering on the ion impact energy E_i, the biasing potential V_{as} of the samples with respect to the anode was varied between -200 V and -380 V. The ion impact energy in VISIONI is related to this biasing according to the relation

$$E_i = q_e(V_{pl} - V_{as}) \tag{7.1}$$

with V_{pl} the plasma potential in the centre of the plasma chamber with respect to the anode which was in the previous chapter determined to be of the order of 4 V. To study the dependence of the physical sputtering on the type of molecular deuterium ion, exposures were performed for different values of the neutral deuterium pressure p. Most exposures were performed at a pressure of 0.3 Pa. For this pressure it was shown in the previous chapter that the ions are composed out of about 80% D_3^+ ions and 20% D_2^+ ions. Three exposures were performed at a lower pressure of 0.05 Pa. This was

the lowest pressure for which a stable plasma could still be obtained. For this pressure it was shown in the previous chapter that the ions are composed out of about 70% D_2^+ ions and 30% D_3^+ ions. The different exposure conditions are summarized in table 7.1. All samples were exposed until an ion fluence $\Phi = 10^{25}$ m^{-2} was reached. This fluence was determined by integrating the measured sample current over time and resulted in exposure times of about six hours. The potential difference between the anode and the filaments and between the anode and the target plate was always set to 80 V. The heating current through the tungsten filaments was changed during the exposures such that the target current I_t remained constant at a value of 2 A for the 0.3 Pa exposures and 1 A for the 0.05 Pa exposures. This was done to avoid the drift of the primary electron emission rate discussed in the previous chapter. In this way the plasma was kept as constant as possible during the exposure.

Different analysis techniques were applied to the samples. The mass was measured before and after exposure with a precision of 0.1 mg to determine the mass loss Δm. From the mass loss the average crater depth Δt was calculated as

$$\Delta t = \frac{\Delta m}{\rho_{Cu} \pi r_{se}^2} \tag{7.2}$$

and the sputtering yield Y as

$$Y = \frac{\Delta m N_A}{M_{Cu} \Phi \pi r_{se}^2} \tag{7.3}$$

with $M_{Cu} = 63.546$ g/mol the molar mass of copper. The surface impurity concentrations were determined by means of EDX. The surface morphology was studied by means of SEM. The shape of the erosion crater was characterized by white light and laser profilometry. The eroded volume and thus also the mass loss and the sputtering yield could be calculated by subtracting the profilometry data before and after exposure.

7.1.2 Surface impurity concentrations

The surface impurity concentrations were determined by means of EDX. The atomic percentages of the different impurities found after exposure are summarized in table 7.2. The main impurities found are carbon and oxygen with typical atomic percentages of respectively $20a\%$ and $4a\%$ and are homogeneously spread over the surface. However, the concentrations of carbon and oxygen determined by means of EDX are prone to large errors. EDX is less sensitive for low Z elements. Furthermore, carbon and oxygen can also be deposited on the sample during EDX analysis. This was confirmed by the fact that for unexposed copper samples similar carbon and oxygen concentrations were observed. Thus most probably the carbon and oxygen impurities are not caused by exposure in VISIONI. The presence

Table 7.2: The surface impurity concentrations measured on the copper samples by means of EDX after exposure to a deuterium plasma in VISIONI

	Cu [a%]	**C** [a%]	**O** [a%]	**Al** [a%]	**W** [a%]
Cu1	67.6	26.5	5.1	0.3	0.5
Cu2	75.5	22.3	3.8	0.3	0.0
Cu3	76.2	19.9	3.9	0.0	0.0
Cu4	76.9	19.3	3.3	0.3	0.2
Cu5	77.2	19.2	3.4	0.1	0.1
Cu6	74.4	21.0	4.0	0.3	0.2
Cu7	81.7	15.0	3.1	0.0	0.1
Cu8	75.1	21.3	3.3	0.1	0.1
Cu9	76.5	19.7	3.2	0.3	0.3

of oxygen is probably due to exposure to oxygen in the air. Therefore, it is thought that the oxygen is eroded away rapidly during the exposure in VISIONI and then appears again after the exposure due to contact with oxygen in the air. Hence, the effect of oxygen on the physical sputtering should be limited. Carbon can contaminate the surface due to exposure to CO_2 in the air, deposition of dust particles, polishing using SiC paper and contamination of the plasma chamber from previous campaigns with graphite samples and methane plasmas. Thus it is possible that carbon remains at the surface also during the exposure in VISIONI. As the atomic fraction of carbon is rather high, it might have an important influence on the physical sputtering of the copper samples.

Besides oxygen and carbon also trace amounts below $0.5a\%$ of tungsten and aluminium were found. These species were not present before exposure. They are found homogeneously spread over the exposed part of the surface. Tungsten is probably due to evaporation of the tungsten filaments, while aluminium is probably due to physical sputtering of the macor ring of the sample holder by the impinging deuterium ions from the plasma. As the atomic fractions of tungsten and aluminium are very low the effect on the physical sputtering will not be significant.

The information depth of the EDX analysis was about 0.6 μm. The mass of the copper incorporated in this top layer is about 0.54 mg. The measured impurity weight percentage was never more than about $15w\%$. Therefore, the possible contribution of impurity erosion and deposition to the mass loss will be of the order of the precision of balance of 0.1 mg. Thus for mass losses significantly above 0.1 mg the deduced physical sputtering yield will not be influenced significantly by erosion and deposition of impurities.

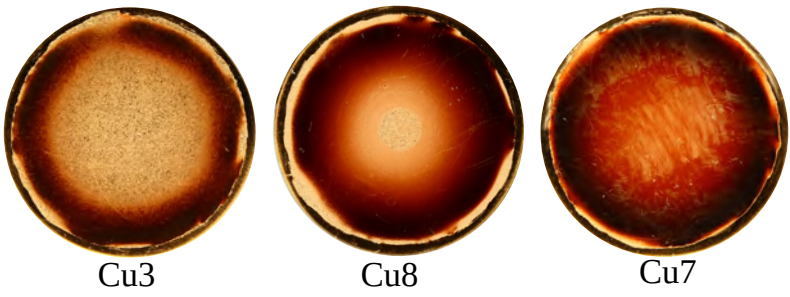

Figure 7.1: Photographs showing the different colours shades visible on the copper sample surfaces after exposure to a deuterium plasma in VISIONI

7.1.3 Colour shades and surface morphology

Figure 7.1 shows photographs of the three typical colour shade patterns exhibited by the exposed copper surfaces. The transition between the different colour shades when moving radially from the edge towards the centre is very striking. It starts with the shiny unexposed edge which was covered by the sample holder during the exposure. The colour shade patterns in the edge of the exposed surface area are the same for all copper samples. They vary from yellow over red to black. When moving further towards the centre one can observe the inverse transition from black over red towards yellow. Some samples such as Cu3 have a very large central yellow area, while others such as Cu8 have a wider red band. Sample Cu7 even has a fully red centre. Curiously some samples exposed at the same conditions had significantly different colour shade patterns. Hence, no clear correlation between the exposure conditions and the colour shade patterns could be determined.

At first it was thought that the different colours might be due to copper oxide formation. Two types of copper oxide exist, Cu_2O which has a red colour and CuO which has a black colour. However, the EDX analysis showed that oxygen is present homogeneously distributed over the whole surface. Furthermore, XRD analysis showed that no crystalline copper oxide phases are present on the exposed surfaces. Thus another phenomenon has to be responsible for the different colour shades.

By studying the surface morphology with SEM a clear correlation was found between the surface morphology and the different colours. Figure 7.2A shows the typical surface morphology in the edge of the exposed samples. At the right one can see the unexposed part indicated with the number 1. Figure 7.2B zooms in on this region. Only some lines are visible on this further flat surface due to polishing. In the centre of figure 7.2A the edge of the exposed area indicated with the number 2 can be observed. Figure 7.2C zooms in on this region. There is a clear transition from a slightly

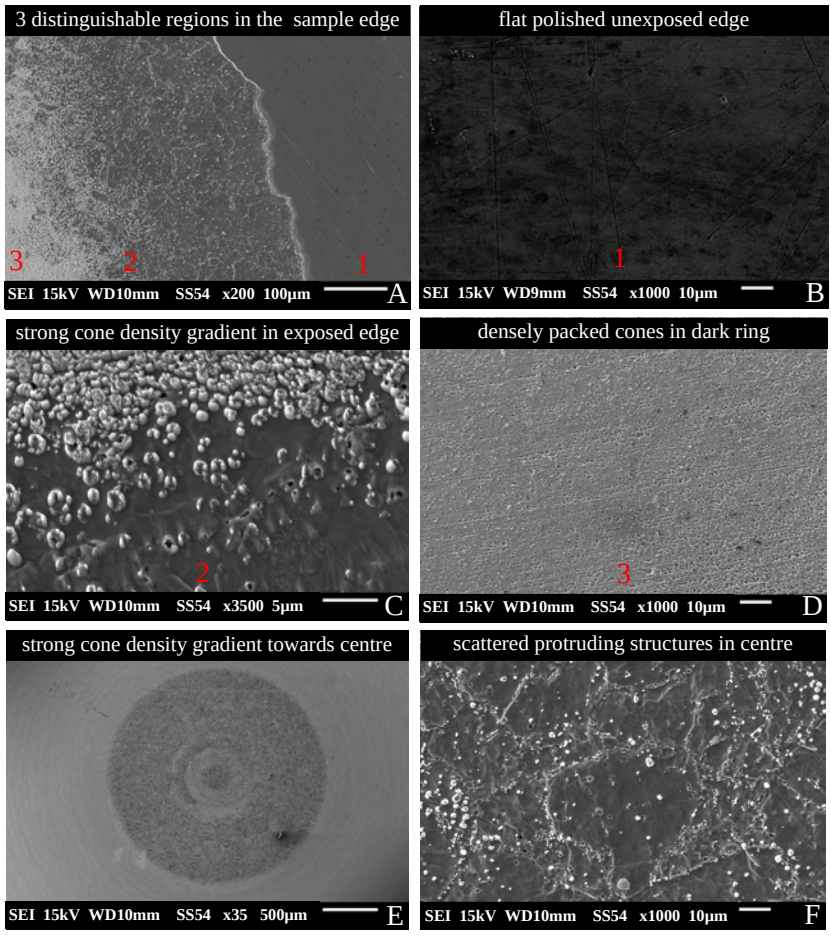

Figure 7.2: SEM pictures showing the typical surface morphology of the copper sample surfaces after exposure to a deuterium plasma in VISIONI

roughened surface with some scattered etch pits and protruding structures to a more dense population of protruding structures. Eventually on the left side of figure 7.2A, as shown in more detail in figure 7.2D, the protruding structures become so densely packed that the underlying surface is no longer visible.

The increasing density of protruding structures observed in the edge of the samples correlates nicely with the transition from yellow over red towards black on the photographs in figure 7.1. This is not just an accidental correlation. The surface morphology can also explain the colours. As the protruding structures become more densely packed, light impinging on the

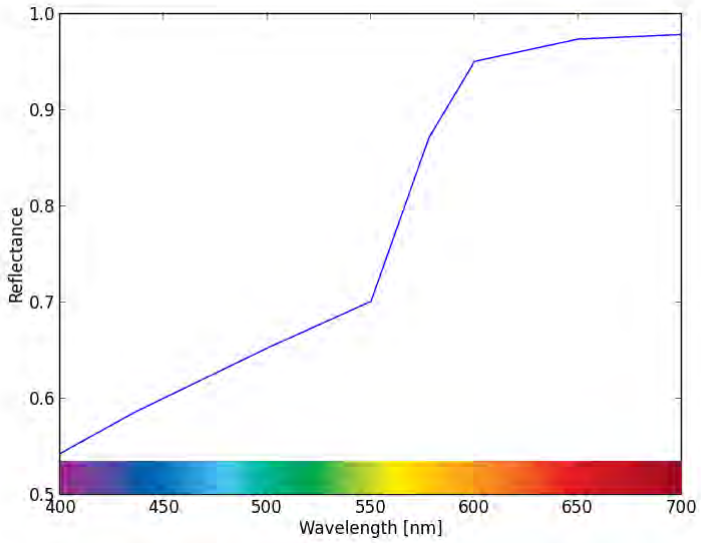

Figure 7.3: Copper visible light reflectance [187]

samples needs more and more reflections to escape from the surface. The reflectance data from [187] plotted in figure 7.3 show that the reflectance of copper in the visible range starts to increase strongly in the yellow region and reaches a maximum in the red region. This leads to a change of the apparent colour from yellow to red and eventually even to black when more and more reflections are needed for impinging light to escape from the surface.

The same effect is responsible for the transition back from black over red to yellow when going further towards the centre of the samples. This is illustrated in figure 7.4E for a sample with a small yellow circle in the centre such as sample Cu8 shown on the central photograph in figure 7.1. The small yellow circle corresponds with a region where the density of protruding structures is strongly diminished. A zoom in the centre of the yellow circle in figure 7.4F shows that the underlying surface is again clearly visible with only a few scattered protruding structures and etch pits. It seems that the protruding structures and etch pits are concentrated along certain lines which are probably grain boundaries. From this discussion it can be concluded that the different colours observed on the copper samples after exposure to a deuterium plasma in VISIONI are caused by variations in the density of protruding structures created under ion bombardment.

The question now remains how these protruding structures are formed. A literature study was performed to look for possible mechanisms. The

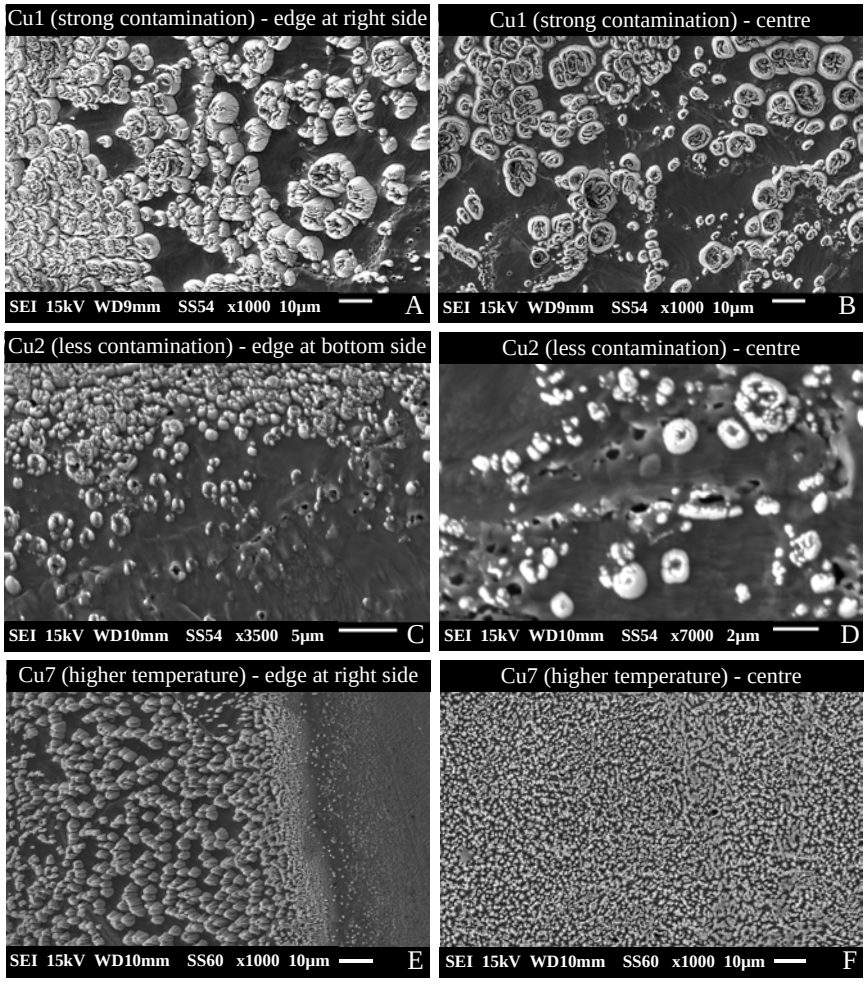

Figure 7.4: SEM pictures showing the variety in shape and orientation of the protruding structures on the copper sample surfaces after exposure to a deuterium plasma in VISIONI

study in [188] shows that for well polished and very pure copper samples regular pyramids and etch pits are created under argon ion bombardment of copper with a strong dependence on the crystal orientation. It is argued in [188] that these structures are probably induced by dislocations at the surface present already before ion bombardment or induced by the ion bombardment. The structures found on our samples are clearly no regular pyramids. Furthermore, no difference in surface morphology was observed

between different grains. Therefore, the protruding structures found in our study are most probably not induced by surface dislocations specific for certain crystal orientations.

In [189] irregular structures similar to the structures found on our samples were observed to be formed on copper under influence of argon ion bombardment. These structures were eventually eroded again after receiving enough ion fluence. It is argued in [189] that these structures are caused by asperities present on the surface before exposure. Such asperities can also be expected in our case due to cutting of the samples followed by imperfect polishing. As explained in [59] a more careful sequence of different polishing procedures is needed in order to obtain an asperity-free surface. The formation of protruding structures induced by small asperities on the surface is predicted by analytical sputtering theory [190], [59] and simulations [189]. Hence, asperities present on the copper surface before exposure are probably an important factor in the formation of the protruding structures observed in our study.

Above a critical surface temperature of 470 K and in the presence of a significant amount of carbon on the copper surface also cone formation was observed in [189]. In contrast to the more irregular structures discussed above these cones were found to be more resistant against subsequent erosion. It is argued in [189] that these cones are formed under influence of impurity segregation by thermal diffusion. The segregated impurities locally reduce the erosion rate leading to asperities which then can again evolve to protruding structures as described above. Carbon impurities appear to play an important role also in our studies. Sample Cu1 was the first copper sample exposed after an experimental campaign with graphite samples. This resulted in a carbon surface concentration of $26.52a\%$ which is significantly higher than the carbon surface concentrations of about $20a\%$ found on the other exposed samples. This seems to be correlated with the fact that the protruding structures observed on sample Cu1 had a diameter of the order of 10 μm, while for all other exposed samples the diameter of the protruding structures was only of the order of 1 μm. This can be seen by comparing the SEM pictures in figures 7.4A and 7.4B with the SEM pictures in figures 7.4C and 7.4D. Furthermore, also the temperature effect could be observed in our studies. During exposure the copper sample temperature was normally kept at 310 K. To investigate a possible temperature effect sample Cu7 was exposed with a surface temperature of 500 K, so above the critical temperature for carbon segregation on copper found in [189]. This was the only sample for which cone like structures were found after exposure as can be seen in figures 7.4E and 7.4F. It can be concluded that besides asperities also carbon contamination and surface temperature play an important role in the formation of the protruding structures in our study.

Analytical sputtering theory [190], [59] and simulations [189] predict that the protruding structures induced by pre-existing asperities under ion bombardment are aligned with the ion impact direction. This is in agree-

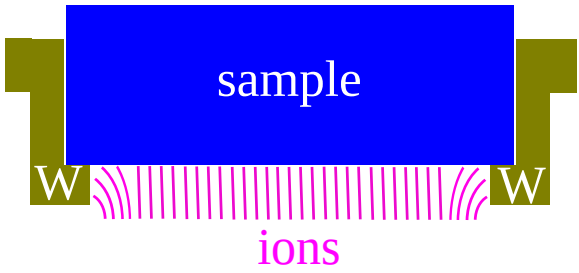

Figure 7.5: The leading edge of the protruding tungsten ring supporting the sample bends the electric field at the edge of the sample which leads to non-normal ion impact and reduction of the local fluence

ment with the results from our exposures. Figure 7.5 schematically shows the bending of the electric field at the edge of the sample due to the leading edge of the tungsten ring supporting the sample. This leads to non-normal ion incidence at the edge of the sample. The effect of the difference in ion impact angle between the centre and the edge of the samples can be observed by comparing the SEM pictures on the left in figure 7.4 taken at the edge of the samples with the SEM pictures on the right in figure 7.4 taken in the centre of the samples. One can clearly see that the protruding structures are in the centre directed along the surface normal, while at the edge they are tilted due to non-normal ion impact. This effect caused by the protruding sample holder was also observed in the PISCES-B linear plasma device [191]. Hence, the orientation of the protruding structures is in agreement with theoretical predictions.

Another remaining question is why some areas on the copper samples have a high density of protruding structures, while other areas have only a limited amount of scattered protruding structures. The strong gradient of the protruding structure density in the edge of the exposed area might be an effect of the tungsten ring supporting the sample. As can be seen schematically in figure 7.5 the local ion fluence decreases towards the edge of the sample as part of the ions end up on the leading edge of the tungsten ring instead of the sample. This could explain the transition from only a few scattered protruding structures in the yellow ring at the edge to the very dense population of protruding structures in the black ring and then again to a few scattered protruding structures in the central yellow area. In the yellow ring at the edge the received fluence is probably too low for the creation of the protruding structures. In the black ring the received fluence might be optimal to create the protruding structures. In the central yellow area the fluence is probably already too high and the created protruding structures are eroded again. The area of the central yellow region differs strongly between the different samples. For some samples the yellow region

extends almost up to the black ring, while for other samples there is a broad red band in between. Most striking is the fact that there appears to be no correlation with the exposure conditions. Even samples with the same exposure conditions often have significantly different colour shade patterns. Therefore, it is thought that the different colour shade patterns in the centre are related to differences in the amount of pre-exposure asperities produced by cutting or polishing of the samples. The exact mechanism is, however, not clear. For sample Cu7, which was exposed with a surface temperature of 500 K, figure 7.4F shows that even in the centre a high density of cones was found. This is also reflected in the fact that the red area covers the whole central area as shown in figure 7.1 and is in agreement with the observations in [189] that the cones formed above the critical temperature for carbon segregation by thermal diffusion are more stable against erosion.

7.1.4 Profilometry

The copper samples were analysed with white light profilometry after exposure with the purpose of determining the volume of the erosion crater and the physical sputtering yield. However, it turned out that the shape of the surface before exposure was not flat but convex. Due to preferential polishing of the edges the centre was several tens of micrometers higher than the edges. Therefore, it was not possible to calculate the eroded volume as the reference surface before exposure was not known accurately enough. Only for copper sample Cu8 the surface was analysed also before exposure with white light profilometry. Figure 7.6 shows a comparison of the 2D white light profilometry data for this sample before and after exposure. The 2D profilometry data measured before exposure in the top left plot clearly exhibits a convex shape due to preferential polishing of the edges. The 2D profilometry data measured after exposure in the top right plot looks very similar to the photograph of sample Cu8 shown in the centre of figure 7.1. The yellow and red regions in the photograph correspond with the respectively lower and higher lying regions in the 2D profilometry plot. The black regions in the photograph had too low reflectivity for obtaining white light profilometry data. These regions are shown in white in the 2D profilometry plot.

The profilometry data before and after exposure can be compared in more detail if they are matched by means of a reference height and a reference position. The matching was done by taking a circular scan of the profilometry data along the unexposed edge. The matching of these circular profiles before and after exposure by shifting the height and rotating the sample is shown on the left plot in figure 7.7. With the reference height and the reference position determined, it was then possible to compare the profilometry data before and after exposure in more detail and to calculate the erosion depth by subtracting the data after exposure from the data before exposure. The bottom plot in figure 7.6 shows a 2D plot of the erosion

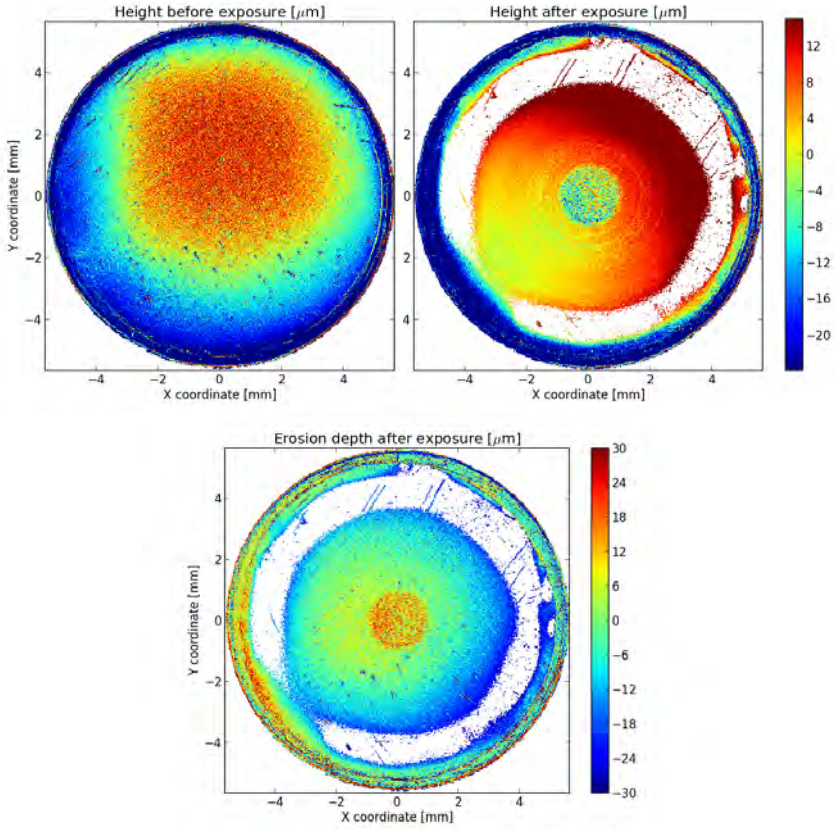

Figure 7.6: 2D white light profilometry plots for copper sample Cu8 before (top left) and after exposure to a deuterium plasma in VISIONI (top right) together with a 2D plot of the erosion depth by subtracting the data (bottom). The white colour indicates that no data could be obtained.

depth. The right plot in figure 7.7 shows the comparison of a radial profile through the centre before and after exposure. These plots show that the central area lies as expected below the original surface. However, the edge regions lie significantly above the original surface. Also striking is the sharp drop in height between the red and the yellow areas of the photograph in figure 7.1 in the centre of the sample. It is thought that this strange behaviour is just an artefact of the white light profilometer due to multiple reflections on the densely packed protruding structures in the red area. This is supported by three facts. Firstly, based on the white light profilometry the volume of the sample has increased during exposure which contradicts the measured mass loss. However, if one only uses the profilometry data

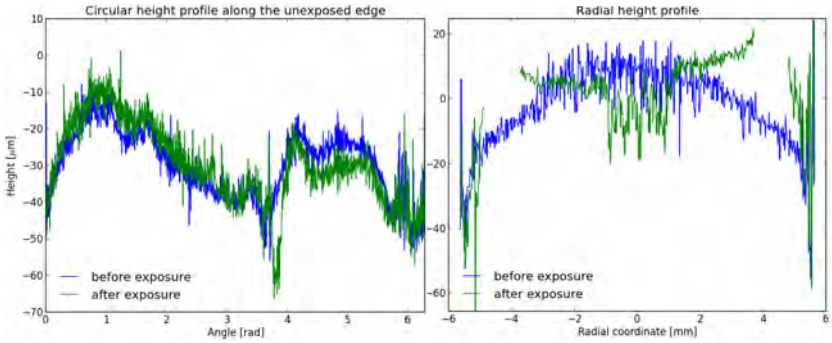

Figure 7.7: 1D white light profilometry profiles for copper sample Cu8 obtained before and after exposure to a deuterium plasma in VISIONI. Left a circular profile along the unexposed edge. Right a radial scan through the centre.

from the central yellow area and extrapolates the average erosion depth measured in this region over the whole exposed area, then the calculated eroded volume and mass loss is in good agreement with the measured mass loss. Secondly, SEM on the cross section of a similar sample that was cut in two did not exhibit the sharp drop observed with white light profilometry. Thirdly, later analysis of sample Cu8 by means of laser profilometry at Forschungszentrum Jülich gave a completely different result as shown in figures 7.8 and 7.9. In this case the surface after exposure is lying below the original surface over the whole exposed area and no sharp drop is observed between the red and yellow areas. The erosion depth in the centre is higher than in the edge. This can be explained by a reduction of the ion fluence towards the edge due to the presence of the protruding tungsten ring from the sample holder. However, the mass loss calculated from the laser profilometry analysis is a factor 3 higher than the measured mass loss. This could be due to the fact that it was not possible to get a good matching of the circular profiles before and after exposure along the unexposed edge as shown on the left plot in figure 7.9. The reason for this deviation is unclear. Hence, it can be concluded that the white light profilometer does not give reliable results for a surface with closely packed protruding structures.

7.1.5 Physical sputtering yield

The physical sputtering yields calculated from the measured mass loss are plotted in figure 7.10 as function of the ion impact energy. The mass loss results are also listed in table 7.1. The blue and green circles represent the results from respectively the 0.3 Pa and 0.05 Pa exposures. The experimental results are compared with the theoretical Eckstein yield for normal

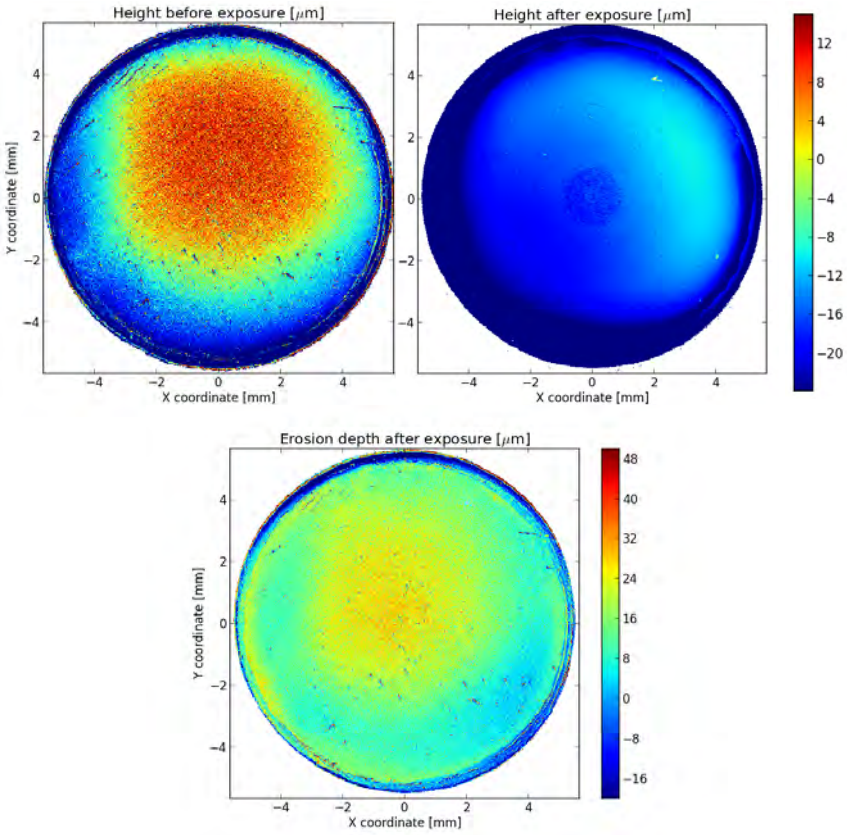

Figure 7.8: 2D profilometry plots for copper sample Cu8 obtained before exposure to a deuterium plasma in VISIONI by means of white light profilometry (top left) and after exposure by means of laser profilometry (top right) together with a 2D plot of the erosion depth by subtracting the data (bottom)

incidence discussed in 2.4.2.3. The full blue line represents the Eckstein yield for 80% D_3^+ ions and 20% D_2^+ ions and should be compared with the blue circles from the 0.3 Pa exposures. The full green line represents the Eckstein yield for 30% D_3^+ ions and 70% D_2^+ ions and should be compared with the green circles from the 0.05 Pa exposures. The Eckstein yields were calculated assuming that a D_i molecular deuterium ion is equivalent to i atomic deuterium ions with each a fraction $1/i$ of the total molecular ion impact energy. This is the assumption that is used in virtually all studies.

One can see that most data points are significantly below the theoretical predictions. There are several possible explanations. Firstly, although as

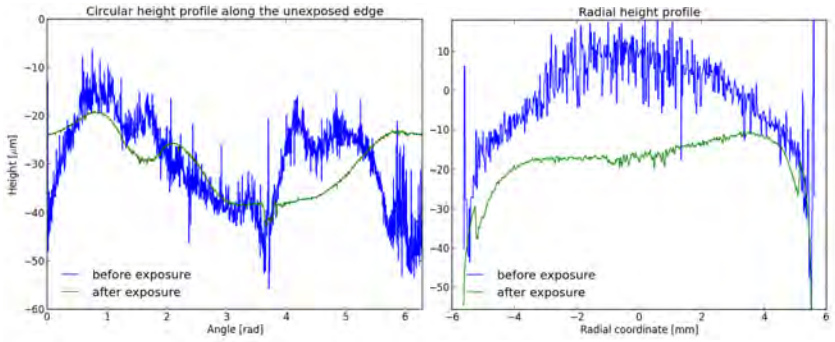

Figure 7.9: 1D profilometry profiles for copper sample Cu8 obtained before exposure to a deuterium plasma in VISIONI by means of white light profilometry and after exposure by means of laser profilometry. Left a circular profile along the unexposed edge. Right a radial scan through the centre.

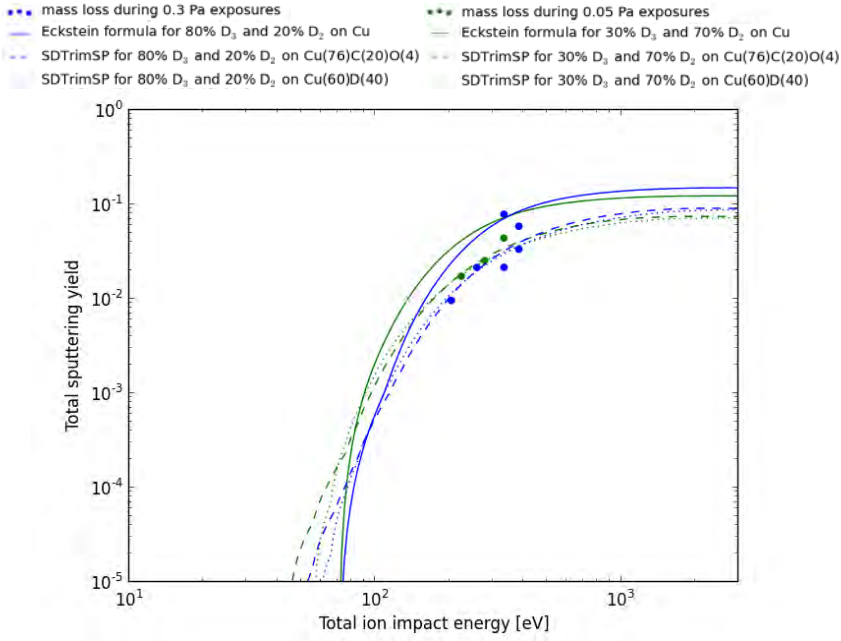

Figure 7.10: The copper physical sputtering yield dependence on deuterium ion impact energy as measured by mass loss after exposure to a deuterium plasma in VISIONI in comparison with the Eckstein formula and SDTrimSP simulations

discussed above the presence of a significant amount of carbon and oxygen impurities does not significantly influence the mass loss measurement, the impurities can strongly influence the physical sputtering yield. The dashed curves show the results from simulations with the SDTrimSP binary collision code discussed in 2.4.2.1 for deuterium impinging perpendicular to a copper surface with $20a\%$ carbon and $4a\%$ oxygen. Similar as for the Eckstein yields the blue and green curves are for the molecular ion compositions of respectively the 0.3 Pa and 0.05 Pa exposures. It can be seen that the impurities significantly reduce the physical sputtering yield in the region of interest and that most data points are now in between the full Eckstein curve and the dashed SDTrimSP curve. The two blue data points that are still below the dashed blue SDTrimSP curve correspond with two exposures during which problems occured with the electronic circuit of VISIONI. This might have influenced the exposure conditions. Secondly, the sputtering yield can also be decreased by a similar amount in the region of interest by deuterium retention in the copper surface. This is illustrated by the dotted blue and green curves in figure 7.10 showing the results from SDTrimSP simulations for molecular deuterium ions with ion compositions corresponding to respectively the 0.3 Pa and the 0.05 Pa exposures impinging perpendicularly on a copper surface with $40a\%$ deuterium. Dilution of the copper atoms by deuterium retention can also lead to enhancement of the physical sputtering yield due to reduced binding energy. This chemical effect is not taken into account in the SDTrimSP binary collision code. However, most probably for the high fluences of VISIONI the dilution effect dominates over the binding energy effect. This was found to be true for deuterium impinging on beryllium by means of MD simulations [192]. Thirdly, as was experimentally observed in [193], also redeposition of eroded species on protruding structures in the regions with a high density of protruding structures can significantly reduce the measured physical sputtering yield. In absence of the protruding structures redeposition is of no concern as the ionization mean free path is typically tens of centimeters in VISIONI. Taking into account the significant presence of carbon and oxygen impurities, the retention of deuterium and the redeposition on protruding structures the physical sputtering yields calculated from the measured mass loss are in good agreement with theoretical predictions. The difference between the theoretical curves for the 0.3 Pa and the 0.05 Pa molecular ion compositions is clearly too small in comparison with the scatter of the experimental data points to say something meaningful about a possible molecular ion effect. As a final remark it can be seen that data points obtained for the same exposure conditions can deviate significantly. The reproducibility of the erosion yield measurements and the error on the experimental data points will be discussed in detail in 7.2.6.

7.2 Physical and chemical erosion of graphite

7.2.1 Description of the experimental campaign

The aim of the second experimental material migration campaign in VISIONI was to study physical sputtering, chemical sputtering and chemical erosion of graphite caused by the impact of the molecular deuterium ions from the plasma. Disc shaped samples with a radius $r_s = 5.65$ mm and a thickness $t_s = 4$ mm were used. First some trial exposures were performed using a very porous type of graphite with a density $\rho_{C1} = 1.685$ g/cm^3 that was readily available. The subsequent exposures were performed using R6650 graphite with a density $\rho_{C2} = 1.755$ g/cm^3. Before exposure the surface of the graphite samples was shortly polished until a smooth surface was obtained. This was done by dry polishing using Struers FEPA P4000 SiC paper. The surface roughness after this treatment was determined to be about 6 μm by means of white light profilometry.

After the surface treatment the graphite samples were exposed to a deuterium plasma in VISIONI. As explained in 3.2.4, due to the geometry of the sample holder only a circular area with radius $r_{se} = 5$ mm was actually exposed to the plasma. An annulus with thickness $dr = 0.65$ mm remained unexposed. The exposures were all performed at a pressure of 0.3 Pa. For this pressure it was shown in the previous chapter that the ions are composed out of about 80% D_3^+ ions and 20% D_2^+ ions. As it turned out in the previous section that the molecular ion effects are not very pronounced, it can be assumed for this study that all ions are D_3^+ ions. All samples were exposed until an ion fluence $\Phi = 10^{25}$ m^{-2} was reached. This fluence was determined by integrating the measured sample current over time and resulted in exposure times of about six hours. The potential difference between the anode and the filaments and between the anode and the target plate was always set to 80 V. The heating current through the tungsten filaments was changed during the exposures such that the target current I_t remained constant at a value of 2 A. This was done in order to avoid the drift of the primary electron emission rate discussed in the previous chapter. In this way the plasma was kept as constant as possible during the exposure. The ion impact energy per deuteron $E_i/3$ was varied between 1 eV and 130 eV by changing the biasing of the sample with respect to the anode in order to study the impact energy dependence of physical and chemical sputtering. Also the sample surface temperature was varied between 310 K and 500 K in order to study the surface temperature dependence of thermal chemical erosion. The different exposure conditions of the R6650 graphite samples are summarized in table 7.3.

Different analysis techniques were applied to the samples. The mass was measured before and after exposure with a precision of 0.1 mg to determine the mass loss Δm. From the mass loss the average crater depth Δt was calculated as

Table 7.3: The exposure conditions and the post-mortem mass loss and profilometry analysis of the R6650 graphite samples exposed to a deuterium plasma in VISIONI

	conditions		mass loss			profilometry			laser profilometry		
	T_s [K]	$E_i/3$ [eV]	Δm [mg]	Δt [μm]	Y/3	Δt [μm]	Δm [mg]	Y/3	Δt [μm]	Δm [mg]	Y/3
C1	310	130	2.7	19.6	0.0483	23.6	3.3	0.0582	18.4	2.5	0.0455
C2	310	110	2.1	15.2	0.0446	17.8	2.5	0.0523	14.1	1.9	0.0412
C3	310	95	1.9	13.8	0.0401	17.7	2.4	0.0514	15.2	2.1	0.0441
C4	310	60	2.0	14.5	0.0421	20.1	2.8	0.0583	16.1	2.2	0.0467
C5	310	30	1.5	10.9	0.0306	-	-	-	-	-	-
C6	310	1	0.3	2.2	0.0044	-	-	-	6.1	0.8	0.0123
C7	370	110	2.2	16.0	0.0461	16.8	2.3	0.0483	14.6	2.0	0.0420
C8	420	110	1.7	12.3	0.0339	9.5	1.3	0.0260	9.6	1.3	0.0263
C9	500	110	2.1	15.2	0.0444	17.8	2.4	0.0517	14.2	2.0	0.0413
C10	310	30	2.3	16.7	0.0483	-	-	-	-	-	-
C11	310	30	2.5	18.2	0.0486	-	-	-	-	-	-
C12	310	30	2.4	17.5	0.0477	-	-	-	-	-	-

$$\Delta t = \frac{\Delta m}{\rho_{C1,2}\pi r_{se}^2} \tag{7.4}$$

and the erosion yield Y as

$$Y = \frac{\Delta m N_A}{M_C \Phi \pi r_{se}^2} \tag{7.5}$$

with $M_C = 12$ g/mol the molar mass of carbon. The surface impurity concentrations were determined by means of EDX. The surface morphology was studied by means of SEM. The shape of the erosion crater was characterized by white light and laser profilometry. The eroded volume and thus also the mass loss and the erosion yield were calculated by subtracting the profilometry data before and after exposure.

7.2.2 Surface impurity concentrations

The surface impurity concentrations were determined by means of EDX. The atomic percentages of the different impurities found after exposure are summarized in table 7.4. The main impurity found is oxygen which typically contributes about $2a\%$ and is homogeneously spread over the surface. However, as mentioned already in the previous section, one has to be careful with oxygen concentrations determined by means of EDX. By analysing unexposed graphite samples it was found that similar oxygen concentrations were present already before exposure. Therefore, the presence of oxygen is probably again due to exposure to oxygen in the air. Therefore, it is thought that the oxygen is eroded away rapidly during the exposure in VISIONI and then appears again after the exposure due to contact with oxygen in the air. Hence, the effect of oxygen on the erosion yield should be limited. Besides oxygen also trace amounts below 1% of tungsten, aluminium and steel elements were found. These species were not present before exposure.

Table 7.4: The surface impurity concentrations of the R6650 graphite samples measured by EDX in atomic percentage after exposure to a deuterium plasma in VISIONI

	C a%	**O** a%	**W** a%	**Al** a%	**Cr** a%	**Fe** a%
C1	96.6	2.3	0.9	0.1	0.0	0.00
C2	98.8	1.2	¡0.1	0.0	0.0	0.00
C3	98.4	1.4	0.12	0.0	0.0	0.00
C4	98.6	1.4	¡0.1	0.0	0.0	0.00
C5	97.5	1.9	0.3	0.0	0.1	0.18
C6	97.7	2.1	¡0.1	¡0.1	¡0.1	0.09
C7	97.4	1.8	0.8	¡0.1	0.0	0.07
C8	98.7	1.2	0.1	¡0.1	0.0	0.00
C9	98.4	1.5	0.1	0.0	0.0	0.00

They are found homogeneously spread over the exposed part of the surface. Tungsten is probably due to evaporation of the tungsten filaments, while aluminium and steel elements are probably due to physical sputtering of respectively the macor ring of the sample holder and the steel target plate by the impinging deuterium ions from the plasma. As the atomic fractions of tungsten, aluminium and steel elements are very low the effect on the erosion will not be significant.

The information depth of the EDX analysis was about 1.6 μm. The mass of the graphite incorporated in this top layer is about 0.3 mg. The measured impurity weight percentage was never more than about 15%. Therefore, the error in the mass loss measurement due to impurities is only of the order of the precision of balance of 0.1 mg. Thus for mass losses significantly above 0.1 mg the deduced erosion yield will not be influenced significantly by erosion and deposition of impurities.

7.2.3 Mass loss analysis

Calculation of the erosion yield from the measured mass loss looks straightforward, but in case of graphite it has turned out that one should be very careful. For the first exposures with the porous graphite erosion yields more than one order of magnitude larger than expected theoretically were calculated based on the measured mass loss. Eventually it turned out that the majority of the mass was lost due to outgassing caused by the heating and the vacuum conditions experienced by the sample during exposure in VISIONI and not due to erosion by deuterium ion bombardment.

An outgassing study was performed for both types of graphite samples used throughout this experimental campaign. For the porous graphite the

outgassing effect was found to be very important. By observing the mass of the samples in time while being exposed to the atmosphere, seemingly random fluctuations of the order of several milligrams were observed. These fluctuations are probably related to fluctuations in the atmospheric pressure and humidity. The samples were then placed in a vacuum oven. Even without heating it was observed that the mass of the samples decreased several milligrams and eventually saturated after several hours in the vacuum oven at a pressure of 10 Pa. Additionally heating the samples in the vacuum oven up to 500 K resulted in a saturation mass about 1 mg lower. The saturation mass reached after bake-out in the vacuum oven could well be reproduced within the measurement error of 0.1 mg. When the samples were again exposed to the atmosphere the mass lost during baking in the vacuum oven was regained. The first half of the mass loss was regained over several tens of minutes, while the remaining half of the mass loss was regained over several days. No such regain of the mass was measured when exposing the samples in the vacuum oven to argon at atmospheric pressure. Therefore, it can be concluded that the mass fluctuations are due to adsorption of oxygen, nitrogen and water vapour from the air in the pores of the graphite. No such outgassing effects could be observed for the R6650 graphite samples. The mass fluctuations for this much less porous material are probably below the measurement error of 0.1 mg.

For the porous graphite the mass loss after exposure was thus found to be mostly due to outgassing under influence of heating and vacuum conditions experienced by the sample during exposure in VISIONI. However, it is still possible to use the mass loss to determine the erosion yield. As the mass reached by baking the samples in the vacuum oven at 500 K for several hours is reproducible, this mass can be defined as the reference mass. The mass before and after exposure should be measured after baking in the vacuum oven to eliminate the mass loss due to outgassing. For the R6650 the mass fluctuations due to outgassing are low enough not to influence the erosion yield calculation. One should, however, always check the effect of outgassing due to heating and vacuum conditions when using the mass loss for calculating the erosion yield of graphite or other light porous materials.

7.2.4 Colour shades and surface morphology

Figure 7.11 shows how the surface of the graphite samples looks like after exposure. Different colour shades can be observed varying from grey to black. The colour shade patterns found on the graphite were very reproducible. For ion impact energies per deuteron below the physical sputtering threshold of about 30 eV the sample was fully black as shown in the left photograph in figure 7.11. For ion impact energies per deuteron above the physical sputtering threshold the sample was grey with a dark black ring at the edge as shown on the right photograph in figure 7.11. This was observed both for the porous graphite and for the R6650 graphite. On the

Figure 7.11: Photograph showing the two typical colour shade patterns found at the graphite sample surfaces after exposure to a deuterium plasma in VISIONI with impact energy per deuteron below (left) and above (right) the physical sputtering threshold for deuterium on carbon

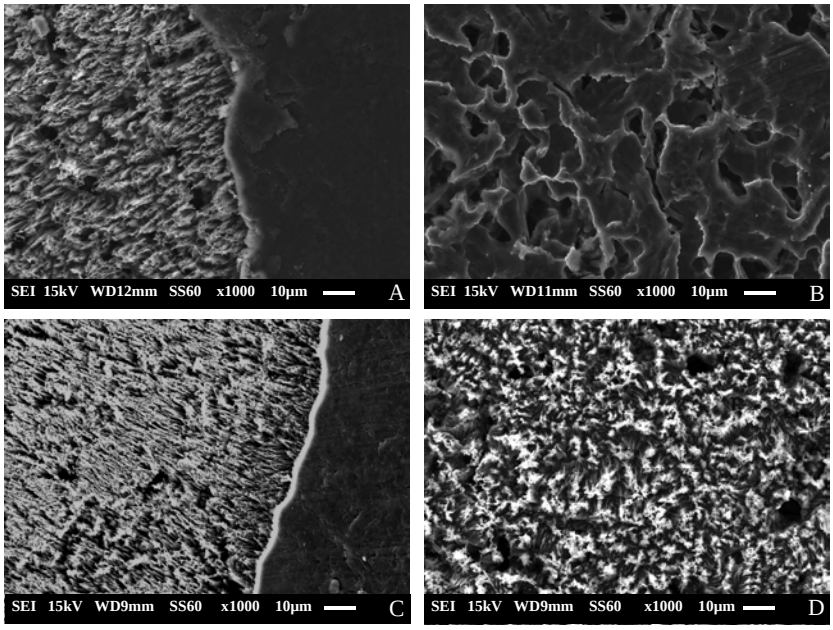

Figure 7.12: SEM pictures showing the typical surface morphology of the graphite sample surfaces after exposure to a deuterium plasma in VISIONI. The letters correspond with the areas indicated in figure 7.11.

photographs it looks like the left sample is not as black as the edge in the right sample. This is just due to a difference in the lighting conditions used

for the photographs. When looking with the naked eye the left sample looks as black as the edge of the right sample over the whole exposed area.

Studying the samples by means of SEM showed that the different colours can be explained by different surface morphologies. The different surface morphologies are shown in figure 7.12. The labels of these SEM pictures correspond with the boxes indicated on the photographs in figure 7.11. In figures 7.12A and 7.12C one can see that for both types of samples there is a very clear transition in the edge from the unexposed smoothly polished surface to the exposed area with a dense population of narrow cone-like structures similar to grass. Multiple reflections are needed for impinging light to reflect from such a grass-like surface morphology which explains the black colour in the edge of both types of samples. In figures 7.12B and 7.12D one can see that the grey centre of the sample shown at the right in figure 7.11 corresponds with a flat porous surface, while the black centre of the sample shown at the left in figure 7.11 corresponds as expected with a grass-like surface morphology.

Possible mechanisms leading to the formation of cones and other protruding structures under influence of ion bombardment were discussed already in detail in the previous section. As the amount of impurities found on the graphite samples was rather limited and as surface temperature had no clear effect on the observed surface morphology, the grass-like structure on the graphite samples is probably induced by asperities present on the surface before exposure due to cutting and polishing of the samples. The SEM pictures in figure 7.12 clearly show that the cones point as expected in the direction of the ion impact. The grass-like surface morphology is not observed in the centre of the samples exposed to ion bombardment above the threshold for physical sputtering. This could be explained by re-erosion of the created cones due to the higher erosion in the centre of these samples. The erosion in the centre is higher than at the edge due to the fluence reduction caused by the tungsten ring from the sample holder, while the erosion on the samples exposed to ion bombardment below the physical sputtering threshold undergo significantly less erosion due to the absence of physical sputtering.

7.2.5 Profilometry

The graphite samples were analysed with white light profilometry with the purpose to determine the volume of the erosion crater and the erosion yield. The R6650 graphite samples were analysed with optical profilometry before and after exposure. The porous graphite samples were analysed with optical profilometry only after exposure. Figure 7.13 shows a comparison of the 2D white light profilometry data before and after exposure for sample C1 which was exposed to ion bombardment above the physical sputtering threshold. The 2D profilometry data measured before exposure in the top left plot shows that the surface before exposure is flat but slightly tilted due to

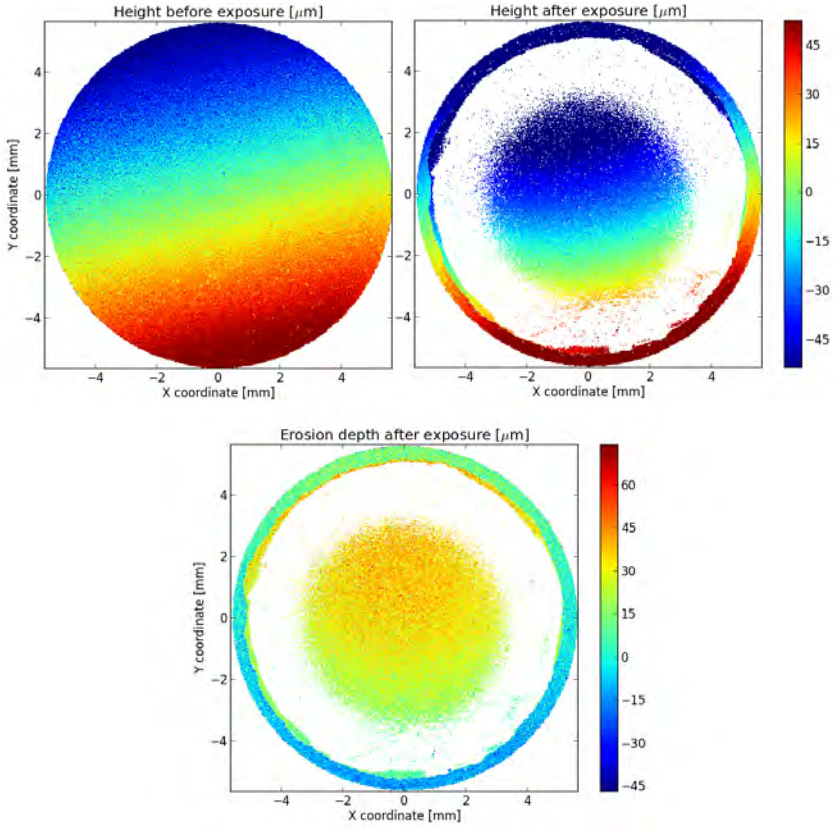

Figure 7.13: 2D white light profilometry plots for graphite sample C1 before (top left) and after exposure to a deuterium plasma in VISIONI (top right) together with a 2D plot of the erosion depth by subtracting the data (bottom). The white colour indicates that no data could be obtained.

cutting. Hence, even though the surface of the porous graphite samples was not analysed before exposure the erosion volume could still be estimated by assuming that the surface before exposure was perfectly flat between the unexposed edges. The 2D profilometry data measured after exposure in the top right plot still exhibits this tilt. The dark ring at the edge had too low reflectivity for obtaining white light profilometry data. This region is shown in white in the 2D profilometry plot. White light profilometry data could not be obtained at all for the samples exposed to ion bombardment below the physical sputtering threshold because the reflectivity was too low over the whole exposed area.

The profilometry data before and after exposure can be compared in

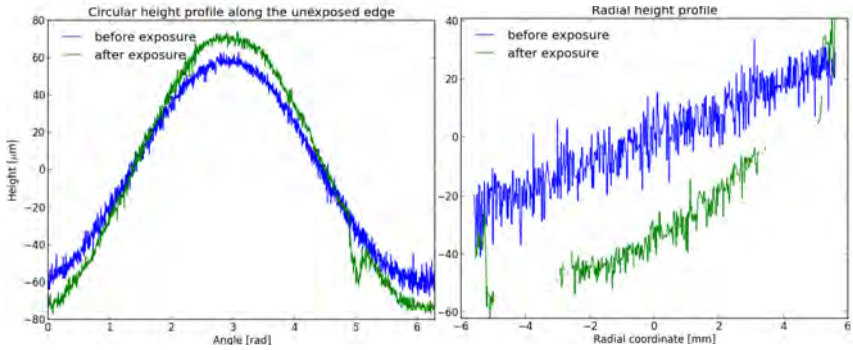

Figure 7.14: 1D white light profilometry profiles for graphite sample C1 obtained before and after exposure to a deuterium plasma in VISIONI. Left a circular profile along the unexposed edge. Right a radial scan through the centre.

more detail if they are matched by means of a reference height and a reference position. The matching was done by taking a circular scan of the profilometry data along the unexposed edge. The matching of these circular profiles before and after exposure by shifting the height and rotating the sample is shown on the left plot in figure 7.14. With the reference height and the reference position determined, it was then possible to compare the profilometry data before and after exposure in more detail and to calculate the erosion depth by subtracting the data after exposure from the data before exposure. The bottom plot in figure 7.13 shows a 2D plot of the erosion depth. The right plot in figure 7.14 shows the comparison of a radial profile through the centre before and after exposure. These plots clearly show that the depth of the erosion crater increases from the edge towards the centre. This is probably caused by the reduction of the local ion fluence at the edge due to the presence of the tungsten ring from the sample holder.

The mass loss calculated from the white light profilometry data agrees reasonably well with the measured mass loss. However, the white light profilometry systematically overestimates the mass loss. This can be explained by the fact that in the calculation for the dark ring in the edge the erosion depth was extrapolated from the centre where the erosion depth is expected to be larger. The profilometry analysis after exposure was repeated with the laser profilometer at Forschungszentrum Jülich because this allowed to get data also for the black edge and the fully black samples. The results of this analysis for sample C1 are shown in figures 7.15 and 7.16. In this case the 2D plot of the erosion depth shows even more clearly that the depth increases from the edge towards the centre. Furthermore, the mass loss calculated from the laser profilometry analysis is in much better agreement

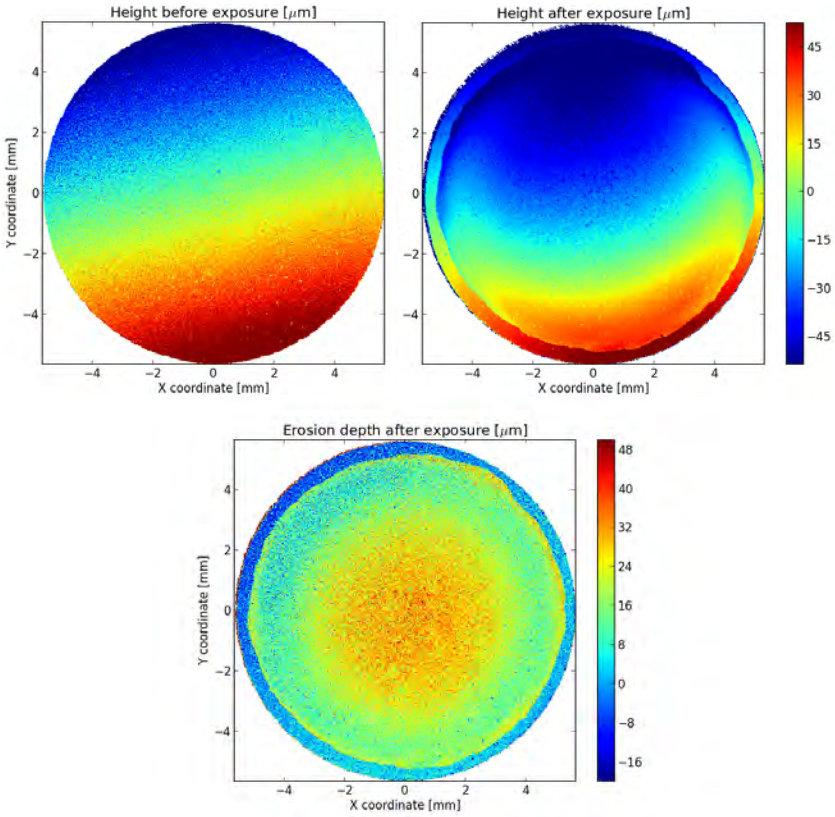

Figure 7.15: 2D profilometry plots for graphite sample C1 obtained before exposure to a deuterium plasma in VISIONI by means of white light profilometry (top left) and after exposure by means of laser profilometry (top right) together with a 2D plot of the erosion depth by subtracting the data (bottom)

with the calculated mass loss because now data is also available for the dark ring at the edge.

7.2.6 Erosion yield

Figure 7.17 shows the carbon erosion yield measured after exposure of graphite samples to a deuterium plasma in VISIONI as function of the ion impact energy. The surface temperature was kept constant at 310 K for these exposures. The green and red symbols represent the data for respectively the porous graphite samples and the R6650 graphite samples. The

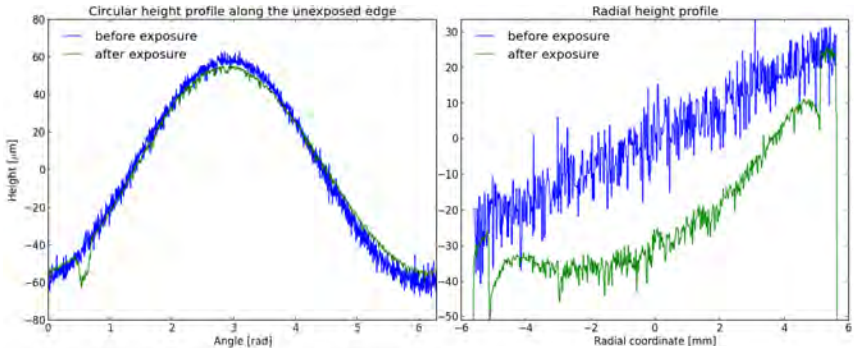

Figure 7.16: 1D profilometry profiles for graphite sample C1 obtained before exposure to a deuterium plasma in VISIONI by means of white light profilometry and after exposure by means of laser profilometry. Left a circular profile along the unexposed edge. Right a radial scan through the centre.

circles, triangles and crosses represent the erosion yield calculated from respectively mass loss, white light profilometry and laser profilometry. The erosion yields per deuteron are plotted as function of the impact energy per deuteron. So the total erosion yields and the total ion impact energies are divided by three to take into account the fact that the plasma is composed mainly of D_3^+ ions. The yields calculated from mass loss and profilometry for the R6650 samples are also listed in table 7.3.

As was already observed in 7.1.5 for the copper exposures, erosion yields measured for the same exposure conditions can deviate sometimes significantly. Therefore, the reproducibility of the experimentally determined erosion yields was studied by repeating the exposure conditions of sample C5 for samples C10, C11 and C12. These additional exposures were performed on three consecutive days about one month after the exposure of sample C5. Less than 2% deviation was found between the erosion yields calculated from the mass loss of samples C10, C11 and C12. This agrees with the expectations as the mass loss and the fluence were measured with an accuracy only a few percent. However, the erosion yield calculated from the mass loss of sample C5 was about 40% lower than the other erosion yields. So, apparently the reproducibily is very good for consecutive exposures, while deviations of tens of percents can be found for exposures separated in time. This was also observed during the experimental campaigns with the porous graphite samples and the copper samples. The large deviations for exposures separated in time are probably related to differences in the impurity content of the plasma chamber due to previous experiments. The impurity content influences the erosion because the impurities can also erode the surface or they can influence the erosion by deposition. Multiple exposures

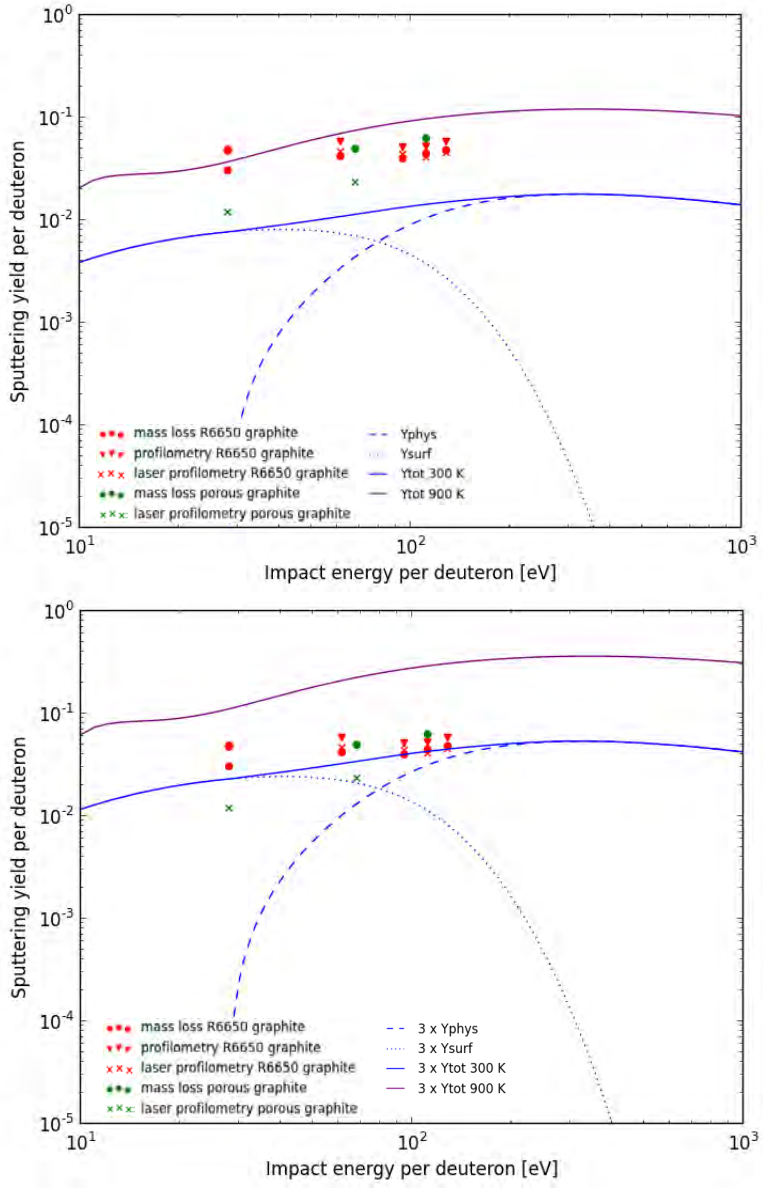

Figure 7.17: The carbon sputtering yield dependence on impact energy as measured by mass loss and profilometry after exposure to a deuterium plasma in VISIONI in comparison with the analytical model discussed in 2.4.3.2

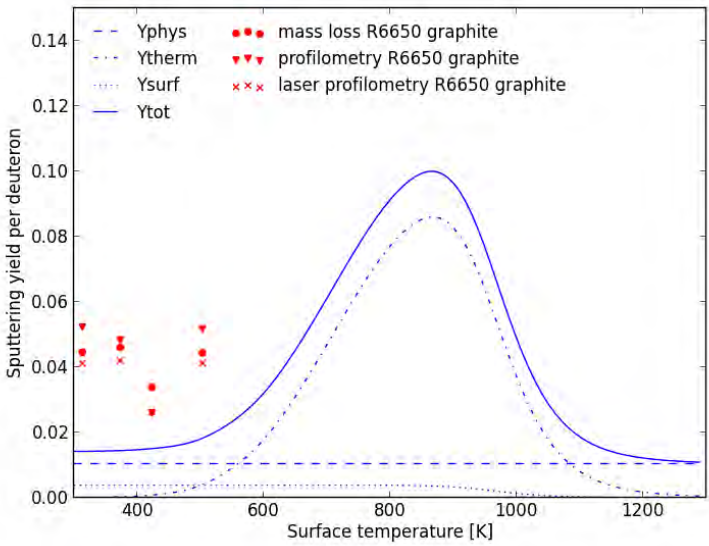

Figure 7.18: The carbon sputtering yield dependence on sample temperature as measured by mass loss and profilometry after exposure to a deuterium plasma in VISIONI in comparison with the analytical model discussed in 2.4.3.2

should be performed for each condition to get better statistics. However, this is very time consuming as one exposure takes one day for changing of the sample and one day for the actual exposure. Furthermore, the impurity content of the plasma during the exposures should be monitored with the energy and mass analyser which was unfortunately not in operation during the presented study. This would allow to investigate the corelation between the impurity content and the erosion yield. Because of this it is very difficult to assign an error bar to the experimental data points.

Taking into account the observed scatter, the agreement between the yields calculated from mass loss and profilometry is very good. Furthermore, also profilometry has its limitations. One source of error is the procedure for matching the profilometry data before and after exposure. For some samples the circular profiles along the unexposed edge deviated significantly before and after exposure. The reason for this deviation is not clear. Another source of error is the fact that the eroded volume and thus also the erosion yield from white light profilometry is calculated based on the average crater depth measured in the central region because the edge had too low reflectivity for the white light profilometer. As the crater depth

at the edge is actually smaller, this is a possible explanation for the systematically higher erosion yields. For the laser profilometry analysis, in which case also the dark edge could be measured, this systematic overestimation is no longer present.

Taking again into account the observed scatter, no significant difference was observed between the erosion yields for the porous graphite and the R6650 graphite. This is what one expects because for the high deuterium fluences to which the samples were exposed the surfaces of different types of graphite will become amorphous hydrocarbon layers which are indistinguishable from each other.

The blue curves on the top plot in figure 7.17 show the erosion yield according to the analytical model discussed in 2.4.3.2 for comparison with the experimental data. The dashed blue curve represents the physical sputtering. The dotted blue curve represents the surface chemical sputtering. The full blue curve represents the sum of physical and chemical sputtering. The full purple curve takes into account the additional thermal chemical erosion for an elevated surface temperature of 900 K which is around the maximum of the thermal chemical erosion. It can be seen that the experimental erosion yields for room temperature follow the same increasing trend with impact energy as the theoretical curve. However, the experimental values are much higher. A locally higher surface temperature cannot explain the deviation. Even the purple curve for a much higher surface temperature of 900 K is laying only just above the experimental data points, while tests with the cold finger showed that the measured temperature at the tip of the cold finger never deviates more than 30 K from the actual surface temperature for relevant power loads. The bottom plot in figure 7.17 compares the experimental data points with the theoretical curves multiplied with a factor 3. This shows that the experimental erosion yields are about a factor 3 higher than the theoretical yields. This is in agreement with the observations in [76]. They exposed graphite to bombardment with H^+, H_2^+ and H_3^+. When looking at the erosion yield per H as function of the impact energy per H, they found that the yield per H was a factor 2-3 higher for the molecular ions H_2^+ and H_3^+ in comparison with the yield for H^+. They attributed this to the possibility that molecular ions do not immediately dissociate when penetrating the graphite at impact energies per deuteron of 100 eV or less. Such a more massive molecular ion can cause more damage and thus also more erosion than an atomic ion. This is also a possible explanation for the deviations from the theoretical yield for D^+ impact in our study.

Figure 7.18 shows the carbon erosion yield determined experimentally after exposure of R6650 graphite to a deuterium plasma in VISIONI as function of the surface temperature. The ion impact energy per deuteron was kept constant at 110 eV for these exposures. The circular and triangular data points represent the sputtering yields calculated respectively from mass loss and profilometry. Taking into account the uncertainties discussed above, one can say that the mass loss and profilometry data is in good agree-

ment with each other and that no significant temperature dependence could be observed in the studied temperature range. This is in agreement with the theoretical expectations according to the model discussed in 2.4.3.2. This model is plotted for comparison in figure 7.18. The dashed curve represents the physical sputtering, the dotted curve the chemical surface sputtering and the dotted dashed curve the thermal chemical erosion. The full curve shows the sum of all contributions. One can see that in the studied temperature range indeed only a very weak temperature dependence could be expected. However, the experimental data points are a factor 2-3 above the theoretical curve. As discussed already above, this could be explained by the fact that the molecular deuterium ions do not immediately dissociate when hitting the surface.

7.3 Carbon migration

7.3.1 Description of the experimental campaign

The aim of the last experimental material migration campaign in VISIONI was to study carbon migration and possible enhanced re-erosion of deposited carbon. For this purpose three polished R6650 graphite samples were exposed to a deuterium plasma with simultaneous injection of trace amounts of $^{13}CH_4$ through the side window of the plasma chamber. The use of ^{13}C marked methane was necessary as carbon is an ubiquitous impurity in the VISIONI plasma chamber. Three other polished R6650 graphite samples were exposed to a deuterium plasma with the same conditions but without $^{13}CH_4$ injection providing a background check.

The exposures were performed with a neutral gas pressure of 0.3 Pa, a discharge potential difference of 80 V, negative biasing of the target plate and the sample with respect to the side and bottom of the plasma chamber with a potential difference of 80 V, a target current of about 2 A, a sample temperature of about 310 K and a total ion fluence of about $10^{25}m^{-2}$. The $^{13}CH_4$ was injected by means of a variable leak valve mounted to the side of the plasma chamber at the side window. The $^{13}CH_4$ flow was adjusted such that the methane contributed only about 1% to the neutral gas pressure. This gave a flow of about 0.0025 sccm or about 10^{17} molecules/s.

Mass loss measurements showed that there was no significant difference between the net erosion with and without $^{13}CH_4$ injection. Thus even with $^{13}CH_4$ injection there is net erosion of the graphite samples. However, even without layer deposition it is expected that at the surface the sample will contain a mixture of the natural isotopic carbon abundance with 98.93% ^{12}C and 1.07% ^{13}C and additional ^{13}C from the injected $^{13}CH_4$. The amount of additional ^{13}C at the surface of the samples was determined after exposure in VISIONI by means of Rutherford Backscatter Spectrometry (RBS). The amount of additional ^{13}C was also simulated with the new version of ERO

for VISIONI described in 4.1.3 to check whether enhanced re-erosion of deposited ^{13}C has to be assumed also in VISIONI in order to get agreement between measurements and simulations.

7.3.2 RBS measurements

In Rutherford Backscattering Spectrometry (RBS) a sample is bombarded by an energetic light ion beam. The backscattered ions are detected at a certain angle and their energy spectrum is used to determine concentration depth profiles of elements heavier than the impinging ions. The peak positions in the spectrum correlate with the masses of the elements present in the sample, while the width of the peaks gives information on the depth distribution of the elements.

After exposure in VISIONI the graphite samples were irradiated by a 3 MeV He^{2+} ion beam at the Tandetron Accelerator of the IFIN-HH facility in Romania [194]. The beam was directed with an angle of 7^o with respect to the sample surface. The beam current was in the range 4-20 nA. The backscattered He^{2+} ions were detected at an angle of 165^o by the ORTEC BU 012-050-100 detector with an energy resolution of 12 keV for 5.486 MeV α particles from ^{241}Am. The energy calibration was performed using a sample with 35 nm gold coated on silicon. The obtained energy spectra were analysed off-line using SIMNRA v. 6.40 [195].

The measured RBS spectra are shown in figure 7.19 in comparison with the spectra simulated with SIMNRA, while the impurity concentration profiles resulting from the SIMNRA simulations are shown in figure 7.20. The plots on the left and the right show the spectra for the samples exposed respectively without and with $^{13}CH_4$ injection. The impurity concentration profiles for oxygen, aluminium, iron and tungsten are in good agreement with the impurity concentrations found by means of EDX as presented in 7.2.2. For the calculation of the carbon concentration profiles it was taken into account that natural carbon contains 98.93% ^{12}C and 1.07% ^{13}C. The black curve represents the concentration profile for this natural abundance, while the red curve represents the additional ^{13}C coming from the injected $^{13}CH_4$. The error on the additional ^{13}C concentration is large due to the very low number of counts. However, there is a significant difference visible between the samples without and with $^{13}CH_4$ injection. The average additional ^{13}C concentrations up to a depth of 200 nm are summarized in table 7.5. The very low values for the samples exposed without $^{13}CH_4$ injection can be considered as zero and are due to the error on the measurements and slight deviations from the theoretical average abundance of carbon isotopes. The values for the samples exposed with $^{13}CH_4$ injection are about 2% which is an order of magnitude higher and clearly reflects the additional ^{13}C from the injection. A concentration of about 2% ^{13}C up to a depth of about 200 nm or $2 \cdot 10^{18}$ atoms/cm^2 corresponds with an areal density of about $4 \cdot 10^{16}$ ^{13}C atoms/cm^2. The slight increase for the three subse-

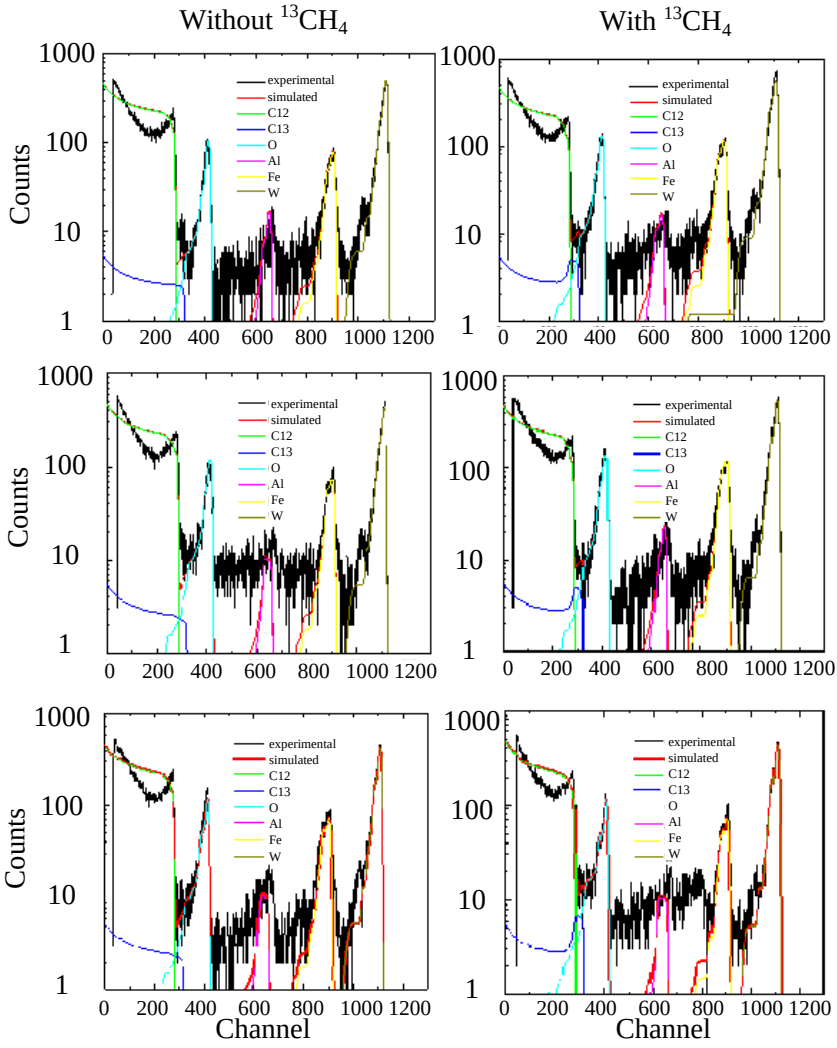

Figure 7.19: Measured RBS spectra of the graphite samples after exposure in VISIONI to a deuterium plasma without (left) and with $^{13}CH_4$ injection (right) in comparison with the spectra simulated with SIMNRA

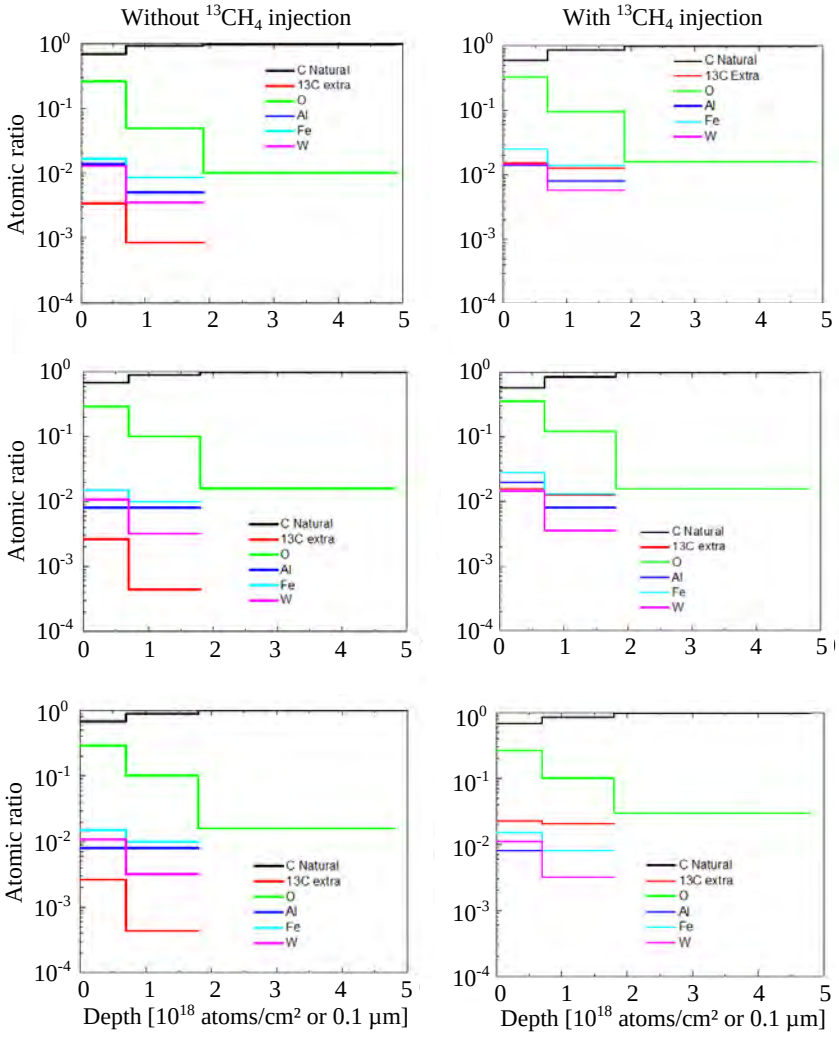

Figure 7.20: Impurity concentration profiles in the graphite samples after exposure in VISIONI to a deuterium plasma without (left) and with $^{13}CH_4$ injection (right) as calculated from the RBS spectra with SIMNRA

Table 7.5: Average additional ^{13}C concentrations up to a depth of 200 nm as determined by means of RBS

	without injection	with injection
sample 1	0.2 %	1.76 %
sample 2	0.15 %	1.87 %
sample 3	0.15 %	2.67 %

quently exposed samples with $^{13}CH_4$ injection can be due to an increasing ^{13}C background from previous exposures or due to statistical fluctuations.

7.3.3 ERO simulations

The ^{13}C deposition was also simulated with ERO. These simulations were performed with the new version of ERO for VISIONI described in 4.1.3. The surface grid spacing was 10 mm, the simulation time step was 10 s and 1000 $^{13}CH_4$ simulation particles were injected per time step. As for the study presented in chapter 5 the new Tichmann sticking probabilities and Eckstein sputtering yields were used.

The ERO simulations showed that the amount of ^{13}C at the surface of the sample saturates after about 1000 s with an areal density of about $2.5 \cdot 10^{16}$ ^{13}C atoms/cm^2 if no enhanced re-erosion is assumed. With an enhancement factor of 50, as was required for the roof limiter experiment in TEXTOR, the eventual areal density is about a factor of ten lower. The RBS measurements gave an areal density of about $4{\cdot}10^{16}$ ^{13}C atoms/cm^2. Taking into account the simplifications in the new version of the ERO code for VISIONI and the rather large error on the areal density obtained from the RBS measurements, the agreement between the measurements and the ERO simulation without enhanced re-erosion can be considered as a very good agreement. The increase of the areal density for subsequent experiments observed in the RBS measurements was not observed in the simulations as the areal density saturates already after about 1000 s. This is probably due to the fact that re-erosion of ^{13}C deposited at the side and bottom of the plasma chamber is not taken into account in ERO. The side and bottom of the plasma chamber are net deposition areas and thus form an increasing source of background ^{13}C without thorough cleaning in between different experiments.

The good agreement between the measurements and the simulations without the assumption of enhanced re-erosion indicates that there is no significant enhanced re-erosion of deposited ^{13}C. This is in strong contrast to the TEXTOR experiments discussed in chapter 5 where very large enhancement factors for re-erosion were needed to get agreement. The most important difference between the experimental campaigns in TEXTOR and

VISIONI is the magnitude of the ion flux hitting the sample. In VISIONI the ion flux is about two orders of magnitude lower than in TEXTOR. Also the flux of ^{13}C and hydrocarbons with ^{13}C towards the sample is about two orders of magnitude lower than in TEXTOR. Recent experiments in TEXTOR showed that the needed enhancement factor for the enhanced re-erosion decreases for lower flux of ^{13}C and hydrocarbons with ^{13}C towards the sample [196]. It was also observed that enhanced re-erosion only takes place in plasma-wetted areas and not in remote plasma-shadowed areas. The explanation for these observations proposed in [196] is that enhanced re-erosion is caused by a saturation effect when too many species are simultaneously trying to stick to the surface of the sample while the surface is being bombarded by a large ion flux. The sticking species are then eroded by the impinging ions before they manage to stick properly to the surface. This mechanism could also explain why enhanced re-erosion was not observed in VISIONI. The flux of sticking species towards the sample surface is even an order of magnitude lower than in the experiment with low injection rate discussed in [196], while the ion flux is two orders of magnitude lower than in TEXTOR. Therefore, the findings in VISIONI seem to support the idea of the saturation effect. However, further studies are definitely required to further clarify the issue.

7.4 Conclusions

- Carbon and oxygen are the dominant impurities found on the surface of the samples after plasma exposure to a deuterium plasma in VISIONI. Also traces of tungsten, aluminium and steel elements were found. Oxygen is probably due to exposure to the air before and after the plasma exposure. The other impurities are inherently present in the plasma and are not straightforward to avoid.

- Bombardment of the samples with molecular deuterium ions creates protruding structures at the surface of the samples varying from broad structures and cones on the copper samples to a grass-like morphology on the graphite samples. These structures are probably induced by asperities present on the surface already before exposure and by carbon contamination. The surface morphology leads to a change of the colour of the samples ranging from yellow over red to black for the copper samples and from grey to black for the graphite samples. This can be explained by reduced reflectivity for more densely packed protruding structures.

- Measurement of the mass loss after plasma exposure is the most convenient method to determine the erosion yield. As long as the mass loss is significantly above the measurement error of the balance this method is very precise. However, one should always be careful that

the deposition of impurities and outgassing are not significantly influencing the mass loss. For the exposures in VISIONI it was found that impurity deposition has no significant effect on the mass loss. The effects of outgassing were found to be important for the porous graphite samples. Fortunately outgassing effects could be eliminated by measuring the mass before and after exposure always after a sufficiently long baking treatment in a vacuum oven.

- Another method to determine the erosion yield is profilometry. This method was found to be less precise than mass loss. It was not possible to simply use the unexposed edge as reference height for the whole surface area because the deviations from a flat surface found before plasma exposure due to cutting and polishing of the samples were of the same order of magnitude or even larger than the typical erosion depth after plasma exposure. Therefore, it was required to perform profilometry also before plasma exposure. The eroded volume was then calculated by subtracting the profilometry data after exposure from the profilometry data before exposure. This required first matching of the profilometry data before and after exposure by looking at the unexposed edge. It turned out that sometimes the profilometry data of the unexposed edge before and after exposure could not be successfully matched. The reason for this is not clear. In the future it would be better to place a clear mark somewhere in the unexposed edge to make the matching procedure more precise. The black regions on the samples could not be measured with white light profilometry due to the low reflectivity in these regions. Furthermore, the red regions on the copper samples with very densely packed protruding structures gave an unphysical surface profile with white light profilometry probably due to multiple reflections on the protruding structures. However, both issues could be resolved by using laser profilometry instead. In case the profilometry before and after exposure could be matched successfully the erosion yield determined from the profilometry was in good agreement with the erosion yield determined from the mass loss.

- The measured erosion yields were compared with theoretical predictions according to the Eckstein formula and SDTrimSP simulations for physical sputtering and according to the analytical model discussed in 2.4.3.2 for chemical erosion. For these predictions it was assumed that an impinging molecular D_n^+ ion with total impact energy E_i dissociates immediately upon impact and is thus equivalent to n impinging atomic D^+ ions with impact energy E_i/n. The measured physical sputtering yields for copper were systematically below the Eckstein yields. However, SDTrimSP simulations showed that this deviation could be explained by the presence of carbon and oxygen impurities on the surface or by retention of implanted deuterium. The measured

erosion yields for graphite, comprising both physical and chemical sputtering, were systematically a factor of about 3 higher than the predictions based on the model discussed in 2.4.3.2. This is in agreement with the observations in [76] which indicated that the erosion yields per H for a given impact energy per H is a factor 2-3 higher for H_2^+ and H_3^+ molecular ions in comparison with atomic H^+ ions. This effect might be caused by molecular ions not immediately dissociating upon impact. The more massive molecular ions can create more damage in the graphite than atomic ions which enhances the chemical erosion.

- Graphite samples were exposed in VISIONI to a deuterium plasma with simultaneous injection of $^{13}CH_4$ to study the migration and possible enhanced re-erosion of ^{13}C. Even with $^{13}CH_4$ injection there was net erosion of the graphite samples. However, RBS measurements of the graphite samples after exposure in VISIONI showed that a significant amount of ^{13}C above the natural abundance was present at the graphite surface. The areal density of additional ^{13}C was in good agreement with ERO simulations. This agreement was obtained without the assumption of enhanced re-erosion. This supports the recently proposed idea that enhanced re-erosion is a saturation effect caused by too many species trying to stick simultaneously to the surface while being bombarded by energetic ions. The sticking species are then eroded by the impinging ions before they manage to properly stick to the surface. In VISIONI this saturation is much smaller as the fluxes of sticking species and impinging ions are about two orders of magnitude lower than for instance in TEXTOR. This could explain the absence of enhanced re-erosion in VISIONI.

Chapter 8

Conclusions

During the first part of this work the enhanced re-erosion of redeposited species was studied by simulating $^{13}CH_4$ injection experiments in the TEXTOR tokamak with the ERO impurity transport code. Firstly, the ERO plasma-surface interaction database was updated. More realistic physical sputtering yields and hydrocarbon sticking probabilities were implemented in ERO. Also additional erosion due to hydrogenic break-up products of injected methane was added in the code. The transport and chemistry of these hydrogenic species in ERO were verified by simulating the Balmer line emission due to these species for a TEXTOR experiment during which $^{13}CH_4$ was injected through a nozzle. ERO modelling of another TEXTOR experiment during which $^{13}CH_4$ was injection through a hole in a roof-like test limiter showed that the simulated ^{13}C deposition efficiency on the roof-like test limiter is not very sensitive to the changes in the plasma-surface interaction database. It was concluded from this study that the uncertainty in the plasma-surface interaction data in ERO cannot explain the need for strongly enhanced re-erosion of redeposited ^{13}C in ERO to reproduce the very low experimentally observed ^{13}C deposition efficiencies in the TEXTOR $^{13}CH_4$ injection experiments. This study confirms that enhanced re-erosion of redeposited species is an important phenomenon. It was not only observed when simulating $^{13}CH_4$ experiments in TEXTOR with ERO. It was also observed during studies at other devices such as JET, AUG and PISCES-B, for other materials such as tungsten and beryllium and when using the EDDY code instead of the ERO code. It is thus clear that the enhanced re-erosion of redeposited species is a generally occurring phenomenon that is critical for the reliable prediction of the eventual erosion/deposition balance in future thermonuclear fusion devices such as ITER and DEMO.

The aim of the second part of this work was to start up material migration studies in the VISIONI plasma simulator with experiments and ERO modelling dedicated to the further study of the enhanced re-erosion of redeposited species. As ERO requires the input of the electric and magnetic

fields and the plasma properties it was first needed to perform a detailed characterization of the device.

The magnetostatic field created by the samarium-cobalt magnets lining the VISIONI plasma chamber was calculated analytically by integrating Biot-Savart's law and was found to be in very good agreement with Hall probe measurements.

For the characterization of the plasma the VMCPT plasma simulation code was developed from scratch. This is a Monte Carlo charged particle tracking code. It takes into account the thermionic primary electron emission by the tungsten filaments, the motion of the charged particles in the magnetostatic field and collisions of the charged particles with the plasma chamber walls, with other charged particles and with neutrals. The main limitation of the code is the fact that the self-consistent electric field cannot be calculated due to the huge amount of CPU time required for this calculation. Only the sheath potential drops at the plasma chamber walls and the tungsten filaments are taken into account. To verify the simulations a movable Langmuir probe and accompanying analysis software were developed for scanning the plasma parameters along the central axis of the plasma chamber.

The combination of the VMCPT simulations and Langmuir probe measurements greatly enhanced the understanding of the plasma properties in VISIONI and how they can be influenced by changing the heating current through the tungsten filaments, the neutral gas pressure and the discharge potential difference between the tungsten filaments and the side and bottom of the plasma chamber. It was found that the electron energy distribution function in VISIONI is bi-Maxwellian with the majority of the electrons belonging to the cold bulk electron population with a temperature of about 1-2 eV and a small fraction of about 1-2 % of the electrons belonging to a hot electron population in the tail of the energy distribution with a temperature of about 20-25 eV. This particular distribution is caused by the limited collisionality in combination with the emission of energetic primary electrons from the tungsten filaments. The characterization also showed that the ions are dominated by D_2^+ ions for lower pressures and D_3^+ ions for higher pressures with a transition around 0.15 Pa due to the efficient conversion process in which D_2^+ ions are converted into D_3^+ ions by collisions with D_2 molecules. Finally, it was also found that there are strong inhomogeneities in the plasma density, the hot electron density and the ion flux towards the target plate caused by magnetic field induced drifts of the primary electrons.

The results from this detailed characterization where then used to develop ERO-VISIONI, a first simplified version of ERO for simulating material migration experiments in VISIONI. It takes into account the particular geometry, magnetic field and plasma properties of VISIONI. Also collisions with the neutral gas and recombination are taken into account in ERO-VISIONI.

Eventually three experimental material migration campaigns were performed in VISIONI. During the first campaign copper samples were exposed to a deuterium plasma to investigate whether VISIONI is an appropriate tool to study erosion yields. It was shown that erosion yields for VISIONI can be determined successfully ex-situ by means of mass loss measurements or optical profilometry. The measured physical sputtering yields for molecular deuterium impact on copper are in reasonable agreement with the theoretical Eckstein sputtering yields if it is assumed that a molecular D_n^+ ion impinging with an energy E_i is equivalent to n atomic D^+ ions with an energy E_i/n and if the decrease of the sputtering yields due to the presence of oxygen and carbon impurities and deuterium retention at the surface is taken into account. This study illustrated that VISIONI is a very suitable tool for the study of erosion yields for molecular deuterium ion bombardment. Also other ions can be used by creating plasmas in different neutral gases. The impact energy of the ions can be tuned by changing the potential difference applied between the sample and the side and bottom of the plasma chamber. Finally, also the sample temperature can be varied by changing the gas flow rate through the cold finger cooling the sample. As exposures of several hours or even days in VISIONI are no problem, it is possible to measure even very low erosion yields.

During the second campaign graphite samples were exposed to a deuterium plasma to investigate chemical sputtering of graphite under molecular deuterium bombardment. This study showed that the chemical sputtering yield of carbon under bombardment with molecular deuterium ions is typically a factor three higher than the theoretical predictions if it is again assumed that a molecular D_n^+ ion impinging with an energy E_i is equivalent to n atomic D^+ ions with an energy E_i/n. This was also observed in other studies and might be caused by molecular ions not immediately dissociating upon impact with the graphite surface. The more massive molecular ions can create more damage in the graphite than atomic ions which enhances the chemical erosion. This enhanced chemical erosion by molecular deuterium ion impact was then also taken into account in ERO-VISIONI.

During the last campaign graphite samples were exposed to a deuterium plasma with simultaneous injection of $^{13}CH_4$ to study the migration and possible enhanced re-erosion of deposited ^{13}C. Even with $^{13}CH_4$ injection there was net erosion of the graphite samples. However, RBS measurements of the graphite samples after exposure in VISIONI showed that a significant amount of ^{13}C above the natural abundance was present at the graphite surface. The areal density of the additional ^{13}C was in good agreement with ERO simulations. This agreement was obtained without the assumption of enhanced re-erosion. This supports the recently proposed idea that enhanced re-erosion is a saturation effect caused by too many species trying to stick simultaneously to the surface while being bombarded by a large flux of ions. The sticking species are then eroded by the impinging ions before they manage to properly stick to the surface. So it is an in-situ effect

and cannot be studied by first depositing a layer and then studying the erosion of this deposited layer. In VISIONI this effect is much smaller as the fluxes of sticking species and impinging ions on the sample are about two orders of magnitude lower than for instance in TEXTOR. This could explain the absence of enhanced re-erosion in VISIONI and indicates that the fluxes of sticking species and impinging ions are two important factors for the enhanced re-erosion of deposited species.

Chapter 9

Outlook

The work presented in this thesis is definitely not a finished story. First of all there are two important issues requiring further studies in order to provide reliable predictions for the erosion/deposition balance in future thermonuclear fusion devices. Firstly, there is still quite some uncertainty on the erosion yields and sticking probabilities required by impurity transport codes such as ERO. More investigations are definitely needed for cases where chemical effects are important such as low impact energies, molecular projectiles and chemical erosion of carbon and beryllium. Also data for mixtures of fusion relevant materials and data for neutron irradiated materials are lacking. Furthermore, all erosion yields and sticking probabilities should be determined for a variety of impact angles and impact energies. Gathering all required data forms a huge task which has to be performed by a combination of molecular dynamics simulations and experimental studies in ion beam facilities and flexible plasma simulators such as VISIONI, PISCES-B, PSI-2 and Magnum-PSI.

Secondly, it was shown in this work that the enhanced re-erosion of redeposited species is a very important issue for future thermonuclear fusion devices. It is observed in different devices, for different materials and with different simulation codes. In some cases the required enhancement factor is very high such as in TEXTOR, while in other cases no enhancement is observed at all as in VISIONI. This work showed that the fluxes of sticking species and impinging ions are two critical factors influencing the enhanced re-erosion. However, the phenomenon should be understood on a more fundamental level in order to make reliable predictions for future thermonuclear fusion devices. Also this should be done by a combination of experiments and simulations. For the experiments plasma simulators such as VISIONI, PISCES-B, PSI-2 and Magnum-PSI are probably most suitable because they are much more flexible than tokamaks. To confirm the effect of the fluxes of sticking species and impinging ions it would be interesting to perform similar injection experiments as presented in this work, but with variations

in the injection rate and the ion flux. Also variations in surface temperature, surface roughness and biasing of the sample should be performed to look at the effect of these parameters on the enhanced re-erosion. The exact mechanism responsible for the enhanced re-erosion cannot be found experimentally or by means of ERO simulations. For this another type of simulations will be required. It would be interesting to test whether the effect can be reproduced with molecular dynamics simulations by releasing species trying to stick to a surface while being bombarded by energetic ions. Hopefully such a combination of experiments and simulations can lead to a full understanding of the enhanced re-erosion of redeposited species.

During this work the VMCPT code was developed from scratch to simulate the plasma in VISIONI. The main shortcoming of this code is the lack of a self-consistent electric field calculation due to CPU time considerations. The self-consistent electric field calculation could be implemented in the future by using a much more efficient algorithm for solving Poisson's equation, massive parallelisation and a state-of-the-art High Performance Computing system. This would make the simulations very realistic and provide detailed information on the electric field. The quality of the simulations is also limited by uncertainties on the reaction cross sections. A combination of dedicated experiments and quantum mechanical calculations is definitely needed in this context.

Although the VMCPT code was developed for VISIONI it could be adapted in the future to simulate the plasma in other devices. In VISIONI the initial electrons are emitted by the heated tungsten filaments. For devices which are not driven by heated filaments, the initial electrons and ions could be provided by seed electrons and ions uniformly distributed over space with a Maxwellian energy distribution. The geometry of the plasma chamber can be modified rather easily in the code, although this could be less straightforward for devices with complex geometries. The collision module can be used directly for other plasma sources. If necessary it would be easy to extend the module with additional collisions. The magnetic field configuration can be adapted by replacing the magnetic field data file or by providing analytical formulas to calculate the magnetic field. For devices with a 2D geometry one can switch on the Poisson solver and calculate the electric field self-consistently because in 2D the CPU time is drastically reduced. The module for integrating the equation of motion is generally valid and is developed such that electric fields can also be taken into account.

The characterization of the VISIONI plasma simulator could be improved on several points. The information on the electric field is rather limited. The VMCPT code only gives an estimation of the sheath potential drop at the side and bottom of the plasma chamber, while the Langmuir probe measurements provided only measurements along the central axis of the plasma chamber and in general Langmuir probe measurements are prone to large errors in determining the plasma potential due to rounding of the

knee in the I-V characteristic. Therefore, it would be interesting to perform more precise measurements with an emissive probe along several lines in VISIONI. Further, Mach probe measurements would be able to provide information on the ion flow velocity.

Based on the detailed characterization of VISIONI a first simplified version of ERO was developed for simulating material migration experiments in VISIONI. ERO-VISIONI could be improved in several ways in the future. First of all the surface mesh could be made more sophisticated. The mesh should be extended to the side and bottom of the plasma chamber in order to take into account also re-erosion of deposited species there. Further, the protruding macor and tungsten-lanthanum rings of the sample holder should be taken into account. Finally, the mesh should have a higher resolution around the sample. All this should not be too difficult with the universal geometry option recently implemented in ERO [197]. Secondly, a more realistic spatial dependence of the electric field should be implemented in ERO-VISIONI as soon as this information is provided by simulations or measurements. For the moment also the friction force due to the ion flow is not taken into account. Once data on the ion flow velocity becomes available this friction force could easily be taken into account in ERO-VISIONI.

Appendix A

Rotation of the coordinate system

Sometimes it is easier to perform calculations in a coordinate system that is rotated with respect to the original coordinate system. After the calculation the results are transformed back to the original coordinate system. Therefore, we need the relation between the original and the new coordinates. It is enough to study the rotation around one of the axes of the original coordinate system. Any rotation can be represented as a sequence of maximally three of these rotations. Assume a general rotation of the coordinate system. In the original coordinate system a vector $\vec{r}$ can be represented as

$$\vec{r} = \sum_{i=1}^{3} r_i \vec{e_i} \tag{A.1}$$

with r_i the coordinates and $\vec{e_i}$ the unit vectors. In the rotated coordinate system one has

$$\vec{r} = \sum_{i=1}^{3} r_i' \vec{e_i}' = \sum_{i=1}^{3} r_i' \left[\sum_{j=1}^{3} (\vec{e_j} \cdot \vec{e_i}') \vec{e_j} \right] = \sum_{j=1}^{3} \left[\sum_{i=1}^{3} (\vec{e_i}' \cdot \vec{e_j}) r_i' \right] \vec{e_j} \tag{A.2}$$

By comparing (A.1) and (A.2) one gets the following relation between the original and new coordinates

$$r_i = \sum_{j=1}^{3} (\vec{e_i} \cdot \vec{e_j}') r_j' = \sum_{j=1}^{3} c_{ij} r_j' \tag{A.3}$$

with c_{ij} the ith component of the new unit vector $\vec{e_j}'$ in the original coordinate system. Consider now a rotation around the z-axis over an angle θ as shown in figure A.1. For this rotation one has

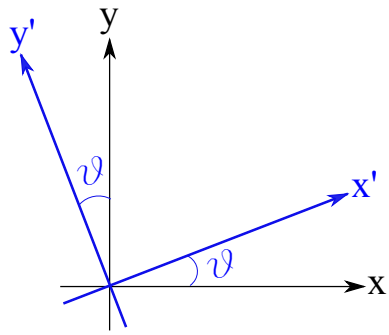

Figure A.1: Rotation of the coordination system around the z-axis

$$\vec{e_x}' = \cos\theta\vec{e_x} + \sin\theta\vec{e_y} \tag{A.4}$$
$$\vec{e_y}' = -\sin\theta\vec{e_x} + \cos\theta\vec{e_y} \tag{A.5}$$
$$\vec{e_z}' = \vec{e_z} \tag{A.6}$$

To transform the coordinates in the rotated coordinate system back to the original coordinate system, according to (A.3), one has to apply the transformation

$$\begin{pmatrix} x \\ y \\ z \end{pmatrix} = \hat{R}_{\theta,z} \begin{pmatrix} x' \\ y' \\ z' \end{pmatrix} \tag{A.7}$$

with

$$\hat{R}_{\theta,z} = \begin{pmatrix} \cos\theta & -\sin\theta & 0 \\ \sin\theta & \cos\theta & 0 \\ 0 & 0 & 1 \end{pmatrix} \tag{A.8}$$

The transformation matrices to go back to the original coordinate system after a rotation around the x-axis or y-axis can be found in the same way

$$\hat{R}_{\theta,x} = \begin{pmatrix} 1 & 0 & 0 \\ 0 & \cos\theta & -\sin\theta \\ 0 & \sin\theta & \cos\theta \end{pmatrix} \tag{A.9}$$
$$\hat{R}_{\theta,y} = \begin{pmatrix} \cos\theta & 0 & \sin\theta \\ 0 & 1 & 0 \\ -\sin\theta & 0 & \cos\theta \end{pmatrix} \tag{A.10}$$

Appendix B

Equivalence of a permanent magnet and an ideal solenoid

Let us start with Maxwell's equations

$$\vec{\nabla} \cdot \vec{D} = \rho_f \tag{B.1}$$

$$\vec{\nabla} \cdot \vec{B} = 0 \tag{B.2}$$

$$\vec{\nabla} \times \vec{E} = -\frac{\partial \vec{B}}{\partial t} \tag{B.3}$$

$$\vec{\nabla} \times \vec{H} = \vec{J_f} + \frac{\partial \vec{D}}{\partial t} \tag{B.4}$$

and the accompanying constitutive relations

$$\vec{D} = \epsilon_0 \vec{E} + \vec{P} \tag{B.5}$$

$$\vec{B} = \mu_0(\vec{H} + \vec{M}) \tag{B.6}$$

In the magnetostatic case this set of equations can be simplified to

$$\vec{\nabla} \cdot \vec{B} = 0 \tag{B.7}$$

$$\vec{\nabla} \times \vec{B} = \mu_0(\vec{J_f} + \vec{\nabla} \times \vec{M}) \tag{B.8}$$

where $\vec{B}$ is the magnetic induction, $\vec{J_f}$ the free electric current density due to unbound charge carriers and $\vec{M}$ the magnetization of the medium. The

first equation shows us that $\vec{B}$ is a solenoidal field. Therefore, it can be written as the rotor of a vector potential $\vec{A}$

$$\vec{B} = \vec{\nabla} \times \vec{A} \tag{B.9}$$

This vector potential is not unambiguously defined. One can always add a vector field $\vec{\nabla}\phi$ because $\vec{\nabla} \times (\vec{\nabla}\phi) = 0$ such that the physical field $\vec{B}$ remains the same. We will work in the Coulomb gauge in which $\vec{A}$ is fixed by demanding $\vec{\nabla} \cdot \vec{A} = 0$. Based on equation (B.8) one can define an equivalent bound current density

$$\vec{J_b} = \vec{\nabla} \times \vec{M} \tag{B.10}$$

related to magnetic dipoles in the magnetized medium. Now combining (B.8-B.10) in the Coulomb gauge one gets

$$\vec{\nabla}^2 \vec{A} = -\mu_0(\vec{J_f} + \vec{J_b}) \tag{B.11}$$

This is Poisson's equation in vector form with $\vec{J_f}$ and $\vec{J_b}$ as sources. In Cartesian coordinates this can be solved using Green's function for Laplace's equation

$$G(\vec{r}, \vec{r}\,') = -\frac{1}{4\pi} \frac{1}{|\vec{r} - \vec{r}\,'|} \tag{B.12}$$

It is the response function for a point source and is thus defined as the solution of the equation

$$\vec{\nabla}^2 G(\vec{r}, \vec{r}\,') = \delta(\vec{r} - \vec{r}\,') \tag{B.13}$$

The vector potential is, therefore, given by

$$\vec{A}(\vec{r}) = \frac{\mu_0}{4\pi} \int d^3r' \; \frac{\vec{J_f}(\vec{r}\,') + \vec{J_b}(\vec{r}\,')}{|\vec{r} - \vec{r}\,'|} \tag{B.14}$$

With (B.9) one gets then for the magnetic field

$$\vec{B}(\vec{r}) = \frac{\mu_0}{4\pi} \int d^3r' \; \left(\vec{J_f}(\vec{r}\,') + \vec{J_b}(\vec{r}\,')\right) \times \frac{(\vec{r} - \vec{r}\,')}{|\vec{r} - \vec{r}\,'|^3} \tag{B.15}$$

This equation can now be applied for the case of a permanent magnet of finite volume in the absence of free currents. In this case $\vec{J_f} = 0$ and $\vec{J_b} = \vec{\nabla} \times \vec{M}$. The last relation is, however, not valid to calculate the current density at the magnet surface. At the interface between the magnet and the surrounding medium $\vec{\nabla} \times \vec{M}$ is undetermined due to the discontinuity of the magnetization $\vec{M}$. Therefore, the contribution of the magnet surface

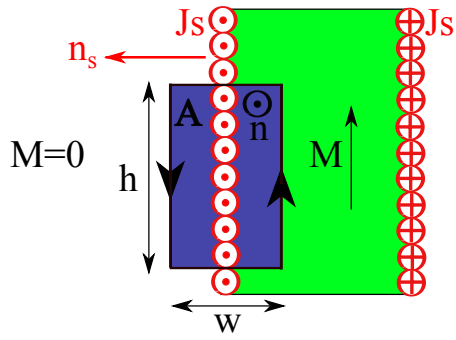

Figure B.1: Sketch for the surface current density calculation for a permanent magnet.

to the magnetic field has to be dealt with in a separate surface integral with a bound surface current density $\vec{J}_s$. One gets then

$$\vec{B}(\vec{r}) = \frac{\mu_0}{4\pi} \int_{V_{\text{magnet}}} d^3r' \ \left(\vec{\nabla}\,' \times \vec{M}(\vec{r}\,')\right) \times \frac{(\vec{r} - \vec{r}\,')}{|\vec{r} - \vec{r}\,'|^3} + \frac{\mu_0}{4\pi} \oint_{S_{\text{magnet}}} d^2r' \ \vec{J}_s(\vec{r}\,') \times \frac{(\vec{r} - \vec{r}\,')}{|\vec{r} - \vec{r}\,'|^3}. \tag{B.16}$$

This can be recognized as Biot-Savart's law for the superposition of the bound volume current density $\vec{J}_b$ and the bound surface current density $\vec{J}_s$. To determine $\vec{J}_s$ one can integrate (B.10) over the surface A shown in figure B.1. Using Stoke's theorem one gets

$$\int_A d^2r \ \vec{n} \cdot \vec{J}_b(\vec{r}) = \int_A d^2r \ \vec{\nabla} \times \vec{M}(\vec{r}) = \oint_{A_c} \vec{dl} \cdot \vec{M} \tag{B.17}$$

By letting the width w of the surface going to zero, the bound volume current density J_b in A/m^2 is transformed into the bound surface current density J_s in A/m. If also the height of the surface h goes to zero, then one sees that the magnitudes of the magnetization M at the surface and the bound surface current density J_s are equal or in vector notation

$$\vec{J}_s = \vec{M} \times \vec{n_s} \tag{B.18}$$

where $\vec{n_s}$ is the magnet's surface normal pointing away from the magnet. It can now be concluded that a magnetized medium such as a permanent magnet is equivalent to a distribution of free electric current characterized by a volume current density $\vec{J}_b = \vec{\nabla} \times \vec{M}$ and a surface current density

$\vec{J}_s = \vec{M} \times \vec{n_s}$. Hence, the set of magnetostatic equations (B.7-B.8) can be replaced by

$$\vec{\nabla} \cdot \vec{B} = 0 \tag{B.19}$$

$$\vec{\nabla} \times \vec{B} = \mu_0 \vec{J} \tag{B.20}$$

with $\vec{J} = \vec{J}_f + \vec{J}_b + \vec{J}_s$. For a homogeneously magnetized permanent magnet $\vec{\nabla} \times \vec{M} = 0$. Therefore, the magnetic field of a homogeneously magnetized permanent magnet is equivalent to the magnetic field caused by an ideal rectangular solenoid with a surface current density $J_s = M$. Important to notice is that $\mu_0 J_s$ is equal to the so called remanent magnetic field or remanence B_r. This is a value that is often tabulated in manufacturer's magnet data sheets. It is the magnetic flux density inside the magnet in absence of externally applied magnetic fields. To measure B_r the magnet is normally embedded in a closed magnetic circuit by means of a return yoke with very high magnetic permeability μ. The magnetic field outside the circuit is then negligible. One can prove that $\mu_0 J_s = B_r$ by integrating equation (B.20) over the same surface A from figure B.1.

Appendix C

Magnetic field calculation for a rectangular magnet

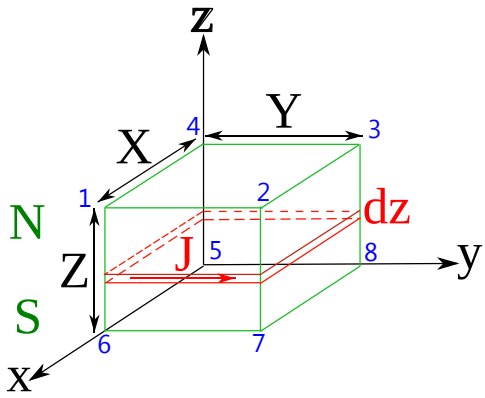

Figure C.1: Sketch for the magnetic field calculation for a rectangular permanent magnet

Assume a permanent rectangular magnet that is magnetized homogeneously along one of its axes. Take the x, y and z-axis along three edges of the magnet with the z-axis pointing towards the northern magnetic pole parallel with the north-south axis as shown in figure C.1. It is proven in appendix B that such a magnet is equivalent to a rectangular solenoid with an electric current homogeneously distributed over its surface in the direction corresponding to the right-hand-rule. Hence, the magnetic field generated by this magnet at the location $\vec{r_p} = (x_p, y_p, z_p)$ can be calculated by integrating Biot-Savart's law

$$d\vec{B} = \frac{\mu_0}{4\pi} \frac{I d\vec{l} \times (\vec{r_p} - \vec{r})}{|\vec{r_p} - \vec{r}|^3} \tag{C.1}$$

over the magnet's surface. Let us first consider the x-component of the magnetic field B_x. The magnetic field dB_x due to a rectangular loop in the xy-plane at height z with infinitesimal thickness dz can be calculated by integrating (C.1) over this loop. The current running through the loop can be written as $J_s dz$ with J_s the equivalent surface current density in A/m. For practical reasons the new variables $\Delta x = x_p - x$, $\Delta y = y_p - y$ and $\Delta z = z_p - z$ are introduced. Only the two parts of the rectangular loop parallel with the y-axis contribute to dB_x. With the notation $[f(x)]_{x=x_1}^{x=x_2} = f(x_2) - f(x_1)$ it one finds that

$$dB_x = \left[d\Delta z \frac{\mu_0 J_s}{4\pi} \int_{\Delta y = y_p - Y}^{\Delta y = y_p} d\Delta y \frac{\Delta z}{\left(\Delta x^2 + \Delta y^2 + \Delta z^2\right)^{3/2}} \right]_{\Delta x = x_p - X}^{\Delta x = x_p} \tag{C.2}$$

With the notation $[f(x,y)]_{x=x_1,y=y_1}^{x=x_2,y=y_2} = \left[[f(x,y)]_{x=x_1}^{x=x_2}\right]_{y=y_1}^{y=y_2}$ and integral identity (3) this is then worked out to be

$$dB_x = \left[d\Delta z \frac{\mu_0 J_s}{4\pi} \frac{\Delta z \Delta y}{(\Delta x^2 + \Delta z^2)\sqrt{\Delta x^2 + \Delta y^2 + \Delta z^2}} \right]_{\Delta x = x_p - X, \Delta y = y_p - Y}^{\Delta x = x_p, \Delta y = y_p}$$

To calculate the total x-component B_x of the magnetic field one has to integrate this result now over the height of the magnet

$$B_x = \int_{\Delta z = z_p - Z}^{\Delta z = z_p} dB_x \tag{C.3}$$

With the notation $[f(x,y,z)]_{x=x_1,y=y_1,z=z_2}^{x=x_2,y=y_2,z=z_2} = \left[\left[[f(x,y)]_{x=x_1}^{x=x_2}\right]_{y=y_1}^{y=y_2}\right]_{z=z_1}^{z=z_2}$ and integral identity (1) this is then worked out to be

$$B_x = \left[\frac{\mu_0 J_s}{8\pi} \ln\left(\frac{\sqrt{\Delta x^2 + \Delta y^2 + \Delta z^2} - \Delta y}{\sqrt{\Delta x^2 + \Delta y^2 + \Delta z^2} + \Delta y} \right) \right]_{\Delta x = x_p - X, \Delta y = y_p - Y, \Delta z = z_p - Z}^{\Delta x = x_p, \Delta y = y_p, \Delta z = z_p}.$$

This expression can be simplified by noting that

$$\begin{aligned} & \left[+ \ln(\sqrt{\Delta x^2 + \Delta y^2 + \Delta z^2} - \Delta y) \right]_{\Delta x = x_p - X, \Delta y = y_p - X}^{\Delta x = x_p, \Delta y = y_p} \\ = \quad & \left[- \ln(\sqrt{\Delta x^2 + \Delta y^2 + \Delta z^2} + \Delta y) \right]_{\Delta x = x_p - X, \Delta y = y_p - X}^{\Delta x = x_p, \Delta y = y_p} \end{aligned} \tag{C.4}$$

Eventually we then get the following equation

$$B_x(x_p, y_p, z_p) = \frac{\mu_0 J_s}{4\pi} \sum_{i=1}^{8} (-1)^i \ln\left(-(y_p - y_i) + \sqrt{(x_p - x_i)^2 + (y_p - y_i)^2 + (z_p - z_i)^2}\right)$$

where the sum over i is over the 8 corner points (x_i, y_i, z_i) of the magnet. From the numbering in figure C.1 it can be seen that neighbouring corner points have opposite sign. The calculation for B_y is analogous and results in the very similar looking equation

$$B_y(x_p, y_p, z_p) = \frac{\mu_0 J_s}{4\pi} \sum_{i=1}^{8} (-1)^i \ln\left(-(x_p - x_i) + \sqrt{(x_p - x_i)^2 + (y_p - y_i)^2 + (z_p - z_i)^2}\right)$$

For B_z the calculation is a bit different. In this case all four parts of the rectangular loop contribute to dB_z and lead to

$$\begin{aligned} dB_z = &- \left[d\Delta z \frac{\mu_0 J_s}{4\pi} \int_{\Delta x = x_p - X}^{\Delta x = x_p} d\Delta x \frac{\Delta y}{(\Delta x^2 + \Delta y^2 + \Delta z^2)^{3/2}} \right]_{\Delta y = y_p - Y}^{\Delta y = y_p} \\ &- \left[d\Delta z \frac{\mu_0 J}{4\pi} \int_{\Delta y = y_p - Y}^{\Delta y = y_p} d\Delta y \frac{\Delta x}{(\Delta x^2 + \Delta y^2 + \Delta z^2)^{3/2}} \right]_{\Delta x = x_p - X}^{\Delta x = x_p} \end{aligned}$$

With integral identity (3) this is then worked out to be

$$dB_z = - \left[d\Delta z \frac{\mu_0 J_s}{4\pi} \frac{\Delta y \Delta x}{\sqrt{\Delta x^2 + \Delta y^2 + \Delta z^2}} \left(\frac{1}{\Delta y^2 + \Delta z^2} + \frac{1}{\Delta x^2 + \Delta z^2} \right) \right]_{\Delta x = x_p - X, \Delta y = y_p - Y}^{\Delta x = x_p, \Delta y = y_p}$$

To get the total z-component of the magnetic field B_z one has to integrate again over the height of the magnet

$$B_z = \int_{\Delta z = z_p - Z}^{\Delta z = z_p} dB_z. \tag{C.5}$$

With integral identity (2) one eventually gets the equation

$$B_z(x_p, y_p, z_p) = \frac{\mu_0 J_s}{4\pi} \sum_{i=1}^{8} (-1)^i \arctan\left(\frac{(x_p - x_i)(y_p - y_i)}{(z_p - z_i)\sqrt{(x_p - x_i)^2 + (y_p - y_i)^2 + (z_p - z_i)^2}} \right)$$

where the sum is again over the 8 corner points of the magnet. The magnetic field caused by the magnet can now be calculated at every location inside or outside the magnet with the exception of some singularities on the edges of the magnet.

Appendix D

Analytical solution of Laplace's equation in a cylinder

We want to calculate the electric potential in VISIONI in absence of the filaments. One then has a cylinder with the top at -100 V and the rest at 0 V. The situation is sketched in figure D.1. The potential inside the cylinder can be found by solving Laplace's equation

$$\nabla^2 V = \frac{1}{r}\frac{\partial}{\partial r}\left(r\frac{\partial V}{\partial r}\right) + \frac{1}{r^2}\frac{\partial^2 V}{\partial \varphi^2} + \frac{\partial^2 V}{\partial z^2} = 0 \tag{D.1}$$

in combination with the appropriate boundary conditions

$$\begin{aligned} V(R,\varphi,z) &= 0 && \text{(D.2)} \\ V(r,\varphi,0) &= 0 && \text{(D.3)} \\ V(r,\varphi,H) &= -100. && \text{(D.4)} \end{aligned}$$

Cylindrical coordinates are used because of the cylindrical symmetry of the system. To solve (D.1) it is assumed that

$$V(r,\varphi,z) = R(r)\Phi(\phi)Z(z) \tag{D.5}$$

By separation of variables it can then be found that

$$\begin{aligned} V(r,\varphi,z) = \sum_{k=0}^{k=+\infty}\sum_{m=0}^{m=+\infty} &[A_{km}J_m(kr) + B_{km}N_m(kr)]\cdot \\ &[C_m\sin(m\varphi) + D_m\cos(m\varphi)]\cdot[E_k\sinh(kz) + F_k\cosh(kz)] \end{aligned} \tag{D.6}$$

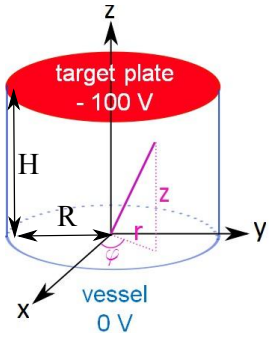

Figure D.1: Scheme of the applied electric potentials in VISIONI without the filaments

J_m is the mth Bessel functions and N_m is the mth Neumann function. Neumann functions, however, have a singularity for $r = 0$. This is of course unphysical. Therefore, $B_{km} = 0$ for all k and m. Further, the system exhibits cylindrical symmetry. Hence, the potential should not depend on φ. This leads to $m = 0$. From boundary condition (D.3) it is easy to see that $F_k = 0$ for all k. Boundary condition (D.2) implies that k can only take the values $k_{mn} = \frac{\chi_{mn}}{R}$ with χ_{mn} the nth zero of the mth Bessel function. Taking all this into account (D.6) can be simplified to

$$V(r,z) = \sum_{n=0}^{n=+\infty} A_n J_0\left(\frac{\chi_{0n}}{R} r\right) \sinh\left(\frac{\chi_{0n}}{R} z\right) \tag{D.7}$$

Now only the coefficients A_n remain unknown. Using the Bessel function identities

$$\int dr r^m J_{m-1}(r) = r^m J_m(r) \tag{D.8}$$

$$\int_0^R dr r J_m\left(\frac{\chi_{mk}}{R} r\right) J_m\left(\frac{\chi_{ml}}{R} r\right) = \delta_{kl} \frac{R^2}{2} \left[J_{m+1}(\chi_{mk})\right] \tag{D.9}$$

these coefficients can be calculated from boundary condition (D.4). The eventual expression for the electric potential becomes

$$V(r,z) = \sum_{n=0}^{n=+\infty} -\frac{200 J_0\left(\frac{\chi_{0n}}{R} r\right) \sinh\left(\frac{\chi_{0n}}{R} z\right)}{\chi_{0n} J_1(\chi_{0n}) \sinh\left(\frac{\chi_{0n}}{R} H\right)}. \tag{D.10}$$

Appendix E

Generation of random numbers

E.1 Monte Carlo codes and random numbers

The use of random numbers is an important characteristic of Monte Carlo codes. From experimental observations and theoretical calculations it is known that some physical variables are distributed according to a specific probability distribution function (PDF). In a Monte Carlo code random numbers are then generated according to this PDF to mimic reality. Computers usually come with a standard pseudo-random generator that generates uncorrelated pseudo-random numbers distributed uniformly between 0 and 1. For better statistics more sophisticated generators such as RANLUX from CERN [141] are advised. They come closer to the ideal random number generator. However, most physical variables are not distributed uniformly. Hence, algorithms are needed to convert the uniformly distributed pseudo-random numbers to numbers distributed according to another PDF.

E.2 Inverse transformation method

The inverse transformation method is an elegant and very efficient algorithm. The computer generates a pseudo-random number R according to a uniform distribution between 0 and 1. The inverse transformation method uses a function $f(R)$ to convert each pseudo-random number R into a variable x that is distributed according to the PDF $P(x)$. This can be expressed mathematically as

$$P(x')dx' = dR \tag{E.1}$$

with $x' = f(R)$ or $R = f^{-1}(x')$. By integrating this equation from $x' = -\infty$ up to $x' = x$ we get

$$F(x) = R \tag{E.2}$$

with $F(x)$ the cumulative PDF of $P(x)$. Inverting this relation results then in

$$x = F^{-1}(R) \tag{E.3}$$

This shows us that the function $f(R)$ we were looking for is the inverted cumulative PDF of $P(x)$. With this function each pseudo-random number R generated by the computer can now easily be converted into a number x that is distributed according to $P(x)$. The only disadvantage of this method is that not all PDF's have an invertible cumulative PDF.

E.3 Uniform distribution over 4π solid angle

A very common PDF is that of directions (θ, ϕ) uniformly distributed over the whole 4π solid angle. The polar angle θ is between 0 and π. The azimuthal angle ϕ is between 0 and 2π. This PDF is less straightforward to generate than might be expected at first sight. The polar angle θ is not uniformly distributed due to the Jacobian $J = \sin\theta$ corresponding to the curvilinear spherical coordinates on the unit sphere. The normalized partial PDF's for θ and ϕ are given by

$$P(\theta)d\theta = \frac{\sin\theta}{2}d\theta \tag{E.4}$$

$$P(\phi)d\phi = \frac{1}{2\pi}d\phi \tag{E.5}$$

Using the inverse transformation method described in section E.2, it can then easily be found that θ and ϕ can be calculated from two pseudo-random numbers R_1 and R_2 uniformly distributed between 0 and 1 according to

$$\theta = \arccos(1 - 2R_1) \tag{E.6}$$

$$\phi = 2\pi R_2 \tag{E.7}$$

E.4 Uniform distribution over circle

The next interesting PDF is that of points (r, ϕ) uniformly distributed over a circle. The radial coordinate r is between 0 and the circle radius R. The polar angle ϕ is between 0 and 2π. This PDF is again less straightforward to generate than might be expected at first sight due to the Jacobian $J = r$

corresponding to the curvilinear cylindrical coordinates. The normalized partial PDF's for r and ϕ are given by

$$P(r)dr = \frac{2}{R^2} r dr \tag{E.8}$$

$$P(\phi)d\phi = \frac{1}{2\pi} d\phi \tag{E.9}$$

Using again the inverse transformation method described in section E.2, it can then easily be found that r and ϕ can be calculated from two pseudo-random numbers R_1 and R_2 uniformly distributed between 0 and 1 according to

$$r = R\sqrt{R_1} \tag{E.10}$$

$$\phi = 2\pi R_2 \tag{E.11}$$

E.5 Cosine distribution with respect to surface normal

Another common PDF is that of directions (θ, ϕ) distributed over a 2π solid angle according to a cosine distribution with respect to the surface normal. The polar angle θ is between 0 and $\frac{\pi}{2}$. The azimuthal angle ϕ is between 0 and 2π. Again taking into account the Jacobian $J = \sin\theta$ for spherical coordinates on the unit sphere, the partial PDF's for θ and ϕ are given by

$$P(\theta)d\theta = 2\sin\theta\cos\theta \tag{E.12}$$

$$P(\phi)d\phi = \frac{1}{2\pi} d\phi \tag{E.13}$$

Using the inverse transformation method described in section E.2, it can then easily be found that θ and ϕ can be calculated from two pseudo-random numbers R_1 and R_2 uniformly distributed between 0 and 1 according to

$$\theta = \arcsin\sqrt{R_1} \tag{E.14}$$

$$\phi = 2\pi R_2 \tag{E.15}$$

E.6 Gaussian distribution

A Gaussian PDF with mean μ and standard deviation σ is given by

$$P(x;\mu,\sigma) = \frac{1}{\sqrt{2\pi}\sigma} e^{-\frac{(x-\mu)^2}{2\sigma^2}} \tag{E.16}$$

The parameters μ and σ can be eliminated by the substitution

$$t = \frac{x - \mu}{\sigma} \tag{E.17}$$

One then gets the standard Gaussian distribution

$$P(t) = \frac{1}{\sqrt{2\pi}} e^{-\frac{t^2}{2}} \tag{E.18}$$

For this PDF it is not possible to directly use the inverse transformation method described above because its cumulative PDF is the error function, which can not be described analytically. One has to take a small detour. It turns out that generating two Gaussian numbers at a time is more efficient. The joint PDF for two random numbers t_1 and t_2 distributed according to a standard Gaussian is given by

$$P(t_1, t_2) dt_1 dt_2 = \frac{1}{2\pi} e^{-\frac{t_1^2 + t_2^2}{2}} dt_1 dt_2 \tag{E.19}$$

This PDF can be converted into cylindrical coordinates by the substitutions

$$r = \sqrt{t_1^2 + t_2^2} \tag{E.20}$$

$$\theta = \arctan \frac{t_2}{t_1} \tag{E.21}$$

The PDF then becomes

$$P(r, \theta) r dr d\theta = \frac{1}{2\pi} e^{-\frac{r^2}{2}} r dr d\theta \tag{E.22}$$

The partial PDFs for r and θ are given by

$$P(r) dr = e^{-\frac{r^2}{2}} dr \tag{E.23}$$

$$P(\theta) d\theta = \frac{1}{2\pi} d\theta \tag{E.24}$$

These PDFs do have invertible cumulative PDFs. Using the inverse transformation method one can find that r and θ can be calculated from two pseudo-random numbers R_1 and R_2 distributed uniformly between 0 and 1 according to

$$r = \sqrt{-2 \ln R_1} \tag{E.25}$$

$$\theta = 2\pi R_2 \tag{E.26}$$

The two standard Gaussian numbers t_1 and t_2 can, therefore, be calculated as

$$t_1 = \sqrt{-2\ln R_1}\cos\left(2\pi R_2\right) \tag{E.27}$$

$$t_2 = \sqrt{-2\ln R_1}\sin\left(2\pi R_2\right) \tag{E.28}$$

By reverting the substitution (E.17) it can be found that two random numbers x_1 and x_2 distributed according to a Gaussian with mean μ and standard deviation σ can be calculated from

$$x_1 = \mu + \sigma\sqrt{-2\ln R_1}\cos\left(2\pi R_2\right) \tag{E.29}$$

$$x_2 = \mu + \sigma\sqrt{-2\ln R_1}\sin\left(2\pi R_2\right) \tag{E.30}$$

This method is called the Box-M*ü*ller method. A more efficient version of this algorithm can be derived. In the so called Marsaglia polar algorithm there is no need to evaluate a sine or cosine. This algorithm works as follows. First one calculates two random numbers v_1 and v_2 uniformly distributed between -1 and 1 from two pseudo-random numbers R_1 and R_2 uniformly distributed between 0 and 1 according to

$$v_1 = 2R_1 - 1 \tag{E.31}$$

$$v_2 = 2R_2 - 1 \tag{E.32}$$

All numbers v_1, v_2 for which $v_1^2 + v_2^2 > 1$ are rejected. In this way $v_1^2 + v_2^2$ is distributed uniformly between 0 and 1 and v_1 and v_2 are the Cartesian coordinates of uniformly distributed points in a circle with radius 1 centred on the origin. Looking back at the Box-M*ü*ller method (E.29-E.30), one can then make the substitutions

$$R_1 = v_1^2 + v_2^2 \tag{E.33}$$

$$\cos\left(2\pi R_2\right) = \frac{v_1}{\sqrt{v_1^2 + v_2^2}} \tag{E.34}$$

$$\sin\left(2\pi R_2\right) = \frac{v_2}{\sqrt{v_1^2 + v_2^2}} \tag{E.35}$$

This leads to the more efficient Marsaglia polar algorithm for generating two random numbers x_1 and x_2 gaussianly distributed with mean μ and standard deviation σ

$$x_1 = \mu + \sigma v_1\sqrt{-\frac{2\ln\left(v_1^2 + v_2^2\right)}{v_1^2 + v_2^2}} \tag{E.36}$$

$$x_2 = \mu + \sigma v_2\sqrt{-\frac{2\ln\left(v_1^2 + v_2^2\right)}{v_1^2 + v_2^2}} \tag{E.37}$$

A Gaussian distribution drops rapidly from its maximum value at the mean μ over a distance of a few σ. This makes it computationally very demanding to generate gaussianly distributed random numbers in the tail a distance l of a few σ away from the mean μ by simply rejecting the lower numbers. The Marsaglia algorithm can, however, easily be modified to do this much more efficiently. The two random numbers x_1 and x_2 in (E.36-E.37) are always bigger than l if

$$\mu + \sigma\sqrt{-2\ln\left(v_1^2 + v_2^2\right)} > l \tag{E.38}$$

or equivalently if

$$v_1^2 + v_2^2 < \exp\left(\frac{-(l-\mu)^2}{2\sigma^2}\right) \tag{E.39}$$

Since $0 \leq v_1^2, v_2^2 < 1$ one should then have in the limiting case that only one of the numbers v_1 and v_2 has a non-zero value

$$v_1, v_2 < \exp\left(\frac{-(l-\mu)^2}{4\sigma^2}\right) \tag{E.40}$$

This can be easily fulfilled by modifying (E.31-E.32) to

$$v_1 = (2R_1 - 1)\exp\left(\frac{-(l-\mu)^2}{4\sigma^2}\right) \tag{E.41}$$

$$v_2 = (2R_2 - 1)\exp\left(\frac{-(l-\mu)^2}{4\sigma^2}\right) \tag{E.42}$$

These limitations for v_1 and v_2 are necessary, but not sufficient to get gaussianly distributed random numbers bigger than l. The probability to get a rejection because x_1 or x_2 is below l is now, however, drastically decreased with respect to the original Marsaglia algorithm.

Appendix F

Technical details VMCPT

F.1 Compiling the code

On a UNIX system the code can easily be compiled by using the makefile. The source and header files should be in one directory together with the makefile. By entering the command *make ser* the serial version of VMCPT will be compiled and the executable *vmcpt.ser* will be created. By entering the command *make par* the parallel version of VMCPT will be compiled and the executable *vmcpt.ser* will be created.

On a Windows system one can for instance use Microsoft Visual Studio. All source and header files should be added to the project. The code can then easily be compiled by building the solution.

F.2 Running the code

To run the code on a UNIX system one should put the *vmcpt.ser* or *vmcpt.par* executable, the *bfield.dat* magnetic field data file and the *inputfile.dat* input file in one directory. The serial version can be started by going to the appropriate directory and entering the command *./vmcpt.ser inputfile.dat*. The parallel version can be started by going to the appropriate directory and entering the command *mpirun -np n ./vmcpt.par inputfile.dat* with n the number of processors to be used.

On a Windows system using Microsoft Visual Studio one should put the *bfield.dat* magnetic field data file and the *inputfile.dat* input file in the directory of the project. The name of the input file has to be specified under *Command Arguments* in the *Debugging* section of the project *Configuration Properties*. The simulation can then be started by choosing *Start Without Debugging* in the *Debug* menu.

F.3 Short description of the code

F.3.1 Header files

The header files *collisions.h*, *distributions.h*, *error.h*, *fields.h*, *initialize.h*, *mathematics.h*, *ranlxd.h*, *ranlxs.h*, and *trajectories.h* contain the function declarations of the source files with the same name. The header file *const.h* contains definitions of physical constants such as π, m_e, q_e, k, ϵ_0 and μ_0. Further it also contains constants related to the geometry of the plasma chamber, the strength of the permanent magnets and some more technical parameters. The header file *struct.h* declares the different structures used in the code.

F.3.2 Source files

bfield.cpp	
read_bfield	reads the magnetic field components and magnitude from the *bfield.dat* data file and stores the data
calc_bfield	calculates the magnetic field components and magnitude analytically and writes the data to the *bfield.dat* data file
bfield	updates the magnetic field of a particle
bx_rect	returns the x-component of the magnetic field of a rectangular magnet centred on the origin of the coordinate system and magnetized along the z-axis
by_rect	returns the y-component of the magnetic field of a rectangular magnet centred on the origin of the coordinate system and magnetized along the z-axis
bz_rect	returns the z-component of the magnetic field of a rectangular magnet centred on the origin of the coordinate system and magnetized along the z-axis
bx_wire	returns the x-component of the magnetic field of a wire centred on the origin of the coordinate system and oriented along the z-axis with an electric current in the positive z direction

by_wire	returns the y-component of the magnetic field of a wire centred on the origin of the coordinate system and oriented along the z-axis with an electric current in the positive z direction
b_visioni	calculates the magnetic field at a certain location in VISIONI
efield.cpp	
efield	updates the electric field of a particle
laplace_solver	solves Laplace's equation in VISIONI in the absence of plasma and stores the electric field components and the electric potential
poisson_solver	solves Poisson's equation taking into account the space charges of the plasma and stores the electric field components and the electric potential
poisson_initialization	initializes the data structure before solving Poisson's equation
init_rhs	initializes the right hand side of Poisson's equation based on the charged particle positions
distributions.cpp	
secondary_electron_energy_ion	picks the energy for a secondary electron produced by ionization from the appropriate distribution
secondary_electron_energy_wall	picks the energy for a secondary electron produced at the wall from the appropriate distribution
gaussian	picks random numbers from a gaussian distribution with the possibility to specify a lower limit
vector_cosine	picks a unit vector from a cosine distribution with respect to a given vector
angle_cosine	picks an azimuthal and polar angle from a cosine distribution with respect to a given vector
vector_uniform_sphere	picks a unit vector from a uniform distribution over the whole 4π solid angle
angle_uniform_sphere	picks an azimuthal and polar angle from a uniform distribution over the whole 4π solid angle

scattering_angles	picks an azimuthal and polar scattering angle from the appropriate distributions for a given collision
random_filament_position	picks a starting position from a uniform distribution over the surface of the tungsten filaments
random_maxwell_velocity	gives a particle a velocity vector picked from an isotropic Maxwellian distribution with a lower limit for the z-component
collisions.cpp	
mred	calculates the reduced mass of two particles
rescale_relative_velocity	calculates the rescaled relative velocity vector for a collision taking into account the energy loss and the change in reduced mass
rotate_relative_velocity	rotates the relative velocity vector for a collision with given azimuthal and polar scattering angles
post_collision_velocities	updates the velocity and energy of two colliding particles for a given azimuthal and polar scattering angles and collision type
null_collision	takes into account collisions of charged particles with neutrals using the null collision method
neutral_collision	lets two particles undergo a given collision and if necessary removes or creates particles
ee_binary_collision	takes into account electron-electron Coulomb collisions with the binary collision method
calc_sigma	calculate the cross section for a given reaction and impact energy
load_null_collision_data_janev	loads all data needed for taking into account collisions between particles
initialize.cpp	
initialize_particle	fills in all needed fields of the particle data structure to initialize a new particle
read_input_file	reads input parameters from the input file

remove_lost_particles	removes particles lost during collisions with other particles or the walls
load_particles	loads particles from previous output files if a previous simulation has to be resumed
calculate_sheath	calculates the sheath potential drop at the side and bottom of the plasma chamber by requiring global neutrality of the plasma
calculate_vmax	calculates the parameter vmax for the null collision method
reset_outputstruct	sets all fields of the output data structure to zero
rescale_weight	rescales the weight of the super-particles if the maximum number of super-particles has been reached
mathematics.cpp	
calloc_4d_double	allocates memory for a 4D data structure of doubles
azimuth	returns the azimuthal angle with respect to the x-axis for a given position in the xy-plane
absol	returns the absolute value of a double
cross_product	calculates the cross product of two vectors
scalar_product	returns the scalar product of two vectors
norm	calculates the norm of a vector
normalize	normalizes a vector
vec_min	calculates the difference of two vectors
vec_plus	calculates the sum of two vectors
vec_eq	sets a vector equal to another vector
vec_mult	multiplies a vector with a scalar
energy	returns the energy of a particle
transformation_matrix	calculates the transformation matrix to go from a rotated coordinate system with the z-axis along a given vector back to the original coordinate system

normal_to_reference	transforms a unit vector with given azimuthal and polar angle in the rotated coordinate system back to the original coordinate system using the given transformation matrix
normal_to_reference2	transforms a vector given in the rotated coordinate system with the z-axis along a given vector back to the original coordinate system
shuffle	shuffles an array randomly
interpolate	interpolates the y value for a given x from a given set of (x,y) data points
trajectories.cpp	
accelerate_particle	updates the velocity and energy of a particle after acceleration in the electric field during half of a time step
sheath_acceleration	updates the velocity and energy of a primary electron after acceleration in the sheath potential drop normal to the surface of the filaments
rotate_velocity	updates the velocity of a particle after gyration in the magnetic field during a full time step using the Boris method
shift_velocity	shifts the velocity of a particle backwards in time over half of a time step for the leapfrog integration scheme
move_particle	updates the position of a particle after moving during a full time step
reflection	takes into account reflection of a particle with the plasma chamber walls
calculate_trajectory	calculates the trajectory of a particle in the electromagnetic field up to a given time
move_particles	calculates the trajectory of all tracked particles until the end of the main time step

Bibliography

[1] D. J. C. MacKay. *Sustainable Energy - Without the Hot Air*. UIT Cambridge, 2009.

[2] J. Ongena and G. Van Oost. Energy for future centuries, prospects for fusion power as future energy source. In *Proceedings of the 9th Carolus Magnus Summer School on Plasma and Fusion Energy Physics*, 2009.

[3] J. Wesson. *Tokamaks*. Oxford University Press, 2004.

[4] http://www.tokamak.info.

[5] http://cnx.org/contents/031da8d3-b525-429c-80cf-6c8ed997733a@8.8:255.

[6] B. Povh, K. Rith, C. Scholz, and F. Zetsche. *Particles and Nuclei*. Springer, 2005.

[7] http://www.kayelaby.npl.co.uk.

[8] A. Piel. *An Introduction to Laboratory, Space, and Fusion Plasmas*. Springer, 2010.

[9] tokamak.e-monsite.com.

[10] G. Van Oost and E. Rebhan. Thermonuclear burn criteria. In *Proceedings of the 9th Carolus Magnus Summer School on Plasma and Fusion Energy Physics*, 2009.

[11] P. C. Stangeby. *The Plasma Boundary of Magnetic Fusion Devices*. Taylor & Francis, 2002.

[12] J. P. Freidberg. *Plasma Physics and Fusion Energy*. Cambridge University Press, 2007.

[13] http://www.iter.org.

[14] S. Tanaka, S. O'hira, and Y. Ichimasa. Overview of tritium safety studies in japan. *Fusion Engineering and Design*, 63-4:139–152, 2002.

[15] L. D. Landau and E. M. Lifshitz. *Statistical Physics Part 1.* Pergamon Press, 1980.

[16] M. A. Lieberman and A. J. Lichtenberg, editors. *Principles of Plasma Discharges and Materials Processing.* John Wiley & Sons, Inc., 2005.

[17] P. K. Chu and X. Lu, editors. *Low Temperature Plasma Technology, Methods and Applications.* CRC Press, 2014.

[18] A. Bogaerts, E. Bultinck, M. Eckert, et al. Computer modeling of plasmas and plasma-surface interactions. *Plasma Processes and Polymers*, 6:295–307, 2009.

[19] J. van Dijk, G. M. W. Kroesen, and A. Bogaerts. Plasma modelling and numerical simulation. *Journal of Physics D: Applied Physics*, 42:190301, 2009.

[20] C. K. Birdsall and A. B. Langdon. *Plasma Physics via Computer Simulation.* IOP Publishing Ltd, 1991.

[21] R. W. Hockney and J. W. Eastwood. *Computer Simulation Using Particles.* IOP Publishing Ltd, 1988.

[22] K. Nanbu. Probability Theory of Electron-Molecule, Ion-Molecule, Molecule-Molecule, and Coulomb Collisions for Particle Modeling of Material Processing Plasmas and Gases. *IEEE Transactions on Plasma Science*, 28:971–990, 2000.

[23] D. Pagano, C. Gorse, and M. Capitelli. Modeling Multicusp Negative-Ion Sources. *IEEE Transactions on Plasma Science*, 35:1247–1259, 2007.

[24] S. D. Rockwood. Elastic and inelastic cross sections for electron-Hg scattering from Hg transport data. *Physical Review A*, 8:2348–2358, 1973.

[25] G. J. M. Hagelaar and L. C. Pitchford. Solving the Boltzmann equation to obtain electron transport coefficients and rate coefficients for fluid models. *Plasma Sources Science and Technology*, 14:722–733, 2005.

[26] L. L. Alves. Fluid modelling of the positive column of direct-current glow discharges. *Plasma Sources Science and Technology*, 16:557–569, 2007.

[27] R. D. White, R. E. Robson, S. Dujko, et al. Recent advances in the application of Boltzmann equation and fluid equation methods to charged particle transport in non-equilibrium plasmas. *Journal of Physics D: Applied Physics*, 42:194001, 2009.

[28] S. I. Braginskii. *Review of Plasma Physics vol 1*, chapter Transport processes in a plasma. New York: Consultatns Bureau, 1965.

[29] P. M. Bellan. *Fundamentals of Plasma Physics*. Cambridge University Press, 2006.

[30] F. F. Chen. *Introduction to Plasma Physics and Controlled Fusion*. Plenum Press, 1984.

[31] E. W. McDaniel. *Collision Phenomena in Ionized Gases*. Wiley, 1964.

[32] H. Goldstein. *Classical Mechanics*. Addison-Wesley Publishing Company, 1980.

[33] L. D. Landau and E. M. Lifshitz. *Mechanics and electrodynamics*. Pergamon Press, 1972.

[34] R. J. Goldston and P. H. Rutherford. *Introduction to Plasma Physics*. IOP Publishing Ltd, 1995.

[35] N. Hershkowitz. Sheaths: More complicated than you think. *Physics of Plasmas*, 12:055502, 2005.

[36] K. U. Riemann. The Bohm criterion and sheath formation. *Journal of Physics D*, 24:493–518, 1990.

[37] L. Oksuz and N. Hershkowitz. Plasma, presheath, collisional sheath and collisionless sheath potential profiles in weakly ionized, weakly collisional plasma. *Plasma Sources Science and Technology*, 14:201–208, 2003.

[38] P. D. Prewett and J. E. Allen. The double sheath associated with a hot cathode. *Proceedings of the Royal Society London A*, 348:435–446, 1976.

[39] N. Hershkowitz. *Plasma Diagnostics, Discharge Parameters and Chemistry*, chapter How Langmuir probes work. Academic, Boston, 1989.

[40] R. L. Merlino. Understanding Langmuir probe current-voltage characteristics. *American Journal of Physics*, 75:1078–1085, 2007.

[41] I. H. Hutchinson. *Principles of Plasma Diagnostics*. Cambridge University Press, 2002.

[42] S. B. Song, C. S. Chang, and D. I. Choi. Effect of two-temperature electron distribution on the Bohm sheath criterion. *Phys. Rev. E*, 55:1213–1216, 1997.

[43] J. J. Scholtz, D. Dijkkamp, and R. W. A. Schmitz. Secondary electron emission properties. *Philips Journal of Research*, 50:375–389, 1996.

[44] R. A. Langley, J. Bohdansky, W. Eckstein, et al. Data compendium for plasma-surface interactions. *Nuclear Fusion*, 24:9–117, 1984.

[45] E. W. Thomas. Particle-impact induced electron ejection from surfaces. Technical report, International Atomic Energy Agency, 1995.

[46] H. Mott-Smith and I. Langmuir. The theory of collectors in gaseous discharges. *Physical Review*, 28:727–763, 1926.

[47] J. E. Allen, R. L. F. Boyd, and P. Reynolds. The collection of poisitive ions by a probe immersed in a plasma. *Proceedings of the physical society B*, 70:297–304, 1957.

[48] I. B. Bernstein and I. N. Rabinowitz. Theory of electrostatic probes in a low-density plasma. *Physics of Fluids*, 2:112–121, 1959.

[49] J. G. Laframboise. Theory of spherical and cylindrical langmuir probes in a collisionless, maxwellian plasma at rest. Technical report, University of Toronto Institute of Aerospace Studies, 1966.

[50] F. F. Chen. Langmuir probe analysis for high density plasmas. *Physics of Plasmas*, 8:3029–3041, 2001.

[51] G. Fursey. *Field Emission in Vacuum Microelectronics*. Kluwer Academic / Plenum Publishers, 2005.

[52] E. L. Murphy and R. H. Good. Thermionic emission, field emission, and the transition region. *Physical Review*, 102:1464–1473, 1956.

[53] http://www.hbcpnetbase.com.

[54] C. P. Norris, editor. *Surface Science Research*. Nova Science Publishers, 2005.

[55] E. Lassner and Schubert W.-D. *Tungsten. Properties, Chemistry, Technology of the Element, Alloys and Chemical Compounds*. Kluwer Academic / Plenum Publishers, 1999.

[56] R. Timm and A. Piel. Hysteresis and transition to chaos in a thermionic plasma discharge. *Contributions to Plasma Physics*, 32:599–611, 1992.

[57] R. E. Bunney. Review of literature secondary electron emission. Technical report, NASA, 1964.

[58] R. Behrisch and W. Eckstein, editors. *Sputtering by particle bombardment*. Springer, 2007.

[59] R. Behrisch, editor. *Sputtering by particle bombardment II.* Springer, 1983.

[60] A. Kirschner. Erosion and deposition mechanisms in fusion plasmas. *Transactions of Fusion Science and Technology*, 57:277–292, 2010.

[61] P. Sigmund. Theory of sputtering. I. Sputtering yield of amorphous and polycrystalline targets. *Physical Review*, 184:383–416, 1969.

[62] J. P. Biersack. A Monte Carlo computer program for the transport of energetic ions in amorphous targets. *Nuclear Instruments and Methods*, 174:257–269, 1980.

[63] J. P. Biersack and W. Eckstein. Sputtering studies with the Monte-Carlo program TRIM.SP. *Applied Physics A*, 34:73–94, 1984.

[64] W. Moller, W. Eckstein, and J. P. Biersack. Tridyn - Binary collision simulation of atomic collisions and dynamic composition changes in solids. *Computer Physics Communications*, 51:355–368, 1988.

[65] W. Eckstein, R. Dohmen, and A. Mutzke. Sdtrimsp: A monte-carlo code for calculating collision phenomena in randomized targets. Technical report, Max-Planck-Institut für Plasmaphysik, 2007.

[66] M. T. Robinson and I. M. Torrens. Computer simulation of atomic-displacement cascades in solids in the binary-collision approximation. *Physical Review B*, 9:5008, 1974.

[67] J. Bohdansky. A universal relation for the sputtering yield of monatomic solids at normal ion incidence. *Nuclear Instruments and Methods in Physics Research*, B2:587–591, 1984.

[68] Y. Yamamura, Y. Itikawa, and N. Itoh. Angular dependence of sputtering yields of monatomic solids. Technical report, Institute of Plasma Physics Nagoya University, 1983.

[69] C. Garcia-Rosales, W. Eckstein, and J. Roth. Revised formulae for sputtering data. *Journal of Nuclear Materials*, 218:8–17, 1994.

[70] W. Eckstein and R. Preuss. New fit formulae for the sputtering yield. *Journal of Nuclear Materials*, 320:209–213, 2003.

[71] J. Roth and W. Möller. Mechanism of enhanced sputtering of carbon at temperatures above 1200^{o}C. *Nuclear Instruments and Methods in Physics Research*, B7/8:788–792, 1985.

[72] C. Björkas, K. Vörtler, K. Nordlund, et al. Chemical sputtering of Be due to D bombardment. *New Journal of Physics*, 11:123017, 2009.

[73] J. Küppers. The hydrogen surface chemistry of carbon as a plasma facing material. *Surface Science Reports*, 22:249–321, 1995.

[74] E. Vietzke, V. Philipps, K. Flaskamp, et al. The reaction of atomic hydrogen with a-C:H and diamond films. *Surface and Coatings Technology*, 47:156–161, 1991.

[75] E. Vietzke and V. Philipps. Hydrocarbon formation on carbon surfaces facing a hydrogen plasma. *Fusion Technology*, 15:108–117, 1988.

[76] P. R. Harris, F. W. Meyer, W. Jacob, et al. Molecular size effect in the chemical sputtering of a-C:H thin films by low energy H^+, H_2^+, and H_3^+ ions. *Nuclear Instruments and Methods in Physics Research B*, 269:1276–1279, 2011.

[77] J. Roth and C. Garcia-Rosales. Analytic description of the chemical erosion of graphite by hydrogen ions. *Nuclear Fusion*, 36:1647–1659, 1996.

[78] J. Roth, R. Preuss, W. Bohmeyer, et al. Flux dependence of carbon chemical erosion by deuterium ions. *Nuclear Fusion*, 44:L21–L25, 2004.

[79] W. Eckstein. Calculated sputtering, reflection and range values. Technical report, Max-Planck-Institut für Plasmaphysik, 2002.

[80] K. Ohya and K. Inai. Hydrocarbon redeposition on plasma facing walls intersecting magnetic field at shallow angles. *Japanese Journal of Applied Physics*, 49:096201, 2010.

[81] K. Tichmann, U. von Toussaint, and W. Schwarz-Selinger, T.and Jacob. Determination of the sticking probability of hydrocarbons on an amorphous hydrocarbon surface. *Physica Scripta*, T138:014015, 2009.

[82] R. A. Causey. Hydrogen isotope retention and recycling in fusion reactor plasma-facing components. *Journal of Nuclear Materials*, 300:91–117, 2002.

[83] D. Reiter and R.E.H. Clark, editors. *Nuclear fusion research, Understanding plasma-surface interactions*. Springer, 2005.

[84] W. Jacob. Surface reactions during growth and erosion of hydrocarbon films. *Thin Solid Films*, 326:1–42, 1998.

[85] A. von Keudell and W. Jacob. Elementary processes in plasma surface interaction: H-atom and ion-induced chemisorption of methyl on hydrocarbon film surfaces. *Progress in Surface Science*, 76:21–54, 2004.

[86] C. Hopf, T. Schwarz-Selinger, W. Jacob, and A. von Keudell. Surface loss probabilities of hydrocarbon radicals on amorphous hydrogenated carbon film surfaces. *Journal of Applied Physics*, 87:2719–2725, 1999.

[87] A. von Keudell, C. Hopf, T. Schwartz-Selinger, and W. Jacob. Surface loss probabilities of hydrocarbon radicals on amorphous hydrogenated carbon film surfaces: Consequences for the formation of re-deposited layers in fusion experiments. *Nuclear Fusion*, 39:1451–1462, 1999.

[88] M. Mayer and V. Rohde. Further insight into the mechanism of hydrocarbon layer formation below the divertor of ASDEX upgrade. *Nuclear Fusion*, 46:914–920, 2006.

[89] D. A. Alman and D. N. Ruzic. Molecular dynamics simulation of hydrocarbon reflection and dissociation coefficients from fusion-relevant carbon surfaces. *Physica Scripta*, T111:145–151, 2004.

[90] A.R. Sharma, R. Schneider, U. Toussaint, and K. Nordlund. Hydrocarbon radicals interaction with amorphous carbon surfaces. *Journal of Nuclear Materials*, 363-365:1283–1288, 2007.

[91] E. D. de Rooij, A. W. Kleyn, and W. J. Goedheer. Sticking of hydrocarbon radicals on different amorphous hydrogenated carbon surfaces: a molecular dynamics study. *Physical Chemistry Chemical Physics*, 12:14067–14075, 2010.

[92] K. Tichmann, U. von Toussaint, and W. Jacob. Determination of the sticking coefficient of energetic hydrocarbon molecules by molecular dynamics. *Journal of Nuclear Materials*, 420:291–296, 2012.

[93] J. Roth, E. Tsitrone, A. Loarte, et al. Recent analysis of key plasma wall interaction issues for ITER. *Journal of Nuclear Materials*, 390-391:1–9, 2009.

[94] G. Federici, C. H. Skinner, J. N. Brooks, et al. Plasma-material interactions in current tokamaks and their implications for next step fusion reactors. *Nuclear Fusion*, 41:1967–2137, 2001.

[95] G. Federici, P. Andrew, P. Barabaschi, et al. Key ITER plasma edge and plasma-material interaction issues. *Journal of Nuclear Materials*, 313-316:11–22, 2003.

[96] U. Samm. TEXTOR: A pioneering device for new concepts in plasma-wall interaction, exhaust and confinement. *Fusion Science and Technology*, 47:73–75, 2004.

[97] O. Neubauer, G. Czymek, B. Giesen, et al. Design features of the tokamak TEXTOR. *Fusion Science and Technology*, 47:76–86, 2004.

[98] http://www.fz-juelich.de.

[99] B. Schweer, S. Brezinsek, H. G. Esser, et al. Limiter lock systems at TEXTOR: Flexible tools for plasma-wall investigation. *Fusion Science and Technology*, 47:138–145, 2004.

[100] R. Ding, A. Kirschner, D. Borodin, et al. Simulation of light emission from hydrocarbon injection in TEXTOR using the ERO code. *Plasma Physics and Controlled Fusion*, 51:055019, 2009.

[101] S. Brezinsek, A. Pospieszczyk, D. Borodin, et al. Hydrocarbon injection for quantification of chemical erosion yields in tokamaks. *Journal of Nuclear Materials*, 363-365:1119–1128, 2007.

[102] O. Schmitz, I. L. Beigman, L. A. Vainshtein, et al. Status of electron temperature and density measurement with beam emission spectroscopy on thermal helium at TEXTOR. *Plasma Physics and Controlled Fusion*, 50:115004, 2008.

[103] A. Kreter, P. Wienhold, D. Borodin, et al. Study of local carbon transport on graphite, tungsten and molybdenum test limiters in TEXTOR by $^{13}CH_4$ tracer injection. *Journal of Nuclear Materials*, 363-365:179–183, 2007.

[104] P. Wienhold, H. G. Esser, D. Hildebrandt, et al. Investigation of carbon transport in the scrape-off layer of TEXTOR-94. *Journal of Nuclear Materials*, 290-293:362–366, 2001.

[105] S. Brezinsek, G. Sergienko, A. Pospieszczyk, et al. Characterization of the deuterium recycling flux in front of a graphite surface in the TEXTOR tokamak. *Plasma Physics and Controlled Fusion*, 47:615–634, 2005.

[106] P. Wienhold, F. Weschenfelder, and J. Winter. Colorimetry of interference colours to investigate thickness changes of protective coatings in TEXTOR. *Nuclear Instruments and Methods in Physics Research B*, 94:503–510, 1994.

[107] S. Tominetti, J. Camposilvan, and A. Perujo. Hydrogen isotopes recycling studies at JRC Ispra. *Vuoto*, XXVI:13–17, 1997.

[108] I. Uytdenhouwen, J. Schuurmans, M. Decréton, et al. Installation of a plasmatron at the Belgian Nuclear Research centre and its use for plasma-wall interaction studies. *Plasma and Fusion Science*, 996:159–165, 2008.

[109] B. Unterberg, R. Jaspers, R. Koch, et al. New linear plasma devices in the trilateral euregio cluster for an integrated approach to plasma surface interactions in fusion reactors. *Fusion Engineering and Design*, 86:1797–1800, 2011.

[110] G. J. van Rooij. Laboratory experiments and devices to study plasma surface interaction. *Fusion Science and Technology*, 61:266–272, 2012.

[111] R. Limpaecher and K. R. MacKenzie. Magnetic multipole containment of large uniform collisionless quiescent plasmas. *Review of Scientific Instruments*, 44:726–731, 1972.

[112] I. G. Brown, editor. *The physics and technology of ion sources*. Wiley-VCH Verlag GmbH & Co. KGaA, 2004.

[113] K. N. Leung, N. Hershkowitz, and K. R. MacKenzie. Plasma confinement by localized cusps. *Physics of Fluids*, 19:1045–1053, 1976.

[114] C. Gauthereau and G. Matthieussent. Plasma density profiles in discharges surrounded by magnetic mutipole walls. *Physics Letters*, 102A:231–234, 1983.

[115] http://www.smma.org/pdf/permanent-magnet-materials.pdf.

[116] P. Campbell. *Permanent Magnet Materials and their Application*. Cambridge University Press, 1994.

[117] http://www.hidenanalytical.com.

[118] http://www.hidenanalytical.com/.

[119] http://www.eirene.de/manuals/hydhel.pdf.

[120] R. K. Janev, D. Reiter, and Samm U. Collision processes in low-temperature hydrogen plasmas. Technical report, Forschungszentrum Jülich, 2003.

[121] R. T. Brackmann, W. L. Fite, and R. H. Neynaber. Collisions of electrons with hydrogen atoms. *Physical Review*, 112:1157–1161, 1958.

[122] J. Callaway. Scattering of electrons by atomic hydrogen at intermediate energies: Elastic scattering and n = 2 excitation from 12 to 54 eV. *Physical Review A*, 32:775–783, 1985.

[123] J.-S. Yoon, M.-Y. Song, J.-M. Han, et al. Cross sections for Electron Collisions with Hydrogen Molecules. *Journal of Physical and Chemical Reference Data*, 37:913–931, 2008.

[124] T. Tabata and T. Shirai. Analytical cross sections for collisions of H^+, H_2^+, H_3^+, H, H_2 and H^- with hydrogen molecules. *Atomic Data and Nuclear Data Tables*, 76:1–25, 2000.

[125] D. Naujoks, R. Behrisch, J. P. Coad, and L. C. J. M. De Kock. Material transport by erosion and redeposition on surface probes in the scrape-off layer of JET. *Nuclear Fusion*, 33:581–590, 1993.

[126] A. Kirschner, V. Philipps, J. Winter, et al. Simulation of the plasma-wall interaction in a tokamak with the Monte Carlo code ERO-TEXTOR. *Nuclear Fusion*, 40:989–1001, 2000.

[127] M. I. Airila, L. Aho-Mantila, S. Brezinsek, et al. ERO modelling of local deposition of injected $^{1}3C$ tracer at the outer divertor of JET. *Physica Scripta*, T138:014021, 2009.

[128] A. Kirschner, K. Ohya, D. Borodin, et al. Prediction of long-term tritium retention in the divertor of ITER: influence of modelling assumptions on retention rates. *Physica Scripta*, T138:014011, 2009.

[129] D. Borodin, A. Kirschner, A. Kreter, et al. Modelling of Be transport in PSI experiments at PISCES-B. *Journal of Nuclear Materials*, 390-391:106–109, 2009.

[130] D. Borodin, A. Kirschner, S. Droste, et al. Modelling of chemical erosion mitigation experiments at PISCES-B using the 3D Monte-Carlo code ERO. *Physica Scripta*, T128:127–132, 2007.

[131] D. Borodin, A. Kirschner, D. Nishijima, et al. Modelling of impurity transport in the linear plasma devices PISCES-B and Pilot-PSI using the Monte-Carlo code ERO. *Contributions to Plasma Physics*, 50:432–438, 2010.

[132] L. Aho-Mantilla, M. Winschmeier, K. Krieger, et al. Effect of $E \times B$ driven transport on the deposition of carbon in the outer divertor of ASDEX Upgrade. *Journal of Nuclear Materials*, 415:S231–S234, 2011.

[133] V. A. Abramov, Y. L. Igitkhanov, V. I. Pistunovich, and V. A. Pozharov. First wall and divertor plate sputtering in a tokamak reactor. *Journal of Nuclear Materials*, 162-164:462–466, 1989.

[134] http://open.adas.ac.uk/.

[135] W Lotz. An Empirical Formula for the Electron-Impact Ionization Cross-Section. *Zeitschrift für Physik*, 206:205–211, 1967.

[136] http://www.hydkin.de/.

[137] R. K. Janev and D. Reiter. Collision processes of CH_y and CH_y^+ hydrocarbons with plasma electrons and protons. *Physics of Plasmas*, 9:4071–4081, 2002.

[138] S. Droste, A. Kirschner, D. Borodin, et al. Modelling of $^{1}3CH_4$ injection experiments with graphite and tungsten test limiters in TEXTOR using the coupled code ERO-SDTrimSP. *Plasma Physics and Controlled Fusion*, 50:015006, 2008.

[139] M. I. Airila, T. Ikonen, D. Borodin, et al. Improvement of surface processes modelling in the ERO code. *Journal of Nuclear Materials*, 390-391:175–178, 2009.

[140] D. Reiter, P. Bogen, and U. Samm. Measurement and Monte Carlo computations of Hα profiles in front of a TEXTOR limiter. *Journal of Nuclear Materials*, 196-198:1059–1064, 1992.

[141] http://luscher.web.cern.ch/luscher/ranlux/.

[142] I. Fujino, A. Hatayama, and N. Takado. Analysis of electron energy distribution of an arc-discharge H^- ion source with Monte Carlo simulation. *Review of Scientific Instruments*, 79:02A510, 2008.

[143] R. Terasaki, I. Fujino, A. Hatayama, et al. 3D modeling of the electron energy distribution function in negative hydrogen ion sources. *Review of Scientific Instruments*, 81:02A703, 2010.

[144] C. Yang, X-B Wu, and D-G Liu. Three-dimensional particle-in-cell with Monte Carlo collision simulation of the electron energy distribution function in the multi-cusp ion source for proton therapy. *Chinese Physics C*, 36:1013–1018, 2012.

[145] J. Bretagne, W. G. Graham, and M. B. Hopkins. A comparison of experimental and theoretical electron energy distribution functions in a multicusp ion source. *Journal of Physics D: Applied Physics*, 24:668–671, 1991.

[146] J. Bretagne, G. Delouya, C. Gorse, et al. Electron energy distribution functions in electron-beam-sustained discharges: application to magnetic multicusp hydrogen discharges. *Journal of Physics D: Applied Physics*, 18:811–825, 1985.

[147] J. Bretagne, G. Delouya, C. Gorse, and M. Bacal. On electron energy distribution functions in low-pressure magnetic multicusp hydrogen discharges. *Journal of Physics D: Applied Physics*, 19:1197–1211, 1986.

[148] P. J. Eenshuistra, R. M. A. Heeren, A. W. Kleyn, and H. J. Hopman. Dissociation and vibrational excitation of H_2 molecules and wall influence on the densities in a multicusp ion source. *Physical Review A*, 40:3613–3625, 1989.

[149] A. Bogaerts and R. Gijbels. Effects of adding hydrogen to an argon glow discharge: overview of relevant processes and some qualitative explanations. *J. Anal. At. Spectrom.*, 15:441–449, 2000.

[150] A. I. Livshits, F. E. Balghiti, and M. Bacal. Dissociation of hydrogen molecules on metal filaments in H^- ion sources. *Plasma Source Science and Technology*, 3:465–472, 1994.

[151] M. Mozetič, M. Drobnič, and A. Zalar. Recombination of neutral hydrogen atoms on AISI 304 stainless steel surface. *Applied Surface Science*, 144-145:399–403, 1999.

[152] K. W. Ehlers and K. N. Leung. Some characteristics of tungsten filaments operated as cathodes in a gas discharge. *Review of Scientific Instruments*, 50:356–361, 1979.

[153] J. P. Boris. Relativistic plasma simulation - Optimization of a hybrid code. In *Proceedings of the 4th Conference on Numerical Simulation of Plasmas*, pages 3–67, 1970.

[154] C. F. Barnett, J. A. Ray, and J. C. Thompson. Atomic and molecular collision cross sections of interest in controlled thermonuclear research. Technical report, Oak Ridge National Laboratory, 1964.

[155] J.-S. Yoon, Y.-W. Kim, D.-C. Kwon, et al. Electron-impact cross sections for deuterated hydrogen and deuterium molecules. *Reports on progress in physics*, 73:116401, 2010.

[156] B. H. Bransden and C. J. Joachain. *Physics of atoms and molecules*. Longman Group Limited, 1983.

[157] A. Okhrimovskyy, A. Bogaerts, and R. Gijbels. Electron anisotropic scattering in gases: A formula for Monte Carlo simulations. *Physical Review E*, 65:037402, 2002.

[158] V. Vahedi and M. Surendra. A Monte Carlo collision model for the particle-in-cell method: applications to argon and oxygen discharges. *Computer Physics Communications*, 87:179–198, 1994.

[159] E. Chacon-Golcher and K. J. Bowers. Particle-in-Cell with Monte Carlo Collisions Gun Code Simulations of a Surface-Conversion H^- Ion Source. *Communications in computational physics*, 4:659–674, 2008.

[160] T. Takizuka and H. Abe. A binary collision model for plasma simulation with a particle code. *Journal of Computational Physics*, 25:205–219, 1977.

[161] C. Chan, T. Intrator, and N. Hershkowitz. The effect of secondary electrons on plasma potential in a multi-dipole device. *Physical Letters*, 91A:167–170, 1982.

[162] http://www.mpi-forum.org/docs/.

[163] G. Hager and G. Wellein. *Introduction to High Performance Computing for Scientists and Engineers*. CRC Press, Taylor & Francis Group, 2011.

[164] http://www.ugent.be/hpc/.

[165] https://www.python.org/.

[166] http://easygui.sourceforge.net.

[167] http://www.py2exe.org/.

[168] J. G. Laframboise and J. Rubinstein. Theory of a cylindrical probe in a collisionless magnetoplasma. *Physics of Fluids*, 19:1900–1908, 1976.

[169] http://newville.github.io/lmfit-py.

[170] A. Kirschner, P. Wienhold, V. Philipps, et al. Modelling of carbon transport in fusion devices: evidence of enhanced re-erosion of in-situ re-deposited carbon. *Journal of Nuclear Materials*, 328:62–66, 2004.

[171] A. Kirschner, A. Kreter, P. Wienhold, et al. Deposition and re-erosion studies by means of local impurity injection in TEXTOR. *Journal of Nuclear Materials*, 415:S239–S245, 2011.

[172] K. Ohya and A. Kirschner. Modeling of erosion and deposition by the Monte Carlo codes EDDY and ERO. *Physica Scripta*, T138:014010, 2009.

[173] R. P. Doerner, D. Nishijima, and T. Scharz-Selinger. Measuring the difference between gross and net erosion. *Nuclear Fusion*, 52:103003, 2012.

[174] J. Vanderlinde. *Classical Electromagnetic Theory*. Kluwer Academic Publishers, 2005.

[175] X. Gou, Y. Yang, X. Zheng, et al. Analytic expression of magnetic field distribution of rectangular permanent magnets. *Applied Mathematics and Mechanics (English edition)*, 25:297–306, 2004.

[176] F. Bancel. Magnetic nodes. *Journal of Physics D: Applied Physics*, 32:2155–2161, 1999.

[177] http://web.mit.edu/viz/soft/visualizations/DLIC/DLIC.htm.

[178] A. Sundquist. Dynamic Line Integral Convolution for visualizing streamline evolution. *IEEE Transactions on Visualization and Computer Graphics*, 9:273–282, 2003.

[179] J. C. De Vos. A new determination of the emissivity of tungsten ribbon. *Physica*, 20:690–712, 1954.

[180] K. Poelmans. Investigation of the secondary ionization effect and the validation of the single fixed langmuir probe in the plasmatron visioni (master thesis). Technical report, Ghent University, 2013.

[181] E. Chang and S.-F. Wong. Isotope effects in molecular scattering by electrons. *Physical Review Letters*, 38:1327–1330, 1977.

[182] M. Bacal. Physics aspects of negative ion sources. *Nuclear Fusion*, 46:S250–S259, 2006.

[183] M. B. Hopkins, M. Bacal, and W. G. Graham. Electron energy distribution functions and negative ion concentrations in tandem and hybrid multicusp negative hydrogen ion sources. *Journal of Physics D*, 24:268–276, 1990.

[184] I. Méndez, F. J. Gordillo-Vázquez, V. J. Herrero, and I. Tanarro. Atom and ion chemistry in low pressure hydrogen DC plasmas. *Journal of Physical Chemistry A*, 110:6060–6066, 2006.

[185] K. Sawada and T. Fujimoto. Effective ionization and dissociation rate coefficients of molecular hydrogen in plasma. *Journal of Applied Physics*, 78:2913–2924, 1995.

[186] Y. Lee, R. A. Gough, K. N. Leung, et al. A compact filament-driven multicusp ion source. *Nuclear Instruments and Methods in Physics Research B*, 119:543–548, 1996.

[187] G. Joseph. *Copper: Its trade, manufacture, use and environmental status*. ASM International, 1999.

[188] J. L. Whitton, L. Tanović, and J. S. Williams. The production of regular pyramids on argon ion bombarded surfaces of copper crystals. *Applications of Surface Science*, 1:408–413, 1978.

[189] R. S. Robinson and S. M. Rossnagel. Ion-beam-induced topography and surface diffusion. *Journal of Vacuum Science Technology*, 21:790–797, 1982.

[190] R. Kelly and O. Auciello. On the origin of pyramids and cones on ion-bombarded copper surfaces. *Surface Science*, 100:135–153, 1980.

[191] R. P. Doerner, M. J. Baldwin, and D. Nishijima. Plasma-induced morphology of beryllium targets exposed in Pisces-B. *Journal of Nuclear Materials*, 2014.

[192] C. Björkas and K. Nordlund. Variables affecting simulated Be sputtering yields. *Journal of Nuclear Materials*, 439:174–179, 2013.

[193] R. P. Doerner, C. Björkas, D. Nishijima, and T. Scharz-Selinger. Erosion of beryllium under high-flux plasma impact. *Journal of Nuclear Materials*, 438:S272–S275, 2013.

[194] http://tandem.nipne.ro/ tnd3m/index.html.

[195] M. Mayer. SIMNRA User's Guide, Report IPP 9/113. Technical report, Max-Planck-Institut für Plasmaphysik Garching, 1997.

[196] A. Kirschner, P. Wienhold, D. Borodin, et al. Studies of impurity migration in TEXTOR by local tracer injection. *Journal of Nuclear Materials*, 438:S723–S726, 2013.

[197] D. Matveev, P. Wienhold, A. Kirschner, et al. Deposition of tungsten and carbon at local plasma-shadowed areas in textor test limiter experiments. 21st International Conference on Plasma Surface Interactions, 2014.